Intrabasinal Sediments and Tectonostratigraphy of the N.E. Lau Basin: Contributions to Extensional Models of Back-Arc Basins

JESSIE KEHEW

Thesis submitted to the University of Ottawa
in partial fulfillment of the requirements for the
Master's degree in Earth Sciences

Department of Earth and Environmental Sciences
Faculty of Science
University of Ottawa

© Jessie Kehew, Ottawa, Canada, 2023

Abstract

Sediment deposited in back-arc basins preserves a record of the extensional, volcanic and tectonic history of the arc-backarc systems. Back-arc sedimentation is of particular interest as seafloor massive sulfide deposits may be preserved in back-arc basin sediments.

The study of back-arc sedimentation using acoustic data, such as high-resolution sub-bottom profiling data (Parasound) and seismic reflection data, can be a much more cost effective approach than analysis of sediments recovered from drill cores. In this study, we use these two acoustic datasets to build a facies model of sedimentation in the northeast Lau Basin, an actively opening back-arc basin in the southwest Pacific Ocean. Using 830 km of Parasound and 730 km of seismic lines along 4 transects of the Lau Basin, we constructed one of the most detailed models of sedimentation in a back-arc basin to date. Parasound data show distinct echoes with sub-bottom reflections indicative of a high proportion of hemipelagic sediment, whereas the indistinct echoes with few to no sub-bottom reflections indicate a higher proportion of coarse, bedded, volcaniclastic turbidites. Hyperbolic echoes are associated with regions of rugged or uneven terrain characterized by exposed, rough basement or deposits formed by contour currents, turbidity currents, slumps or slides. These relationships form the basis of an echo-facies legend developed for typical back-arc basin sediments. The echo-facies observed in the Parasound, and confirmed by deeper-penetrating seismic reflection data, provide important insights into the sedimentary processes involved in back-arc sedimentation. We observed mass transport deposits (MTDs) in all of the sub-basins and slope deposits within and on the flanks of active rifts (e.g., the Fonualei Rift and Spreading Centre, FRSC), suggesting a direct correlation between MTDs and zones of active rifting. We observed an overall increase in sediment thickness toward the Tofua Arc which suggests it is the main sediment source, but local variations in sediment thickness suggest significant input from local intrabasinal seamounts. The uppermost echo-facies in over 60% of the sub-basins in the study area is dominated by hemipelagic material, which suggests an abrupt transition in the dominant sediment source from volcaniclastic to hemipelagic at around 0.3 Ma, when a period of volcanic quiescence from the Tofua Arc began. The study shows that a near complete record of basin evolution can be constructed using geophysical and acoustic methods and that this work may help to locate future drill sites where in situ data can be collected.

Résumé

Les sédiments déposés dans les bassins d'arrière-arc conservent l'histoire de l'extension, du volcanisme et de la tectonique des systèmes d'arc-arrière-arcs. La sédimentation de l'arrière-arc est particulièrement intéressante car les dépôts de sulfures massifs peuvent être préservés dans les sédiments des bassins d'arrière-arc.

L'étude de la sédimentation en arrière-arc à l'aide de données acoustiques, telles que les données de profilage sous-marin à haute résolution (Parasound) et les données de réflexion sismique, peut constituer une approche beaucoup plus économique que l'analyse des sédiments récupérés à partir de carottes de forage. Dans cette étude, nous utilisons ces deux types de données acoustiques pour construire un modèle de faciès de sédimentation dans le bassin de Lau nord-est, un bassin d'arrière-arc qui s'ouvre activement dans le sud-ouest de l'océan Pacifique. En utilisant 830 km de lignes Parasound et 730 km de lignes sismiques le long de 4 transects du bassin de Lau, nous avons construit l'un des modèles les plus détaillés de sédimentation dans un bassin d'arrière-arc à ce jour. Les résultats de l'étude des données Parasound montrent que les échos distincts avec des réflexions sous le fond indiquent une plus grande proportion de sédiments hémipélagiques, tandis que les échos indistincts avec peu ou pas de réflexions sous le fond indiquent une plus grande proportion de turbidites volcanoclastiques grossiers et lités. Les reflets hyperboliques sont associés avec des régions au relief irrégulier, caractérisées par un soubassement exposé et rugueux ou par des dépôts formés par des courants de contour, des courants de turbidité, des effondrements ou des glissements. Ces relations constituent la base d'une légende d'écho-faciès élaborée pour les sédiments typiques des bassins d'arrière-arc. Les écho faciès observés dans le Parasound, et confirmés par les données de réflexion sismique à pénétration plus profonde, fournissent des indications importantes sur les processus sédimentaires impliqués dans la sédimentation de l'arrière-arc. Nous avons observé des dépôts de transport de masse (MTD) dans tous les sous-bassins, ainsi que des dépôts de pente à l'intérieur et sur les flancs des rifts actifs (par exemple, le Fonualei Rift and Spreading Centre, FRSC), ce qui suggère une corrélation directe entre les MTD et les zones de rifting actif. Nous avons observé une augmentation globale de l'épaisseur des sédiments en direction de l'arc de Tofua, ce qui suggère qu'il s'agit de la principale source sédimentaire, mais les variations locales de l'épaisseur des sédiments suggèrent également un apport significatif des monts sous-marins

intrabasinal locaux. Dans plus de 60 % des sous-bassins dans la zone d'étude, l'écho faciès supérieur est dominé par du matériel hémipélagique, ce qui suggère une transition abrupte de la source sédimentaire dominante de volcanoclastique à hémipélagique aux alentours de 0.3 Ma, lorsqu'une période de quiescence volcanique de l'Arc de Tofua a commencé. L'étude montre qu'un enregistrement presque complet de l'évolution du bassin peut être construit à l'aide de méthodes géophysiques et acoustiques et que ce travail peut aider à localiser les futurs sites de forage où des données in situ peuvent être collectées.

Acknowledgements

The completion of this thesis was possible due to the ongoing support of many people, whom I would like to thank.

Thank you to Dr. Mark Hannington, my thesis supervisor, for providing me with academic support and once-in-a-lifetime opportunities throughout my project. I am grateful to have had the chance to learn from your expertise, both in the field and in the classroom.

I would also like to thank Dr. Alan Baxter for your guidance, patience and encouragement. This project would not have been possible without your support, and your dedication to your students is remarkable.

Thank you to Dr. Michael Riedel for welcoming me on the SO294 expedition and for sharing your expert Parasound knowledge. Our Zoom calls at the beginning of my project were crucial to my success as a Parasound interpreter.

To my fellow graduate students, Mary Besaw, Alexandra Gray, Michael Ryan and Celeste Cunningham: thank you for the long talks, the laughs and the ArcGIS tutorials. I'm glad to have been surrounded by such kind people over these past years.

Last but not least, thank you to my dear family, my wonderful friends and my loving partner. This project would not have been possible without you, and I can't thank you enough for all your love and support.

This research is a product of the Metal Earth Project funded by the Canada First Research Excellence Fund (CFREF) in partnership with the Marine Mineral Resources Group at the GEOMAR-Helmholtz Centre for Ocean Research Kiel. The Helmholtz Association, NSERC, and CFREF are acknowledged for their support through research grants and project funding. This is contribution MERC-ME-2023-29 to the modern-ancient crust project of the Metal Earth program.

Table of Contents

List of Figures

List of Tables

Chapter 1: Introduction

1.1 Back-Arc Basin Extension

Back-arc basins (BABs) are complex systems where convergent and divergent plate boundary processes interact. Early studies (Gaskell et al., 1959; Shor, 1964; Murauchi et al., 1968) suggested that the crust in back-arc basins was similar to oceanic crust. This led Karig (1971) to propose that back-arc basins are semi-isolated, extensional basins located behind volcanic island arcs and are formed due to tectonic extension over subduction zones. Most of the world's BABs are concentrated in the Western Pacific Ocean, but they are also found in the northeastern Indian Ocean, Western Atlantic Ocean and the Northern Mediterranean Sea.

A recent review by Artemieva (2023) describes the two main models proposed to explain how back-arc basins open: i.e., trench rollback (Elsasser, 1971; Moberly, 1972) (Figure 1.1) and slab 'sea anchor' models (Scholz and Campos, 1995). The trench rollback model suggests that the subducting plate sinks into the mantle more rapidly than it converges with the overlying plate, which causes the trench to migrate toward the subducting plate (Martinez et al., 2007). This initiates extension in the back-arc which the overlying plate accommodates through crustal rifting. The slab "sea anchor" model suggests that the overriding plate moves away from the trench, and the subducted slab remains in place, acting as an anchor (Martinez et al., 2007). The initial rifting usually occurs at the volcanic arc front (Molnar and Atwater, 1978), which is a region prone to extension due to melt emplacement, high heat flow and gravitational stresses (Martinez et al., 2007). Several other models have been proposed, although they are not as widely accepted as the trench rollback or slab 'sea anchor' models. One set of models suggests that trench retreat of westward dipping subduction zones is caused by eastward horizontal mantle 'wind' (Uyeda and Kanamori, 1979; O'Connell and Hager, 1991; Ricard et al., 1991). Another group of models propose that extension in back-arc basins is driven by asthenospheric upwelling (Karig, 1971; Sleep and Toksöz, 1971; Billen and Gurnis, 2001; Kneller and van Keken, 2008; Wirth and Korenaga, 2012; Lee and Wada, 2017). Examples of extension driven by mantle flow include the mantle wedge corner flow model, in which downward mantle motion caused by the subducting slab results in a convective flow in the mantle wedge that induces extension in the overriding plate (Shemenda, 1993). Elsewhere, such as in the North Fiji Basin, plate rotation is

the driving force behind lithospheric extension (e.g., the "saloon-door" model: Kimura and Tamaki, 1986; Otofuji, 1996). In this study, we assume the trench rollback model.

BABs typically have multiple crustal-scale boundaries, including spreading centres, arc rifts, propagating rifts, triple junctions and transform zones that enclose volcano-sedimentary sub-basins. Where these boundaries intersect, they commonly form microplates that move and rotate independently. The interaction of these microplates results in complex tectonic regimes, periodically isolating or juxtaposing different sub-basins. Some are volcanically active, and some become passive depocenters for volcaniclastic and hemipelagic sediments. In addition to rifting, extension may be accompanied by the formation of oceanic crust at new spreading centres. Back-arc basin spreading centres have bathymetric and magnetic fabrics similar to those of mid-ocean ridges (Taylor et al. 1996), but they are typically only active for a few tens of millions of years. Extension stops and the system becomes extinct in response to far-field changes in plate motions and subduction (Martinez et al., 2007). Once extinct, these systems can be reactivated, as in the Philippine Sea (Martinez et al., 2007) where the Parece Vela and Shikoku back-arc basins opened from the late Oligocene to the Middle Miocene until extension stopped (Okino et al., 1998; Okino et al., 1999). Then, a new arc was formed that eventually rifted and formed the Izu back-arc rift zone and the Mariana Trough (Martinez et al., 2007). Another distinct difference between mid-ocean ridges and BABs is the source of the magma erupted at the neovolcanic zones. Magma erupted into the back-arc region is formed by partial melting of supra-subduction zone (SSZ) mantle (Hawkins, 1995). The melt compositions range from mid-ocean ridge basalt-like (MORB) tholeiites to arc-like calc-alkaline basalts and felsic rocks (Pearce et al., 1984). Commonly, MORB-like crust is dominant in the center of the basins at the spreading ridges, and arc-like crust occurs at the margins (Hawkins, 1995).

Active BABs are characterised by horst and graben structures, with steep margins from the initial rifting of the crust (Karig, 1971). They are typically on the order of 100s of km wide and range from 0.8 km to 3.6 km deep (Artemieva, 2023). They range from wide, V-shaped basins (Lau Basin), to narrow elongate basins (Mariana Trough) or irregular rounded basins (North Fiji Basin) (Figure 1.2). Two examples illustrate the sizes and shapes of BABs. The characteristic 'V' shape of the Lau Basin is attributed to multiple southward propagating spreading centres. It

is approximately 500 km wide in the north, 150 km wide in the south, and approximately 850 km long. In contrast, the Mariana Trough has a distinctive crescent-moon shape, reaching over 1000 km in length and ranging from approximately 50 km to 200 km wide. The length of the back-arc basin is controlled for the most part by the length of the corresponding subduction segment (Artemieva, 2023).

Hydrothermal activity is typically associated with extension in volcanically active back-arc basins. BABs host hydrothermal vent systems that are mineralogically and chemically more complex than those at mid-ocean spreading ridges due to the range of crustal compositions (Hannington et al., 2005). These vent systems are associated with seafloor massive sulfide (SMS) deposits considered to be modern analogues of ancient volcanogenic massive sulfide (VMS) deposits. In these complex settings, SMS deposits can form at the seafloor or by sub-seafloor replacement in synvolcanic sedimentary basins. Some of the largest VMS deposits in the geological record are considered to have formed within back-arc basin sedimentary successions (e.g., Large, 1992). The depositional environment of the host sediments can provide insight into the controls on massive sulfide formation thereby informing exploration for VMS systems in ancient settings.

1.2 Back-Arc Basin Sedimentation

Most back-arc basin studies focus on the kinematics, magmatism and hydrothermal activity. Back-arc sedimentation is comparatively little studied. One challenge in studying back-arc sedimentation is the difficulty in acquiring data, since sediment cores are expensive and challenging to collect. The work of various international drilling programs (e.g., IODP, ODP, DSDP), however, have contributed important data to this area of study. Based in large part on drilling results, Karig and Moore (1975) concluded that BABs in isolated oceanic settings exhibit a consistent and predictable pattern of sedimentation, whereas BABs near continental margins and terrigenous sources of sediment lack a consistent sedimentation pattern. They noted that there are four main sources of sediment in isolated BABs: (i) volcaniclastic material from the adjacent active volcanic arc, (ii) clays that form by the weathering of volcanics, (iii) biogenic input (mainly carbonate for basins above the carbonate compensation depth, CCD), and (iv)

wind-blown continental dust. These sediments are not evenly distributed across the back-arc region. For example, volcaniclastic deposits form thick successions near the arc and thin with increasing distance from the arc. Karig and Moore (1975) proposed a three-stage sequence of sedimentation in isolated BABs. In the first stage, when the basin begins to extend, there are high rates of production of volcaniclastic material from the active arc. Volcaniclastic sediment covers the entire basin, which may still be quite narrow. During the second stage, as the basin becomes wider, facies differentiation begins with volcaniclastic material from the arc decreasing in thickness away from the arc. In this stage, a volcaniclastic apron or submarine fan complexes may develop along the length of arc. Brown clays, with high proportions of montmorillonite, become more abundant with increased distance from the arc. The third stage begins when spreading ends and basin opening stops. During this stage, if the volcanic arc is still active, the sedimentation pattern is largely unchanged, but if the arc becomes extinct, then the dominant facies becomes biogenic hemipelagic sediments. This generalized sequence provides an important link to the evolving tectonic setting and a solid foundation for interpretation of BAB sedimentation in this study.

1.3 Study Area

The Lau Basin is a type-example of a back-arc basin and has been studied extensively since the 1970s (Figure 1.3). In 2019, the RV Sonne SO267 ARCHIMEDES I expedition set out to investigate microplate evolution, arc rifting processes and associated hydrothermal systems (Hannington et al., 2019). To do this, SO267 collected many new datasets with a focus on the northeastern Lau Basin, including bathymetry, reflection and refraction seismic surveys, gravity, magnetics, heat flow and sub-bottom profiling (Parasound). This study examines data from four of the SO267 seismic transects: P03 to P06 in an area of 315 km by 150 km, from 17°18’37” S to 18°43’48” S and 176°18’22” W to 173°27’44” (Figure 1.4).

The Lau Basin lies at the boundary between the Indo-Australian and Pacific plates where the Pacific Plate subducts under the Tonga and Kermadec microplates, along the Tonga-Kermadec trench (Bird, 2003). The western boundary of the basin is the inactive Lau Ridge, and the eastern boundary is the Tonga Ridge and active Tofua Arc (Figure 1.3). Here, rollback of the subducting slab induces extension in the upper plate which controls the ongoing extension of the basin

(Hawkins, 1995). This system has the fastest subduction rate in the world, with the Pacific Plate subducting beneath the Tonga and Kermadec microplates at ~240 mm/yr (Bevis et al. 1995). Like most back-arc basins, the Lau Basin opened through two main processes: first extension and rifting, then seafloor spreading. The Lau and Tonga arcs, which were once a single arc, are thought to have been active as early as 44 to 45 Ma, based on K-Ar ages of rhyolites from the Ocean Drilling Project (ODP) Leg 135 site 841 and from the Eua volcano on the Tonga forearc (Hawkins et al., 1994). Extension and rifting of the Lau Ridge began at around 6 Ma, continuing until about 5.5-5 Ma when seafloor spreading began (Hawkins, 1995). New oceanic crust was produced by the Eastern Lau Spreading Center (ELSC), which was a southward propagating rift (Taylor et al., 1996). The ELSC is still active, opening at 65 mm/yr at the southern portion, increasing northward to 90 mm/yr (Taylor et al., 1996). Initially the north-south trending ELSC comprised two segments. The northeastern segment propagated south more quickly than the southern segment, which resulted in an overlapping spreading regime. At around 2 Ma, the ELSC rotated 15-25° clockwise triggering the formation of the Peggy Ridge transform fault and the southward propagating Central Lau spreading center (CLSC: Taylor et al., 1996). The Tofua arc on the eastern flank of the basin remained active throughout (Hawkins, 1995) and the basin has continued to open at a rate of about 160 mm/yr (Hawkins, 1995).

A number of different physiographic features control the basin architecture (Figure 1.3). The Lau Ridge, which forms the western boundary of the basin, is the early remnant arc that extends for 2400 km north-northeast. In the northwest, the basin is bound by the Northwest Lau Spreading Center (NWLSC), which connects at its southwestern tip to Peggy Ridge (PR) and at the northeastern tip to the Rochambeau Bank, a northwesterly elongated seamount (Figure 1.5). The Peggy Ridge is a northwest trending volcanic feature occupying an early transform fault (Hawkins, 1995). The southeastern tip of PR is connected to the CLSC by a series of en echelon spreading segments referred to as the Lau Extensional Transform Zone (LETZ). The CLSC is a 190-km long, southward propagating spreading center that transitions through a ‘relay zone’ to the northern termination of the ELSC. The northern boundary of the basin is a complicated deformation zone, including extensive strike slip faulting along the former Vitiaz Trench. The northeast boundary is dominated by the Mangatolu Triple Junction (MTJ) and Fonualei Rift and Spreading Center (FRSC).

Zellmer and Taylor (2001) recognized a third microplate in the north of the basin, the Niuafo'ou microplate, located between the Tonga and Australian plates and bound by the FRSC in the east and the Peggy Ridge, LETZ and CLSC in the west. The southern boundary of the Niuafo'ou microplate is not well-defined but overlaps the relay zone between the CLSC and ELSC. The presence of three diverging plates (Tonga, Niuafo'ou and Kermadec) suggests the existence of a triple junction between them, however such a structure has not yet been identified (Zellmer and Taylor, 2001). Rather, the sub-basin architecture described in this study suggests that a diffuse plate boundary may now be emerging. Within the Lau Basin are many small sub-basins, which opened in response to regional and local extension (Figure 1.6). Their opening is directly related to the interaction of the extensional features in the basin and microplate movement and provide a record of the larger basin evolution. For example, a group of deep nodal basins at the overlap between the ELSC and the CLSC are potential hallmarks of an emerging plate boundary in the south of Niuafo'ou. More recent sub-basins can be observed at the southern termination of the FRSC, where rifting is propagating into the arc crust. We show that more than 30,000 km^2 of the northern Lau Basin (about 47% of the entire basin) is occupied by discrete and coalesced sub-basins. We have conducted a detailed analysis of the deposits within these sub-basins to better understand back-arc basin sedimentation and the link between sub-basin fill and the tectonic regime.

1.4 Thesis Objectives

The objectives of this study are to better understand the processes of back-arc basin sedimentation using acoustic data to characterise the depositional history of more than 60 sub-basins identified in the Niuafo'ou microplate. We selected this part of the northeast Lau Basin (Figure 1.4) and created a database of the acoustic properties of the sedimentary units the sub-basins and slope deposits recorded in both seismic reflection and higher frequency sub-bottom profiling (see Appendix D). We first created a legend of the acoustic properties, referred to in the thesis as "echo facies", guided in part by comparison with echo facies from other studies (e.g., Damuth and Olson, 2015; Fierens et al., 2019) in particular where the sediment makeup is known from intersecting cores. Using the established echo facies of cored sections as a training set, we

have interpreted the types of deposits (composition and grain size) of the sedimentary units and created maps of their distribution. The structural and sedimentological history of the sub-basins, derived from their sedimentary infill, was then used to investigate the extensional history of this part of the Lau Basin. By identifying and analyzing the thicknesses of the sedimentary units, the location and geometry of faults and other structures in the basins and considering the age of the underlying crust inferred from spreading rates and magnetic chrons, we aimed to establish the relative ages of inception of local subsidence and corresponding extension.

1.5 Data Acquisition

The major dataset generated in the study is a compilation of the characteristics of sedimentary units based on their acoustic properties from the analysis of sub-bottom profiling echograms recorded by the ATLAS Parasound system referred to as 'Parasound'. Additional datasets used in this study are seismic reflection data and ship-based multibeam bathymetry, including backscatter data. All data were collected during the R/V Sonne research cruise SO267 (Hannington et al., 2019). The seismic data extend to mid-crustal level, while the Parasound uses a frequency of 0.5-6.0 kHz to image the top 200 m of sediment. This is the first detailed sedimentological study of the Lau Basin using Parasound data.

Sub-bottom profiling (SBP) is a high frequency seismic reflection survey where a source emits an acoustic signal that travels through the water column and penetrates the seafloor. When the signal encounters a change in physical properties between layers of sediment, it is reflected along the interface and recorded by the transducer. The strength of the reflected signal (Rayleigh coefficient of reflection, R) is determined by the contrast in acoustic impedance between the two layers (Penrose et al., 2005). Acoustic impedance is defined as:

$$Z = Vp \times \rho$$

where Vp is P-wave velocity and ρ is density. The reflection coefficient, R, is defined as:

$$R = \frac{Z_2 - Z_1}{Z_2 + Z_1}$$

The resulting echograms show the seafloor reflection and the boundaries between sub-seafloor sedimentary layers (Figure 1.7). Echogram quality is best in regions with a smooth seafloor, where the angle of incidence is close to 0°. In regions with rugged bathymetry, steep slopes or scarps, the angle of incidence is greater than 0°, which produces hyperbolic echoes (Figure 1.8).

Although 3.5 kHz echosounders have been used as sub-bottom profilers for many decades, Parasound resolves some key issues that this method presents. Traditional 3.5 kHz systems are generally used in deep-tow systems that require a slower operating speed and expensive towing materials. 3.5 kHz echosounders have a wide beam width (~ 30°; Saleh and Rabah, 2016), which can cause side echoes (Grant and Schreiber, 1990). Side echoes are produced by acoustic signals with wide beam widths and prominent side lobes, which have a larger seafloor footprint (> 30% of water depth). Side lobes are acoustic energy that is produced outside of the beam width. The acoustic signal will reflect off of the highest bathymetric point in the footprint, so larger footprints increase the chances of recording seafloor asperities rather than the sub-bottom reflections (Figure 1.9).

Parasound is a method of echosounding that employs the parametric effect to create high resolution sub-bottom profiles. The parametric effect is a phenomenon arising from the nonlinear acoustic properties of water (Berktay, 1965), whereby two primary high-frequency (PHF) signals emitted simultaneously create two secondary frequencies by interference. A secondary low-frequency (SLF) signal is produced that is equal to the difference between the PHF signals, and a secondary high-frequency (SHF) signal is produced that is equal to the sum of the initial frequencies (Westervelt, 1963). The SLF is the frequency used for sub-bottom profiling and is produced in the narrow beamwidth (e.g., 4.5° - 5°) of the two PHFs which produces a more focused beam and higher resolution echogram as there are no side lobes (Grant and Schreiber, 1990) (Figure 1.10). This more focused beam has a footprint approximately 7% of the water depth and a vertical resolution of up to 15 cm. The narrow SLF beam also has enough energy to penetrate up to 200 m into the sediment. The strength of the acoustic signal controls the depth of acoustic penetration, and features such as bedforms can scatter the acoustic energy, thereby reducing the strength of the signal and the depth of penetration. In the case of the ATLAS Parasound P70 system used on the RV Sonne SO267 cruise, the PHFs were 18-20 kHz and 22-

24 kHz, which produced a SLF of approximately 4 kHz and a SHF of 40-42 kHz. Parasound also operates with a hull-mounted transducer, which allows for regular vessel operating speeds and the simultaneous collection of other geophysical data.

Grouping echograms with similar reflection patterns, amplitudes, geometries and degrees of continuity provides a means of classifying different sedimentary facies and interpreting the sedimentary processes that formed them. This is referred to as “seismic facies,” “echo character” (Damuth, 1975) or “echo facies” (Fierens et al., 2019). For example, an echogram displaying many flat-lying, continuous sub-bottom reflections is distinctly different from an echogram displaying a strong seafloor refection with no sub-bottom reflections (Figure 1.11). Echo facies can be calibrated with core to correlate the echoes to sediment composition, grain size and structures. By mapping the echo facies to show their regional distribution, it is possible to infer some aspects of the sedimentary processes, such as sediment source and mode of deposition (e.g., hemipelagic sedimentation, bottom current deposition, etc.). Damuth (1975) calibrated echo characteristics with piston cores in order to identify the sediment type and/or the sedimentary processes that caused the echo. The results of his study suggested that distinct echoes with sub-bottom reflections corresponded to a higher proportion of clay-sized sediment, whereas the indistinct echoes with few to no sub-bottom reflections corresponded to a higher proportion of coarse (silt, sand, gravel), bedded, terrigenous sediment. Hyperbolic echoes were associated with regions of rugged or uneven terrain, caused by exposed, rugged basement or deposits produced by sedimentary processes such as contour currents, turbidites, slumps or slides. These relationships form the basis of a new echo-facies legend developed for the Lau Basin sediments in this study.

1.6 Publications and Presentations

The results of this study have been presented at three conferences:

Kehew, J. (2022) Intrabasinal sediments and tectonostratigraphy of the Lau Basin: Assessing linear vs diachronous models for the opening of the Lau back-arc basin. Oral Presentation

at the annual Ottawa-Carleton Geoscience Centre Graduate Seminar. Ottawa, ON. April 13.

Kehew, J., Hannington, M.D., Baxter, A.T., Diekrup, D., Riedel, M., Petersen, S. (2021) Intrabasinal sediments and tectonostratigraphy of the Lau Basin: Assessing linear vs diachronous models for the opening of the Lau back-arc. Poster Presentation and Abstract at the Student Minerals Colloquium of the Annual Prospectors and Developers Association of Canada Conference. Toronto, ON, March 8-11.

Kehew, J., Hannington, M.D., Baxter, A.T., Riedel, M., Diekrup, D., Petersen, S. (2021) Intrabasinal sediments and tectonostratigraphy of the Lau Basin: Assessing linear vs diachronous models for the opening of the Lau back-arc basin. Oral Presentation and Abstract at the Annual Meeting of the Geological Association of Canada Mineralogical Association of Canada (GAC-MAC). London, ON. November 1-5.

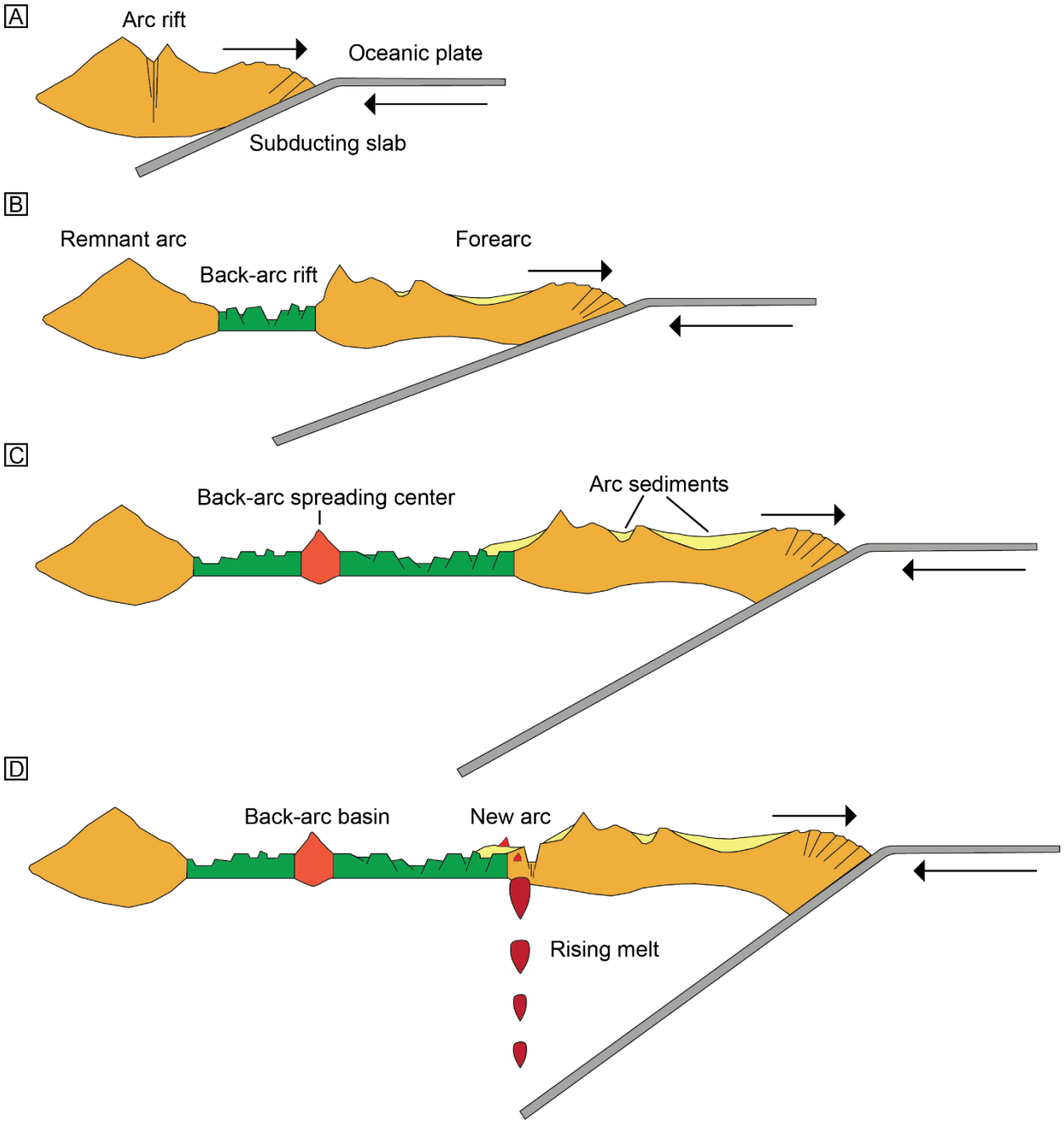

Figure 1.1 Schematic diagram of the trench rollback model (modified from Fassbender, 2023). A) The oceanic plate subducts beneath the overriding plate, and the trench migrates toward the subducting plate, causing extension in the overriding arc. B) Extension is first accommodated by back-arc rifting followed by the initiation of a back-arc spreading center (C). Arc sediments drape the arc crust. D) Hydrous fluxing from the subducting plate results in mantle melting (Martinez et al., 2007), which rises to the surface and forms a new arc.

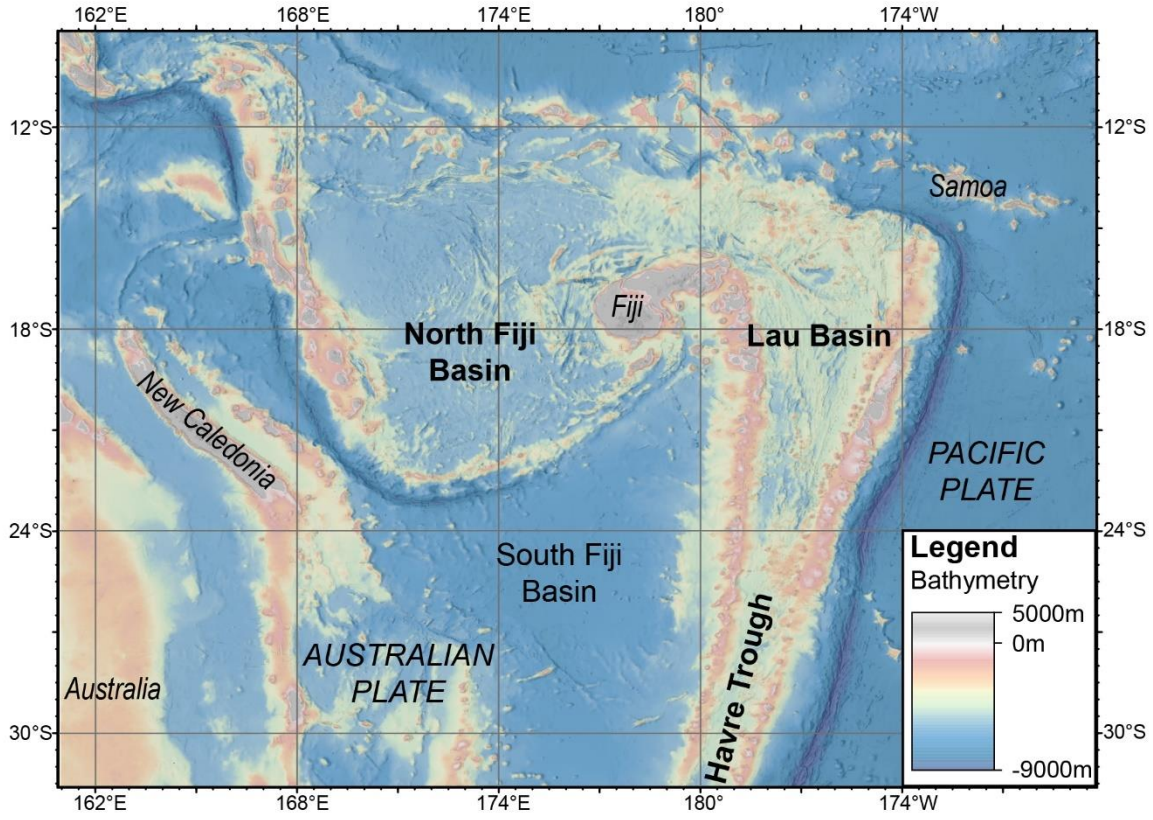

Figure 1.2 Back-arc basins of the south-western Pacific Ocean. The Lau Basin, North Fiji Basin and Havre Trough are active back-arc basins, while the South Fiji Basin is inactive.

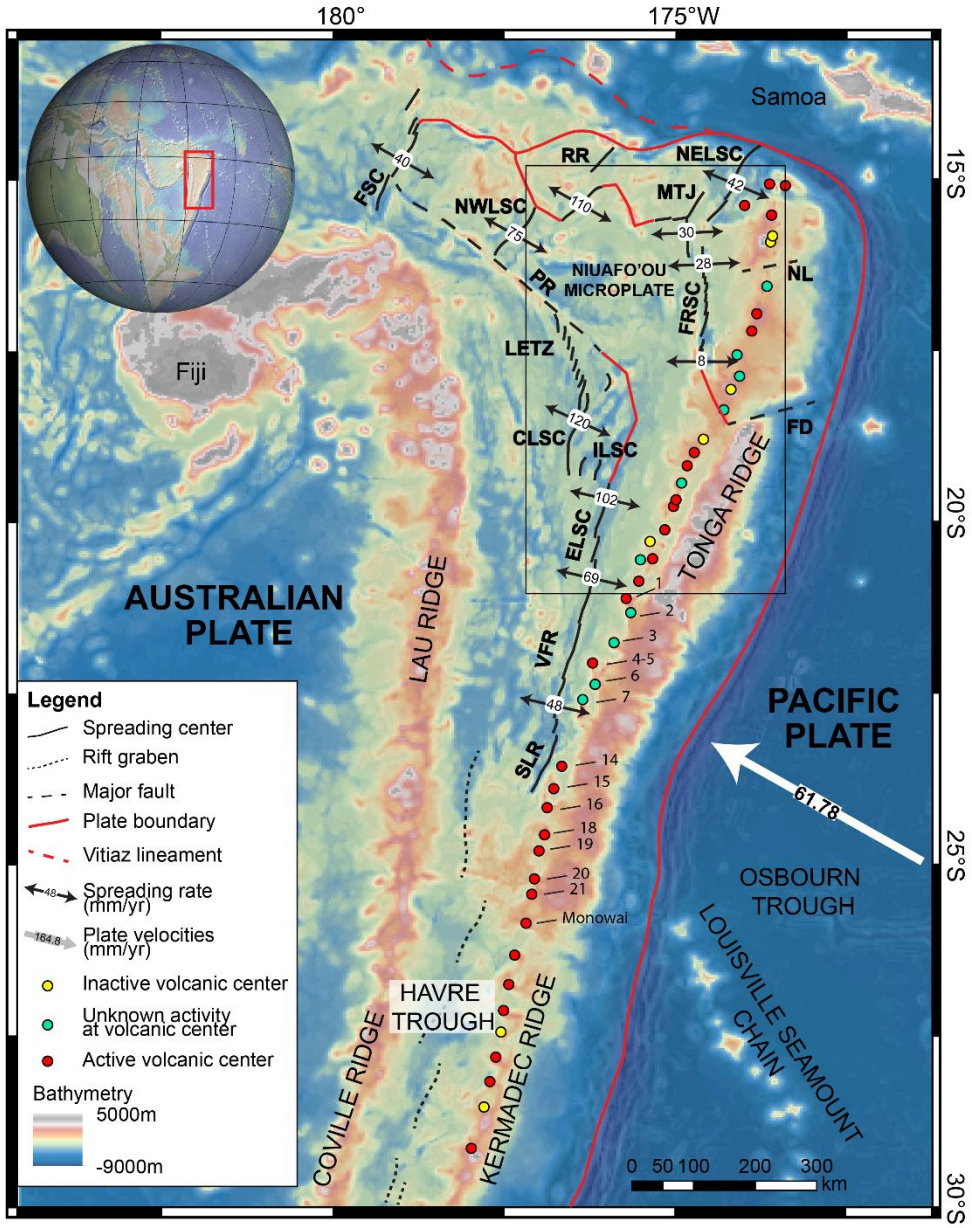

Figure 1.3 Bathymetric map of the Tonga-Kermadec system (Modified from Gray, 2022). The characteristic V shape of the Lau Basin is defined by the Lau Ridge in the west and the Tonga Ridge and Tofua Arc in the east. The map highlights the microplate boundaries and spreading centers from Bird (2003), modified by Baxter et al. (2020), and rift grabens from Campbell et al. (2007). Motion of the Pacific plate is in mm/yr, measured by GPS (Argus et al., 2011). The location of Figure 1.4 is indicated by a black rectangle. Rochambeau Rifts (RR) and Northwest Lau Spreading Center (NWLSC) spreading rates (mm/yr) and spreading vectors (black arrows) are from Lupton et al. (2015). Spreading rates and vectors for the Northeast Lau Spreading

Center (NELSC), Mangatolu Triple Junction (MTJ), Fonualei Rift and Spreading Center (FRSC), Central Lau Spreading Center (CLSC), Eastern Lau Spreading Center (ELSC) and Valu Fa Ridge (VFR) are from Sleeper and Martinez (2016) and Baker et al. (2019). Spreading rates and vectors of the Futuna Spreading Centre are from Pelletier et al. (2001). The Fonualei Discontinuity (FD) and the Niuatoputapu Lineament (NL) are relics of arc-trench extension. Peggy Ridge (PR) may be the location of a transform fault (Hawkins et al. 1995). The Lau Extensional Transform Zone (LETZ) is a set of en echelon spreading segments that connect the southern tip of PR to the CLSC.

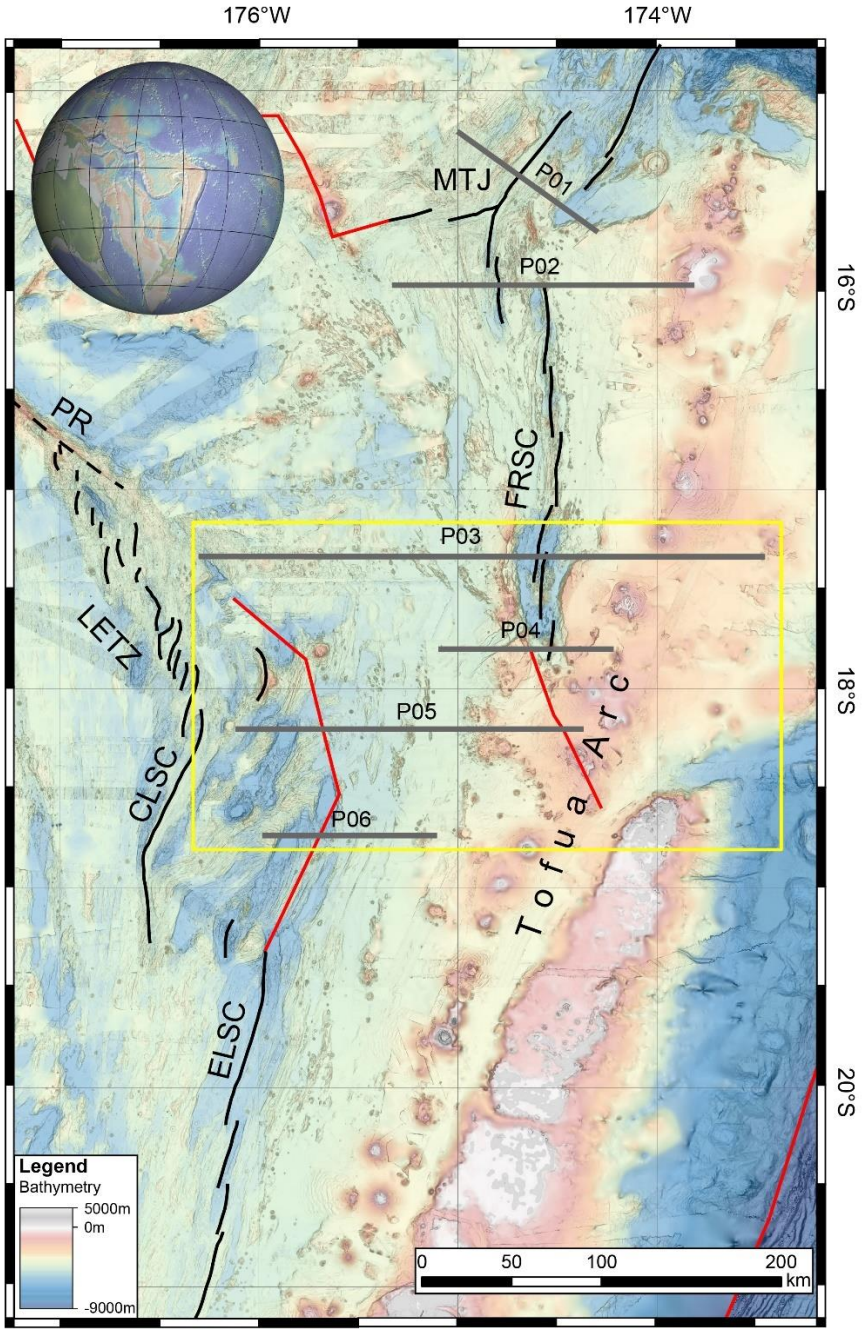

Figure 1.4 Study area within the Lau Basin. Reflection seismic and refraction profiles P01 to P06 with coincident Parasound data from RV Sonne SO267 expedition (Hannington et al., 2019) are marked by grey lines. The study area for this thesis is outlined by the yellow box and contains seismic lines P03 to P06. The spreading axes of the Fonualei Rift and Spreading Center (FRSC), Central Lau Spreading Center (CLSC) and Eastern Lau Spreading Center (ELSC) are in black. Microplate boundaries from Bird (2003), modified by Baxer et al. (2020) are in red.

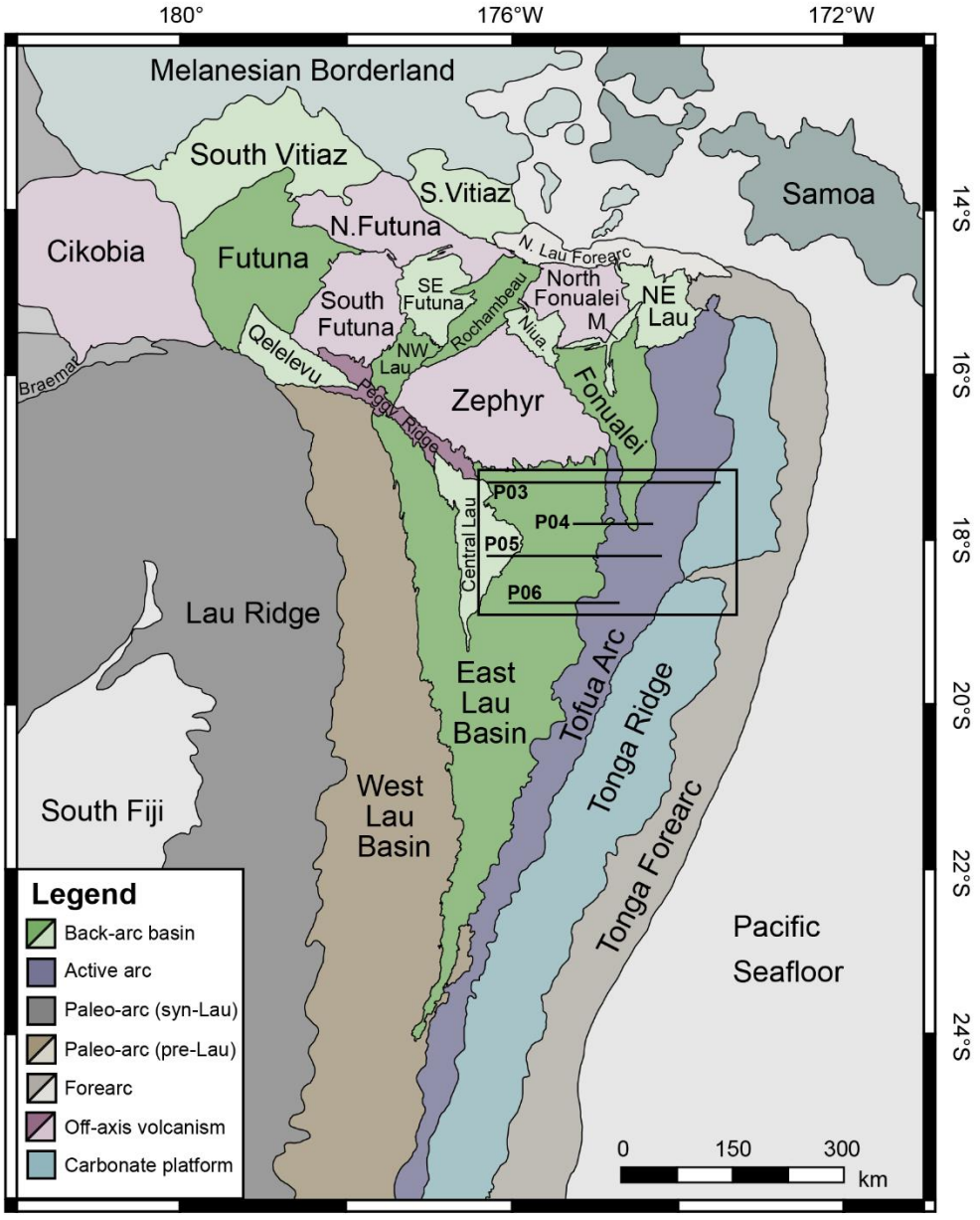

Figure 1.5 Geologic assemblage map of the Lau Basin (modified from Stewart et al., 2022). Study area and locations of seismic transects are shown in black. Darker shades in the legend indicate assemblages containing eruptive material with published age constraints, while the lighter shades do not have such constraints.

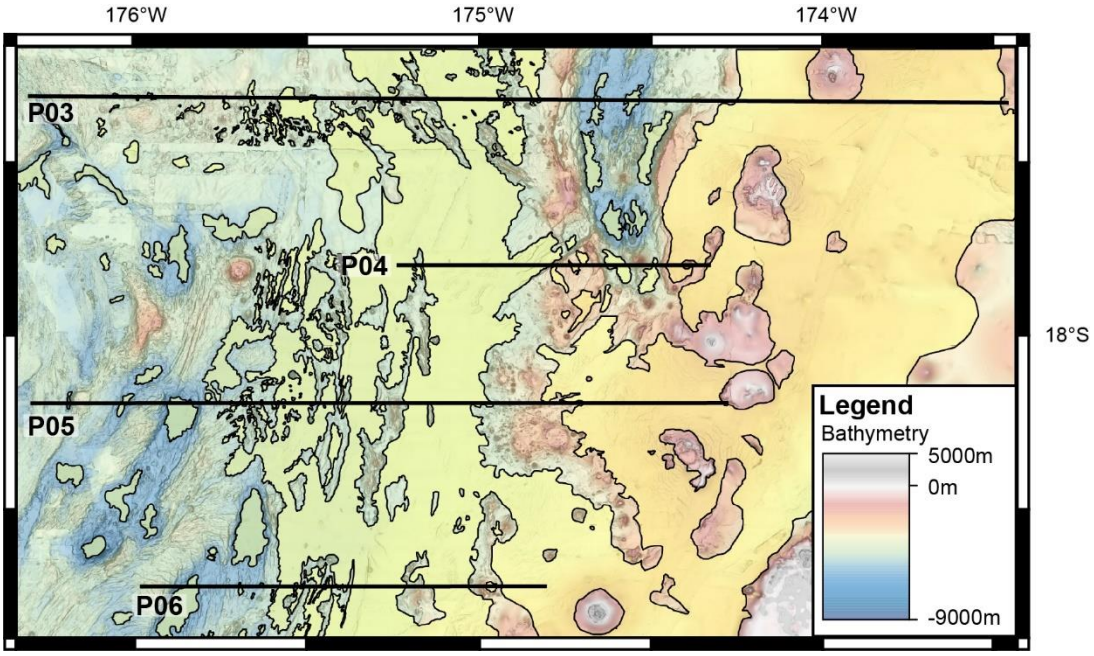

Figure 1.6 Distribution of sub-basins that opened during crustal rifting and seafloor spreading bound by structures such as faults and volcanic ridges creating space in which sediment accumulates. 47% of the study area is covered in some thickness of sediment, shown by the yellow polygons. Different types of sub-basins include nodal basins that formed in response to the overlap of the ELSC and CLSC, with distinct boundaries on all sides, as well as interconnected sub-basins with less obvious polygonal shapes.

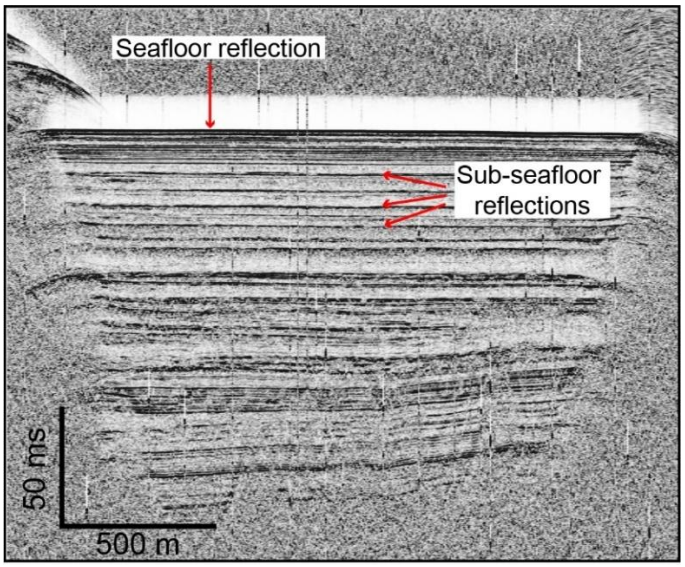

Figure 1.7 Example of a Parasound echogram highlighting the initial reflection of the seafloor and subsequent sub-seafloor reflections. Reflections occur at the interface between two sedimentary layers with different densities. The white strip above the seafloor reflection is an artifact caused by the high change in density between seawater and the seafloor. Vertical scale is 50 ms, which is equal to approximately 38 m, assuming a sound velocity of 1520 m/s.

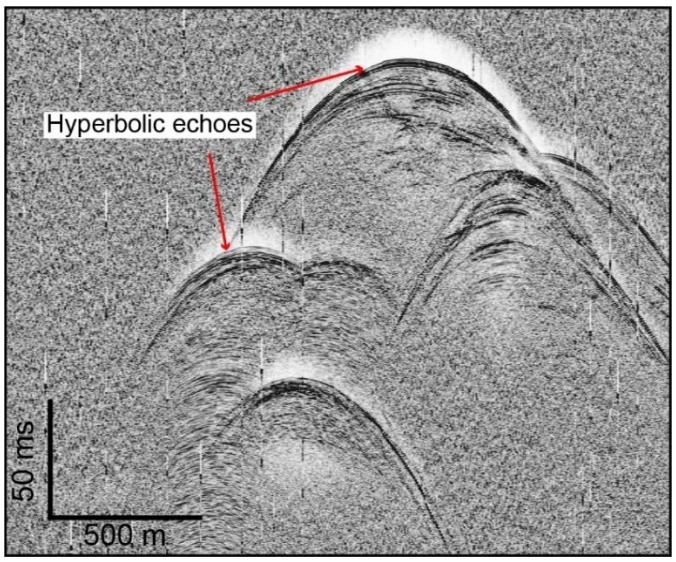

Figure 1.8 Example of a Parasound echogram showing hyperbolic echoes that occur when the angle of incidence is greater than 0°. Regions with steep slopes or rugged bathymetry produce echograms with hyperbolic echoes.

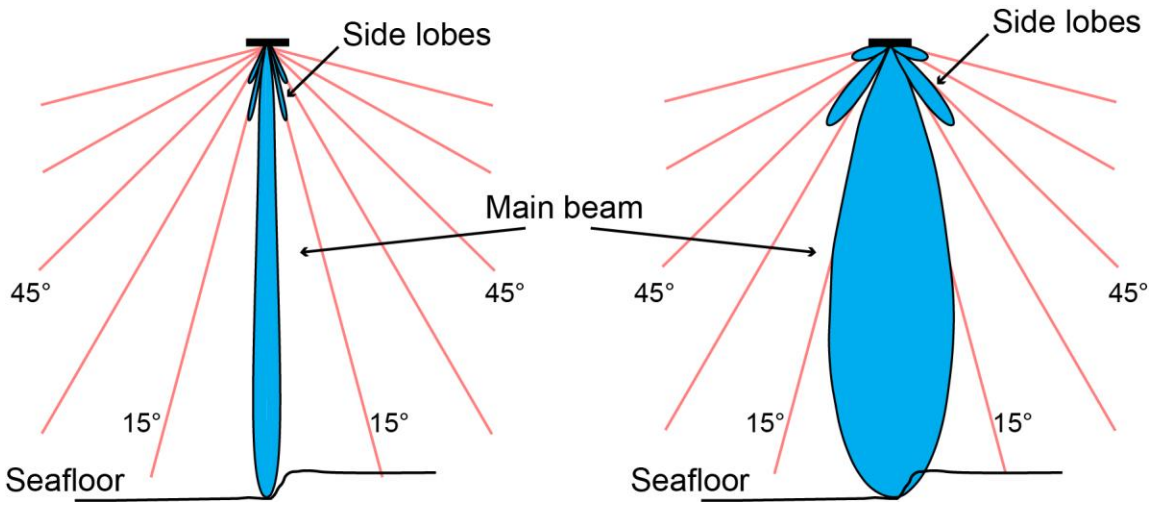

Figure 1.9 Comparison between the acoustic beams of Parasound (left) and traditional 3.5 kHz sub-bottom profilers (right). Parasound has a beam width of 4.5° to 5°, a footprint of approximately 7% water depth and small side lobes, while traditional 3.5 kHz systems have a beamwidth of approximately 30° a footprint of approximately 30% water depth and larger side lobes. The larger beamwidth can record seafloor asperities which can obscure the sub-bottom reflections and reduce data quality.

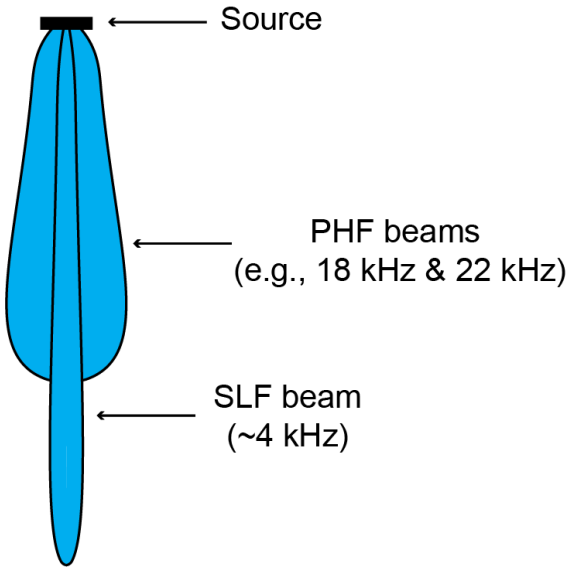

Figure 1.10 Schematic illustration of the Parasound beams employing the parametric effect to produce a low frequency signal in a narrow beam. Two primary high frequency (PHF) beams with frequencies approximately 4 kHz apart (in this example, 18 kHz and 22 kHz) are emitted

simultaneously from a source, which produces a secondary high frequency (SHF) beam equal to the sum of both PHFs and a secondary low frequency (SLF) beam that is equal to the difference between the two PHFs (4 kHz in this example).

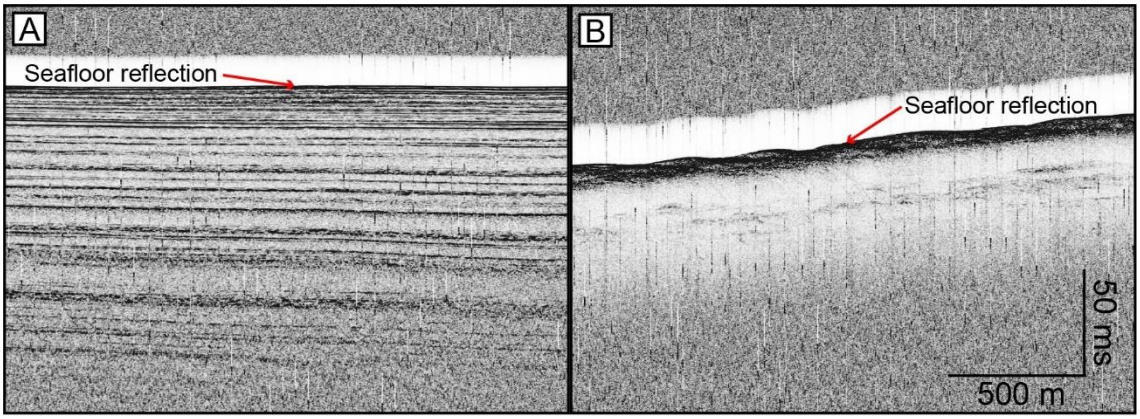

Figure 1.11 Example of an echogram with many strong, continuous sub-bottom reflections (A) and one with few, discontinuous sub-bottom reflections (B).

Chapter 2: Stratigraphy and Sedimentary History of the Lau Basin

2.1 Introduction

Although arc and back-arc volcanism produce significant quantities of volcaniclastic material, details on the structure, sedimentology and stratigraphy of back-arc basin sedimentation are lacking (Artemieva, 2023). Karig and Moore (1975) proposed a broad two-stage sedimentation model with progradation of volcaniclastic material from the arc towards the centre of the back-arc basin followed by a cover of finer-grained units after basin opening has ended. Most of what is known about back-arc sedimentation is from ancient examples (e.g., Busby-Spera, 1988) or from sites drilled as part of the DSDP, IODP, and ODP programs (Hussong et al., 1982; Klein and Lee, 1984; Hawkins et al., 1994). Modern geophysical and acoustic methods are providing a more complete picture of sedimentation in back-arc basins. What is often missing, however, is a clear history of subsidence in adjacent sub-basins that tracks the regional extension.

Over 50 years of marine research has taken place in the Lau Basin, making it one of the best regions in the world to study arc-backarc processes including back-arc sedimentation. This study focuses on the sedimentary sub-basins and slope deposits located along four transects across the arc-backarc transition with recently acquired seismic reflection profiles and Parasound data (SO267 expedition: Hannington et al., 2019) (Figure 2.1). Four east-west cross-sections, 290 km, 100 km, 215 km and 125 km long, respectively, were surveyed at 17°20’S, 17°48’S, 18°12’S and 18°44’S (Figure 2.2). Whereas the seismic reflection lines provide deep (up to 8 km) sections of the structure and thickness of back-arc sediments at a regional-scale, the Parasound acoustic data images the top 200 m of sediment in detail and with nearly continuous coverage of the map area. Sub-bottom profiling has been used since the late 1960s (e.g., Hollister, 1967; Embley, 1975; Damuth, 1973, 1975) to identify recent sedimentary history, depositional processes and sediment transport pathways (e.g., Damuth and Olson, 2015; Catteano et al., 2020; Damuth, 1975). However, because of the low resolution of early systems, in most studies, the entire echogram was commonly assigned a single echo facies corresponding to an entire sedimentary section. Higher-resolution data obtained by Parasound can identify multiple echo facies within an echogram, enabling the investigation of facies changes, creation of echo facies maps, and tracking the evolution of sedimentation through time. The present study in the Lau Basin is one

of the first applications of this technique to reconstruct the history of sedimentation at the scale of an entire basin with direct links to the tectonic history.

Numerous sub-basins containing sediment have been imaged in the high-resolution bathymetry along each profile. The largest are situated to the west of the FRSC on ELSC crust, which is the oldest crust in the study area. Others are located in the overlap zone between the CLSC and ELSC, and at the propagating rift tip of the FRSC. Significant and marked variation in the sediments detected in the Parasound data suggests that different types of sediment are contained in these sub-basins, and it should be possible to characterize the changing depositional environments that produced these distinct sedimentary units or formations. To test this, we identified and compiled all the sedimentary units in the sub-basins and slope deposits based on their echo facies. The different echo facies were classified in terms of distinct acoustic properties that correspond to relative grain size (i.e., proportions of coarse and fine material) and structure, such as the frequency of strong sub-bottom reflections and or the presence of acoustically transparent units. These variations were recorded for each facies and then interpreted in terms of depositional process or sedimentary history by comparison with sediments recovered during ODP Leg 135 (Hawkins et al., 1994). Although limited groundtruthing data are available for the Parasound data in the study area, the ODP drill cores provide a key training set for the classification of sedimentary successions in the back-arc sub-basins.

This chapter aims to answer the following research questions:

1. Can we create an echo facies legend for back-arc basin sediments?
2. What are the regional trends in echo facies distribution?
3. Is volcaniclastic sedimentation a localized or regional process?
4. Can we correlate changes in echo facies with changes in the tectonic regime of the Lau Basin?

2.2 Previous Work

In 1992, the Ocean Drilling Program (ODP) Leg 135 retrieved cores from eight sites in the Lau Basin (Hawkins et al., 1994). This was one of several drilling projects that took place in back-arc basins and their associated forearcs in the western Pacific Ocean (Parson et al., 1992a). The main objectives of Leg 135 were to better understand the nature of the crust and the geologic history of the back-arc basin opening (Parson et al., 1992a). Full sedimentary successions were recovered, providing a near continuous record of the western Lau Basin. Thorough sedimentological, geochemical and biostratigraphic analyses provided new data on sediment composition, modes of deposition, hydrothermal activity and tectonic controls on sedimentation in the earliest history of opening.

Six sites were drilled in the sub-basins of the western Lau Basin, between 18°30’ S and 20°50’ S (Rothwell et al., 1994a; Figure 2.1). These Sites (834-839) all have a similar basin fill, with a lower succession of volcaniclastic sediment and an upper succession of hemipelagic clayey nannofossil ooze (Parson et al., 1992; Figure 2.3). Each site records a pattern of increasing volcaniclastic sand and silt with depth (Rothwell et al., 1994b), and an abrupt transition from coarse, volcaniclastic sediment to hemipelagic sediment at different ages at each site, which indicates a hiatus in volcaniclastic sedimentation. The transition to hemipelagic sedimentation occurs earlier in the west than the east of the study area, which suggests that the beginning of the period of volcaniclastic quiescence migrated toward the arc over time (Rothwell et al., 1994a). The main conclusions were that sedimentation during the Pliocene in the western part of the basin was dominated by volcaniclastic sedimentation, mainly from intrabasinal seamounts, whereas the Pleistocene was dominated by hemipelagic sedimentation (Rothwell et al., 1994a).

At each site, the upper sedimentary succession consists of brown, oxyhydroxide-stained hemipelagic clayey nannofossil ooze and calcareous turbidites (Parson et al., 1992). At some of the sites, in the upper sedimentary succession, the clayey nannofossil ooze contains interbeds of epiclastic vitric sands, ash layers from airfall events, mud-clast conglomerates, and rafted blocks. The conglomerates and rafted blocks are mass transport deposits (MTD), and their deposition was interpreted to coincide with the early propagation of the ELSC and CLSC into the basin,

during which slope instability was triggered by crustal rifting (Parson and Hawkins, 1994; Parson et al, 1994). The calcareous turbidites in the upper sedimentary succession are similar in appearance to hemipelagic deposits. Hemipelagic deposits are deposited out of the water column and have sedimentation rates on the order of mm/ka. Hemipelagic turbidites, or "hemipelagites", are T_e turbidites (Bouma, 1962) composed of hemipelagic material and are assumed to have been deposited instantaneously during resedimentation of hemipelagic sediment by turbidity currents. Several characteristics including grain size, texture, geochemistry and presence or absence of bioturbation were used to distinguish the hemipelagic sediment from the hemipelagic turbidites (Rothwell et al., 1994b). The identification of resedimented units has important implications for the calculation of sedimentation rates. Rothwell et al. (1994b) concluded that resedimented hemipelagic material made up approximately 17% of the sediment in the upper succession (termed Unit 1) at Site 834 and approximately 66% of the sediment at Site 835. By subtracting the thickness of resedimented units from the total thickness of hemipelagic material and using biostratigraphic ages, they calculated the rates of purely hemipelagic sedimentation. From these results, they determined that hemipelagic sedimentation occurred at a rate of 14.6 mm/ka at Site 834 and 14.4 mm/ka at Site 835.

The lower sedimentary succession of epiclastic vitric sands and silts with interbeds of clayey nannofossil ooze was interpreted to have been deposited as sediment-gravity flows (Parson et al., 1992). Rothwell et al. (1994a) proposed that the gravity flows were primarily derived from adjacent volcanic ridges. This lower succession is thought to consist of proximal deposits because of the needle-like shaped volcaniclastic grains, which would not be preserved if sediment was transported over long distances (Bednarz and Schmincke, 1994). Geochemical analysis of glass grains at each site showed three regions based on silica concentration (Rothwell et al., 1994a). Volcanic glass from Sites 834 and 835 has a wide range of total silica, glass from Sites 837-839 has a bimodal distribution of silica concentrations, and from Site 836 low total silica concentrations. This strongly suggests that the source of volcaniclastic material was different for each of these areas, with limited dispersal of the volcanic products from intrabasinal seamounts (Bednarz and Schmincke, 1994; Clift and Dixon, 1994).

We compare these findings with the sediment record in the eastern part of the basin, deduced from echo facies distribution in the Parasound and corresponding seismic reflection data from SO267 in a region more proximal to the arc. We examine whether the upper and lower successions observed during ODP Leg 135 can be correlated to units in the east and therefore extrapolated across the basin. In particular we examine whether MTDs can be recognized in the Parasound data and correlated with the propagation of the ELSC and CLSC as proposed from the earlier drilling.

2.3 Sedimentary Sub-Basin Classification

To characterise each of the sub-basins observed in the Lau Basin, a hierarchical framework of sedimentary units was developed following the standard lithostratigraphic classification scheme from the International Commission on Stratigraphy (Salvador, 1994; Murphy and Salvador, 1999). The sub-basin fill in most of our study area corresponds broadly to a single formation-level designation in the geological map of Stewart et al. (2022) (Figure 2.4). Formations are defined as spatially and/or temporally distinct lithostratigraphic units identified by recognizable volcanic or sedimentary facies, geomorphological expression, sampling and geophysical data (Stewart et al., 2022). The next rank in our study (sedimentary unit) corresponds to the member level. The lowest rank in our study corresponds to beds and bedsets, as defined by Boggs (2013).

Sedimentary unit and sub-unit

The foundational stratigraphic rank in this study is the sedimentary unit. In the Parasound data, sedimentary units are defined as one or more acoustic reflections with a distinct character that are interpreted to reflect a single depositional event or a sequence of depositional events of the same type. Multiple sedimentary units can be distinguished by repeated echo facies in a single sub-basin. From the comparisons with drilled or cored sedimentary successions, we can also interpret the composition.

We equate sedimentary units to the ‘member’ rank of Stewart et al. (2022). Members are defined as sub-divisions of formations, which are mappable at a scale of 1:100,000 – 1:200,000 (e.g.,

individual volcanic flow sequences). Member-level volcanic units have been mapped in several studies in the area (Mensing, 2020; Gray, 2022).

Individual sub-bottom reflections in a sedimentary unit are designated sub-units, which are the rank corresponding to beds and bedsets. Sub-units represent a single flow or depositional event. Boggs (2013) defines a bed as a tabular or lenticular sedimentary layer, greater than 1 cm thick with a distinct lithology, texture or structure that distinguishes it from overlying and underlying strata. A simple bedset is defined as a group of beds with similar composition, texture and internal structure (Boggs, 2013). The maximum resolution of the parasound data is 15 cm and therefore individual beds and bedsets cannot be easily distinguished

Sub-basin fill

Sub-basin fill belongs to the rank above sedimentary units and refers to sediments within small basins (0.8 km to 45 km in size) located within larger basins (up to 100s of km in size). In other studies, sub-basins are sometimes referred to as mini-basins (e.g., Damuth and Olson, 2015). In this study, the sub-basins are clearly identified in seismic reflection data and bathymetry. Sedimentary units comprising the sub-basin fill begin to accumulate as soon as the basin opens, and the distinct history of the sub-basin is recorded in the sedimentary infill. Individual sub-basins and their contained sediments are mappable at 1:1,000,000 scale, similar to the formation-level units in Stewart et al. (2022).

Sub-basin groups

Groups of sedimentary units in different tectonically related sub-basins are referred to as sub-basin groups and are the rank above individual sub-basin fill. They include sedimentary units from one or more sub-basins with similar characteristics, such as sediment depth, composition, seafloor morphology, or inferred age. Sub-basin groups are interpreted to share a similar tectonic history and age of sub-basin initiation.

Sub-basin groups are the lithostratigraphic equivalent of the assemblage level of Stewart et al. (2022). Assemblages are defined as one or more geological formations grouped in terms of their origin, lithology, inferred age and tectonic and structural regime. Many of the sub-basin groups

described here correlate with the assemblage boundaries of Stewart et al. (2022) (e.g., Central Lau Basin, Fonualei and Tofua Arc), but some sub-basin groups are broken out at a finer scale (e.g., Western ELSC, Eastern ELSC, Nodal Basins). Sub-basin group boundaries are displayed in Figure 2.5.

Sedimentary Basin

The highest rank of classification is the basin, which is defined as a regional topographic depression formed by large-scale crustal subsidence where sediment accumulates uniformly but may be contained in numerous sub-basins (cf. Boggs, 2013). Sedimentary basins are the lithostratigraphic equivalent of a sub-province of Stewart et al. (2022) which is a region that is a part of a single tectonic system, with distinct lithological, stratigraphic and structural characteristics, bound by large crustal-scale structures. The whole of the Lau Basin is considered such a feature, belonging to the Lau Tonga Arc-Backarc (LTAB) system (Collot et al., 2011; Stewart et al., 2022). The LTAB is a subdivision of the larger Indo-Australian Margin Province (Stewart et al., 2022). There is no comparable rank to Province in the sedimentary basin hierarchy of this study.

2.4 Echo Facies and Legend Construction

In the classification schemes developed by Damuth (1975, 1978, 1980) Damuth and Hayes (1977) and Damuth and Olson (2015), one "echo facies" is used to describe all of the echoes from the seafloor to the maximum depth of acoustic penetration, taking into account both the properties of the echoes as well as the seafloor topography (Figure 2.6). This approach is useful for creating maps of the distribution of sediment types and depositional processes at a basin and sub-basin scale. However, it is not particularly useful for reconstructing the sedimentary history of a sub-basin, because the entire echogram is assigned only one seismic facies or echo type. A Parasound ‘echogram’ typically has many echoes that have varying amplitudes, frequency/spacing, and continuity. Multiple echo facies can be resolved corresponding to different sedimentary units of a single sub-basin, each with a distinct depositional history.

We have developed a new classification scheme that assigns different sedimentary units to each echo facies, taking advantage of the higher resolution of Parasound. To consistently identify

similar units within different sub-basins, an echo facies legend was constructed (Table 2.1) with eleven units that are commonly observed in the Parasound profiles. Each echo facies has a distinct acoustic signature that is associated with specific sedimentological and depositional attributes. Four main descriptors are used to characterize the echoes: (i) ‘strong reflection’, (ii) ‘prolonged echo’, (iii) ‘acoustically transparent’, and (iv) ‘hyperbolic echoes’. “Strong reflections”, are high amplitude, thin reflections that are typically continuous throughout a sub-basin. The water-column sediment interface (seafloor) is an example of a ‘strong reflection’ caused by the difference in the acoustic properties of water and sediment (Figure 2.7a). A “prolonged echo” is a seafloor reflection that is diffuse, dark and fades in amplitude with depth (Figure 2.7b). Sedimentary units that do not have internal reflections appear white to light grey in colour in the echograms and are referred to as “acoustically transparent” units (Figure 2.7c). “Hyperbolic echoes” have a hyperbolic shape that typically overlaps with other hyperbolae (Figure 2.7d). This echo type is caused by reflections off steep slopes or uneven relief on the seafloor.

Echograms containing multiple strong sub-seafloor reflections have been found to contain little to no (0-5%) bedded coarse-grained (silt, sand, gravel) sediment (Damuth, 1980). Sediments with this echo facies could be hemipelagic carbonate oozes, fine ashfall, upper division turbidites or distal aeolian airfall. Echograms containing acoustically transparent or prolonged echoes have been found to contain moderate (0-30%) to high (5-100%) amounts of coarse-grained sediment (Damuth, 1980). Coarse-grained units could be lower division turbidites, mass transport deposits, pumice rafts or coarse-grained volcaniclastic sediment.

We inspected type examples of echograms from the SO267 Parasound data and assigned sedimentary composition and depositional processes to the 11 different echo facies in Table 2.1. These were selected with reference to the echo facies from Damuth and Olson (2015) and Fierens et al. (2019), which were developed using actual sediment cores and core log-seismic integration. While many of the observed features of the echo facies in the Parasound data are similar to those in the larger seismic reflection surveys, the two data sets are at very different scales. Whereas the vertical resolution of the seismic reflection data is 100s of meters to kilometers, the vertical resolution of the Parasound data can be as small as 15 cm. This means it

is possible for individual beds to be imaged but features at depths greater than 200 m in some seismic sections (e.g., Jegen et al., 2023) are not imaged in the Parasound.

Echo facies 1: Strong, thin, continuous reflections

Echo facies 1 comprises strong, thin reflections (approximately 20 cm to 75 cm thick) that are continuous and parallel along the length of the section, draping over the underlying sedimentary units or bedrock (Figure 2.8a). The corresponding sedimentary units are interpreted as thinly bedded, matching the thickness of the reflections according to McKee and Weir (1953). They are considered to be either hemipelagic sediments, fine ashfall, or upper-division turbidites (T_c, T_d, T_e in the Bouma sequence; Bouma, 1962). Echoes of this type have been correlated in reference cores to clay-sized material with few to no silt and/or sand interbeds (Damuth, 1980; Damuth and Olson, 2015).

Echo facies 2: Acoustically transparent

Echo facies 2 is characterised as acoustically transparent with no internal reflections (Figure 2.8b). This echo facies is always bound on the top surface by a strong reflection with the acoustic signal fading with depth. It is sometimes bound on the bottom by another strong reflection. The corresponding sedimentary unit is interpreted to be coarse-grained material, (i.e., silt-sized grains to boulders: Damuth, 1980), but there is no obvious internal structure. Because of the homogenous acoustic signature, we interpret these units as having been deposited in a single event (e.g., a mass flow). A similar echo facies is described by Damuth and Olson (2015) with the corresponding cores comprised of mass transport deposits, specifically debrites. Anastasakis (2007) correlated acoustically transparent echo facies to cores consisting of volcaniclastic turbiditic megabeds, with grain sizes ranging from fine-grained sand to fine silt. Acoustically transparent units could also represent deposits of channel splays.

Echo facies 3: Acoustically transparent with strong, thin reflections

This echo facies combines the character of echo facies 1 and 2 and is subdivided into 3 sub-facies.

Echo facies 3A: Acoustically transparent with few strong, thin reflections

Echo facies 3A is dominated by acoustically transparent sub-units with few strong, thin internal reflections (Figure 2.8c). The strong reflections are parallel and the spacing of the acoustically transparent areas ranges from regular to irregular. The sedimentary units are interpreted to be coarse-grained material with intercalated fine-grained sub-units and could represent several volcaniclastic flow events with interbeds of hemipelagic material or fine ash.

Echo facies 3B: Acoustically transparent with many-strong, thin reflections

Echo facies 3B is similar to 3A, consisting of acoustically transparent sub-units but with a higher proportion of strong, thin internal reflections (Figure 2.8d). The sedimentary units are interpreted to be coarse-grained material with a high proportion of fine-grained interbeds. The strong reflections of the fine-grained sub-units suggest that they are hemipelagic sediments or fine ash. The acoustically transparent sub-units are thinner than those in echo facies 3A, so we interpret them to represent smaller flow events or more distal deposits of larger flow events.

Echo facies 3C: Undulatory and acoustically transparent with strong, thin reflections

Echo facies 3C also consists of acoustically transparent sub-units with strong, thin internal reflections, but this echo facies is differentiated by its undulatory internal reflections and upper and lower contacts (Figure 2.8e). The wavelengths of the undulations are on the order of hundreds of metres to several kilometers. Bedforms of this magnitude qualify as sediment waves and are interpreted to have been formed syn-deposition by turbidity currents or reworked by bottom currents after the initial deposition. As in the other echo facies, the acoustically transparent portion is interpreted to be coarse-grained volcaniclastic material, while the strong, thin reflections are interpreted to be hemipelagic material or fine-grained ash.

Echo facies 4: Multiple acoustically transparent basal zones overlain by strong, thin reflections

Echo facies 4 consists of repeating packages of basal, acoustically transparent zones overlain by several strong, thin reflections (Figure 2.8f). It has a distinct stacking pattern in Parasound profiles. The basal zones and overlying strong reflections are parallel and continuous across the sub-basins. The acoustically transparent basal portion is interpreted to be coarse-grained material, and the overlying reflections are interpreted to be fine-grained material. We interpret this echo facies to be a set of very thick turbidites, as the stacking of fine-grained material over

coarse grained material is characteristic. Using Bouma sequence terminology, the acoustically transparent portion would be a T_a (massive or graded sandstone), T_b (planar laminated sandstone) and/or T_c (ripple cross-laminated sandstone), collectively referred to as "lower-division turbidites". However, planar lamination and ripple cross-laminations are thinner than 15 cm, which is the maximum resolution of the data, so it is not possible to distinguish between T_a, T_b, or T_c turbidites. The thin, strong reflections overlying the transparent unit would correspond to T_d (planar laminated silt and mud) and/or T_e (massive or planar laminated mud), collectively referred to as "upper division turbidites". The packages of coarse and fine sediment are around 10 m thick, which are much thicker turbidites compared to those in other sedimentary basins. However, echo facies 4 closely resembles unusually thick beds called megabeds found in the Cretan basin (Anastasakis, 2007). These megabeds are described as thick (~10 m thick) sequences of volcaniclastic material produced by volcanic eruptions interbedded with turbidites.

Echo facies 5: Prolonged echo with an incoherent internal structure

Echo facies 5 has a prolonged echo of moderate strength, sometimes with discontinuous internal reflections (Figure 2.8g). This echo facies is often located on the margins of sub-basins and slope-deposits, where the seafloor is inclined. The prolonged echo is associated with coarse-grained sediments (Fierens et al., 2019), and the incoherent internal structure, combined with the discontinuous internal reflections, suggests that the sediments represent a mass-transport deposit (MTD). Those with some internal reflections may be slumps or slides, whereas those with no internal reflections may be debrites. Reference cores in Damuth and Olson (2015) consist mainly of slumps and debrites.

Echo facies 6: Distorted echoes with overlapping hyperbolae

This echo facies consists of distorted reflections resulting from the reflection off rugged seafloor bathymetry or steep slopes, especially at the edges of the basins or near volcanic ridges and cones. This echo facies is subdivided into two sub-facies, 6A and 6B.

Echo facies 6A: Distorted hyperbolic echoes with sub-bottom reflections

Echo facies 6A is characterised by overlapping hyperbolae with visible, discontinuous sub-bottom reflections (Figure 2.8h). Although it is sometimes difficult to characterise the reflections

due to the distorted signal, their discontinuous nature indicates the presence of sedimentary cover above a rugged seafloor or steep slopes. Typically, grain size and sedimentary structures cannot be resolved in these echoes, although sediment thickness often can.

Echo facies 6B: Distorted hyperbolic echoes with no sub-bottom reflections
Echo facies 6B is characterized by overlapping hyperbolae without sub-bottom reflections (Figure 2.8i). This echo facies indicates that the seafloor is rugged or steep but does not provide any information about sedimentary cover.

Echo facies 7: Lenticular, with acoustically transparent internal zones
Echo facies 7 consists of lens-shaped acoustically transparent zones that pinch out laterally, with a bottom contact reflection that is concave up and a top contact that is flat-lying (Figure 2.8j). The sedimentary units are interpreted to be coarse-grained channel fill of volcaniclastic material. This echo facies is typically associated with multiple sinuous depressions at the seafloor, which appear to be channels that have been partially infilled by sediment.

Echo facies 8: Very strong reflections with poorly defined boundaries
Echo facies 8 is a ‘cloud’ of strong reflections that crosscut the sedimentary units around it and reduce the acoustic penetration beneath it (Figure 2.8k). This echo facies is sometimes associated with intersecting faults, and is typically a few hundred metres wide, but does not span entire sub-basins. It is interpreted to be the acoustic signature of gas, melt or alteration and possibly mineralization of the sediments.

2.5 Detailed Methodology

2.5.1 Sub-Basin Characterization and Sediment Thickness

A comprehensive subset of the Parasound echograms collected during SO267 and used to characterize the echo facies of each sub-basin is presented in Appendix C. The sub-basins are bathymetric depressions bound on all or most sides by highs that are either volcanic features (cones, ridges, etc.) or fault scarps or blocks. Slope deposits occur on sloped areas that accumulate sediment but are not necessarily in depression or bound by positive bathymetric

features. No minimum slope value is assigned for these deposits, but the overall trend must be sloping to be considered a slope deposit. Slopes range from 0.5° to 6°, and the average slope is 2.9°.

A total of 63 sub-basins and slope deposits were identified along the four transects (P03-P06) considered in the study (Figure 2.5). Sub-basins were named alphabetically from west to east, and the slope deposits are identified numerically from west to east. Sedimentary units within each-basin were identified by interrogating the Parasound echograms. The data were viewed and processed using the Kingdom Suite software. The first processing step equalizes reflection amplitudes vertically along each seismic trace to improve the visibility of deeper reflective events which have experienced amplitude decay. This is done using an Automatic Gain Control (AGC) function, which allows these deeper reflections to be viewed and interpreted (Figure 2.9). In the application of AGC, a specified time window (40 ms in this study) is progressively moved down the time axis and the root mean square (RMS) of the amplitudes in the window is calculated (Dondurur, 2018). The RMS is then multiplied by the amplitude of the central sample within the time window. The time window moves down one sample at a time and repeats the same calculations to the end of the time axis. AGC adjusts the relative amplitude information, so the resulting echograms cannot be used with confidence for quantitative interpretation. The echograms processed with AGC were also viewed using the "seismic envelope attribute", which describes the reflection strength (instantaneous energy of a reflection) and displays both positive and negative events as absolute values.

Once the character of the reflections was defined, they were assigned echo facies according to the echo facies legend and interpreted in terms of different types of sedimentary units. In some instances, two adjacent sedimentary units were assigned the same echo facies, and this can be for a number of different reasons. For example, subtle differences in the sedimentary units may not be distinguished in the echo facies legend, such as a difference in the distribution and/or thickness of the strong reflections and transparent echoes, and the presence of different sedimentary structures. For the sedimentary units that were assigned to the mapped echo facies, we used a code beginning with the transect number, followed by a letter for sub-basin identifier or number for slope deposit identifier, and finally the sediment unit number in lower-case Roman

numerals. The sedimentary units are described from the seafloor downward, so unit "i" is at the seafloor. For example, sedimentary unit P03-N-ii is the second sedimentary unit from the seafloor in sub-basin N on seismic transect P03. Sedimentary units that are deeper than the maximum penetration depth of Parasound were assigned an echo facies of 'X'.

The sedimentary units from each sub-basin are presented in stratigraphic columns to graphically display the echo facies observed in Parasound (Figure 2.10). The stratigraphic columns were created with *Strater* software, which uses the thickness and echo facies data from the database to create stratigraphic column graphics.

Parasound penetration depth is limited, and only the sedimentary units that were imaged were included in the quantitative analysis. The sediment-basement contact was visible in about half (43%) of the sub-basins and slope deposits; for the remainder, we used the available seismic reflection profiles to estimate sediment thickness. However, by combining Parasound and seismic reflection data, we were able to show the sediment thickness distribution on a much larger scale than previously attempted with Parasound alone. Sediment thicknesses in both the Parasound and seismic reflection data were calculated from two-way travel times (TWT), using an average sound velocity in the sediments of 1520 m/s:

$$Thickness\ (m) = \frac{TWT\ (s)}{2} \times 1520 \frac{m}{s}$$

2.5.2 Grain-Size Estimation

From the echo facies database (Appendix D), the proportions of coarse- and fine-grained material in each sub-basin were assessed. Percentages of coarse and fine material were assigned to each echo facies based on comparisons with sediment compositions in core by Damuth (1980), Fierens et al., (2019) and Damuth and Olson (2015) (Table 2.2). 'Coarse-grained' is defined as silt- to gravel-sized sediment, and 'fine-grained' as clay-sized sediment (Damuth, 1980). In this study, following the sediment descriptions from ODP Leg 135, we assume the coarse fraction is volcaniclastic material sourced from intrabasinal seamounts or the active Tofua arc, and the fine fraction is hemipelagic material, which is a combination of dominantly

carbonate/siliceous oozes, or fine ash, either deposited as airfall and transported through the water column or redeposited from underwater eruptions.

Echo facies 1 is interpreted to be entirely fine-grained material, similar to echo facies IB from Damuth (1980), 1A from Damuth and Olson (2015) and S3 from Fierens et al. (2019). Sediment corresponding to this echo facies contains 0-5% (average of 3%) silt to sand-sized volcaniclastic material (Damuth, 1980, and references therein), but we assign a value of 100% fine-grained sediment for this study.

Echo facies 2 is the coarse-grained endmember, similar to echo facies T (for transparent) from Fierens et al. (2019), echo facies 5 from Damuth and Olson (2015), and cores described by Kolla et al. (1980). Sediment corresponding to this echo facies consists of coarse-grained sand and is assigned a value of 100% coarse-grained sediment in this study.

Echo facies 3A, 3B and 3C, which are defined as acoustically transparent with strong reflections, are interpreted to have an intermediate composition of coarse and fine sediment. Echo facies 3B and 3C include numerous strong reflections and so are most similar to echo facies 1, with a high proportion of fine-grained sediment. In contrast, echo facies 3A has fewer strong reflections, and thicker acoustically transparent sub-units and is interpreted to have a higher proportion of coarse-grained material than 3B and 3C. Echo facies 3A, 3B and 3C are similar to echo facies IIA from Damuth (1980), 2 from Damuth and Olson (2015) and S4 from Fierens et al. (2019). In Damuth (1980, and references therein), cores corresponding to this echo facies contain 0-30% (average of 11.2%) silt to sand-sized sediment. Echo facies 3A is assigned a composition of 20% coarse material and 80% fine material; 3B and 3C are assigned 10% coarse material and 90% fine material.

Approximately 70% of echo facies 4 is acoustically transparent, and 30% has strong reflections. Thus, we interpret echo facies 4 to be 70% coarse-grained material and 30% fine. Echo facies 5 is characterised by a prolonged echo, similar to echo facies IIB from Damuth (1980), 3 from Damuth and Olson (2015) and O (for opaque) from Fierens et al. (2019). Cores corresponding to this echo facies contain between 5 and 100% (average 54.3%) silt to sand-sized sediment

(Damuth, 1980, and references therein). This echo facies is typical of MTDs such as debrites, which contain varying proportions of coarse and fine material. Thus, we have assigned values of 50% coarse and 50% fine material to the sediment corresponding to echo facies 5. Grain-size proportions cannot be calculated for the echo facies 6A and 6B because of the hyperbolic echoes, and so these sedimentary units are not included in the analysis.

The granulometric proportions defined above were used to calculate the average granulometric makeup of each sub-basin group. The sedimentary unit data are recorded as a thickness with an associated echo facies. In order to calculate an average grain size within multiple sub-basins, we must take into consideration the full "volumes" (i.e., the map area) of each sub-basin and not just the sediment thickness This is important when averaging the sediment composition of adjacent sub-basins with different widths. For example, a 10-km wide sub-basin with 50 m of coarse sediment and no fine sediment will significantly skew the average if adjacent basins with the same thickness of sediment are only 1 km wide and dominated by fine sediment.

To appropriately weight the sediment proportions in each sub-basin, we used the following equation, where *W* is the width of each sub-basin, *x* is the thickness of coarse or fine sediment and *d* is the total thickness of the sediment visible in Parasound.

$$Weighted\ Average = \frac{(W_1 \times x_1) + (W_2 \times x_2) + \cdots (W_n \times x_n)}{(W_1 \times d_1) + (W_2 \times d_2) + \cdots (W_n \times d_n)}$$

In the two examples given above, the average percentage of coarse-grained material is 91% and the percentage of fine-grained material is 9%, even though the basins have the same thicknesses of coarse and fine material. This calculation uses the total thickness of sediment visible in Parasound, rather than the total thickness measured from the seismic data, since the grain-size interpretations can only be applied to the Parasound echo facies. We have applied this weighting to all of the sub-basins with the results presented in Table 2.3.

2.6 Results

To build a comprehensive database of recent back-arc sedimentation in the central Lau Basin, this study used the seismic transects as guides. Four lines about 50 km apart and 100-300 km in

length were surveyed, from north to the south (P03-P06). Multiple datasets were recorded along these transects, including Parasound, multichannel seismic reflection (MCS), seismic refraction, magnetics, and gravity. A total of 63 sub-basins were identified along the four transects (Figure 2.5). A brief description of the transects is provided below and then a more detailed description of the sub-basins identified. The sub-basins range in size from 0.8 km to 45 km in width, and the sediment thicknesses range from 0 m to 1081 m. Overall, the basins are deeper closer to the Tonga arc, reflecting the ages of the basins. The asymmetric opening of the Lau Basin means that the oldest basins are in the east, and they become progressively younger toward the active spreading centers in the middle of the basin (ELSC, CLSC, LETZ). The thickest sediments along the transects are at the arc-backarc transition, with an overall fining of material to the west, with increasing distance from the arc.

Line P03 is oriented east-west at 17°18’37” S, between 176°18’22” W and 173°27’44” W. It is 290 km long and includes crust formed at the Eastern Lau Spreading Center (ELSC) and the Fonualei Rift and Spreading Center (FRSC). It then crosses the arc-backarc transition to the active Tofua arc. 22 sub-basins (P03-A to P03-W) and 1 slope deposit (P03-1) were identified along P03 (Figure 2.11). The sub-basins and slope deposits range in width from 0.8 km to 45 km (average 6.1 km), with sediment thicknesses from 9.9 m to 954.6 m (average 151.4 m). (Note: there is no sub-basin P03-O, which was reclassified as slope deposit P03-1.)

The P04 line is located along 17°47’58” S, between 174°19’33” W and 175°14’57” W and is 96.5 km long. This transect intersects crust formed at the ELSC, and the southern termination of the Fonualei Rift and Spreading Center FRSC. It then crosses the arc-backarc transition into the Tofua Arc. An additional 35 km of Parasound data was recorded at the western end of the seismic line, which are also included in this study. Along the P04 transect, there are nine sub-basins (P04-A to P04-I) and three slope deposits (P04-1 to P04-3) (Figure 2.11). The sub-basins range in width from 3.2 km to 24.0 km (average 11.1 km) and the sediment infill ranges in thickness from 17.5 m to 448.4 m (average 140.5 m). The slope deposits range in width from 4.1 km to 5.7 km (average 4.8 km) with sedimentary thicknesses ranging from 40.3 m to 171.8 m (average 110.0 m).

The P05 line is 214 km long and located at 18°11’54” S, between 174°16’31” W and 176°17’57” W. This seismic transect intersects crust formed by the Central Lau Spreading Center (CLSC), the ELSC and the Tofua Arc. Along the P05 line, we identified 14 sub-basins (P05-A to P05-N) and one slope deposit (P05-1) with widths from 1 km to 28.5 km (average 8.3 km), and sediment thicknesses from 0 m to 997 m (average 444 m) (Figure 2.12).

The P06 line is the southernmost seismic reflection transect in the study area. It is 124 km long, between 175°58’54” W and 174°48’08” W at 18°43’48” S and crosses crust formed by the ELSC and the Tofua Arc. There are 11 sub-basins (P06-A to P06-K) and two slope deposits (P06-1 and P06-2). Sediment thicknesses range from 41 m to 1081 m (average 283 m) and widths range from 1.6 km to 15.6 km (average 6.5 km) (Figure 2.12).

The characteristics of the 63 sub-basins and slope deposits are presented in Appendix D and are summarized here. The interpretations of the lithologic makeup are shown in schematic stratigraphic columns Figure 2.10. Total sediment thicknesses have been obtained from the combination of Parasound and seismic reflection data, wherever the sediment-basement contact is visible. The sedimentary unit descriptions including unit thickness, echo facies and grain sizes are from the Parasound data. The average proportions of different sediment types in sub-basin groups are given in percentages calculated from the echo facies using weighted values, discussed in the Methodology.

The sub-basins are grouped according to assemblages defined in Stewart et al. (2022). As the Lau Basin has evolved, crustal extension and sub-basin opening has occurred from east (early) to west (late) along the spreading centers, but also from north to south, as the spreading centers propagated southward. To reflect this basin evolution, we describe the stratigraphy of the sub-basins from west to east. There are six sub-basin groups. Beginning in the west, they are designated by their association with (i) the CLSC, (ii) the relay zone between the CLSC and ELSC (nodal sub-basins), (iii) western ELSC, (iv) eastern ELSC, (v) FRSC and (vi) Tofua Arc (Figure 2.5).

2.6.1 CLSC Sub-Basin Group

The CLSC group is located on the P05 transect and comprises the two westernmost sub-basins, P05-A and P05-B. Crust underlying this sub-basin group formed at the CLSC between 0.0 Ma and 0.78 Ma (Zellmer and Taylor, 2001). P05-A and P05-B are 7.9 km wide and 1.7 km wide, with bottoms (depths to the seafloor) at 2560 m and 2505 m, respectively and are bounded by volcanic ridges and cones. The CLSC is approximately 3 km to the east of P05-A and approximately 8 km to the west of P05-B. The Parasound data show little to no sediment fill, but the clear depressions in the seafloor suggest that these are recently formed and are slowly beginning to accumulate sediment. The echo-character in both sub-basins is hyperbolic (echo facies 6B; Figures C.36 and C.37), consistent with a lack of sediment and a hummocky seafloor indicative of recent basaltic flows.

2.6.2 Nodal Sub-Basin Group

This group includes the nodal sub-basins located on the P05 and P06 transects (P05-C, P05-D and P06-A). They are characterised by their rounded shape and steep slopes. P05-C is underlain by crust formed at the CLSC while P05-D and P06-A are underlain by crust formed at the ELSC. The age of the underlying crust is between 0 Ma and 0.78 Ma (Zellmer and Taylor, 2001). The sub-basins range from 2.6 km to 8.4 km in width (average 5.9 km) with bottoms at depths from 3007 m to 3182 m (average 3101 m). The sediment fill ranges from 44.8 m to 238.6 m thick (average 144.7 m) and is made up of 58% fine-grained material and 42% coarse-grained material. They are interpreted to be nodal basins formed by subsidence between overlapping spreading segments in relict back-arc crust (i.e., failed spreading centers). The overlap between the spreading segments accounts for the rounded shape, and there is a strong northeast-southwest fabric formed by the ridges and sub-basins. Basins of this type are common at overlapping spreading centers where the overlapping zones of extension curve toward each other (Macdonald and Fox, 1983). Typically, the spreading centers do not meet head-on, and a shear zone develops between them. This type of deformation occurs when the distance between the overlapping spreading centers is small, and spreading rates are high (Macdonald and Fox, 1983).

Two of the sub-basins (P05-D and P06-A) contain echo facies 4, which consists of repeating acoustically transparent packages overlain by several strong, thin reflections (Figures C.39 and C.51). These are the only observed occurrences of echo facies 4 in this study and are interpreted to be a turbidite sequence. Sub-basins P05-C and P05-D are in the transition zone between CLSC crust and ELSC crust. These are among the deepest sub-basins in the study area and contain sediment that is interpreted to be 57% fine-grained material and 43% coarse-grained volcaniclastic material. In both sub-basins, the lower succession of sediment is volcaniclastic with interbedded fine-grained material (P05-C-ii, P05-D-ii to P05-D-v), followed by an upper hemipelagic unit (P05-C-i, P05-D-i; Figures C.38 and C.39). Sub-basin P06-A is located on distal back-arc crust of the ELSC and has a distinctive oval shape in plan view. This sub-basin measures 6.8 km wide at a water depth of 3114 m and is bounded by ridges on both sides. It contains 150.5 m of sediment that is 59% fine-grained material, and 41% coarse-grained material. Coarse volcaniclastic material is abundant in the lower unit (P06-A-ii) corresponding to echo facies 3A, and the overlying unit (P06-A-i) corresponding to echo facies 4 is interpreted to be complete turbidite sequences (Figure 51). Two normal faults crosscut the entire sedimentary sequence, suggesting recent extension in this basin.

2.6.3 Western ELSC Sub-Basin Group

The Western ELSC sub-basin group is located on P03, P05 and P06 and comprises 13 sub-basins and 1 slope deposit: P03-A to P03-F, P05-E to P05-H, P06-B to P06-D, and P06-1. The basement underlying the western ELSC sub-basins was formed along the distant ELSC (Stewart et al., 2022). Under P03 and P05 the crust is between 0.78 Ma and 2.6 Ma, and under P06 the crust is between 0 Ma and 0.98 Ma (Zellmer and Taylor, 2001). The sub-basins are narrow, ranging from 0.8 km to 2.2 km in width (average 1.6 km) with bottoms at depths from 2042 m to 2710 m (average 2395 m). This group is characterized by rugged basement with many ridges and cones as bounding structures (Figure 2.5). The infilling sediment ranges from 9.8 m to 96.5 m thick (average 44.4 m) and contains 66% fine-grained material and 14% coarse-grained material. In this sub-basin group 20% of the sediment belongs to echo facies 6A or 6B (distorted echoes), in which the grain size distribution is unknown. The sub-basins along the P06 transect are slightly wider and contain thicker sediment fill than those to the north along lines P03 and P05. Additionally, there is slight decrease in sub-basin width toward the east along lines P05 and P06.

The western ELSC sub-basins along P03 range from 0.8 km to 2 km in width, with an average width of 1.5 km at depths from 2042 m to 2598 m (average 2201 m). The main bounding structures are volcanic ridges, but some sub-basins are bounded by cones and faults. Sediment thicknesses range from 9.8 m to 57 m (average 27.5 m) with 16% fine-grained hemipelagic material and 2% coarse-grained volcaniclastic material. The echo facies in four of the six sub-basins (P03-A, P03-C, P03-E, P03-F; Figures C.1, C.3, C.5, C.6) is 6A, which is a hyperbolic echo facies with some sub-bottom reflections, but a signature distorted enough to prevent the interpretation of sediment type. As a result, 82% of the sediment in these sub-basin groups is of unknown grain size. The distorted echoes are due to the rugged bathymetry and the narrow widths of the sub-basins, which can cause side echoes. Echo facies 1, 3A and 3B are observed in sub-basins P03-B and P03-D (Figures C.2 and C.4), but none of the sedimentary units appear to be correlatable between the sub-basins.

The western ELSC sub-basins along P05 are 1 km to 1.8 km wide (average 1.4 km) at water depths from 2431 m and 2574 m (average 2493 m). They are bounded by volcanic ridges and cones. Sedimentary fill is thin, ranging from 31.2 m to 58.5 m (average 48.2 m), and consists of 80% fine-grained material and 20% coarse-grained material. The basement on which the sediment is deposited is rugged, with a strong NE-SW trending fabric among the volcanic ridges. The underlying crust is interpreted to be spreading center crust (Schmid et al., 2020). There are no sedimentary units that can be correlated between all of the sub-basins, partly because of the thinness and lack of signal in the Parasound but also because of the rugged topography and complex mix of hemipelagic and coarse clastic sediment types.

The western ELSC sub-basins on P06 (P06-B to P06-D, P06-1) range in width from 1.6 km to 2.2 km (average 1.9 km) at water depths from 2420 m to 2710 m (average 2587 m) and are all ridge-bounded. The sediment fill ranges from 41 m to 96.5 m thick (average 68.0 m) and is made up of 82% fine-grained material and 18% coarse-grained material. Toward the east the sub-basins become slightly narrower (P06-B is 2.2 km wide and P06-D is 1.7 km wide) and sediment fill becomes considerably thicker (41 m in P06-B and 96.5 m in P06-D). Although the echo facies are not the same in the four sub-basins and the one slope deposit, they all contain a lower

succession of volcaniclastic sediment intercalated with fine-grained material (echo facies 3A, 3B, 2) and a top unit (unit i) of hemipelagic sediment (echo facies 1; Figures C.52 to C.55).

2.6.4 Eastern ELSC Sub-Basin Group

The Eastern ELSC sub-basin group covers all four transects (P03-P06) and comprises 16 sub-basins and 1 slope deposit: P03-G to P03-N, P04-A to P04-D, P05-I to P05-L and P05-1, and P06-E to P06-I. These sub-basins are underlain by crust formed along the ELSC (Stewart et al., 2022) and range from 0.8 km wide to 34 km in width (average 9.7 km wide) at depths from 2059 m to 2499 m (average 2350 m). Although mainly bound by volcanic ridges they are more widely spaced than the western ELSC sub-basins and they are wider and more continuous. The sediment fill in this sub-basin group ranges from 19.8 m to 448.4 m thick (average 153.2 m thick) and contains 84% fine-grained sediment and 16% coarse-grained sediment.
From the magnetic chrons of Zellmer and Taylor (2001), the crust beneath P03-G to P03-J is between 0.78 Ma and 2.6 Ma, and beneath P03-K to P03-N it is 2.6 Ma to 3.05 Ma. Along P04, the crust beneath each sub-basin has a different age: under P04-A it is between 1.76 and 1.98 Ma, P04-B is between 0.78 Ma and 2.6 Ma, P04-C is between 1.98 Ma and 2.6 Ma and P04-D is between 1.98 Ma and 3.05 Ma. The crust under P05-1 and P05-I to P05-J is between 0.78 Ma and 2.6 Ma, and under P05-K to P05-L it is between 1.98 Ma and 2.6 Ma. Finally, the crust under P06-E is between 0.78 Ma and 0.98 Ma; at P06-F to P06-H it is between 1.05 Ma and 1.76 Ma, and at P06-I it is between 1.98 Ma and 2.6 Ma.

Among this group, there is a distinct change in the seafloor morphology, from the rugged volcanic ridges of the westernmost ELSC sub-basins, to smooth, wide, sediment filled sub-basins with some volcanic ridges and cone volcanoes in the east. This change is abrupt and very obvious and may be related to a change in the underlying crust type (cf. proximal and distal back-arc domains of Schmid et al., 2020) (Figure 2.5). The sub-basins widen from the west to the east, but there is no trend in the basin morphology from the north to the south. In general, the sediment fill thickens from the west to the east with the thickest sediment in the sub-basins adjacent to the Tofua Arc. In the sub-basins along the P04 and P05 transects, the uppermost unit (unit i) of hemipelagic material increases in thickness from west to east (Figure 2.10).

The easternmost sub-basins (P03-N, P04-D, P05-L and P06-I; Figures C.14, C.27, C.48, C.60) are seemingly connected. Sediment thicknesses are broadly the same; 319.2 m, 448.5 m, 304.0 m and 394.5 m in sub-basins P03-N, P04-D, P05-L and P06-I, respectively. The sedimentary units generally consist of lower mixed coarse-grained volcaniclastic material and hemipelagic material overlain by echo facies 1, which is entirely hemipelagic material. In P05-L, the upper hemipelagic unit is absent, which suggests recent deposition of volcaniclastic material. Sub-basins P03-N, P04-D, P05-L and P06-I contain 82.4%, 92.4%, 82.6% and 91.4% fine-grained material, respectively and 17.6%, 7.6%, 17.4% and 8.6% coarse-grained material.

The eastern ELSC sub-basins along P03 (P03-G to P03-N; Figures C.7 to C.14) range from 0.8 km to 25.8 km in width (average 6.5 km), at depths from 2059 m to 2376 m (average 2276 m). The bounding structures are mainly volcanic ridges, but also include volcanic cones, faults and debris fields around volcanic cones. Sediment thicknesses range from 19.8 m to 319 m (average 85 m), and the sediment is 81% fine-grained material and 19% coarse-grained material. In general, both sediment thickness and sub-basin width increase from west to east. However, sedimentary units in these sub-basins are not correlatable; each sub-basin has a distinct sedimentary sequence consisting of some combination of echo facies 1, 2, 3A, 3B and 5 (Figure 2.10). Echo facies 1 is present as the top unit in sub-basins P03-H, P03-I, and P03-L to P03-N. The absence of this echo facies in sub-basins P03-G, P03-J and P03-K suggests that there was no period of quiescence in these basins during which accumulation of hemipelagic sediment could have occurred. Sub-basins P03-G and P03-L both contain echo facies 5, interpreted to represent mass-transport deposits, most likely caused by slope instability. These are the only instances of echo facies 5 in the eastern ELSC sub-basins.

Sub-basin P03-N has one of the best Parasound sections of all the sub-basins in this study, as it contains a clear record of faults, buried ridges, unconformities and the acoustic signal penetrates deep into the sediment (133 m deep). Two strong reflections that have poorly defined boundaries and resemble a cloud are located at the intersection of two faults with opposing dips (Figure 2.13). These anomalies are thought to be associated with hydrothermal fluid flow (discussed in section 2.7.5). This sub-basin contains many normal faults, some of which reach the seafloor while others only cut units P03-N-vi and P03-N-vii (Figure 2.13).

The sub-basins along P04 (P04-A to P04-D) are narrowest in the west (3.2 km, P04-A) and widen toward the east (34.0 km, P04-D). The sub-basins range in width from 3.2 km to 34 km (average 16.9 km) at depths from 2277 m to 2499 m (average 2396 m) and are bound mainly by volcanic ridges and in some cases by faults. The thickness of the infilling sediment ranges from 95.0 m to 448.4 m (average 220.6 m) and it consists of 86% fine-grained sediment and 14% coarse-grained sediment. The upper sedimentary units in P04-A (P04-A-i, P04-Aii; Figure C.24), P04-B (P04-B-i, P04-B-ii; Figure C.25), P04-C (P04-C-i, P04-C-ii; Figure C.26) and P04-D (P04-D-i, P04-D-ii; Figure C.27) are the same, consisting of echo facies 1 (hemipelagic material) overlying echo facies 3A (coarse volcaniclastic sediment intercalated with hemipelagic sediment) (Figure 2.10). From west to east the upper unit (unit i, echo facies 1) increases in thickness from 10.6 m in P04-A to 14.4 m in P04-C. In sub-basin P04-D, two lens-shaped, acoustically transparent units (echo facies 7) measuring 600 m and 700 m wide, are interpreted to be coarse channel fills (Figure 2.14). In plan view, these features are sinuous and appear to originate from the graben on the western flank of the FRSC. Sediment on the flanks of the channel consists of many strong, thin reflections, which we interpret to be fine-grained levee deposits. These channels are evidence of significant sediment transport from the FRSC to the eastern ELSC sub-basins. Another feature observed in P04-D is the pervasive deformation in the entire sedimentary succession, which has undulatory sedimentary features that may be sediment waves, and depressions that may be created by channels or faulting.

Between the western and eastern failed spreading centers of the ELSC, there is a series of wide deep sub-basins (P05-1, P05-I to P05-L; Figures C.44 to C.48) that range from 1.6 km to 28.5 km in width (average 11.2 km) at water depths of 2283 m to 2491 (average 2422 m) and are bound by volcanic ridges. Sediment thicknesses range from 85.9 m to 304 m (average 176.3 m) and the sediment is composed of 83% fine-grained material and 17% coarse-grained material. Notably, P05-1 and P05-I to P05-K contain the same four upper sedimentary units (P05-1-i to P05-1-iv, P05-I- to P05-K-i – iv), which suggests a shared depositional history. The lower sedimentary units (ii to iv) are volcaniclastic sediment intercalated with fine-grained material. As in P04-A to P04-D, these units thicken from west to east (8.4 m in P05-1 to 17.5 m in P05-K).

In sub-basin P05-I, there are several buried ridges and volcanic edifices visible in the Parasound (Figure C.45), similar to the cone volcanoes and ridges exposed at the seafloor. The sediment surrounding these volcanic features is relatively undisturbed, indicating that it was deposited after the formation of these features (post-depositional magmatism would have resulted in an upward doming of the sediment: Jackson et al., 2013). On the eastern boundary of sub-basin P05-L, there are many small cones concentrated in the area between the ELSC and the Tofua Arc visible in the bathymetry. The volcanic cones appear to be young, and backscatter in this area indicates less sediment cover. The Parasound data show normal faults in sub-basins P05-I, J and K indicating recent extension. Some of the faults reach the surface, cross cutting all the units, whereas others only cut the bottom four units. The two sets of shallower and deeper faults are interpreted to represent two different extensional events, occurring before and after the deposition of the youngest unit (unit i).

The eastern ELSC sub-basins along P06 (P06-E to P06-I; Figures C.56 to C.60) range in width from 3.5 km to 13.3 km (average 7.5 km wide) at depths from 2215 m to 2473 m (average 2361 m). The sub-basins are bound by volcanic ridges and cones and faults. Sediment fill ranges from 68.4 m to 394.4 m thick (average 185.4 m thick) and is 87% fine-grained material and 13% coarse-grained material. Sub-basin width, sedimentary units and grain size are highly variable in this sub-basin group. However, the overall sediment pattern consists of a lower succession of intercalated volcaniclastic and hemipelagic material (echo facies 2, 3A and 3B) overlain by hemipelagic material (echo facies 1). Normal faults are observed in most of the sub-basins but are most numerous and prevalent in P06-E (Figure C.56). In this sub-basin some of the faults reach the surface, whereas others stop at the contact between P06-ii and P06-iii, indicating two generations of faulting. In P06-F, the sedimentary units are undulatory, and there are several offsets in the seafloor (Figure 2.15). This appears to be the result of post-depositional faulting, as the faults cut through the entire sedimentary sequence. In contrast, the uneven seafloor and undulatory sedimentary units in P06-H and P06-I are likely caused by deposition on an uneven seafloor since there are fewer faults and the undulatory sedimentary units are continuous.

2.6.5 FRSC Sub-Basin Group

The FRSC sub-basins are interpreted to be the youngest rift-related sub-basins in the arc-backarc system. This group includes sub-basins P03-P to P03-T and P04-G and P04-H. The crust here was formed at the FRSC, so the sub-basins have a maximum age of 3.8 Ma (Stewart et al., 2022). The crust underlying P04-G and P04-H is between 2.6 Ma and 3.05 Ma, but there is inconclusive magnetic data at P03-P to P03-T. The sub-basins range from 0.9 km to 6.7 km in width (average 3.0 km) at depths from 1960 m to 3042 m (average 2567 m). The bounding structures include normal faults, rotated blocks, volcanic ridges and volcanic cones. Sediment ranges in thickness from 28 m to 257.6 m (average 125.9 m) and is composed of 59% fine-grained material and 41% coarse-grained material.

Sub-basins P03-P to P03-S (Figures C.16 to C.19) are formed along the axis of the FRSC, while P03-T (Figure C.20) is formed on distal back-arc crust and P04-G and P04-H (Figures C.31 and C.32) are formed on rifted arc crust (Stewart et al., 2022). P03-T, P04-G and P04-H are at much shallower water depths (from 1960 m and 2226 m) than P03-P to P03-S, which are between 2797 m and 3042 m deep. In general, the sub-basins widen toward the south (P04-G, P04-H). Echo facies 5 (interpreted to be MTDs) is the dominant echo facies and is present in each of the sub-basins within this group. Echo facies 3A and 3B (volcaniclastic sediment intercalated with hemipelagic material) are also present but less common.

Sub-basins P03-P to P03-T range from 0.9 km to 2.9 km in width (average 1.8 km) at water depths from 2221 m to 3042 m (average 2757 m). Sub-basin depth increases from west to east, from P03-P to P03-S, but decreases at P03-T, which is at the shallowest water depth among the sub-basins. In general, the sub-basins widen toward the east. They are mainly formed by rotated blocks, so the bounding structures are faults and ridges. The sediment fill ranges from 85.1 m to 185.4 m thick (average 119.2 m) and consists of 59% fine-grained material and 41% coarse-grained material. The P03 transect crosses the FRSC at the southern termination of the spreading center, which lies between P03-R and P03-S, so it is a region of active tectonic extension. The steep scarps along the normal faults provide a lot of instability, and as a result, MTDs (echo facies 5) are the most common sedimentary units in this group. Sub-basins P03-Q and P03-S contain only echo facies 3A (P03-Q-ii, P03-S-i; coarse-grained material intercalated with fine-grained material), which suggests no influence of MTDs.

Sub-basins P04-G and P04-H are 6.7 km and 4.9 km in width, at water depths of 2226 m and 1960 m, respectively. They are located on either side of the central volcanic cone at the axis of the rift. The sub-basins are bound by normal faults associated with the rifting. The sediment fill is 257.6 m thick in P04-G and 28.1 m thick in P04-H and is made up of 59% fine-grained material and 41% coarse-grained material. Sub-basin P04-G has two sedimentary units (P04-G-i and P04-G-ii) separated by an angular unconformity. The lower unit (P04-G-ii) has faint reflections in the west that become convoluted toward the east which suggests that it could be a slump deposit (echo facies 5). A period of non-deposition, indicated by the unconformity, was followed by deposition of the upper unit (P04-G-i) which is relatively flat-lying, consisting of strong reflections intercalated with acoustically transparent units (echo facies 3B) and infills the topography of the deformed lower unit (Figure C.31). Sub-basin P04-H, on the east side of the central volcano, has a very poor Parasound record (Figure C.32). The prolonged echo (echo facies 5; P04-H-i) suggests that the sediment is coarse-grained and highly reflective. This could be coarse rubble on the flank of the volcano, which would cause the surface to be more reflective, or it could be the hard rock base of the volcano with little to no sediment cover.

2.6.6 Tofua Arc Sub-Basin Group

The easternmost sub-basins are located on the Tofua arc. Included in this group are sub-basins and slope deposits P03-1, P03-U to P03-W, P04-1 to P04-3, P04-E, P04-F P04-I, P05-M P05-N, P06-J, P06-K and P06-2. Magnetic data at the P04, P05 and P06 sub-basins suggest the age of the crust could be between 2.6 Ma and 3.05 Ma, but the magnetic anomalies along P03 are unclear (Zellmer and Taylor, 2001) and more likely reflect local volcanism that has overprinted the Tofua Arc. As a result, the age of the crust underlying the intra-arc sub-basins is uncertain. They range from 1.3 km to 45.0 km in width (average 12.0 km) at depths from 959 m to 2356 m (average 1533 m). The sub-basins are bound by volcanic cones and ridges, faults, and rotated blocks. The sediment fill ranges from 17.5 m to 1080 m (average 421.8 m) and consists of 72% fine-grained material and 28% coarse-grained material.

This is a region where the older arc basement has been faulted, folded and buried by thick successions of sediment. Many of the presently active sub-basins may have opened during the

initial rifting of the Tonga Ridge, around 6 Ma (Hawkins, 1995). However, some of the sub-basins appear to be bound by more recent volcanic ridges or cones on at least one side (e.g., P03-U, P03-W). There are many volcanic features that push up into and crosscut the sedimentary units in the sub-basins, and some of these form bounding structures. P03-1, P04-E and P04-F to the west of the FRSC are interpreted to have opened as the FRSC propagated southward through arc crust. P04-1 is in a northeast-southwest trending graben west of the FRSC (Figure 2.5). It contains a slope deposit that is interpreted to be associated with more recent rifting of the arc and is underlain by distal back arc crust (Stewart et al., 2022). As elsewhere in the region, echo facies 1 is the upper unit (unit i) in twelve of the fifteen sub-basins. In the three sub-basins that do not contain echo facies 1 (P03-V, P04-2, P04-3), the upper unit is echo facies 5, interpreted as MTDs.

The sub-basins on the arc crust (in the east) are generally wider than those off the arc (in adjacent back-arc crust in the west). The Tofua arc sub-basins along P03 (P03-1, P03-U to P03-W) range from 1.3 km to 45.0 km in width (average 17.3 km) at depths from 1278 m to 1916 m (average 1602 m). The bounding structures are volcanic cones and ridges, faults and rotated basement blocks. The sediment fill ranges from 111.7 m to 954.6 m thick (average 473.7 m) and consists of 71% fine-grained sediment and 29% coarse-grained sediment. Sub-basins P03-U to P03-W are interpreted to have opened during the initial rifting of the arc, and as a result contain thick sedimentary successions. The echo facies sequences vary among these sub-basins but consist of a lower unit (P03-U-ii, P03-V-ii, P03-W-ii; Figures C.21, C.22, C.23) of volcaniclastic sediment with or without intercalated hemipelagic material (echo facies 3A, 3B and 2), and are overlain by hemipelagic material (echo facies 1) or a MTD (echo facies 5). There are many normal and thrust faults that cut through different sedimentary layers, which suggests that several deformational events have occurred during the history of these sub-basins. P03-1 is a slope deposit, in which sediment dips to the west and consists of a lower unit (P03-1-ii) of volcaniclastic sediment intercalated with hemipelagic material (echo facies 3B) and an upper unit (P03-1-i) of hemipelagic material (echo facies 1; Figure C.15).

Along P04, this group of sub-basins and slope deposits are narrower and shallower (P04-1 to P04-3, P04-E to P04-I; Figures C.28 to C.35). They range from 3.2 km to 14.2 km in width

(average 5.9 km) at depths from 959 m to 2356 m (average 1596 m). The bounding structures are normal faults, volcanic ridges and cones. The infilling sediment ranges from 17.5 m to 171.8 m thick (average 71.1 m) and consists of 68% fine-grained material and 32% coarse-grained material. P04-1 is a slope deposit located on the southeastern flank of a recently formed graben that branches off the FRSC. This graben acts as a sediment pathway that connects the FRSC to the ELSC sub-basins and channelizes sediment flow (as seen in P04-D). The sediment here belongs to echo facies 1 (hemipelagic material). As it is located on the outer banks of the graben, this sediment could be a levee deposit of the channels in the graben.

P05-M and P05-N are located on the Tofua Arc and are mainly visible in the seismic reflection data. They are 20 km and 23 km in width, at depths of 1348 m and 1028 m, respectively and are bounded by volcanic cones and rotated blocks. Sediment thickness is 997 m in P05-M and 873.2 m in P05-N and the sediment is made up of 84% fine-grained material and 16% coarse-grained material. They appear to have once been separate sub-basins that with time were filled with sediment such that they are now connected. In P05-M, there is a lot of folding of the sediment, resulting in sub-vertical dips of bedding in some places (Figure 2.12). At the surface, the sediment is on the sloping flank of a volcano of the Tofua Arc where there are strong undulations at the seafloor that appear to be large sediment waves. Here, the deformation is intense, with steep folds and concentrated faulting. Some chaotic reflections beneath the undulatory surface may be MTDs, as this is a likely environment where slope instability could occur. Elsewhere, the deformation is weaker, with slight faulting disrupting otherwise flat-lying, continuous reflections.

In P05-N, a large depression can be seen in the middle of the basin in the seismic data, with a concave-upward shape in most of the deeper sediment (Figure 2.12). This suggests a period of subsidence that occurred after the deposition of the deeper sediments. There is a change in reflection strength in the seismic data at approximately 1.90 s TWT (~1440 m), where the signal intensity increases toward the surface. The change in reflection strength ranges in depth from 1.5 s TWT at the edge of the concave region to 1.9 s TWT at the maximum depth, indicating a change in sedimentary composition (e.g., a change in the proportions of coarse and fine material) rather than the expected uniform increase in compaction with depth. Above this depth, the

sediment begins to infill the topography, and the reflections begin to flatten out. Unlike sub-basin P05-M, where the top layer of sediment is deposited on a steep slope, the upper units in P05-N (P05-N-i and P05-N-ii) are deposited on the shallow slope of the arc and are flat-lying. The sediment here is much better stratified and is more continuous than in sub-basin P05-M downslope of the Tofua Arc, where many of the seismic reflections are chaotic and irregular. Onlapping sedimentary layers in the seismic reflection data for P05-M mark an angular unconformity that slopes toward the east. In both sub-basins there are many faults, some of which reach the surface, while the majority do not and stop about 80 ms TWT (~ 60 m) below the seafloor.

Along P06, the Tofua Arc sub-basins (P06-J, P06-K, P06-2) range from 3.8 km to 15.6 km in width (average 10.9 km) at depths from 1437 m to 1941 m (average 1663 m). They are mainly bound by volcanic cones, but P06-K is deposited in a caldera. Sediment fill ranges from 237.9 m to 1081 m thick (average 711.9 m) and is 65% fine-grained material and 35% coarse-grained material.

P06-J contains a sedimentary succession at the bottom of the sub-basin (visible in seismic data) that has strong, continuous reflections and a depression in the center of the sub-basin (Figure 2.12). Overlaying these sediments is a unit with much weaker reflections, occasional short discontinuous strong reflections, and an upper contact that is very irregular and undulatory. The top unit has strong, continuous reflections and infills the undulations and has a flat upper contact. The undulations present in this sub-basin have a wavelength of 1 km to 2 km and are likely sediment waves formed by bottom currents. P06-2 is a slope deposit on the flanks of a volcanic cone and contains a lower succession of volcaniclastic sediment intercalated with hemipelagic sediment (echo facies 3A, 3B, 2) and an upper unit of hemipelagic material (Figure C.63), similar to the adjacent basin P06-J. This suggests that the most recent sedimentary history is similar for both the sub-basins and slope deposits. In the seismic data, however, the sedimentary history appears to be different. The sedimentary succession in the slope deposit (P06-2) consists of a lower unit of weaker reflections that are chaotic and undulatory with occasional, discontinuous strong reflections. The upper contact slopes slightly toward the east and is

undulatory. The upper unit contains stronger reflections that are relatively flat lying, and the upper contact is mostly flat with some undulations.

P06-K is the only sub-basin included in this study that formed within the caldera of a volcano. There are many other calderas in the Lau Basin that likely contain sub-basins, however, the caldera that hosts P06-K is the only one crossed by a seismic transect in the study area. It contains a lower unit (P06-K-ii) of volcaniclastic material intercalated with hemipelagic material (echo facies 3B) and an upper unit (P06-K-i) of hemipelagic material (echo facies 1; Figure C.62).

2.7 Quantitative Analysis

The results of this study show that sub-basin development is mainly controlled by the morphology of the underlying crust, the proximity to the Tofua arc and local volcanic activity. The 63 identified sub-basins and slope deposits cover an area of approximately 30,804 km^2 and are divided into six sub-basin groups. Echo facies distribution, sediment thicknesses, and interpreted grain sizes provide important information on the regional variation of sediment sources and depositional processes. ODP Leg 135 drill cores showed mainly upward-fining depositional sequences, where the uppermost sediments are dominated by hemipelagic sedimentation with coarser volcaniclastic sediment mainly sourced from intrabasinal seamounts (Rothwell et al., 1994a). The widely spaced drill cores, however, are much further from the Tofua Arc and the FRSC and provide a regional scale insight into the earliest stages of opening of the Lau Basin. The Parasound surveys in this study focus on the last few m.y. of sediment deposition in the currently active back-arc region and arc-backarc transition of the eastern Lau Basin, with nearly continuous sub-bottom profiling from which we interpret more detailed spatial and temporal variations in sedimentation. The close proximity of the study area to the Tofua Arc and FRSC highlights their strong influence on regional sedimentation, which is generally more complicated than previously thought, based on the low resolution of early sub-bottom profilers (Figure 2.16). We illustrate the complexity now visible in high-resolution Parasound data based on six analyses: sub-basin distribution, sediment thickness distribution, echo facies distribution, sediment grain size distribution, proximity of the upper-most sedimentary unit to the sediment source and sediment volume calculation.

2.7.1 Sub-Basin Distribution

The distribution of the sub-basins and slope deposits in the study area is shown in Figure 2.17. The map shows the distribution of sediment but not sediment thickness (discussed below). It was created by identifying smooth regions in the bathymetry with a slope of less than 3°. The identified basins and slope deposits cover 30,804 km^2, which makes up 47% of the map area. Basins formed in arc crust contain thicker, continuous accumulations of sediment. Within the rifted arc crust of the FRSC, sediment deposition is mainly between rotated crustal blocks and in grabens. Basins that are actively extending in the arc-backarc transition and proximal back-arc region are wider, interconnected and accumulate more sediment (Eastern ELSC sub-basins). Farther west, the sub-basins most closely associated with active back-arc spreading become narrower and more isolated. In this area the sub-basins are sparse and small, and much of the crust is not sedimented (Western ELSC, CLSC and Nodal Basins). The main controls on sedimentation in the different sub-basins are the age of the basins, the nature of the subsidence (which is related to the type of underlying crust and its deformation history), and the sedimentation rates. Sediment produced at the Tofua Arc blankets the arc and proximal back-arc crust formed at the ELSC. Toward the west with increased distance from the arc, newer crust formed at the ELSC and CLSC has more ridges and cones and a smaller sediment input from the arc, resulting in more isolated, narrow basins and less sediment overall. Newly rifted crust at the FRSC also has narrow sub-basins with relatively little sediment, despite their great depth, owing to their young age.

2.7.2 Sediment Thickness Distribution

Using the Inverse Distance Weighted (IDW) algorithm in ArcMap, we produced a sediment isopach map to analyze the distribution of sediment thickness throughout the study area (Figure 2.18). This map interpolates the sediment thickness between sub-basins where there are no data. In the IDW interpolation, a search radius with minor semi-axis (east-west) of 0.1 decimal degrees was used; to capture data from the adjacent lines, a major semi-axis (north-south) of 0.3 decimal degrees was used. From this map and the stratigraphic columns (Figure 2.10) we observe several regional trends in sediment thickness.

The thickest sediments in the study area are at the arc front in the Tofua Arc sub-basin group but there is a notable thinning at the southern tip of the FRSC, which is actively rifting into the arc crust. The Tofua Arc sub-basins have been accumulating volcaniclastic and hemipelagic sediment since the initiation of the Tofua Arc at about 3 Ma (Stewart et al., 2022), which accounts for the thick sedimentary successions. There is generally decreasing sediment thickness away from the arc, but it is highly variable, reflecting localized or distributed extension in the back-arc. From east-to-west, away from the Tofua Arc, there is a decrease in sediment thickness in the eastern ELSC, western ELSC and finally the CLSC. The increase in sediment thickness in the east illustrates the significant contribution of sediment from the Tofua arc to the sedimentary fill of the back-arc sub-basins. The CLSC sub-basins are characterised by a lack of sediment because they have opened most recently from seafloor spreading and they are the youngest sub-basins in the study area. However, there are local anomalies that reflect variably distributed extension in the back-arc. For example, the nodal sub-basins in the relay zone between the CLSC and ELSC are anomalously deep with thicker sedimentary successions compared to other sub-basins with similar widths. The opening of these sub-basins is interpreted to be associated with the overlapping extension of the CLSC and the ELSC. The underlying crust is between 0.0 Ma and 0.78 Ma (Zellmer and Taylor, 2001) which indicates that the basins opened relatively recently. In this case, the thick sediment fill suggests rapid deposition from a local source. We interpret the source to be volcaniclastic sediment from an intrabasinal seamount, redeposited by turbidity currents. Similarly, the sedimentary sub-basins of the FRSC contain sediment of variable thickness, despite their young age, most likely related to seismicity that triggered MTDs which can be localized deposits. Some variability in sediment thicknesses in the western and eastern ELSC sub-basins also suggests localized depositional controls.

2.7.3 Echo Facies Distribution

Stratigraphic columns based on echo facies for each of the sub-basins and slope deposits have been compiled in Figure 2.10. Three main echo facies are observed: the most common echo facies are 3A and 3B (mixed volcaniclastic and hemipelagic sediment); echo facies 5 (MTDs) is mainly found proximal to the FRSC but also in the eastern ELSC sub-basin group; the top unit in 39 of 63 sub-basins is echo facies 1 (hemipelagic sediment). The proportions of each echo facies comprising the entire sedimentary succession are summarized in Table 2.4, calculated using the

weighted average method described in Section 2.4.3. Echo facies 1 (hemipelagic sediments, fine ashfall, or upper-division turbidites) accounts for 12.3% of the total sediment in the study area which demonstrates that there have been relatively fewer periods of purely hemipelagic sedimentation. Echo facies 2, 3C, 4, 6A and 6B each make up less than 6% of the total sediment in the study area, suggesting that their associated depositional processes (i.e., proximal mass flows, sediment-wave forming bottom currents, proximal turbidity currents) play a lesser role in the Lau Basin. Coarse-grained material intercalated with fine-grained material is the dominant sediment (echo facies are 3A and 3B), which makes up over 70% of the sediment pile in the study area. These facies are indicative of periods of deposition of volcaniclastic material interspersed with periods of quiescence during which the finer-grained material (hemipelagic sediment or other clay-sized sediment) was deposited. The frequency of these episodes is on the order of 10s of episodes per sedimentary unit. Echo facies 3A and 3B may also represent multiple sediment gravity flows, where the acoustically transparent sub-units are coarser sediment, and the stronger reflections are interbeds of finer sediments deposited between flow events. Echo facies 3 is roughly equally divided between sub-facies 3A and 3B, confirming that there were many periods of mixed hemipelagic and volcaniclastic sedimentation, or frequent alternation between periods of increased volcanic activity and volcanic quiescence. Echo facies 5 is mainly found in the FRSC which is an ideal location for MTDs as the steep rift flanks and seismicity (Baxter et al., 2020) are especially conducive to slope instability. 24 sub-basins do not follow the fining upward trend which indicates that deposition across the back-arc is also influenced by local physiographic conditions such as flows from intrabasinal seamounts and mass-transport deposits triggered by seismicity and slope instability.

Within some sub-basin groups there are trends in the echo facies and sequences of sedimentary units that can be correlated between sub-basins, whereas in other groups the echo facies are heterogeneous and cannot be correlated as easily. For example, the echo facies in the western ELSC vary between each sub-basin, which suggests that they had distinct depositional histories. We interpret the source of sediment to be the same for the sub-basins of this group (i.e., volcaniclastic material from local intrabasinal seamounts and the Tofua Arc and hemipelagic sediments), but since the echo facies are not correlatable, we suggest that the depositional processes were controlled by independent volcaniclastic flows and turbidity currents. This is

supported by the abundance of volcanic cones and ridges, which isolate the sub-basins and control local deposition. The eastern ELSC sub-basins along P03 are also characterized by heterogeneous sequences of echo facies that are impacted by local volcanism from the surrounding intrabasinal seamounts.

Two examples of well-correlated homogeneous sedimentary sequences between sub-basins are P04-A to P04-C, and P05-I to P05-K. In P04-A to P04-C, the sequence consists of two lower units of echo facies 3A or 3B that are consistently overlain by echo facies 1. In P05-I to P05-K the deposition of the upper sedimentary sequence (P05-I- to P05-K-i – iv) is interpreted as several eruptive events that deposited material in all the sub-basins, with intervening periods of quiescence during which the hemipelagic material was deposited and then an extended period of hemipelagic sedimentation. A similar sequence is seen in a nearby slope deposit (P05-1). Although the depositional processes, and possibly even the individual events, responsible for these units are likely the same in each sub-basin, the variation in sediment thickness suggests that there are local controls on deposition such as distance from the volcaniclastic source.

The only instances of echo facies 4, which alternate between thick, acoustically transparent, volcaniclastic layers and multiple thin, strong reflections indicating hemipelagic layers, are in the nodal basins P05-D and P06-A. This repetitive layering of echo facies appears very similar to that of a turbidite, with coarser-grained, massive or graded beds on the bottom, followed by fine-grained, thinly bedded units above. These large units (~ 10 m), however, bear a resemblance to turbiditic megabeds (Anastasakis, 2007). Repetition of this sedimentary succession in P05-D and P06-A suggests that there have been at least 3 (but likely more) eruptive events and turbidity currents that were confined to each sub-basin, consistent with the steep slopes of the bounding sub-basin walls where slope instability could trigger turbidity currents.

The regional echo facies trends suggest an element of widespread homogenous sedimentation, but local variation within the back-arc sub-basins suggests a strong influence from intrabasinal seamount volcanism and other local depositional controls such as seismicity and variable sediment pathways.

2.7.4 Sediment Grain-Size Distribution

Figure 2.19 and Figure 2.20 show the proportions of coarse- and fine-grained material for each sedimentary unit in stratigraphic columns and by IDW in a map view. The map of sediment coarseness was calculated in the same way as the IDW map of sediment thickness in section 2.7.2. Together, the two Figures highlight regional and temporal variations in the distribution of coarse and fine material described above, with local variations in sediment coarseness due to intrabasinal volcanism and the influence of redeposited sediments. Using the assigned proportions of coarse- and fine-grained material from Table 2.2, the total granulometric makeup for each sub-basin group and for the entire study area was calculated using the Weighted Average calculation described in Section 2.5.2 (Table 2.3). In the study area, 22% of the sediment is coarse-grained, 77.3% is fine-grained, and 0.7% of the sediment is of unknown grain-size (the latter because no grain-size information can be extracted from echo facies 6A and 6B with hyperbolic echoes).

Figure 2.20 shows the notable increase in coarse sediment with proximity to the arc. In the FRSC in particular, sediment coarseness is high due to the MTDs which are interpreted to consist of 50% coarse- and 50% fine-grained material. There is also significant variability in sediment coarseness across the back-arc sub-basins. The nodal basins in the relay zone between the ELSC and CLSC also contain abundant coarse-grained material which we have attributed to the thick successions of turbidites (echo facies 4) which contain basal sub-units of redeposited volcaniclastic sediment overlain by sub-units of fine-grained material and are interpreted to consist of 70% coarse- and 30% fine-grained material.

2.7.5 Proximity to Sediment Source

Some modes of deposition in different sub-basins suggest close proximity to the source, such as MTDs and thick, massive flows, while others suggest the sediment source is far away, such as hemipelagic deposits. From this, a proximity scale from 1-6 was developed, with 1 being the most proximal and 6 being the most distal from the sedimentary source. Since sub-basins often comprise several sedimentary units with different echo facies, we first examined the proximity value of the top echo facies, representing the current position of the sub-basin to their

sedimentary source. Echo facies 5, which is interpreted to be MTDs, was assigned proximity value 1, as these deposits are often triggered by flank collapse and are deposited near their source. Echo facies 2, which is interpreted to be a coarse-grained mass flows deposited rapidly during a single flow event, was assigned proximity value 2. The rapid deposition of a thick succession of material suggests that the transport distance was short, and the sediment source was proximal. Echo facies 4 consists of approximately 70% coarse-grained material and 30% fine-grained material and is interpreted to have been deposited by proximal turbidity currents since the coarse-grained sub-units (acoustically transparent) are thick. Echo facies 4 is thus assigned a proximity value of 3. Echo facies 3A consists of approximately 20% coarse-grained material intercalated with 80% fine-grained material and was assigned a proximity value of 4. It is interpreted to be deposited during several events, as sub-units of coarse-grained material, with short periods of quiescence during which fine-grained material could settle. Echo facies 3A is interpreted to be deposited by turbidity currents relatively close to their source, but more distal than echo facies 4. Echo facies 3B and 3C are assigned a proximity value of 5. They both consist of approximately 10% coarse-grained material intercalated with 90% fine-grained material. The coarse-grained sub-units in this echo facies are typically thinner than those of echo facies 3A, which suggests more distal deposition of sediment-gravity flows. Finally, echo facies 1, which is interpreted to be hemipelagic material, is assigned a proximity value of 6. This echo facies does not suggest a dominant influence from volcaniclastic sources and therefore is interpreted as the most distal echo facies.

The assigned values are shown in map view in Figure 2.21 to illustrate the proximity of the most recently deposited sedimentary unit to the source of sediment. The most proximally-sourced sediments are in the FRSC and the Tofua Arc sub-basin groups. Rifting occurring in the FRSC, and the steep slopes of the Tofua Arc volcanoes are triggers for MTDs which are deposited relatively proximal to their source. Additionally, these sub-basins are the closest to the Tofua Arc, which produces a large volume of sediment. Sub-basins in the eastern ELSC group are overall the least proximal to their sediment source, indicated by a dominance of hemipelagic sedimentation and fine-grained ashfall, most likely from the Tofua Arc. This also suggests a relative absence of intrabasinal seamount volcanism in this region. The western ELSC sub-basins and the nodal sub-basins contain sediments with a wide range of proximity to their source, which

suggests that the volcanism and slope instability in this region is controlled locally. Deeper sedimentary units were not analyzed but could similarly be used to investigate the change in proximity to the sedimentary source in each sub-basin through time.

2.7.6 Sediment Volume Calculations

To illustrate sediment accumulation at the sub-basin scale, we have attempted a sediment volume calculation using sediment thickness from the seismic reflection and Parasound data. We chose P05-D as an example because it is crossed by multiple lines, including both Parasound and seismic reflection (Figure 2.22). The calculation was completed using the Kingdom Software as described in Appendix A. Where the dominant sediment source is volcaniclastic material from intrabasinal seamounts and the active arc, the sediment volume provides information about eruptive input of adjacent volcanoes and seamounts. Sub-basin P05-D has 1) well-defined boundaries; 2) multiple Parasound sections south of the seismic transect, which provide complete sediment thickness information; 3) a clearly visible sediment-basement contact in the seismic and Parasound data, which are all necessary for the volume calculations.

The model viewed in the 3D-viewer of the Kingdom software, VuPak, shows the interpolated topography of the sediment-basement contact (Figure 2.23). In the centre of the model, the sediment-basement contact bows upward which is an artifact caused by the absence of data at this location. The available data indicate a gross sediment volume of 11.8 km^3 for the sub-basin. In P05-D, 55% of the sediment is fine-grained and 45% is coarse-grained, which equates to 6.49 km^3 and 5.31 km^3, respectively. If the coarse-grained sediment is volcaniclastic material, we can assume that 5.31 km^3 of eruptive material was deposited in the basin during multiple eruptive events and so can be compared to the possible source volumes from eruptions recorded in the region (see Discussion).

The model does not consider sediment compaction which begins once sediment is buried, and the degree of compaction increases with burial depth (Chapman, 1983). The rate of compaction at a given depth is controlled by the rate of sediment loading, the permeability of the sediment and the sediment grain size and composition (Chapman, 1983). It is difficult to approximate the degree of compaction in P05-D, since we lack all the required information to create an accurate

model, however, we estimate very little effect of compaction at the scale of the sub-basin. Although we have interpreted the grain size of the sedimentary units, we only distinguish between clay-sized sediment and sediment coarser than silt; more detailed grain size information is necessary to calculate sediment compaction. Sediment compaction curves from Athy (1930) show that at approximately 283 m sediment depth, the depth of P05-D, mudstones, siltstones and sandstones lose less than 5% porosity at the bottom of the sub-basin; the remaining sedimentary fill above this point loses less than 5% porosity during compaction.

2.8 Discussion

This study has examined, for the first time using Parasound data, the processes of sedimentation in a rapidly opening back-arc basin and the development of sedimentary sub-basins spanning at least 5 m.y., including the distribution of different sub-basin types, the associated stratigraphic sequences, grain-size distribution of the sediment, thickness distribution, echo facies distribution, and variations in sedimentation rate. The study provides a glimpse at modern sedimentation in the basin, compared to studies of older sediment captured in deeper seismic reflection data. Importantly, these shallow sediments are often not observed in seismic data, so little is known about the earliest deposition in these types of basins. Actively subsiding basins in the study area reveal this early history. We show 1) that rapid early sedimentation in back-arc basins is dominated by mass-transport deposits proximal to the actively rifting arc, 2) that sediment thickness increases with proximity to the arc, even in the youngest basins, and 3) that back-arc sediments become finer as the basin evolves. The basin infill records the non-uniform opening of the back-arc region and the importance of distributed extension as the basin evolved. The study highlights different sediment sources and depositional processes, the volumes of sediment involved, and the significance for other processes occurring in the sub-basins (e.g., hydrothermal alteration and mineralization: see below).

There are three main sources for the sediment in the Lau Basin: the Tofua Arc, intrabasinal seamounts and volcanic ridges, and hemipelagic material (e.g., Figure 2.24). Bednarz and Schmincke (1994) concluded from sedimentological and geochemical studies of ODP Leg 135 cores that the Lau Basin margins provided minimal sediment input to the basin, but rather explosive rhyolitic eruptions from seamounts were the dominant contributor of volcaniclastic

material. The sub-basins in our study are located significantly closer to the Tofua Arc and the FRSC, thereby experiencing a higher degree of sediment input from these sources. That the arc is contributing a significant amount of volcaniclastic sediment to the study area is supported by the observed increase in sediment thickness toward the arc. Previous work from ODP Leg 135 identified several processes of sediment accumulation in the Lau Basin including pyroclastic flows from intrabasinal or arc volcanism, remobilization and redeposition of volcaniclastic sediment and fallout from the water column (Figure 2.24). We see evidence for these in the Parasound data and used this to constrain the interpretations of each echo facies.

Bednarz and Schmincke (1994) identified four different types of volcaniclastic deposits from core: primary subaerial fallout tephras, epiclastic deposits, subaqueous fallout and pyroclastic deposits and hyaloclastites. Primary subaerial fallout tephras are volcanic ash deposits that have undergone minimal reworking, experiencing some grading and occasionally hosting interbeds of hemipelagic sediment. Epiclastic deposits are volcaniclastic turbidites that originate from the Lau Ridge or Tofua Arc from submarine or subaerial eruptions. Subaqueous fallout deposits and pyroclastic flow deposits are thought to be similar to subaerial pyroclastic flows and are sourced from intrabasinal seamounts, forming deposits ranging up to 10s of m thick. Finally, hyaloclastites are composed of angular, vitric shards that are formed during the quenching of pillow basalts and lava tubes. Although it is not always possible to distinguish these different types of deposits in the Parasound data, it is likely that the acoustically transparent echo facies with variable amounts of intercalated strong, thin reflections (echo facies 2, 3A, 3B, 4) correspond to the epiclastic deposits, subaqueous fallout deposits and pyroclastic flow deposits. The primary subaerial fallout tephras could be mistaken for hemipelagic deposits in Parasound, and the hyaloclastites would be impossible to identify without cores.

Rothwell et al. (1994b) found that the fine-grained sediment was deposited both by hemipelagic sedimentation and redeposited as hemipelagites. We see abundant and widespread hemipelagic sedimentation as strong, thin reflections, although it is not possible to distinguish the depositional mechanism from Parasound echograms. An area where hemipelagites may be observed in Parasound data is in the upper unit (unit i) in the sub-basins along the P04 and P05 which consists of echo facies 1 (hemipelagic sediment) and increases in thickness toward the east

(Figure 2.10). The decrease in hemipelagic sediment toward the west suggests that hemipelagic-dominated sedimentation occurred more recently in the western sub-basins than in the east, consistent with the young age of some of the basins next to the CLSC. However, variation in the thickness of this unit could also be attributed to hemipelagites deposited by turbidity currents, which can be more localized. There is evidence in the Parasound data for MTDs as prolonged echoes with no internal structure. These deposits are probably similar to the MTDs observed by Rothwell et al. (1994b) and identified as mudclast conglomerates.

2.8.1 Mass-Transport Deposits Indicate Proximity to Active Rifting

The FRSC is a region of active arc rifting and seafloor spreading that is propagating southward, cutting through the Tofua Arc. An interesting observation from the stratigraphic columns is that echo facies 5, which is interpreted to represent MTDs, is almost exclusively found within the presently active rift zones, including sub-basin P05-H at the northern termination of the ELSC, the FRSC or on its flanks, and on rifted Tofua Arc crust (Figure 2.10). MTDs may also be present in other sub-basins, deeper than the maximum penetration depth of Parasound, as they would have been deposited during earlier phases of sub-basin formation. The sub-basins where echo facies 5 is dominant in the FRSC are P03-P to P03-T and P04-F to P04-I. These are V-shaped sub-basins, created by the rotation of crustal blocks during rifting. The bounding walls and flanks are steep, and the MTDs are likely caused by mass-wasting due to slope instability. P03-T, the furthest sub-basin to the east in the FRSC, as well as P04-G and P04-H, are all adjacent to volcanic cones. These cones provide a sediment source as well as the steep slope required to cause the rapid deposition of large volumes of sediment of an MTD (Figure 2.25). Along P04, sub-basins P04-F and P04-I, as well as slope deposits P04-2 and P04-3, are all located on the flanks of the FRSC on crust formed by the Tofua Arc. Rifting of this crust also provides the instability required to mobilize sediment as an MTD.

P03-V is another sub-basin formed on Tofua Arc crust, but in this case, it is adjacent to a large arc volcano (Volcano J). Here, the trigger for sediment mobilization could be either slope instability or large eruptive events that displace previously deposited sediment down the steep slopes of the cone. This is probably true for many of the volcanoes along the arc, although Volcano J was deemed inactive by Keller et al. (2008) because it is covered by carbonates. Echo

facies 5 in P03-L could be related to the adjacent volcanic cone, where the bathymetry shows a rubble field surrounding it.

2.8.2 Sediment Thickness Increases with Proximity to the Arc

The increase in sediment thickness toward the arc, as seen in Figure 2.18, is up to 1081 m. This suggests very high sedimentation rates, considering the young ages of the sub-basins. An increase in sediment thickness near the active arc is expected, because of the large volume of material produced by the active arc volcanism. The stratigraphic columns illustrate this trend very clearly as there is an abrupt transition between thin and thick sedimentary successions between sub-basins formed on ELSC crust and those formed on Tofua Arc crust. The increase in sediment thickness is evident from a distance of at least 250 km, confirming material from widespread volcanism at the arc is transported beyond the sub-basins immediately adjacent to the arc. Bednarz and Schmincke (1994) concluded that the majority of the volcaniclastic material in cores distal to the Tofua arc was sourced from nearby seamounts. However, we show a significant input of volcanic-derived and mass transport deposits with proximity to the arc. Two notable exceptions are sub-basins P05-D and P06-A, which are nodal basins with sediment thicknesses of 238 m and 150 m, respectively. They are surrounded by sub-basins with much less sediment, suggesting that the steep flanks and depth of the nodal basins may be preferred catchments for resedimented material. These sub-basins contain thick successions of echo facies 4, which is interpreted to represent Bouma-type turbidites that could account for the anomalously thick sediment.

2.8.3 Back-Arc Sediments Become Finer as the Basin Evolves

At the beginning of sub-basin opening, there was abundant volcaniclastic material as the crust rifted and seafloor spreading initiated. During the initial opening of the Lau Basin, sediment deposition was even closer to the remnant arc and the active arc, both of which provided a source for sediment (Hawkins, 1995). As the basin opened through seafloor spreading, individual sub-basins were progressively distanced from the active rifting zones, and there was a significant decrease in the volcaniclastic input for those sub-basins with increasing hemipelagic sedimentation. A thick succession of hemipelagic material indicates volcanic quiescence to allow

for the fine sediment to accumulate and/or greater distance from a source of coarse material. Echo facies 1 is the most recently deposited unit in 39 of the sub-basins in the study area (62%), and ranges from 2.3 m to 40.3 m in thickness, with an average thickness of 10.6 m. Using a sedimentation rate of 32 mm/ka for hemipelagic and hemipelagite units calculated in the western Lau Basin ODP drilling (Rothwell et al., 1994b), this would correspond to an average age of 331 ka. From this we would conclude that the most recent period of basin-wide quiescence began around 331 k.y. ago with a fining upward sequence mainly preserved in areas where the back-arc basin is not undergoing rifting. However, since 1774, 77 eruptions have been recorded along the in the Tongan section of the Tonga-Kermadec arc (Global Volcanism Program, 2013) and these eruptions also contribute to the sedimentation. Furthermore, in the 24 cases where the top unit is not echo facies 1, it is either an MTD (echo facies 5), a volcaniclastic dominated unit (echo facies 2, 3A, 3B, 4) or is obscured by a hyperbolic echo. We interpret from this that although basin-wide quiescence began in the N.E. Lau Basin around 331 k.y. ago, active volcanism and micro-seismicity has persisted at a local scale in sub-basins that are closely juxtaposed to other sub-basins with no volcanism or seismic activity.

2.8.4 Sub-Basin Sediment Volume

We calculated a total volume of 11.8 km^3 for the sediment in a single large nodal basin P05-D. This volume of sediment is similar to the amount of ash that was displaced during the catastrophic Hunga Tonga-Hunga Ha'apai submarine eruption at the arc front in January 2022. The single Hunga Tonga-Hunga Ha'apai eruption produced a plume that rose over 50 km in altitude (Venzke, 2022) and displaced at least 9.5 km^3 of material (Venzke, 2022). For comparison, the Mount St. Helens eruption in 1980 produced 4.2 km^3 of sediment and debris (Wickham, 2009) and the Mount Pinatubo eruption in 1991 produced between 7 km^3 and 11 km^3 of material (Global Volcanism Program, 1991). However, sub-basin P05-D is clearly not a catchment for a single volcanic eruption. More likely it has received sediment many times from much smaller eruptions at the arc front, such as the 2019, Volcano F eruption just south of the FRSC which erupted only ~0.01– 0.04 km^3 (Brandl et al., 2019). Although much smaller, such eruptions are much more common and could contribute significant volumes of volcaniclastic material to the adjacent sub-basins over time. For example, 5 sedimentary units are visible in the Parasound section along the P05 seismic transect, and a sixth in the reflection data. Each

sedimentary unit represents a different depositional event, and includes massive, structureless units and thin, strong, bedded units. Thus, a number of smaller-scale depositional events are responsible for the sedimentary infill of this sub-basin.

We can calculate the volume of each sedimentary unit in this sub-basin to estimate the volume of the individual depositional events. Table 2.5 lists the volumes of each echo facies in P05-D. 1.6% of the sediment infill by volume is interpreted to be hemipelagic material, 66.5% is a mix of hemipelagic and volcaniclastic material, and 31.9% is not visible in Parasound, only in the seismic reflection. Sedimentary unit P05-D-iv is acoustically transparent with no visible internal structure, so it is interpreted to be coarse-grained volcaniclastic sediment. This unit has a volume of 0.708 km^3, similar in size to the amount of material in a single volcanic eruption at the arc front. Sedimentary unit P05-D-ii has at least six sub-units, deposited as turbidites, which have a cumulative volume of approximately 3.269 km^3. The amount of material erupted from the arc that ends up in each sub-basin cannot be known (P05-D is only one of at least 19 sub-basins at this distance from the arc). However, the calculated volumes of the acoustically transparent echo facies in P05-D suggest that it is likely significant (i.e., 30% of the total sediment in the sub-basin).

The sediment-basement contact is only visible in Parasound in 43% of the sedimented basins in this study area. However, comparisons of estimated basin volumes with measured results from P05-D show that order-of-magnitude estimates of the most recent sedimentation are possible for most of the basins with the available data. The entire N.E. Lau Basin is a catchment for a globally significant volume of sediment, partitioned into the many sub-basins described here. An enormous volume of sediment was deposited over the last 6 Ma. The Lau Basin is still opening, but we estimate the total volume of sediment in our study area (the sum of all sub-basins) to be 5,699 km^3. An estimate of sediment volumes is useful for comparison with ancient arc-backarc systems such as in the Abitibi Greenstone Belt. For example, the major metasedimentary assemblage deposited unconformably on the volcanic rocks of the Abitibi Greenstone Belt, the Porcupine Assemblage, has a preserved area of ~10,000 km^2 and its volume is likely the same order of magnitude as the 6 m.y. of sediment deposited in the N.E. Lau Basin.

2.8.5 Implications for Hydrothermal Activity

The geological record shows that large-scale hydrothermal systems associated with arc rifting and back-arc spreading are commonly expressed by subseafloor hydrothermal alteration and mineralization (Hannington et al., 2005). However, few modern examples of this type of hydrothermal activity have been identified because of the obscuring effects of burial by sediment. One of the goals of this study was to explore the possibility of subseafloor mineralization in the sediment-filled sub-basins of the active Lau back-arc. Several of the basins include active normal faulting near magmatic centers that may be sources of heat for subseafloor hydrothermal convection. An anomalous acoustic signature, referred to as echo facies 8, is present in at least two sub-basins (P03-S, P03-N; Figures 2.26 and 2.27). This echo facies is a highly reflective 'cloud' which fully reflects the acoustic signal and blocks the acoustic signal from penetrating deeper. Normal faults are the dominant fault type in these basins and can act as pathways to the seafloor for hydrothermal fluids. In the FRSC (P03-S) there are numerous normal faults, and the spreading center is known to be hydrothermally active. Three hydrothermal plumes along the FRSC (FRSC01, FRSC02 and FRSC03) were located during expeditions by German et al. (2006) and Kim et al. (2009). These vent sites occur immediately to the north and south of the P03 transect. Although the known vent sites are located on volcanic cones in the rift, flanking sediments and sediment in the deeper part of the adjacent basins are mainly volcaniclastic and therefore permeable. Geophysical surveys during SO267 showed increased microseismicity in the basin and a corresponding low resistivity zone at a depth of several kilometers (Schmid et al., 2020; Franz et al., 2021). A dark anomaly is visible at this location in the Parasound of P03-S at a depth of approximately 18 mbsf and measuring approximately 9 m thick and 425 m wide (Figure 2.26). It appears to be contained in several strata and has diffuse boundaries that may represent subseafloor fluid flow or hydrothermal alteration related to the increased faulting. From the Parasound data, assuming the anomaly is 425 m long (perpendicular to Parasound section) the volume of altered/mineralized sediment is estimated to be $1.63 \cdot 10^6$ m^3.

Another promising area is P03-N (Figure 2.27). The older sediment has been deformed and faulted and is separated by an unconformity from the less deformed, younger sediment. The angular discontinuity in the sediments is indicative of block rotation during faulting. Such large,

long-lived structures are a primary control on hydrothermal fluid flow. In the Parasound of sub-basin N, there are two anomalies similar to the one found in P03-S. The high reflectivity clouds are bound on both sides by normal faults that could be the pathways for hydrothermal upflow forming subseafloor "chimneys". The western anomaly is approximately 68 mbsf and is 4.6 m thick and 330 m wide. The eastern anomaly is 52 mbsf and is 6.1 m thick and 310 m wide. Assuming their north-south extent is the same as their east-west extent viewed in Parasound, the volume of altered or mineralized sediment in the western and eastern anomalies is approximately $5.01 \cdot 10^5$ m^3 and $5.86 \cdot 10^5 m^3$, respectively.

Sub-basins P03-S and P03-N are potential targets for further investigation of the nature of these anomalies to determine if they could be sites of actively forming sediment-hosted mineral deposits.

2.8 Conclusions

After over half a century of research in the Lau Basin, the overall patterns of sedimentation and back-arc basin opening are relatively well understood. However, with new Parasound data from the SO267 expedition, we have developed a more detailed history of sedimentation than previously assembled for a similar-sized area in any back-arc basin. We identified 63 sub-basins and slope deposits and their associated echo facies, sediment thickness and proportions of coarse- and fine-grained material. From stratigraphic logs, isopach maps and sediment coarseness maps, we conclude that sedimentation in the N.E. Lau Basin is dominated regionally by arc volcanism and hemipelagic sedimentation, and locally by intrabasinal volcanism and sediment gravity flows triggered by seismicity and steep slopes.

An important objective of the study was to create a detailed echo facies legend to be used to extract sedimentary information from each unit viewed in Parasound. The legend we created is more detailed than legends developed previously by Damuth (1975), Damuth and Olson (2015) and Fierens et al. (2019). From this we characterised each sedimentary unit in each sub-basin and slope deposit, including the composition of the sub-basin fill. By plotting the echo facies distribution in stratigraphic columns, we concluded that there is an overall fining upward in all sub-basins, as hemipelagic sediment is the uppermost unit in 62% of the cases. The widespread

occurrence of hemipelagic sediment as the uppermost sedimentary unit suggests recent volcanic quiescence from the Tofua Arc beginning 331 k.y. ago, or a higher rate of sedimentation of fine-grained material (e.g., as fine ash deposited during short volcanic episodes at the arc front). Coarse-grained units in the other 38% of sub-basins suggest the occurrence of localized volcanic activity from intrabasinal seamounts and MTDs triggered by seismicity at rift zones. The most abundant echo facies are 3A and 3B, which are units composed of both hemipelagic and volcaniclastic sediment. These units are interpreted to represent sediment gravity flows transporting eruptive material, or repeated transitions between volcaniclastic sedimentation and hemipelagic sedimentation. The former is a more likely interpretation. Initial back-arc sedimentation is interpreted to be dominated by MTDs as the steep rift flanks and seismicity trigger mass flows. We observed MTDs in the FRSC and suggest that this is similar to sedimentation during the initial rifting stages of the Lau Basin. This is analogous to the ancient rock record, in which MTDs are often indicative of proximity to a rift zone.

An overall decrease in grain size and sediment thickness with increased distance from the arc highlights the importance of proximity to the arc in controlling the nature of sedimentation in the sub-basins. However, there is significant volcaniclastic input from intrabasinal seamounts, although Bednarz and Schminke (1994) previously emphasized input from the Lau Ridge and Tonga Ridge.

We did not correlate MTDs with rift propagation at the CLSC and ELSC as Rothwell et al. (1994) did, but we identified a unit interpreted to be turbidites (echo facies 4) in P05-D that is interpreted to have opened in response to the overlap of the ELSC and the CLSC.

The detailed sedimentary analysis of the N.E. Lau Basin using Parasound is the first large-scale study of its kind in a young arc- backarc system and the results show the abundance of information that can be extracted remotely from ship-based data, proving the accuracy and resolution of the method. Future work in the area could focus on areas of potential mineralization found within the sediment-filled sub-basins of the FRSC. Sub-basins P03-N and P03-S have three acoustic anomalies interpreted to be possible zones of hydrothermally altered or mineralized sediment. With estimated volumes of $1.63 \cdot 10^6$ m^3, $5.01 \cdot 10^5$ m^3 and $5.86 \cdot 10^5 m^3$,

these are regions that could be explored further for SMS deposits. Another avenue for future research is the calculation of sediment volumes on a larger scale using sub-surface data from Parasound and seismic reflection data. Here we calculated a volume of 11.8 km^3 in one sub-basin (P05-D). The method presented in this study could be used to calculate sediment volumes in the entire back-arc system that could then be linked to better geochronological information.

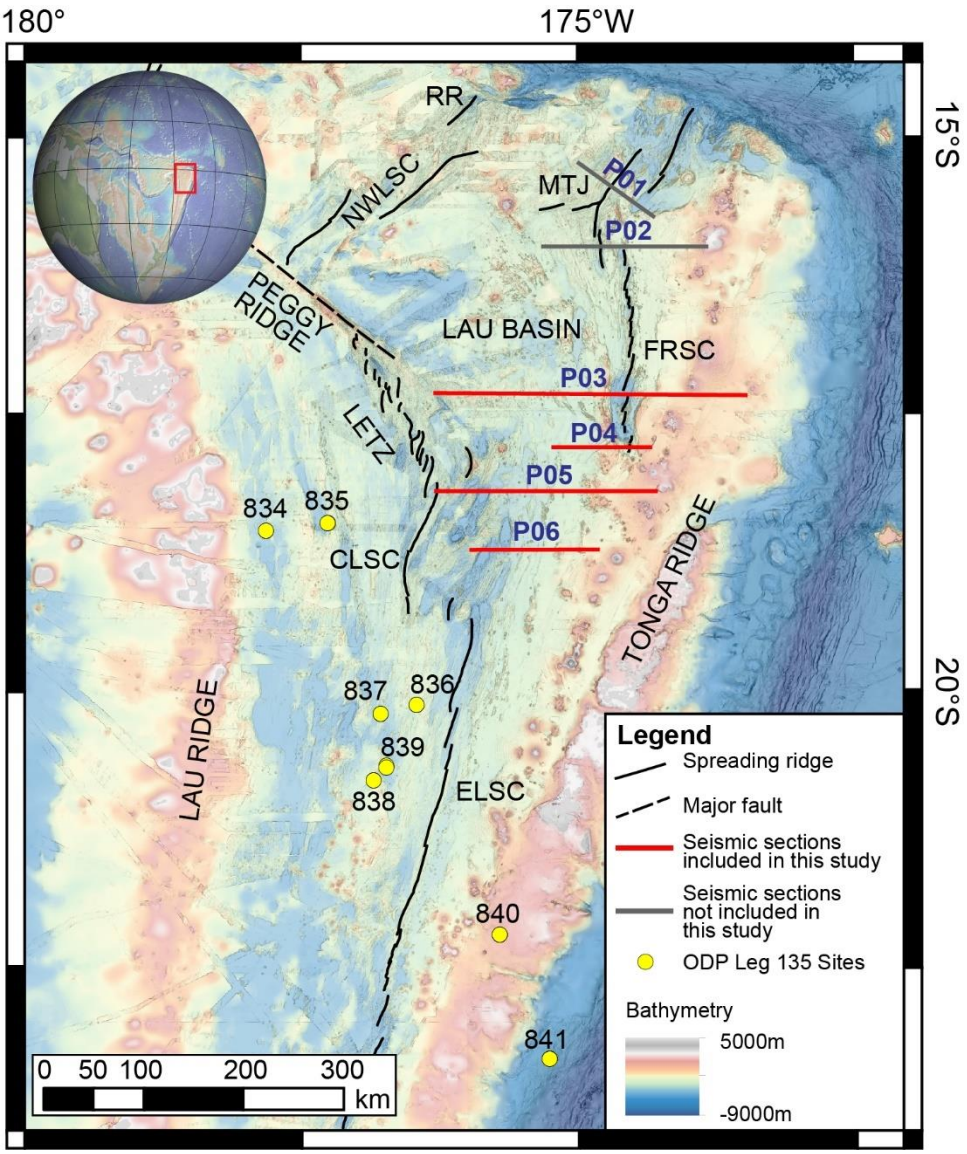

Figure 2.1 Locations of ODP Leg 135 drill sites 834 to 841, spanning the back-arc to the forearc (Hawkins, Parson, Allan et al., 1994). The back-arc sites, 834-839, comprise a complete sedimentary sequence from the underlying basement to the seafloor. Seismic reflection transects were collected onboard the RV Sonne SO267 expedition (Hannington et al., 2019).

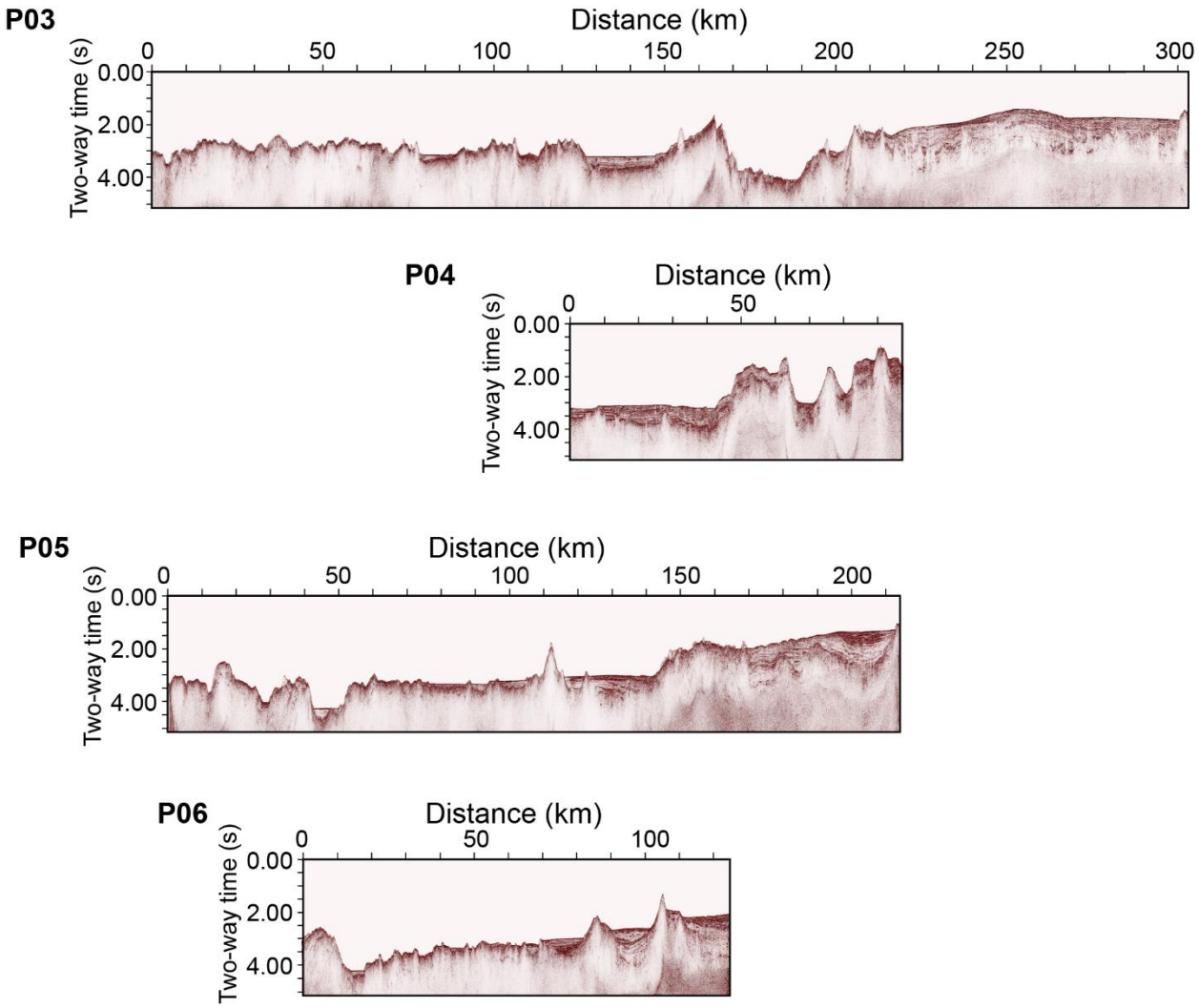

Figure 2.2 Seismic reflection profiles P03 to P06 collected during RV Sonne SO267 expedition (Hannington et al., 2019). The locations of the sections are shown in Figure 2.1. Details of line P03 are presented in Schmid et al. (2020).

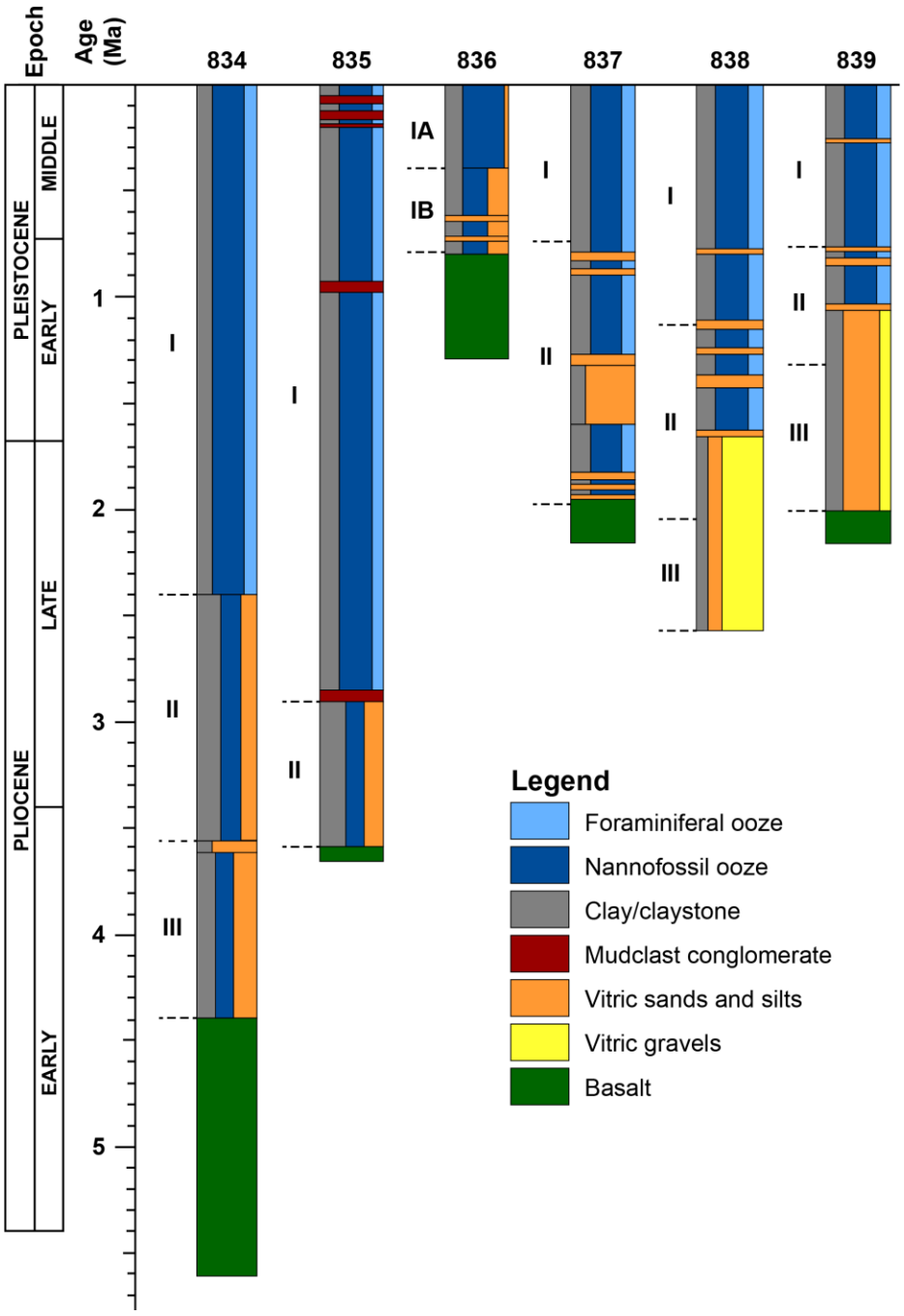

Figure 2.3 Stratigraphic sections of ODP Leg 135 drill sites 834-839 modified from Rothwell et al. (1994a). Vertical scale is in Ma, and stratigraphic ages were constrained by biostratigraphic and paleomagnetic data. A sedimentation rate of 1.5 cm/ka was calculated for the hemipelagic sediment. The cores contain a lower sedimentary sequence of volcaniclastic sediment (Lithologic Units II and III) and an upper sedimentary sequence of hemipelagic clayey nannofossil ooze (Lithologic Unit I).

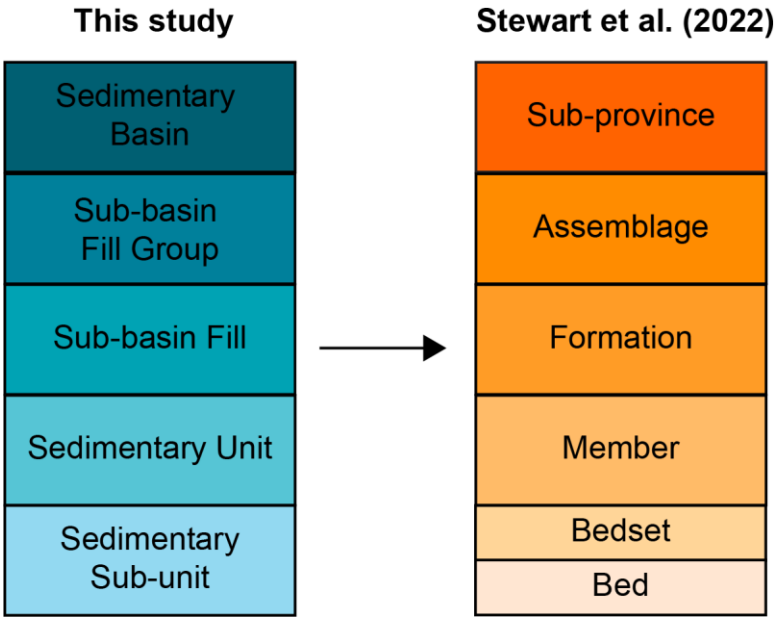

Figure 2.4 Hierarchical rank of stratigraphic units in this study and their lithostratigraphic equivalent from Stewart et al. (2022). Bed and bedset were defined by Boggs (2013) and are equivalent to sedimentary sub-units in this study.

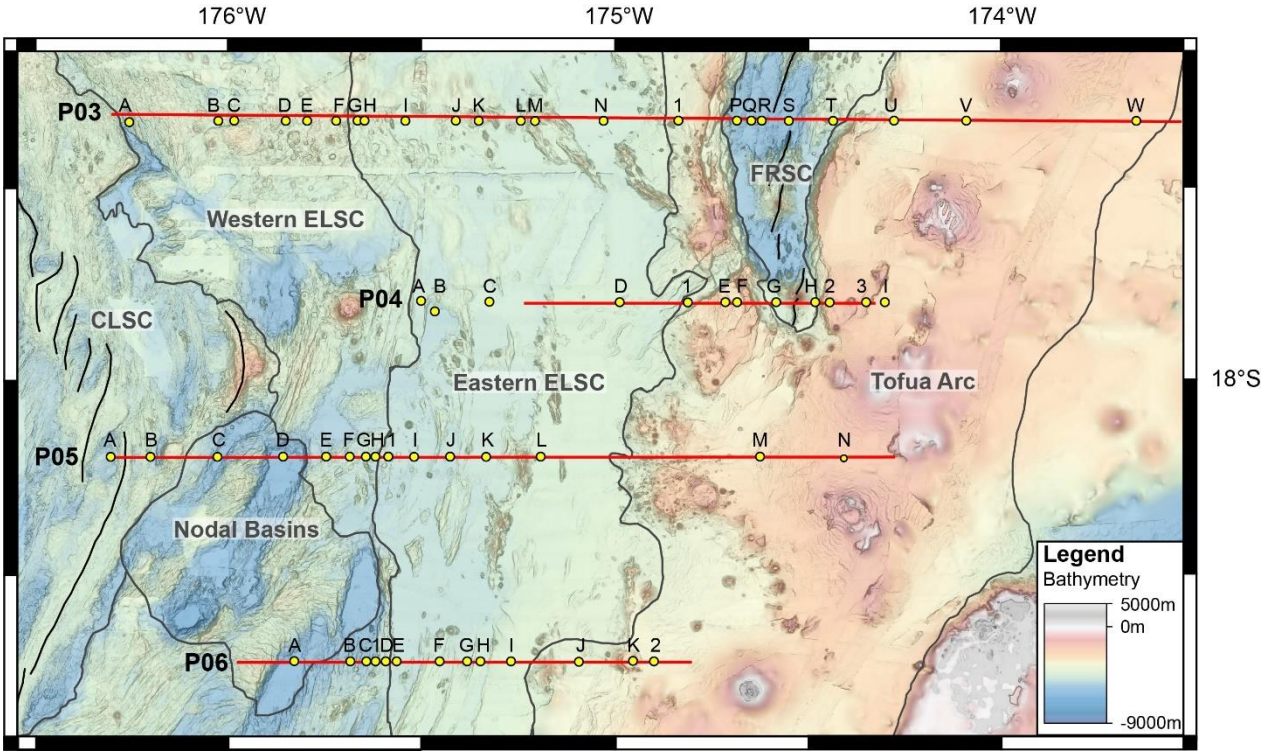

Figure 2.5 Bathymetric map of the study area showing the distribution of the sub-basins (yellow circles) and sub-basin groups (areas outlined in grey).

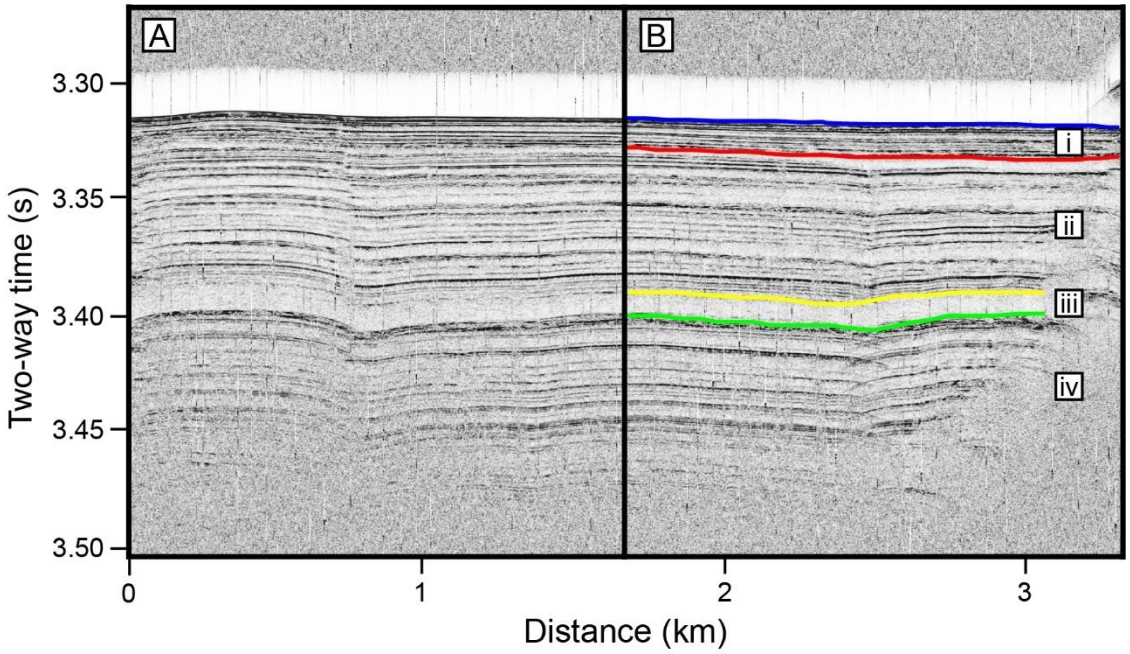

Figure 2.6 A) Example echogram classification used by Damuth (1975, 1978, 1980), Damuth and Hayes (1977) and Damuth and Olson (2015), where the entire echogram is assigned a single echo facies. B) The same echogram showing the classification of echo facies used in this study, divided into sedimentary units (i, ii, iii, iv). In this echogram (i) corresponds to hemipelagic material (echo facies 1), (ii) and (iv) correspond to mixed volcaniclastic and hemipelagic material (echo facies 3B), and (iii) corresponds to coarse-grained volcaniclastic material (echo facies 2). Proportions of coarse and fine sediment are assigned to each echo facies based on sediment compositions of cores published in Damuth (1980), Fierens et al. (2019) and Damuth and Olson (2015). With this method we can observe temporal changes in sub-basins and evaluate the evolution of sedimentary sources and depositional processes.

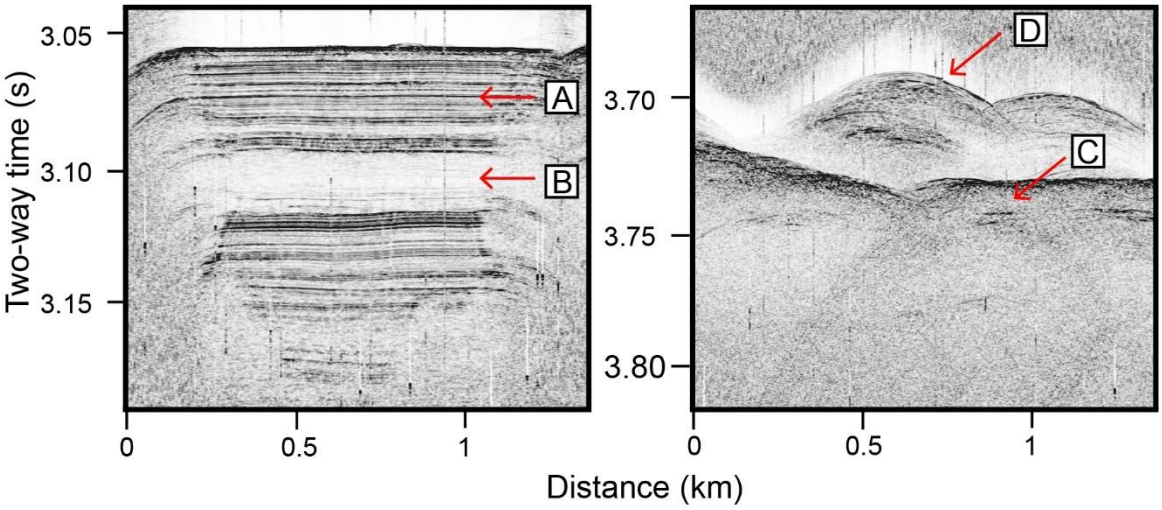

Figure 2.7 Examples of echograms illustrating descriptors used in the text: A) strong reflections, B) acoustically transparent, C) prolonged echo, and D) hyperbolic echo.

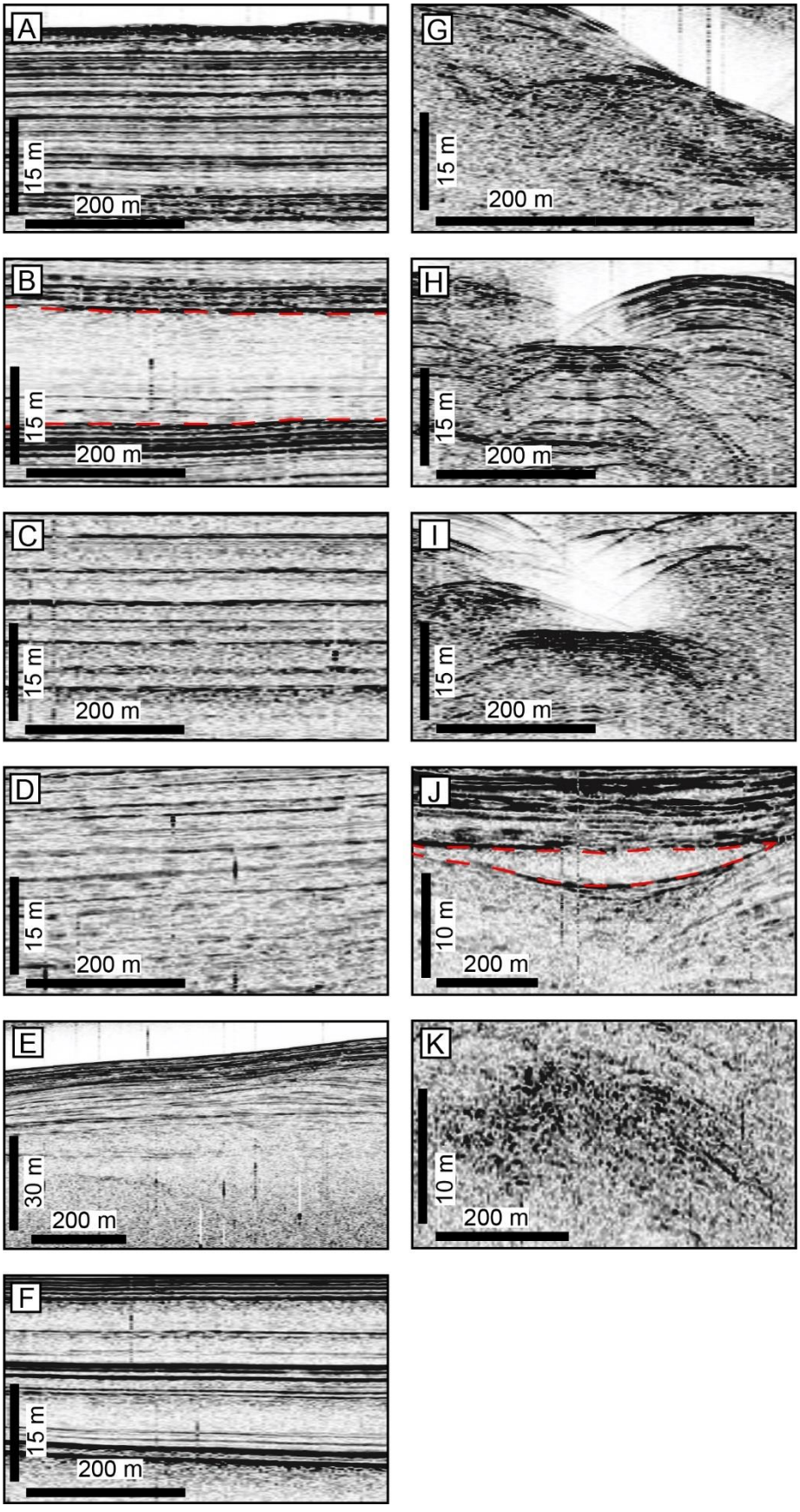
A
15 m
200 m
G
15 m
200 m
B
15 m
200 m
H
15 m
200 m
C
15 m
200 m
I
15 m
200 m
D
15 m
200 m
J
10 m
200 m
E
30 m
200 m
K
10 m
200 m
F
15 m
200 m

Figure 2.8 Echograms of each echo facies (full descriptions in section 2.4 and summarized in Table 2.1): A) Echo facies 1, interpreted as hemipelagic material; B) Echo facies 2, interpreted as coarse-grained volcaniclastic mass flows (outlined in red dashed line); C) Echo facies 3A, interpreted as coarse-grained sediment with few interbeds of fine-grained material; D) Echo facies 3B, interpreted as coarse-grained sediment with many interbeds of fine-grained material; E) Echo facies 3C, interpreted as undulatory units of coarse-grained sediment with interbeds of fine-grained material; F) Echo facies 4, interpreted as full turbidite sequences with interbeds of large volcaniclastic events; G) Echo facies 5, interpreted as MTDs; H) Echo facies 6A, indicating sedimentary cover above rugged seafloor or steep slopes; I) Echo facies 6B, indicating rugged or steep seafloor; J) Echo facies 7, interpreted as coarse-grained channel fill (outlined in red dashed line); K) Echo facies 8, interpreted as possible hydrothermally altered sediments.

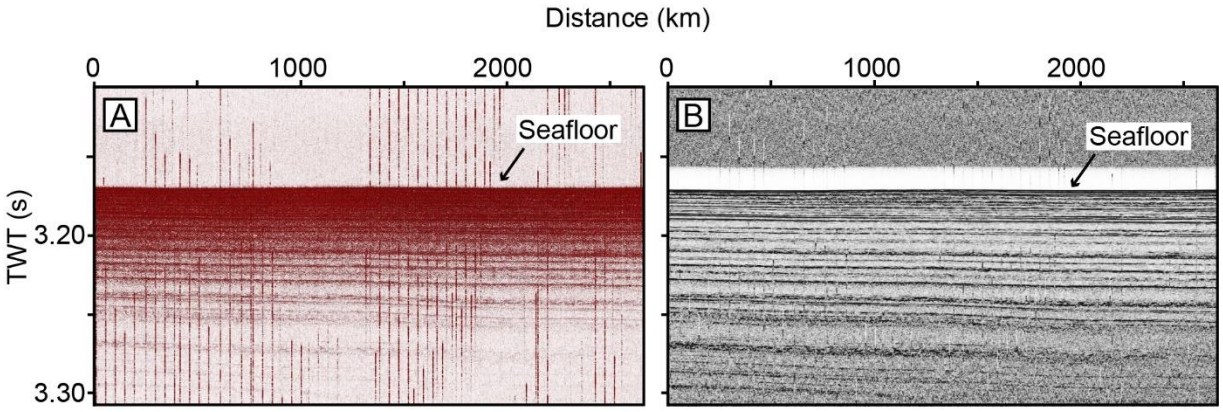

Figure 2.9 A) Example echogram displayed in amplitude mode. Sub-seafloor reflections are difficult to see. B) The same echogram processed using the AGC function in the Kingdom Suite software and displayed using the seismic envelope attribute. Using these display settings, we are able to observe deeper reflections.

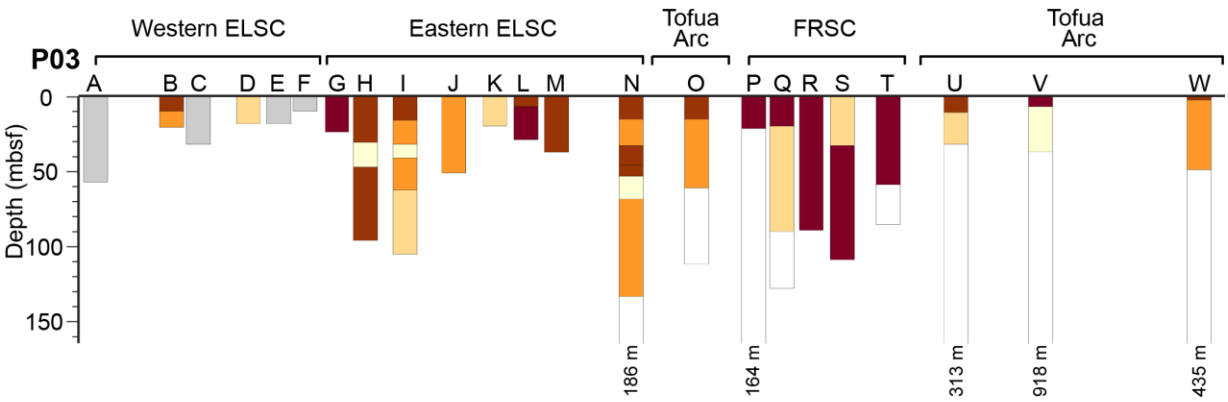
P03
Western ELSC
Eastern ELSC
Tofua Arc
FRSC
Tofua Arc
A B C D E F G H I J K L M N O P Q R S T U V W
Depth (mbsf)
0
50
100
150
186 m
164 m
313 m
918 m
435 m


Legend
Echo facies
1
2
3A
3B
3C
4
5
6A
X

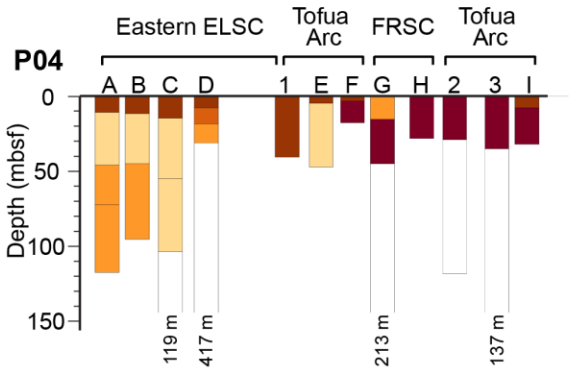
P04
Eastern ELSC
Tofua Arc
FRSC
Tofua Arc
A B C D 1 E F G H 2 3 I
Depth (mbsf)
0
50
100
150
119 m
417 m
213 m
137 m

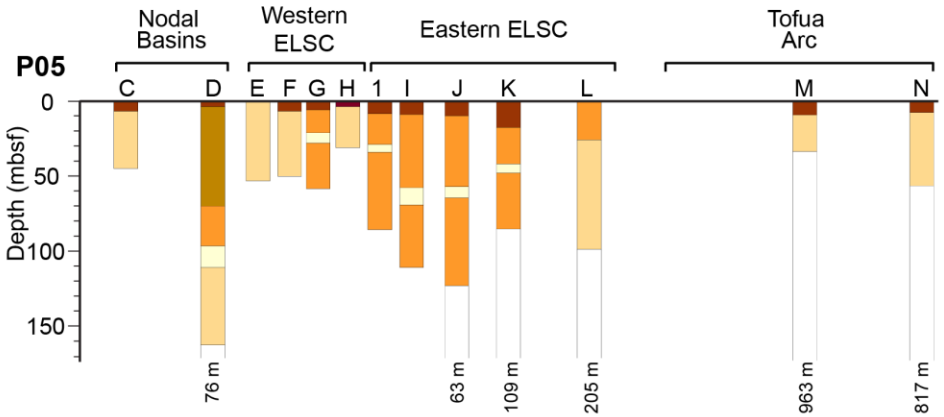
P05
Nodal Basins
Western ELSC
Eastern ELSC
Tofua Arc
C D E F G H 1 I J K L M N
Depth (mbsf)
0
50
100
150
76 m
63 m
109 m
205 m
963 m
817 m

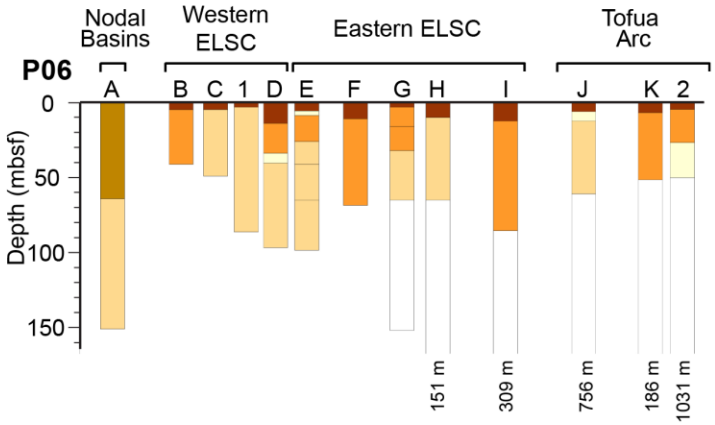
P06
Nodal Basins
Western ELSC
Eastern ELSC
Tofua Arc
A B C 1 D E F G H I J K 2
Depth (mbsf)
0
50
100
150
151 m
309 m
756 m
186 m
1031 m

Figure 2.10 Stratigraphic columns of the sub-basins and the slope deposits of the study area. The sub-basin groups are marked above each transect. In cases where sub-basins contain sedimentary successions thicker than 160 m, the bottom of the column is open, and the total thickness of the lowest unit is indicated, based on the corresponding seismic reflection data in Figure 2.2. The columns are arranged according to their position along each transect, but distances between columns are not to scale. Sub-basins P05-A and P05-B (not shown) are clear depressions that are beginning to fill with sediment but have not measurable accumulation.

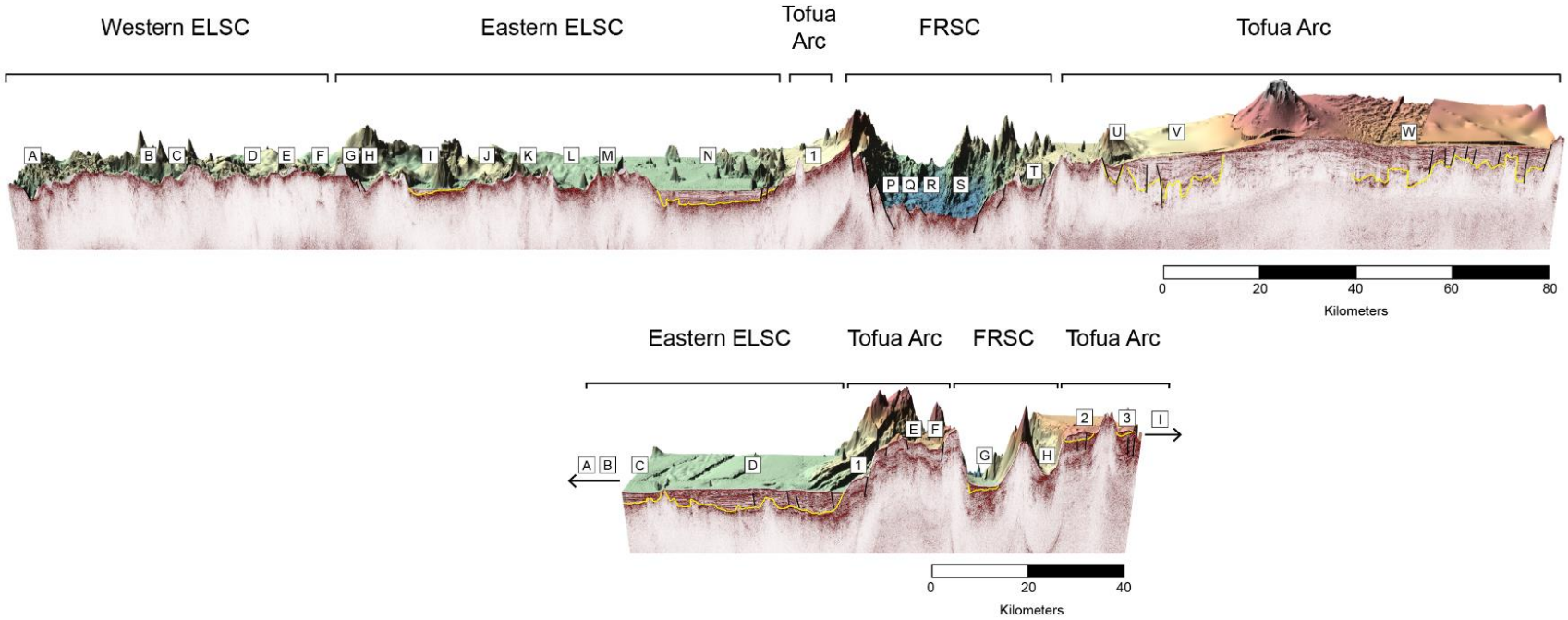

Figure 2.11 3D bathymetric data draped on seismic reflection data along transects P03 and P04. Sub-basins P04-A, P04-B and P04-I are observed only in Parasound and therefore do not show any significant sediment accumulation at the resolution of the seismic reflection data. 3D models were constructed using the Surfer software from bathymetric data.

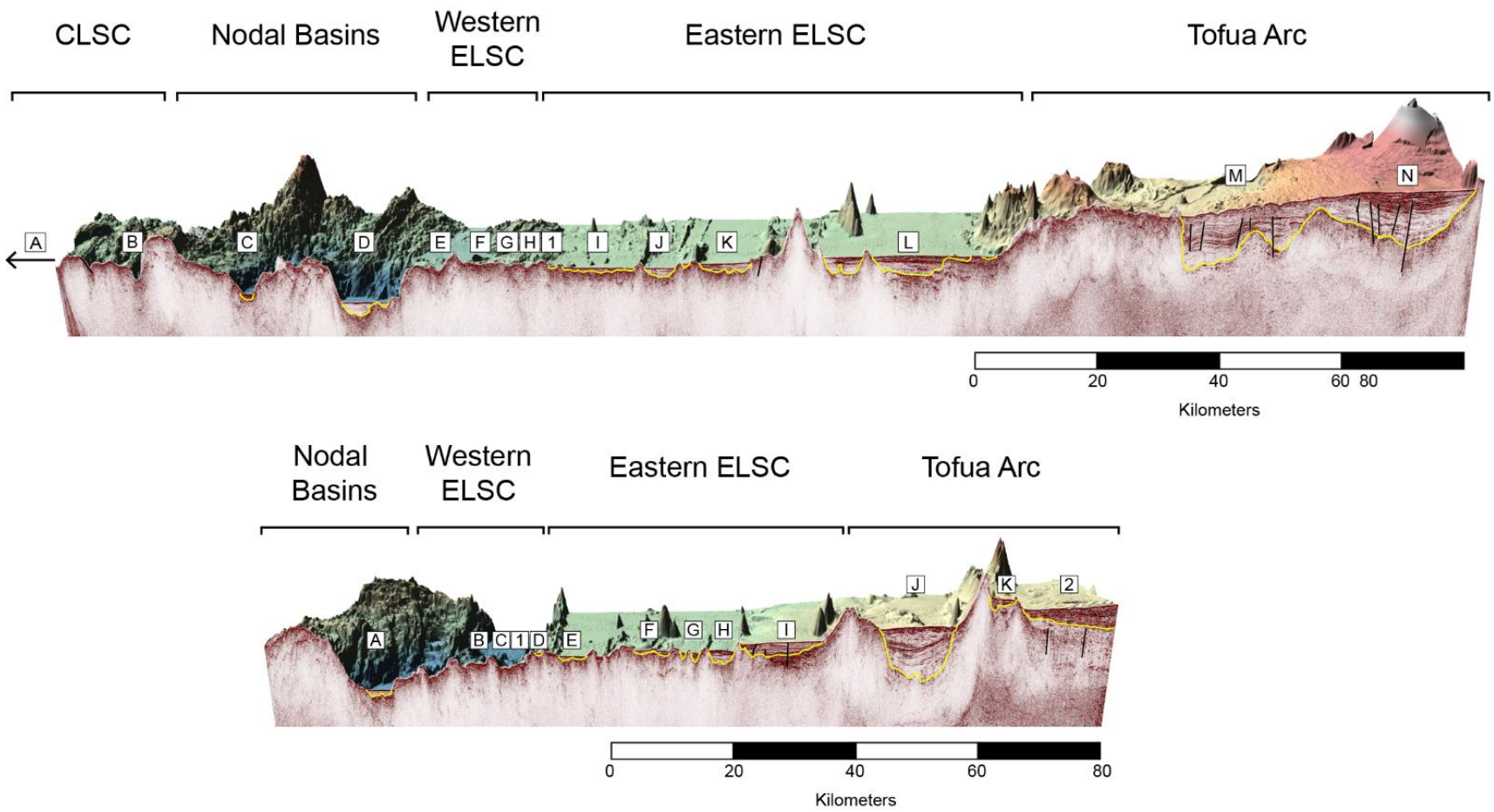

Figure 2.12 3D bathymetric data draped on seismic reflection data along transects P05 and P06.

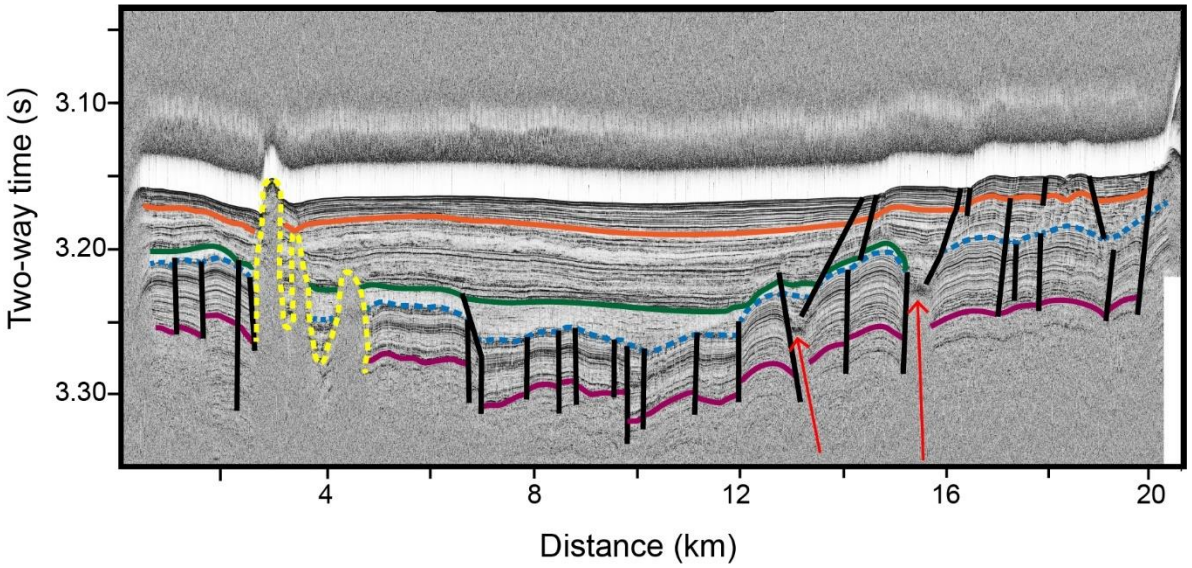

Figure 2.13 Annotated echogram of sub-basin P03-N. Coloured lines separate sedimentary units. An angular unconformity between the older and younger sediment packages is marked by the dashed blue line, where the older sediments are deformed and faulted, and the younger sediments are continuous with few faults. Yellow dotted lines are volcanic ridges. Red arrows point to the two anomalies that are interpreted to be associated with hydrothermal fluid flow. The emplacement of the anomalies is the same in both cases: between two intersecting faults. The sediment depth is deeper than the Parasound penetration depth, so the sediment-basement contact is not visible.

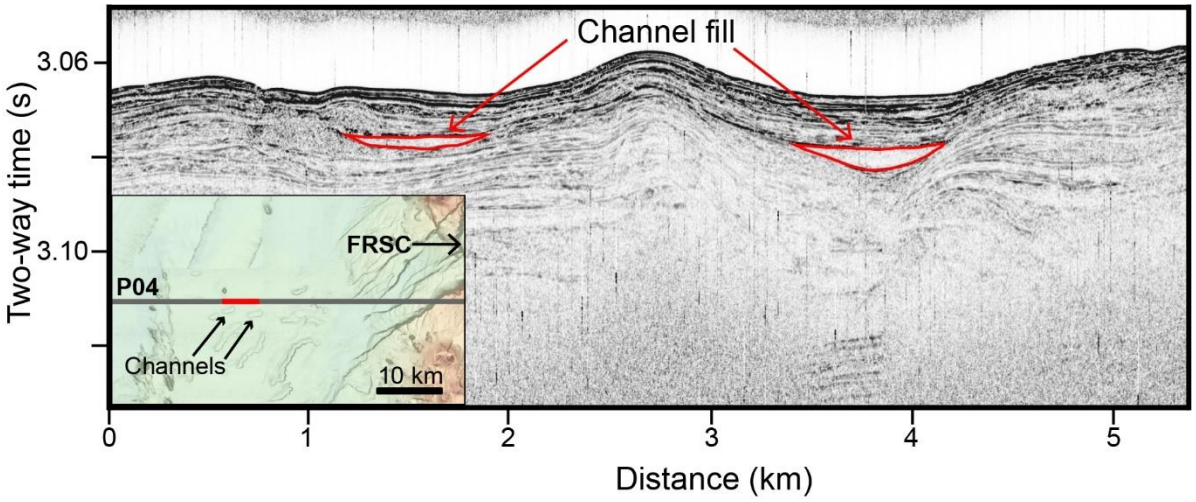

Figure 2.14 Lens-shaped, acoustically transparent units in sub-basin P04-D, interpreted to be buried channel deposits. Bathymetric map inset (from Figure 2.5) shows the location of the echogram and arrows point to the bathymetric depressions interpreted to be the seafloor expression of the channels observed in cross-section in the echogram. Bedded sediment on the flanks of of channel deposits is interpreted to be fine-grained levee deposits. These channels likely formed from an increased input of sediment and the slope of the graben on the western flank of the FRSC.

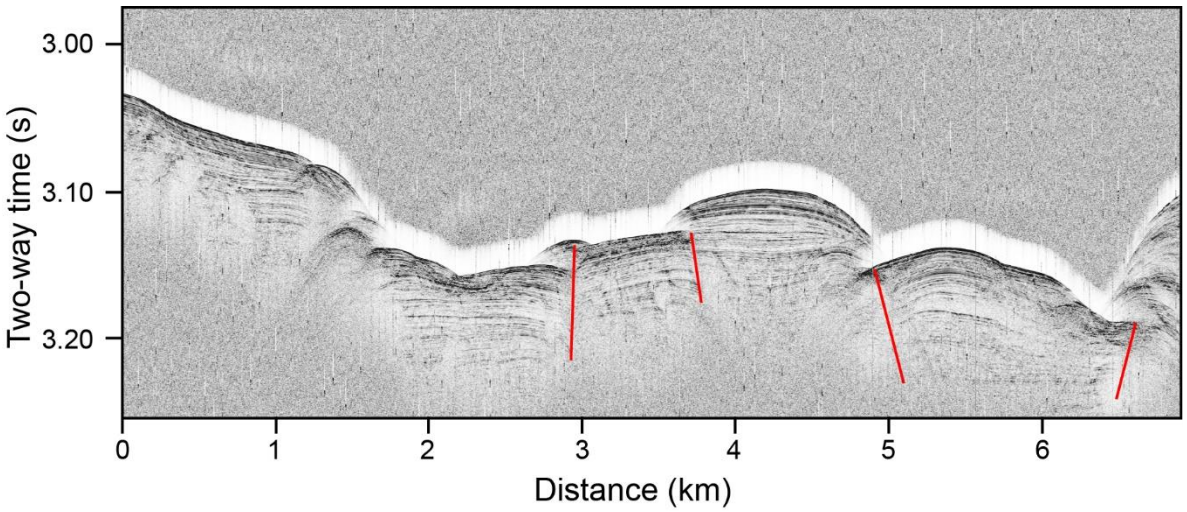

Figure 2.15 Echogram of sub-basin P06-F. Post-depositional normal and thrust faults (outlined in red), possibly as part of a horst-graben system, produce an undulatory seafloor.

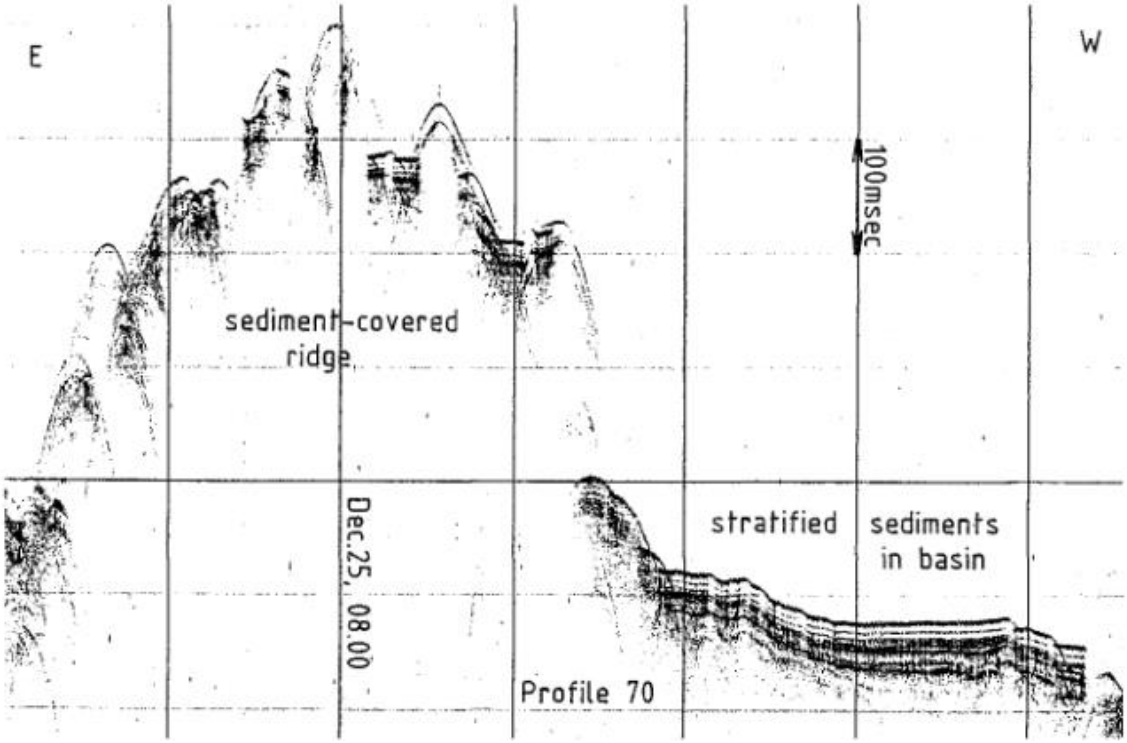

Figure 2.16 Echogram from 3.5 kHz echosounder in Southern Lau Basin, collected during the RV Sonne SO35 expedition (von Stackelberg et al., 1985). Profile is approximately 5.5 km wide. Resolution of echograms from 3.5 kHz sub-bottom profilers is much lower than those from Parasound (e.g., Figures 2.14 and 2.15).

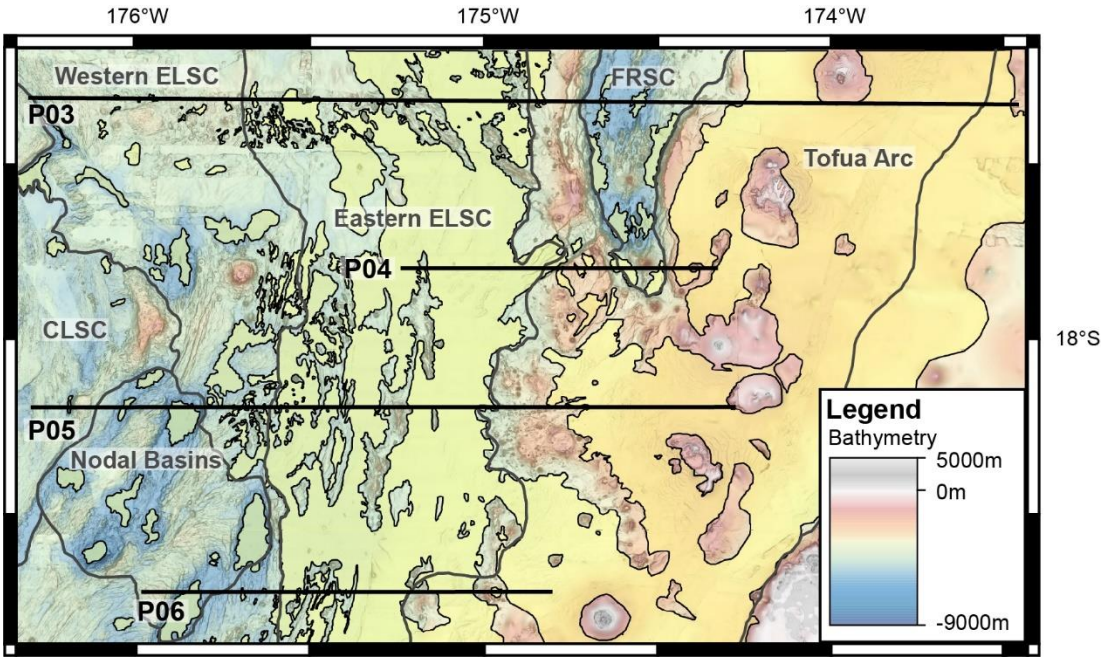

Figure 2.17 Map showing the sedimented regions in the study area (yellow polygons). 47 % of the map area is covered by sediment. Sedimented areas were identified using Parasound and slope maps created in ArcMap, where areas with a slope of less than 3% were assumed to be sedimented. The Tofua Arc and Eastern ELSC sub-basin groups are the most sedimented regions, and the sedimented areas become more sparse towards the west.

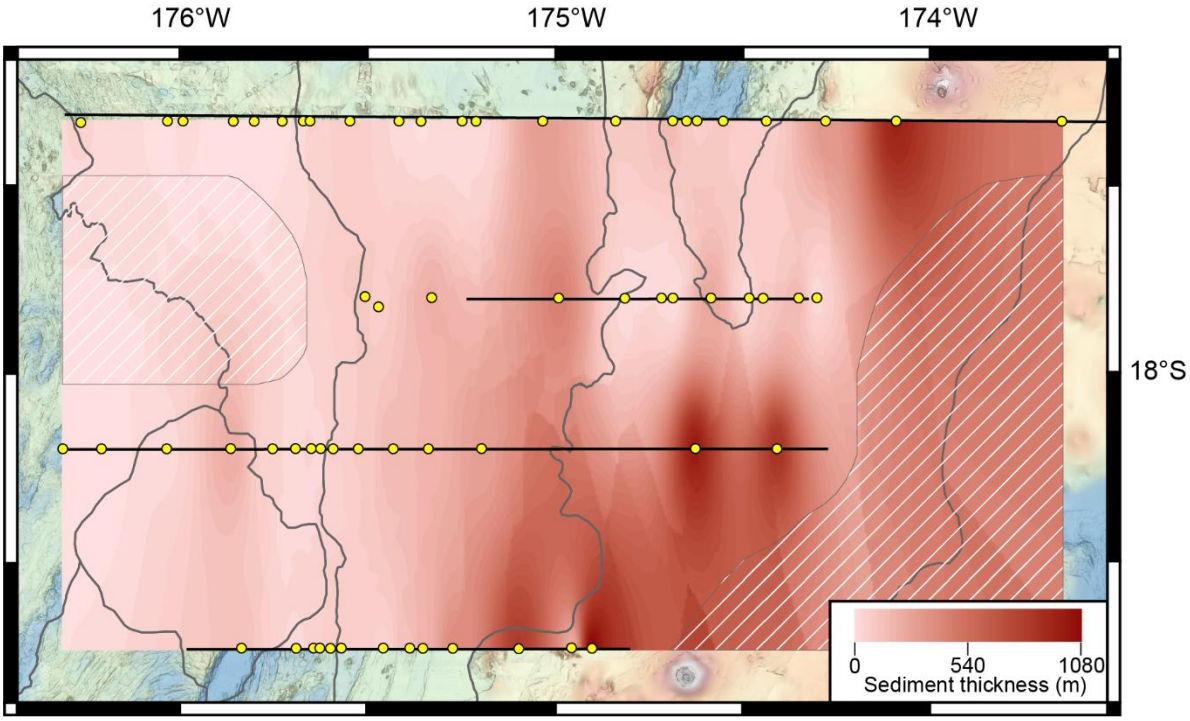

Figure 2.18 Sediment isopach map created using IDW interpolation in ArcMap (see section 2.7.2). Sediment thicknesses from seismic reflection and Parasound data were interpolated between the seismic lines (data points in yellow). Cross-hatched areas indicate regions where insufficient data were available to accurately interpolate data and should be ignored. The thickest sediments are located within the Tofua Arc sub-basin group and in the arc-to-backarc transition adjacent to the Tofua Arc, and generally thin toward the west and within the FRSC.

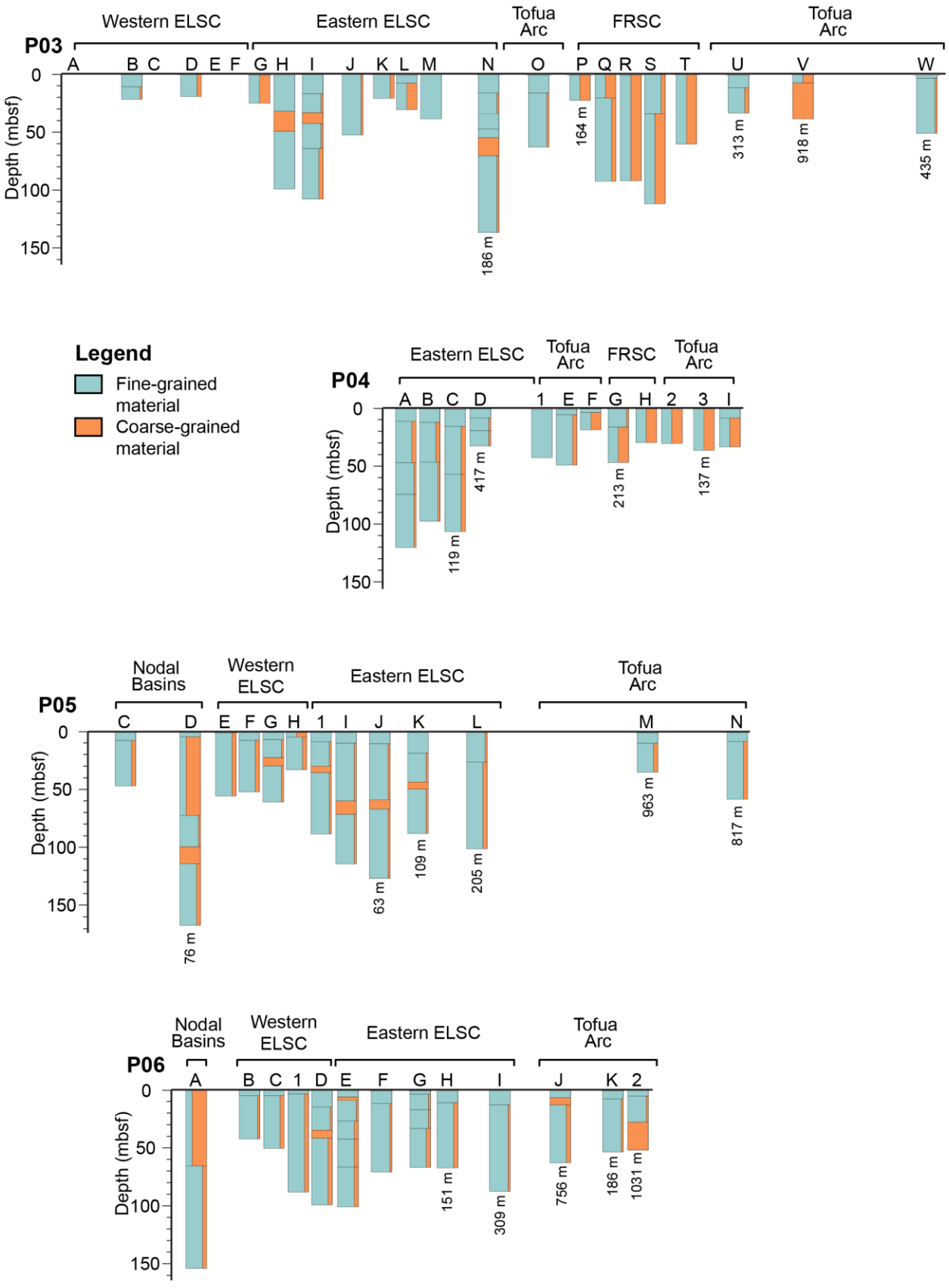
P03
Western ELSC
Eastern ELSC
Tofua Arc
FRSC
Tofua Arc
A B C D E F G H I J K L M N O P Q R S T U V W
Depth (mbsf)
0
50
100
150
186 m
164 m
313 m
918 m
435 m
Legend
Fine-grained material
Coarse-grained material
P04
Eastern ELSC
Tofua Arc
FRSC
Tofua Arc
A B C D 1 E F G H 2 3 I
417 m
119 m
213 m
137 m
P05
Nodal Basins
Western ELSC
Eastern ELSC
Tofua Arc
C D E F G H 1 I J K L M N
76 m
63 m
109 m
205 m
963 m
817 m
P06
Nodal Basins
Western ELSC
Eastern ELSC
Tofua Arc
A B C 1 D E F G H I J K 2
151 m
309 m
756 m
186 m
1031 m

Figure 2.19 Stratigraphic columns of the sub-basins and the slope deposits of the study area showing the proportions of coarse-grained (orange) and fine-grained (blue) material in each sub-basin. In general, the sub-basins contain a lower succession with a high proportion of coarse-grained material which is overlain by a succession of fine-grained material, similar to the ODP Leg 135 Sites described by Rothwell et al. (1994a). Sub-basins that contain hyperbolic echoes (P03-A, C, E, F) or no sediment (P05-A and P05-B) are not shown.

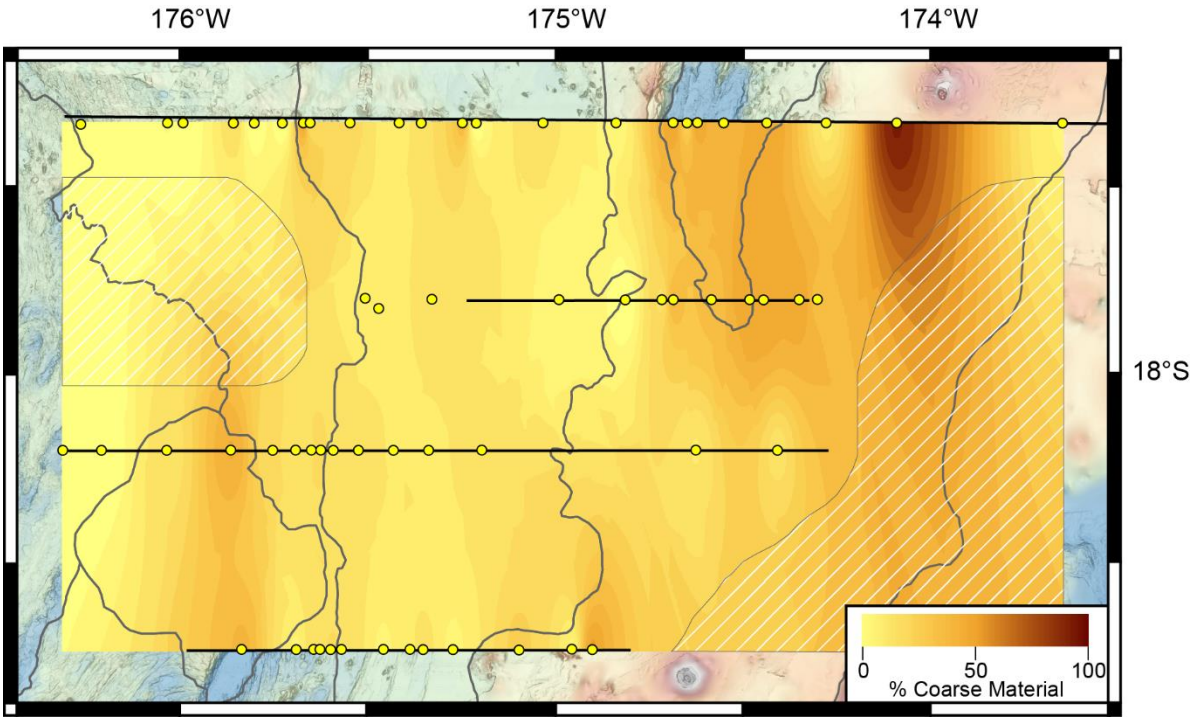

Figure 2.20 Sediment grain size map displaying the proportion of coarse sediment (silt to gravel) across the basin. The map was created by interpolating the average proportion of coarse sediment in each sub-basin (recorded from Parasound echograms) using an IDW technique (data points in yellow). Cross-hatched areas indicate regions where insufficient data were available to accurately interpolate data, and therefore should be ignored. There is an overall coarsening toward the Tofua Arc, within the FRSC, and in the nodal basins near the CLSC, with local variations.

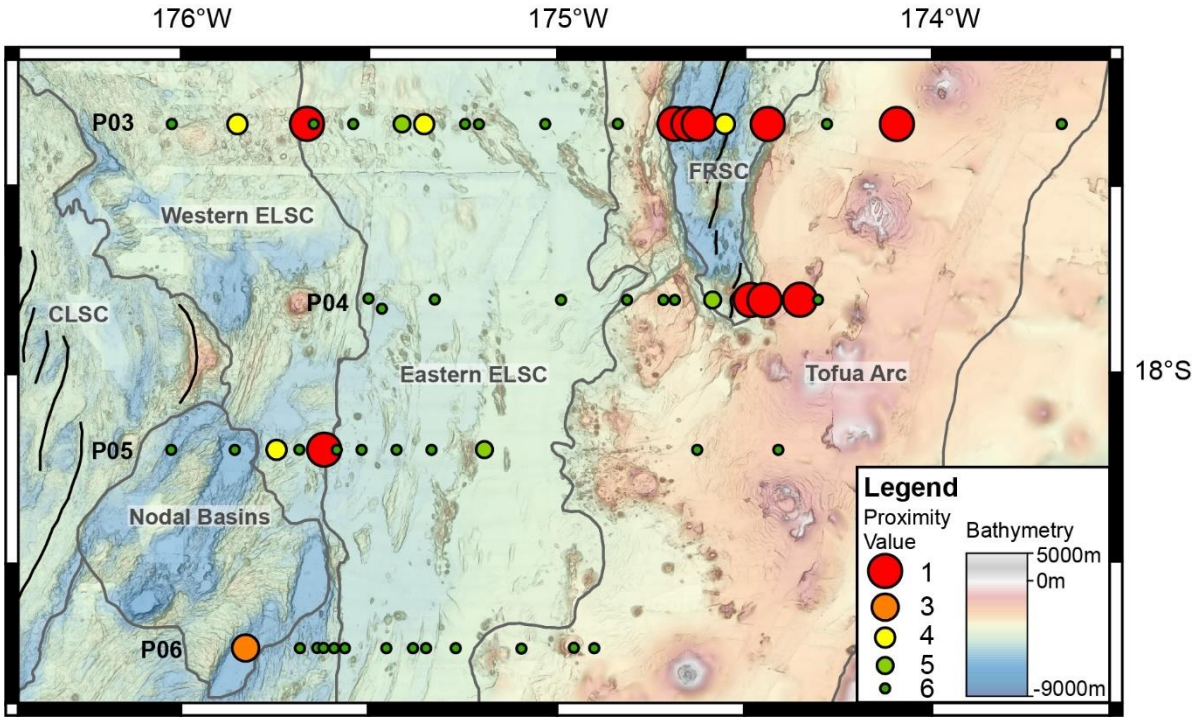

Figure 2.21 Map showing proximity of the uppermost sedimentary units to their sources, based on granulometric composition and interpreted depositional processes (see section 2.7.5). Echo facies with a proximity value of 1 are the most proximal to their source, while echo facies with a proximity value of 6 are most distal from their source. Proximity value 1 is assigned to echo facies 5 (MTDs), proximity value 1 is assigned to echo facies 2 (coarse-grained volcaniclastic mass flows), proximity value 3 is assigned to echo facies 4 (complete turbidite sequences), proximity value 4 is assigned to echo facies 3A (20% coarse and 80% fine material, more distal turbidites), proximity value 5 is assigned to echo facies 3B and 3C (10% coarse and 90% fine material, very distal turbidites) and proximity value 6 is assigned to echo facies 1 (hemipelagic material).

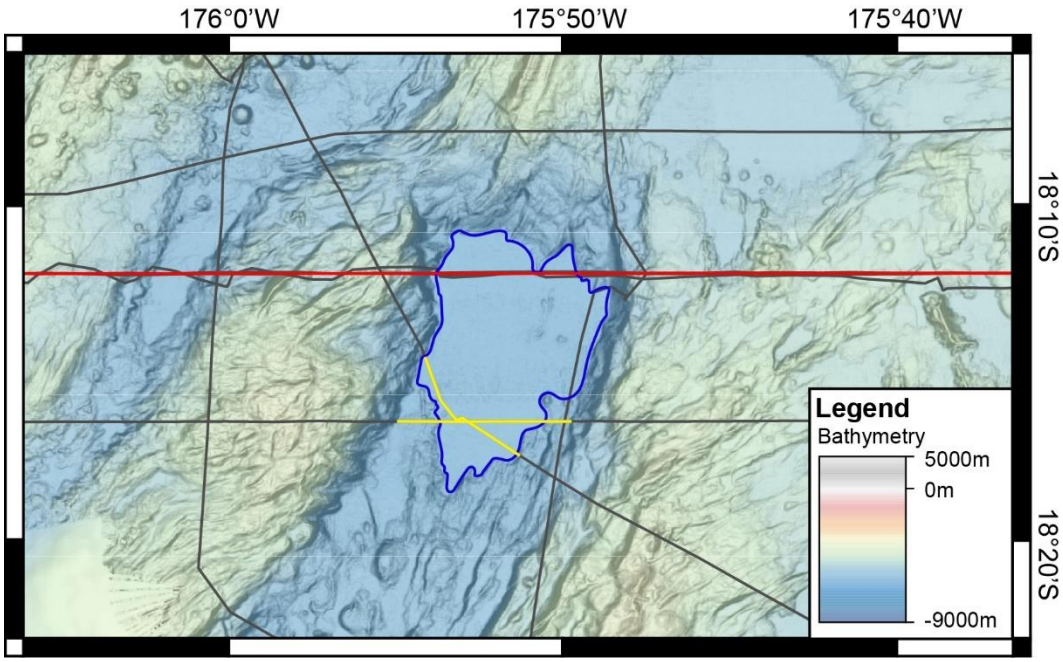

Figure 2.22 Bathymetric map of sub-basin P05-D (outlined in blue) used to illustrate a sediment volume calculation. Volume was determined by interpolating sediment-basement contact horizons and seafloor horizons in seismic reflection and Parasound data and calculating the volume between them. Red line is the P05 seismic transect, and yellow lines are Parasound sections used to pick horizons.

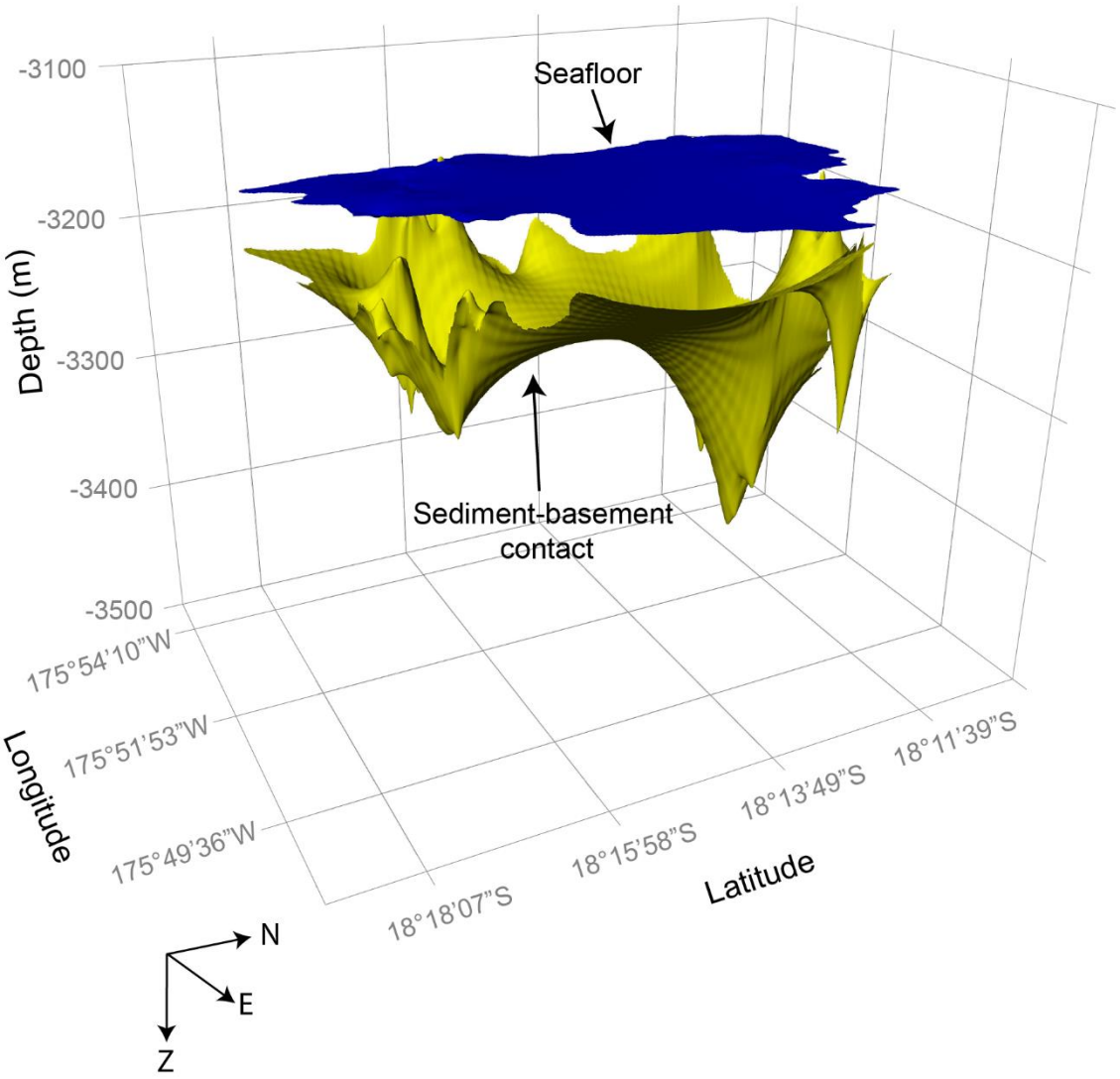

Figure 2.23 3D model of sub-basin P05-D showing the surfaces used to calculate the volume of sediment. The volume calculated from this model is 11.8 km^3.

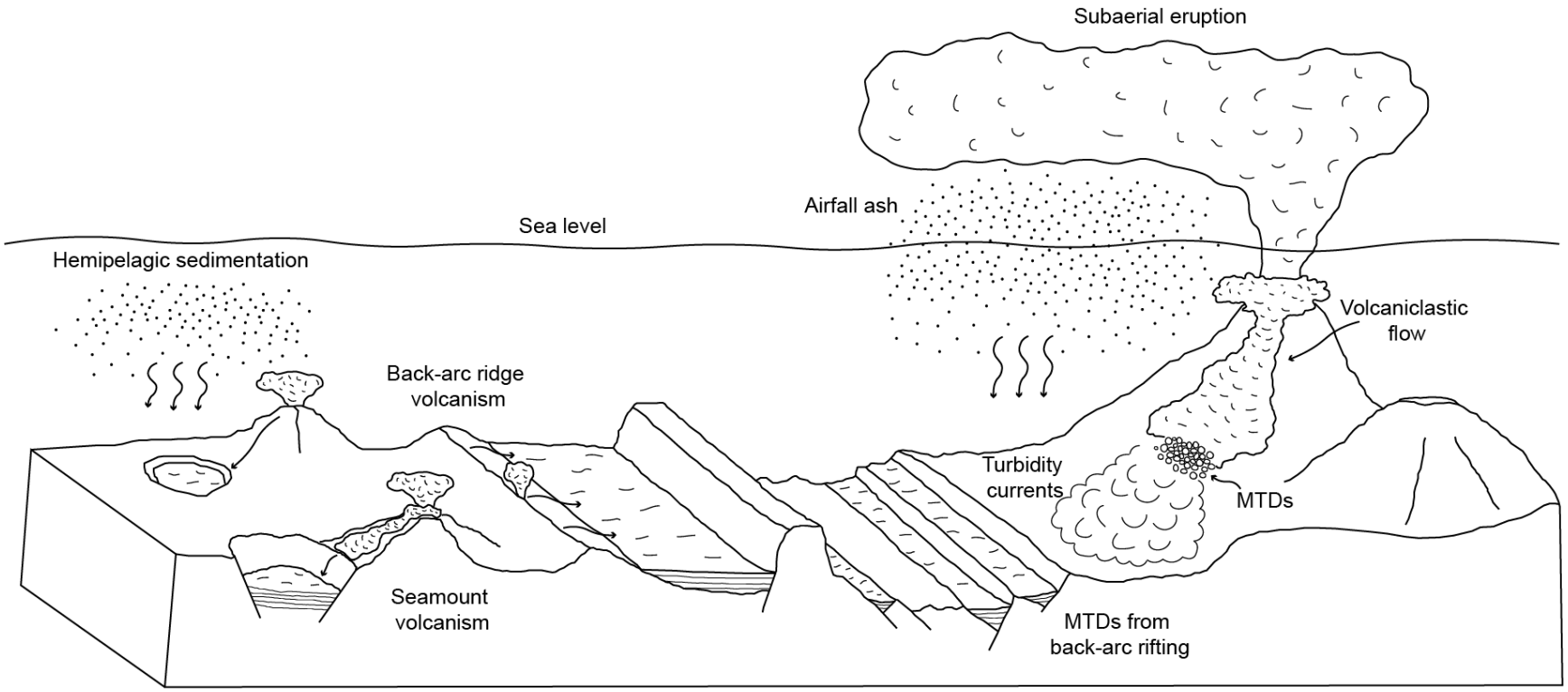

Figure 2.24 Schematic illustration of different sources and processes of sedimentation in back-arc basins. Eruptions from the Tofua Arc produce subaerial plumes from which airfall ash is deposited, and subaqueous volcaniclastic flows which can result in proximal MTDs and distal turbidites. The influence of arc volcanism decreases with distance from the arc, and the thinning of sediments away from the arc reflects the young ages of the sub-basins. Back-arc rifting results in the formation of normal faults and rotated crustal blocks, and the resulting steep flanks cause slope instability which forms MTDs. Volcanism from back-arc ridges and intrabasinal seamounts produces volcaniclastic material that is deposited in back-arc sub-basins as turbidites, mass flows and occasionally MTDs. Background hemipelagic sedimentation occurs continuously, and hemipelagic deposits can be redeposited as hemipelagites.

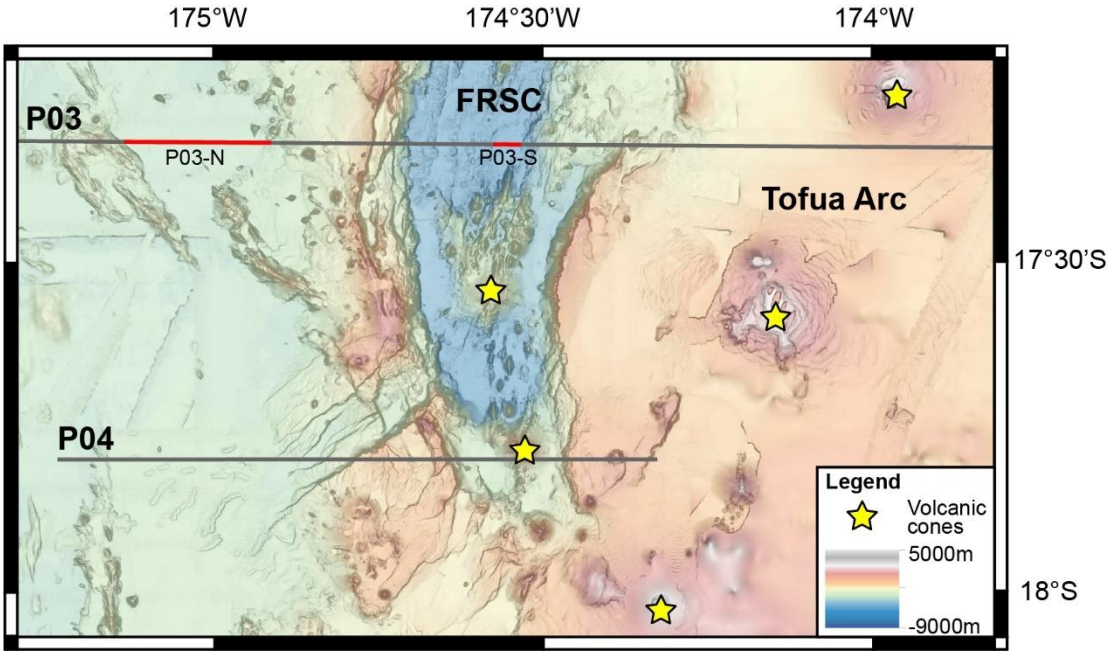

Figure 2.25 Bathymetric map of the FRSC showing the location of axial volcanic cones (yellow stars). These cones produce volcaniclastic sediment and have steep slopes that trigger mass flows filling the adjacent sedimentary sub-basins.

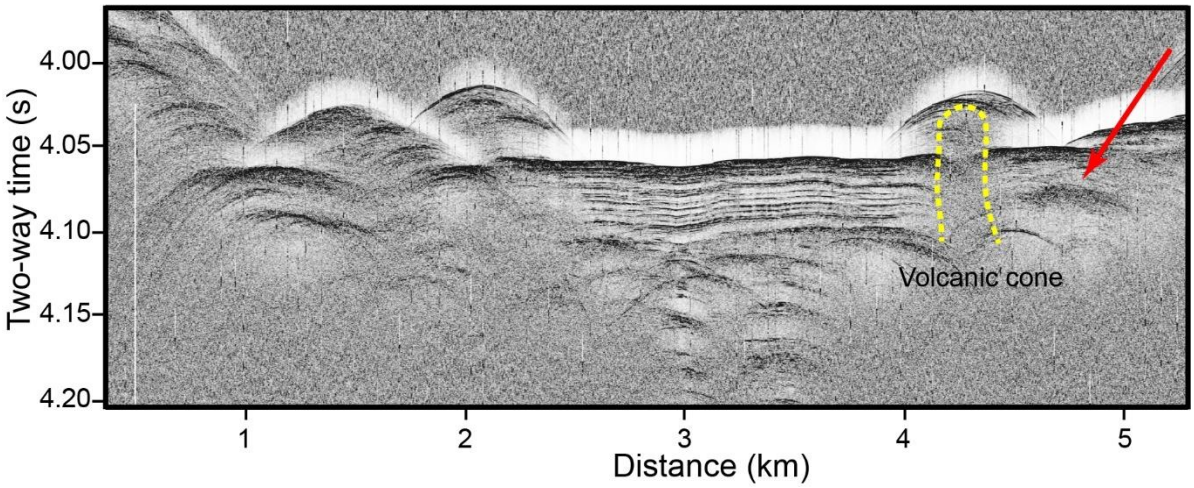

Figure 2.26 Parasound section of sub-basin P03-S shown in Figure 2.25. Red arrow points to the anomaly interpreted to be potentially altered and mineralized sediment. The yellow dotted line outlines a nearby volcanic intrusion. The sediment type is interbedded volcaniclastic and hemipelagic material. Hyperbolic echoes in the west of the section are caused by rugged topography at the outer boundary of the sub-basin.

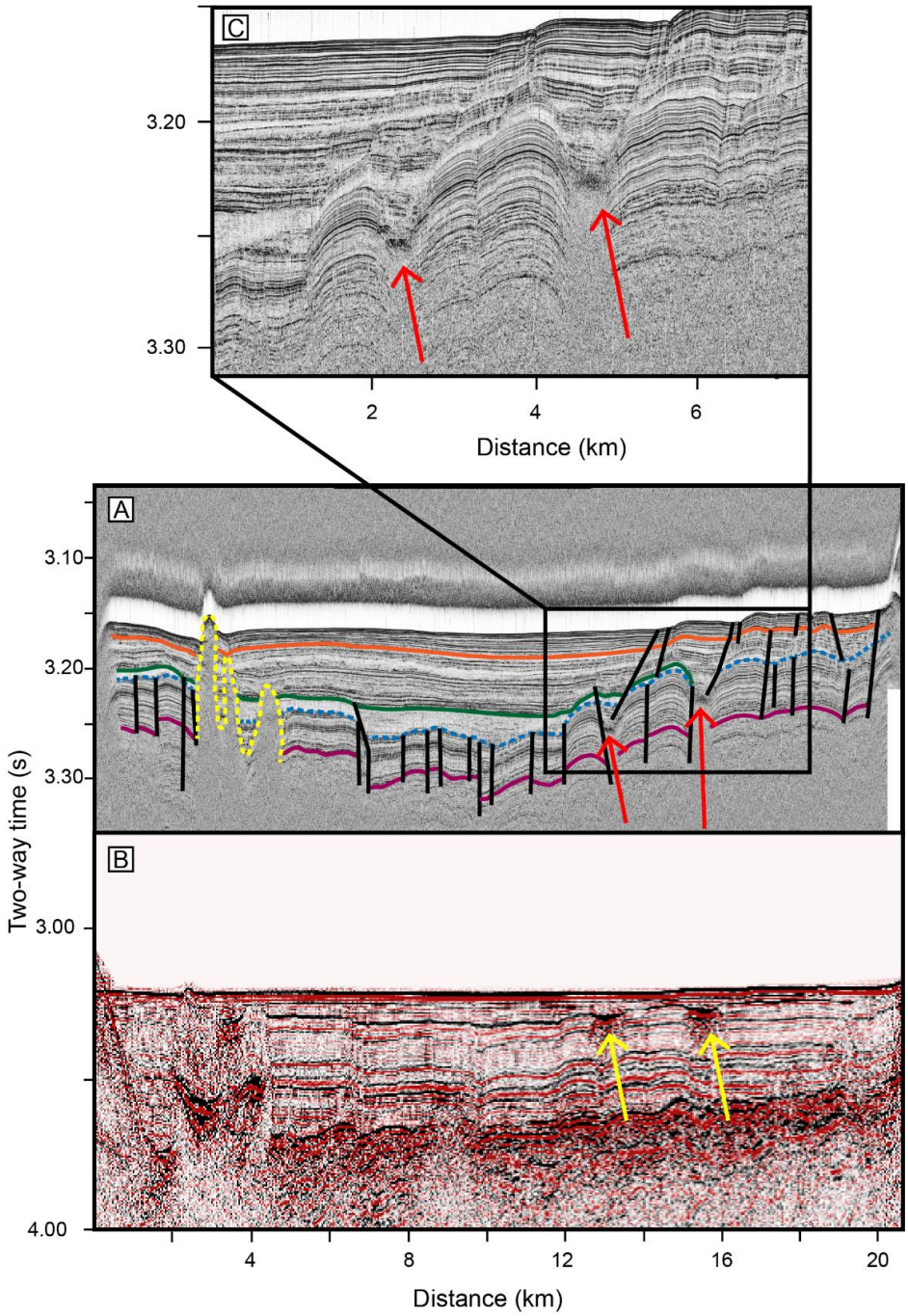

Figure 2.27 A) Parasound echogram of P03-N which contains two anomalies that are interpreted to be associated with hydrothermal upflow (e.g., alteration, mineralization or hydrothermal fluid). B) Bright spots in seismic reflection data correspond to the anomalies in Parasound. Here, however, the deeper penetration reveals disturbed bedded sediment beneath the anomalies. C) Close-up of the Parasound section to display anomalies in higher resolution.

Table 2.1 Echo facies legend developed to enable consistent sub-basin characterization and correlation throughout the study area (following Damuth 1975, 1978, 1980; Damuth and Hayes, 1977; Damuth and Olsen, 2015; Fierens et al., 2019).

Type	Description	Interpretation	Example	Sub-basin [a]
1	Strong, thin, parallel, continuous reflections	Fine-grained sediment. Hemipelagic deposition, fine ashfall or upper-division turbidites.	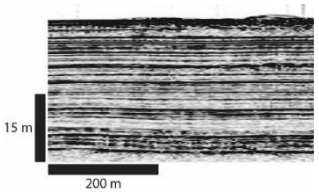	P03-H
2	Acoustically transparent echo bound on at least the top by a strong reflection	Coarse-grained sediment. Predominantly volcaniclastic material ranging in grain size from medium ash to blocks.	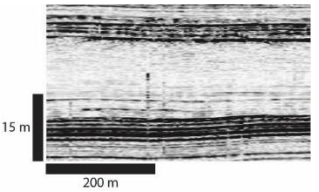	P03-H
3A	Acoustically transparent echoes with occasional interbeds of strong, thin, continuous reflections	Coarse-grained, volcaniclastic sediment with occasional interbeds of hemipelagic material or fine-grained ash.	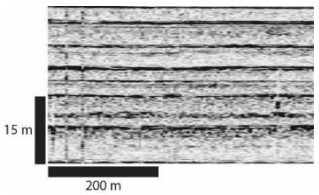	P04-A
3B	Acoustically transparent echoes with frequent interbeds of strong, thin reflections	Coarse-grained, volcaniclastic sediment with frequent interbeds of hemipelagic material or fine-grained ash.	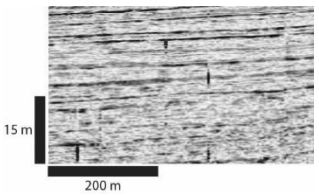	P06-I
3C	Undulatory, acoustically transparent echoes with interbeds of strong, thin reflections	Coarse-grained, volcaniclastic sediment with interbeds of hemipelagic material or fine-grained ash, which has been reworked by bottom currents or deposited on an uneven seafloor.	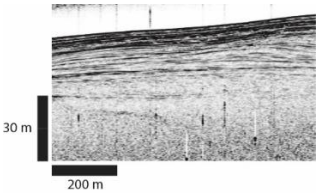	P04-D
4	Repeating packages of a basal, acoustically transparent echo overlain by one to several strong, thin, parallel, continuous reflections	Volcaniclastic turbidites with both upper and lower divisions. Grading from light grey to dark grey in the basal sub-unit is interpreted as compositional grading.	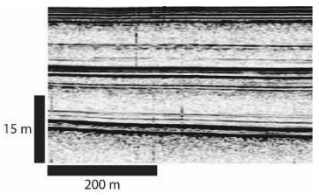	P06-A

Type	Description	Interpretation	Example	Sub-basin [a]
5	Prolonged echo with no internal reflections or some discontinuous internal reflections. Often located upslope from parallel, continuous reflections.	Mass transport deposits of any grain size. Debris flows, slumps, slides.	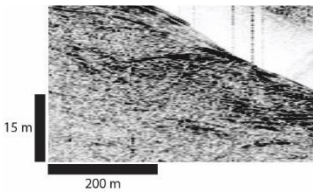	P06-F
6A	Overlapping hyperbolae with some sub-bottom reflections.	Steep or uneven seafloor with sediment cover.	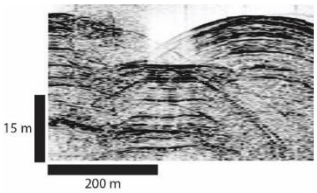	P03-E
6B	Overlapping hyperbolae with no sub-bottom reflections.	Steep or uneven seafloor that may or may not have sediment cover.	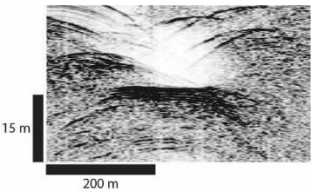	P03-F
7	Lenticular, acoustically transparent echoes.	Coarse-grained channel deposits of volcaniclastic material.	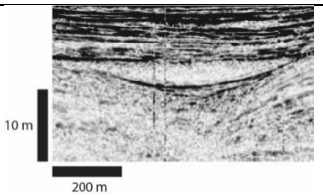	P04-D
8	Cloud of very strong reflections with a stippled texture.	Reflective anomaly attributed to gas or massive sulphide deposits.	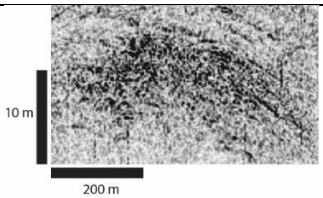	P03-S

[a] Sub-basin from which the example echogram is taken.

Table 2.2 Interpreted proportions of coarse- and fine-grained material in each echo facies.

Echo facies	**Fine-grained material (%)** [a]	**Coarse-grained material (%)**
1	100	0
2	0	100
3A	80	20
3B	90	10
3C	90	10
4	30	70
5	50	50
6A	NA	NA
6B	NA	NA

[a] Grain size proportions are based on echograms with corresponding cores from Damuth (1980), Fierens et al. (2019), Damuth and Olson (2015). Echo facies 6A and 6B are not assigned granulometric proportions because of hyperbolic echoes and absence of identifiable sedimentary units.

Table 2.3 Characteristics of the sub-basin groups organized by seismic transect.

			Width (km)			Sediment thickness (m)			Sediment composition (%) [a]		
Transect	**Sub-basin group**	**Sub-basins**	**Min.**	**Max.**	**Avg.**	**Min.**	**Max.**	**Avg.**	**Fine**	**Coarse**	**Undetermined [b]**
P03	West ELSC	A-F	0.8	2	1.5	9.8	57	27.5	16	2	82
	East ELSC	G-N	0.8	25.8	6.5	19.8	319.2	85	81	19	0
	FRSC	P-T	0.9	2.9	1.82	85.1	185.4	119.2	59	41	0
	Tofua Arc	1, U-W	1.3	45	17.3	111.7	954.6	473.7	71	29	0
P04	East ELSC	A-D	3.2	34	16.9	95	448.4	220.6	86	14	0
	Tofua Arc	1, E, F, 2, 3, I	3.2	14.2	5.9	17.5	171.8	71.1	68	32	0
	FRSC	G, H	4.9	6.7	-	28.12	257.6	142.9	59	41	0
P05	CLSC	A, B	1.7	7.9	-	0	0	0	0	0	0
	Nodal basins	C, D	2.6	8.4	-	44.8	238.6	141.7	57	43	0
	West ELSC	E-H	1	1.8	1.4	31.2	58.5	48.3	80	20	0
	East ELSC	1, I-L	1.6	28.5	11.2	85.9	304	176.3	83	17	0
	Tofua Arc	M, N	20	23	-	873.2	997.1	935.2	84	16	0
P06	Nodal Basins	A	6.8	-	-	150.5			59	41	0
	West ELSC	B-D, 1	1.6	2.2	1.9	41	96.5	68.0	82	18	0
	East ELSC	E-I	3.5	13.3	7.5	68.4	394.4	185.4	87	13	0
	Tofua Arc	J, K, 2	3.8	15.6	10.9	237.9	1081	711.9	65	35	0

[a] Sediment composition was calculated from the proportions of coarse and fine sediment in each echo facies (summarized in Table 2.2), using the weighted average formula described in Section 2.5.2.

[b] Echo facies 6A and 6B do not provide sedimentological information, so those echo facies are considered "undetermined".

Table 2.4 Dominant echo facies in each sub-basin group and in the study area.

	Weighted Average (%) [a]						
Echo facies	**CLSC [b]**	**Western ELSC**	**Eastern ELSC**	**FRSC**	**Tofua Arc**	**Nodal Basins**	**Study Area**
1	0.0	7.9	14.6	0.0	12.6	2.0	12.3
2	0.0	2.1	4.2	0.0	13.1	4.9	6.3
3A	0.0	51.2	32.8	19.0	30.7	44.7	33.3
3B	0.0	18.8	45.5	8.8	33.1	9.0	37.1
3C	0.0	0.0	2.0	0.0	0.0	0.0	1.2
4	0.0	0.0	0.0	0.0	0.0	39.5	3.2
5	0.0	0.4	0.9	72.3	10.4	0.0	5.9
6A	0.0	19.7	0.0	0.0	0.0	0.0	0.6
6B	0.0	0.0	0.0	0.0	0.0	0.0	0.0

[a] Percentages are weighted averages calculated according to the methods in Section 2.5.2.

[b] CLSC sub-basins do not contain sediment, so echo facies proportions are all 0%.

Table 2.5 Volumes of echo facies corresponding to each sedimentary unit in sub-basin P05-D.

Sedimentary unit	**Echo facies**	**Unit thickness (m)**	**Proportion of total volume (%)**	**Unit volume (km^3)**
P05-D-i	1	3.8	1.6	0.189
P05-D-ii	4	66.1	27.7	3.269
P05-D-iii	3B	26.6	11.1	1.310
P05-D-iv	2	14.4	6.0	0.708
P05-D-v	3A	51.7	21.7	2.561
P05-D-vi	X	76.0	31.9	3.764

Chapter 3: Tectonostratigraphic Reconstruction from Sedimentary Basin Analysis

3.1 Introduction

Early models of back-arc basins proposed that they were simple extensional basins where new crust formed along a single spreading center, usually oriented parallel to the subduction zone (Martinez et al., 2007). The Lau Basin, however, contains multiple propagating rifts and spreading centres, transcurrent faults, triple junctions and microplates (Sleeper and Martinez, 2016, Sleeper et al., 2016; Stewart et al., 2022) suggesting a much more complicated tectonic regime. Extension is accommodated along several axes at the same time, and basin opening is diachronous rather than linear. Karig and Moore (1975) recognized that the opening of the Lau Basin was recorded in several sub-basins and concluded that these sub-basins were oldest near the remnant arc and decreased in age toward the active arc. However, Hawkins (1995; and references therein) determined that the locus of crustal growth jumped from west-to-east, accommodated by multiple spreading centers of different ages. Our findings and data from Schmid et al. (2020) and Stewart et al. (2022) indicate an even more complicated progression, with highly asymmetric basin opening in the N.E. Lau, beginning at the ELSC and now at the CLSC. It is clear that the basin history is more complicated than previously hypothesized. Here, we use the sedimentary record of each of the 63 mapped sub-basins in the N.E. Lau to better characterize this most recent phase of opening.

Small, primarily fault-bounded sub-basins formed during both the rifting and spreading stages of the opening of the basin. As soon as the sub-basins opened, they began to accumulate sediment, and this has continued to the present day. A record of this sedimentation is found in the volcaniclastic and hemipelagic deposits of the individual sub-basins described in Chapter 2. By relating them to the structure, composition and age of the underlying crust, we can reconstruct the relative age and tectonic evolution of the basins, including faulting, hydrothermal activity and magmatism. This chapter examines the relationship between the different sub-basin groups and 1) how the locus of extension in the N.E. Lau Basin migrated through time, 2) what processes controlled where extension was localized, and 3) how the tectonostratigraphic evolution can be recognized in the sedimentary successions.

The 63 sub-basins and slope deposits in the study area were assigned to groups: the CLSC, the nodal sub-basins, the western ELSC, the eastern ELSC, the FRSC and Tofua Arc (Figure 3.1). The sub-basin groups are characterized by distinctly different morphology, underlying crust, sedimentary thicknesses and composition, summarized in Table 3.1. Each group is interpreted to have a unique opening history controlled by different processes. By comparing sub-basin widths, sediment thicknesses and makeup, as well as the surrounding structures and features of the underlying crust, we have established a sequence of basin opening along the four east-west transects in the study area (Figure 3.1).

3.2 Determining Ages of Sub-Basins

To determine the basin evolution, we used the inferred age of the basement (considered a maximum age of the basin). The maximum basin age was defined by magnetic isochrons (Taylor et al., 1996; Zellmer and Taylor, 2001; Figure 3.2) and other known crustal ages summarized in Parson and Hawkins (1994) and Stewart et al. (2022). We attempted new sub-basin age calculations using sedimentation rates derived from drill cores recovered during ODP Leg 135 (32 mm/ka for fine-grained hemipelagic and hemipelagite units and 882 mm/ka for coarse-grained volcaniclastic units; Rothwell et al., 1994a). However, in many cases the calculated ages exceeded the maximum age defined by magnetic isochrons, revealing that sedimentation rates in the study area are higher than those recorded during ODP Leg 135. This result is expected, as our study area is much closer to the active arc than Sites 834 and 835 (where the hemipelagic and hemipelagite sedimentation rate was calculated) and Site 838 (where the volcaniclastic sedimentation rate was calculated). To better constrain the rates of sedimentation closer to the arc, we calculated average sedimentation rates (combined volcaniclastic and hemipelagic sedimentation) using the average sediment thickness and the maximum and minimum ages of each sub-basin group. The maximum and minimum basin ages and sedimentation rates are presented in Table 3.2.

The CLSC sub-basin group contains 2 sub-basins. The minimum and maximum ages for this group correspond to the minimum and maximum magnetic chrons and range from 0 Ma to 0.78 Ma. The sub-basins are adjacent to the spreading axis and were formed by spreading at the

CLSC, so they do not contain much sediment. At the limit of detection of about 15 cm of sediment, a basin with no observable sediment in Parasound is likely no older than 5,000 years.

The Nodal Basin sub-basin group contains 3 sub-basins. The minimum age for the basement in this sub-basin group is 0.5 Ma and the maximum age is 0.78 Ma. These sub-basins are interpreted to have opened during the overlap of the ELSC and CLSC, resulting in deep, rounded sub-basins with thick sedimentary successions. Rothwell et al. (1994b) propose that the CLSC propagator passed through the latitude of the Nodal Basin sub-basin group around 0.5 Ma, reflected by a period of increased turbidite and MTD emplacement. Sediments in this group belong mainly to echo facies 3A and 4, which consist of mixed coarse-grained volcaniclastic sediment and fine-grained hemipelagic material. The only occurrences of echo facies 4 (full turbidite successions) are observed here. The average sediment thickness is 145 m with an average sedimentation rate of 237 mm/ka.

The Western ELSC sub-basin group contains 14 sub-basins. The minimum ages for the basement in this sub-basin group range from 0.78 Ma to 2.4 Ma based on the magnetic chrons. The Western ELSC sub-basins are much narrower than those in the eastern ELSC sub-basin group and have thinner sedimentary successions. The terrain is very rugged, with many volcanic cones and ridges, which could mark the transition from rifting to spreading. There is a distinct transition in seafloor fabric (located between P03-F and P03-G) between the eastern and western ELSC sub-basins, which corresponds to a previously recognized change from older to younger back-arc crust between the ELSC and the CLSC (e.g., Schmid et al., 2020). Sediments in the western ELSC sub-basins belong mainly to echo facies 3A and 3B consisting of mixed coarse-grained volcaniclastic sediment and fine-grained hemipelagic sediment. The average sediment thickness is 44 m with an average sedimentation rate of 38 mm/ka.

The Eastern ELSC sub-basin group contains 22 sub-basins. The minimum ages for the basement in this sub-basin group range from 0.78 Ma to 2.6 Ma. The Eastern ELSC sub-basins are wide with thick sedimentary successions. They are likely associated with the initial rifting of the ELSC as it propagated south, since the sub-basins are deeper than most others in the study area. The ELSC basins are located in some of the oldest back-arc crust in the Lau Basin, which may

partly account for their depth, but they are not as deep as the FRSC sub-basins, which formed in older and thicker arc crust that is actively rifting. Sediments in the basin mainly belong to echo facies 3A and 3B which consist of mixed coarse-grained volcaniclastic sediment and fine-grained hemipelagic sediment, and echo facies 1 which consists of fine-grained hemipelagic sediment. The average sediment thickness is 153 m with an average sedimentation rate of 128 mm/ka.

The FRSC sub-basin group contains 7 sub-basins. The minimum ages for the basement in this sub-basin group range from 0.34 Ma to 1.5 Ma (Schmid et al., 2020). The FRSC sub-basins are the most recent sub-basins to have opened in response to a "jump" in the locus of extension back toward the old arc crust (Sleeper et al., 2016; Schmid et al., 2020; Hannington, 2019). The rift has steep flanks and is characterized by thick MTDs. Sediment in these basins mainly belongs to echo facies 5 which consists of mixed volcaniclastic and hemipelagic MTDs. The average sediment thickness is 125.9 m, and the average sedimentation rate is 227 mm/ka.

The Tofua Arc sub-basin group contains 15 sub-basins. The minimum ages for the basement in this sub-basin group range from 0.14 Ma to 6 Ma. This sub-basin group is distinct from the others in that it has two distinct packages of sediments. The first is sediment deposited during the earliest stages of rifting of the Lau Basin around 6 Ma (Parson and Hawkins, 1994), which was followed by a period of quiescence until 3 Ma, when the active Tofua arc initiated. The sedimentary package beneath the Tofua Arc-derived sediments is the thickest, including several sequences visible in the seismic data, and these sub-basins are deformed by faulting and folding. They experienced high sedimentation rates due to active rifting from 6 Ma to 3 Ma. The younger sediments in the basin mainly belong to echo facies 3A and 3B which consist of mixed coarse-grained volcaniclastic sediment and fine-grained hemipelagic sediment. The average sediment thickness is 422 m with an average sedimentation rate of 1542 mm/ka. The flanks of the FRSC include sub-basins that formed on Tofua Arc crust during the initial stages of rifting of the FRSC. They are tilted away from the FRSC and are mainly slope deposits.

3.3 Sub-Basin Opening Order

From the mapped sedimentation in each sub-basin, we have interpreted the order of opening and subsidence along each transect. This is used to interpret the locus of extension at different times during the opening of the entire basin. From the sediment thickness, echo character, and basin morphology, the sub-basins are assigned to different stages of opening.

The oldest group of sub-basins along P03 are those under the Tofua arc (sub-basins U-W). These opened around 6 Ma, during the initial rifting episode of the Tonga Ridge and are buried under volcaniclastics from the active Tofua arc. They have the thickest sediment of all of the sub-basins, up to 954 m, and although sedimentation rates are high at the arc, the great thickness of sediment is consistent with them being the oldest sub-basins in the study area. The next oldest basins on P03 are the ELSC sub-basin group. The ELSC initiated around 5-5.5 Ma (Hawkins, 1995) just to the west of the arc and propagated south. Since the P03 line crosses the ELSC at its northernmost point, the sub-basins at this location would have been among the first to open. We interpret the age of the sub-basins at the northern termination of the ELSC to be close to the age of initiation of back-arc spreading in this area. The difference in the morphological and sedimentological characteristics of the eastern and the western sub-basins suggests that the eastern ELSC sub-basins (sub-basins P03-G to P03-N) opened first, followed by the western sub-basins (sub-basins P03-A to P03-F). The eastern ELSC sub-basins are some of the widest basins along the P03 line (up to 25.8 km wide), with thick sediment up to 319 m that is predominantly fine-grained. The western ELSC sub-basins are underlain by rugged terrain, are narrower (up to 2 km wide) and have thinner sediment (up to 57 m) that is mainly volcaniclastic. Since fine-grained material such as hemipelagic sediment and fine-grained ash has a significantly lower sedimentation rate than the rapidly deposited gravity flows in the western sub-basins, the eastern ELSC sub-basins must be older than those in the west. The adjacent FRSC began to rift around 1.5 Ma and also propagated to the south (Zellmer and Taylor, 2001; Schmid et al., 2020). Slope deposit P03-1 was emplaced west of the FRSC, accumulating up to 112 m of arc-like sediment produced by the rift volcanism. The youngest sub-basins on P03 (P03-P to P03-T) are related to the FRSC spreading, containing up to 185.4 m of volcaniclastic sediment. Instability along the normal faults is indicated by the MTDs and confirms that rifting is still actively occurring, as is magmatism at the rift center (Schmid et al., 2021, Franz et al., 2021).

Along P04, there are correlatable sedimentary packages in the majority of the sub-basins. These units represent widespread sedimentation across many 10s of kilometers. The first sub-basins to open along the P04 transect were those at the northern termination of the ELSC in the Eastern ELSC sub-basin group. They formed as the ELSC propagated southward and accumulated up to 440 m of sediment. They are the widest and deepest sub-basins along this transect, reflecting the spreading asymmetry of the ELSC (Stewart et al., 2022). These older basins are now juxtaposed to much younger sub-basins that opened during the initial rifting stages of the FRSC. Adjacent to the FRSC, the rifted Tofua Arc crust on P04 is tilted away from the rift axis, producing younger sub-basins and slope deposits containing MTDs. The two FRSC sub-basins contain up to 258 m of volcaniclastic and hemipelagic sediment. On the western flank of the FRSC a deep graben now appears to be actively channeling sediment into the ELSC sub-basins, producing the channel deposits and sediment waves observed in P04-D (Figure 3.3). A similar sequence of deposits in the Eastern ELSC sub-basin group may indicate that the sedimentary material from the FRSC is being transported over ~100 km.

The sub-basins on line P05 show that there have been periods of deformation and non-deposition, followed by turbidity currents and bottom currents (which form sediment waves at P05-M). The sub-basins developed along P05 on the Tofua Arc are the oldest based on the significant sedimentary thickness, up to 997 m. Wide sub-basins of the eastern ELSC group on this line have thick sedimentary successions up to 304 m with a mixture of volcaniclastic and hemipelagic deposits, suggesting a long period of sediment accumulation. As observed on P03, the western ELSC sub-basins are much narrower, suggesting that they are younger. P05 crosses the overlap between the western ELSC and the CLSC where spreading initiated more recently, forming the deep nodal sub-basins in the transfer zone. This is the first instance of multiple zones of extension developing simultaneously across the basin within the study area. The two nodal sub-basins crossed by P05 contain up to 239 m of sediment, including turbidites that formed as a result of instability on the steep bounding slopes. Finally, the CLSC sub-basins on P05 contain no detectable sediment, indicating that extension is currently occurring here, while extension in the east jumped to the FRSC.

The opening sequence on P06 follows a similar pattern to P05. The thick sedimentary successions in the Tofua Arc sub-basins (up to 1081 m) are the oldest. As spreading initiated in the ELSC, the eastern ELSC sub-basins accumulated thick successions of sediment up to 394 m. Narrower, shallower sub-basins in the western ELSC have accumulated up to 97 m of sediment. Extension related to the FRSC has not yet reached this position.

3.4 Extensional Model

By relating the sedimentary sub-basins to the crustal evolution of the N.E. Lau Basin and by collating the extensional information by transect, we have identified a multi-stage history of basin evolution (Figure 3.5). The first group of basins to open were the rift-related basins underneath the Tofua Arc. These likely formed during the earliest stages of rifting of the Vitiaz Arc at 6 Ma (Figure 3.5a). The ELSC sub-basins formed in the next stage on the earliest back-arc crust. These basins began opening asymmetrically in the north around 5.3 Ma (Stewart et al., 2022), expanding to the west and propagating to the south. The ELSC propagated into the study area at around 3 Ma (Figure 3.5b). Magnetic ages in all the ELSC sub-basins decrease from east to west and from north to south, consistent with the overall diachronous spreading during the opening of the basin (Figure 3.2). The Eastern ELSC sub-basins are deeper and wider than the Western ELSC sub-basins which suggests that they are older. The next stage of basin evolution was the resumption of volcaniclastic sedimentation in the Tofua Arc sub-basins coincident with the initiation of Tofua Arc volcanism at 3 Ma. Due to a plate reorganization in the northern Lau Basin at 1 Ma, the CLSC and the FRSC initiated on opposite sides of the Niuafo'ou microplate. This resulted in the formation of the CLSC sub-basins and the FRSC sub-basins, which are still actively rifting.

A majority of the sub-basins formed at rifts and spreading centers and migrated away with the progressive opening of the basin. This initial extension is perpendicular to the spreading centers. However, as many of the spreading centres are propagating southwards, there is a second component of basin opening that caused many of the basins to have a north-south elongated shape. This relationship is seen in the connected sub-basins east of the FRSC (P03-N, P04-D, P05-L and P06-I; Figure 3.1) where the basins share the same bounding faults.

Although the basin is only 6 million years old, significant deformation is recorded in the sub-basins, particularly in the older sedimentary package in the Tofua arc sub-basins, including normal faults, thrust faults and open folds (Figure 3.4). Further deformation is seen at a smaller scale in the back-arc sub-basins (e.g., P03-N, P04-B, P05-I, P06-E; Figure 3.6), with different generations of normal faulting that locally has resulted in unconformities. Further analysis of these faults would provide additional information about the recent deformational history in the Lau Basin.

3.5 Potential Applications

The results of this study shed light on back-arc basin sedimentation, both in the modern ocean and potentially in ancient arc-backarc systems. Future work in the Lau Basin could include the collection and analysis of drill core and sediment gravity core to calibrate the Parasound data with groundtruth data. This would improve the precision of the echo facies legend and allow for a more sophisticated interpretation of sediment composition and depositional processes from Parasound data.

The work presented in this thesis may also have applications in the ancient arc-backarc systems preserved in the rock record. For example, mapping signature facies, such as MTDs, at the scale of 10s to 100s of km can provide important clues to the proximity of rifts in ancient volcanic belts. This is of economic importance as the evolution of back-arc basins is a fundamental control on the location of hydrothermal activity, both at the seafloor and in subseafloor sediments. As an example of the potential application, Mueller and Donaldson, (1992) divided sedimentation in the Abitibi Greenstone Belt into four sedimentary cycles. Sedimentary cycle 1, which is interpreted to have occurred during active arc basin formation, comprises deep marine facies, including turbidites and resedimented conglomerates with intercalated hemipelagic units and iron formations. They interpret these facies as submarine fan complexes. In the Timmins region, Born (1996) concluded that sediments from the Tisdale, Porcupine and Pamour Groups were mainly sourced from a continental basement uplift. He also concluded that the deep-marine turbidites and conglomerates were associated with submarine fans. However, neither of these studies link the sedimentary facies to the extensional setting at the time of deposition. We suggest that key relationships observed in the Lau Basin may be analogous to the deep-marine

sediments in the Abitibi Greenstone Belt and thus might be useful guides for placing ancient arc-backarc sedimentation into a modern framework with insights into the sedimentological, structural and tectonic history.

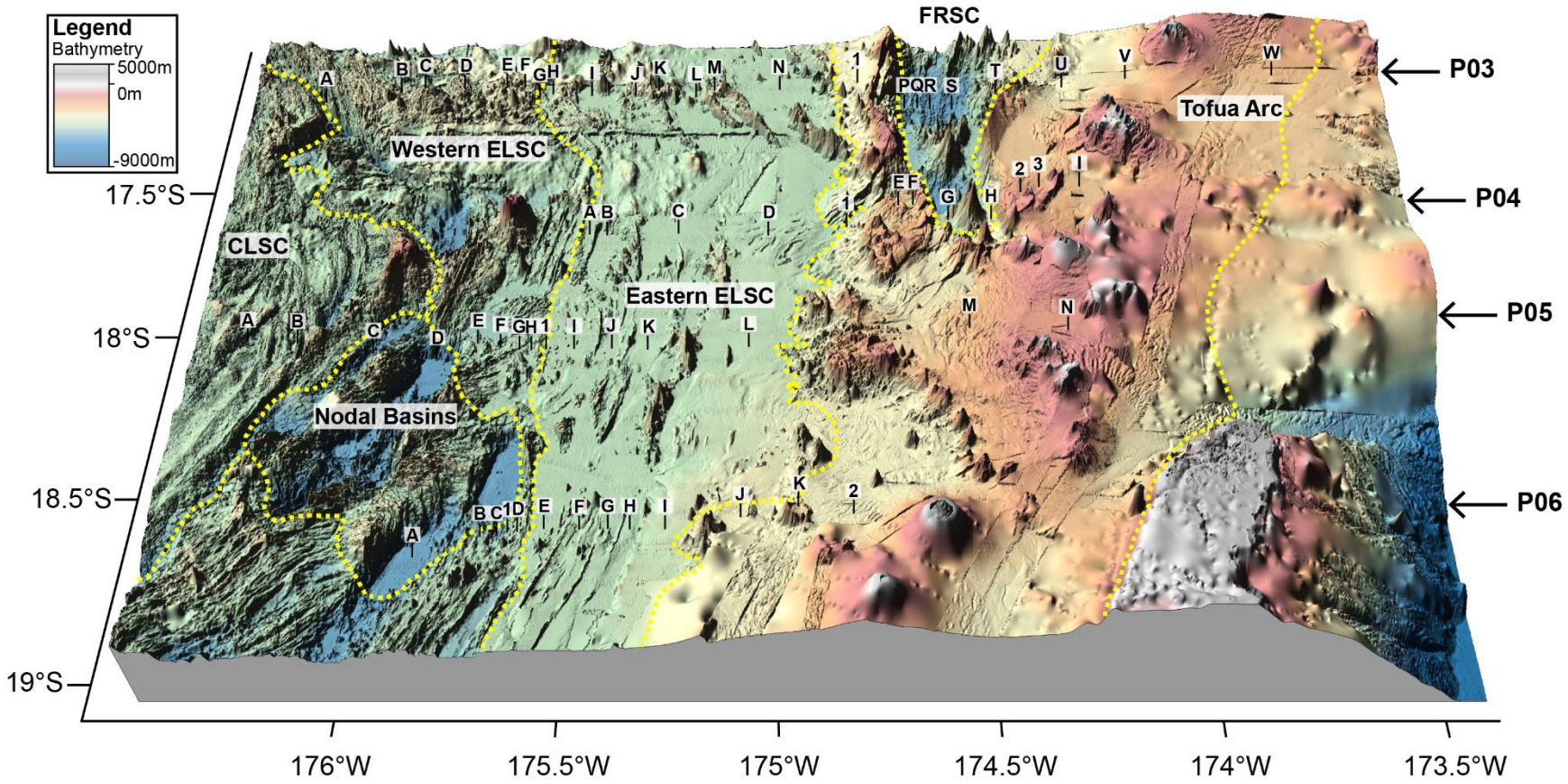

Figure 3.1 3D model of the study area. Sub-basin group boundaries are marked by dashed yellow lines.

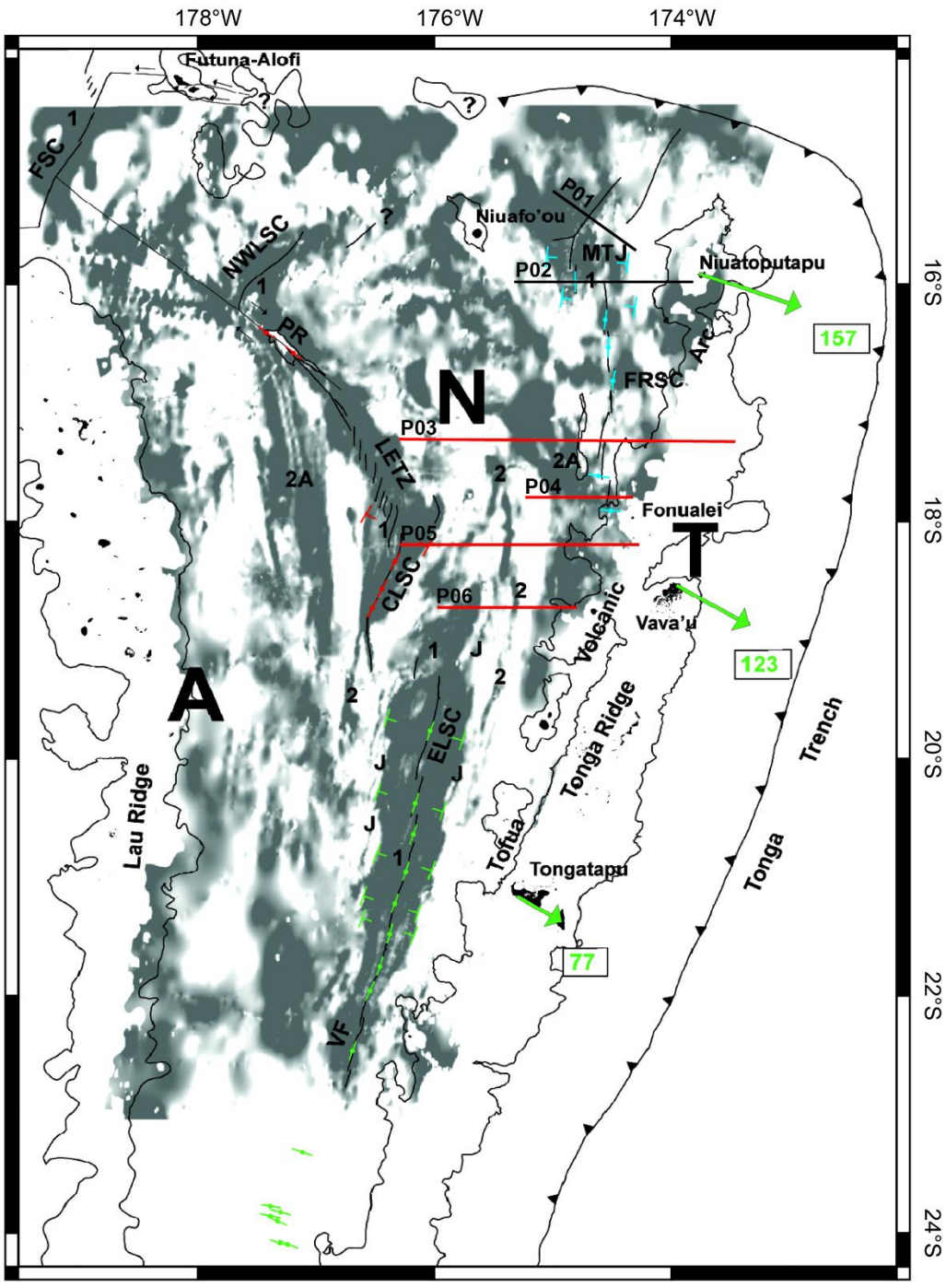
178°W
176°W
174°W
16°S
18°S
20°S
22°S
24°S
Futuna-Alofi
FSC
NWLSC
PR
Niuafo'ou
P01
MTJ
P02
Niuatoputapu
157
Arc
FRSC
N
P03
LETZ
2A
P04
Fonualei
P05
CLSC
P06
Volcanic
Vava'u
123
A
ELSC
Tonga Ridge
Trench
Lau Ridge
Tofua
Tongatapu
77
Tonga
VF

Figure 3.2 Magnetic anomaly map from Zellmer and Taylor (2001) with the seismic transects from RV Sonne SO267 (Hannington et al. 2019) marked by red lines (included in this study) and grey lines (not included in this study). Positively magnetized crust is indicated by shaded grey areas and are labelled with magnetic polarity chrons (Cande and Kent, 1992): 1 = Brunhes normal chron (0 – 0.78 Ma), J = Jaramillo normal subchron (0.98 – 1.05 Ma) within the Matuyama reversed chron, 2 = Olduvai normal subchron (1.76 – 1.98 Ma) within the Matuyama reversed chron, 2A Gauss chron (2.60 – 3.05 Ma). The Australian Plate, Tongan Plate and Niuafo'ou Microplate are indicated by A, T and N, respectively. "T" markers indicate the boundary between the Brunhes and Matuyama chrons (0.78 – 2.59 Ma). Ridge azimuths and the horizontal component of earthquake slip vectors are indicated by a line indicating azimuth with a solid circle. GPS velocities of the Tonga Plate relative to the Australian Plate are shown by green arrows.

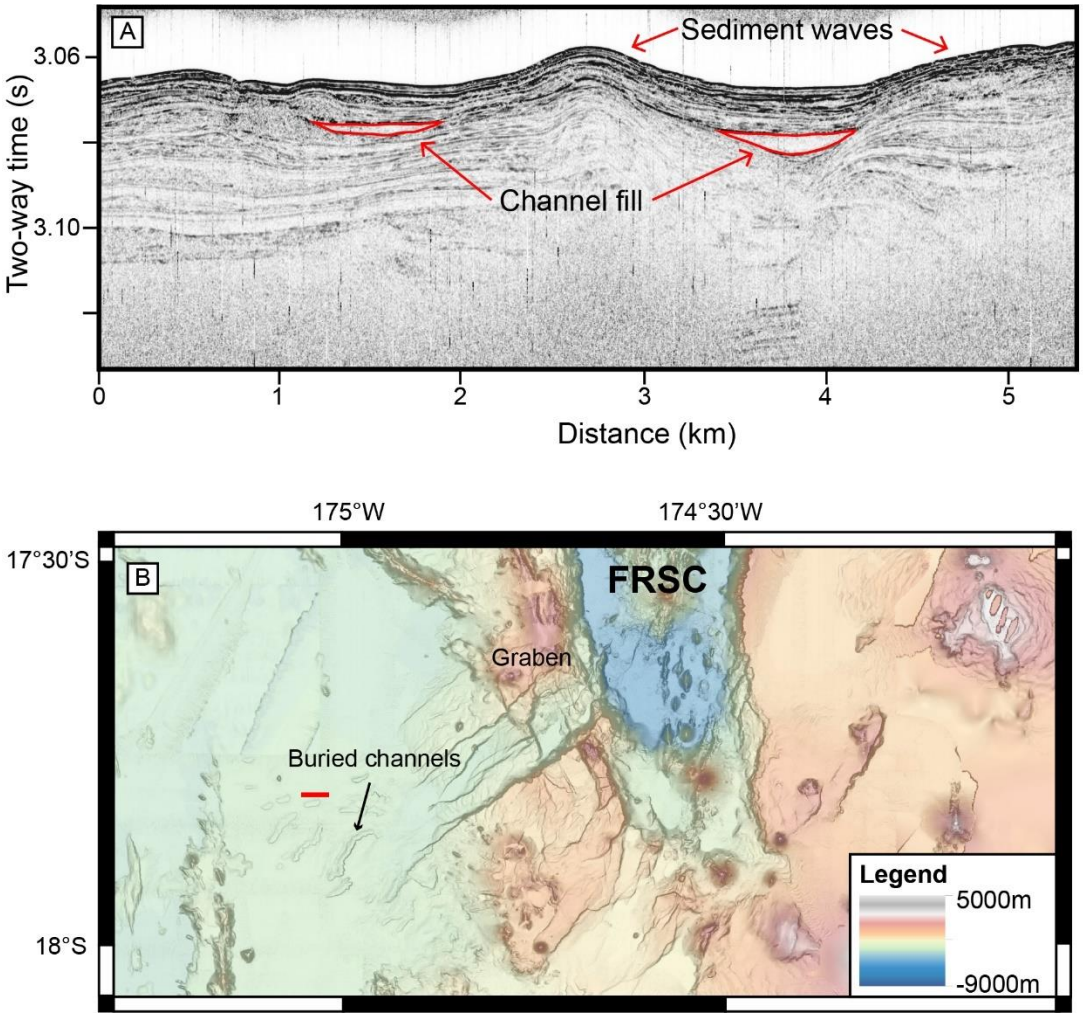

Figure 3.3 A) Parasound echogram of channel fills and sediment waves on P04-D. B) Buried channels appear as sinuous features. Channels likely developed from the graben on the western flank of the FRSC, which has an increased slope. Parasound location is shown by a red line.

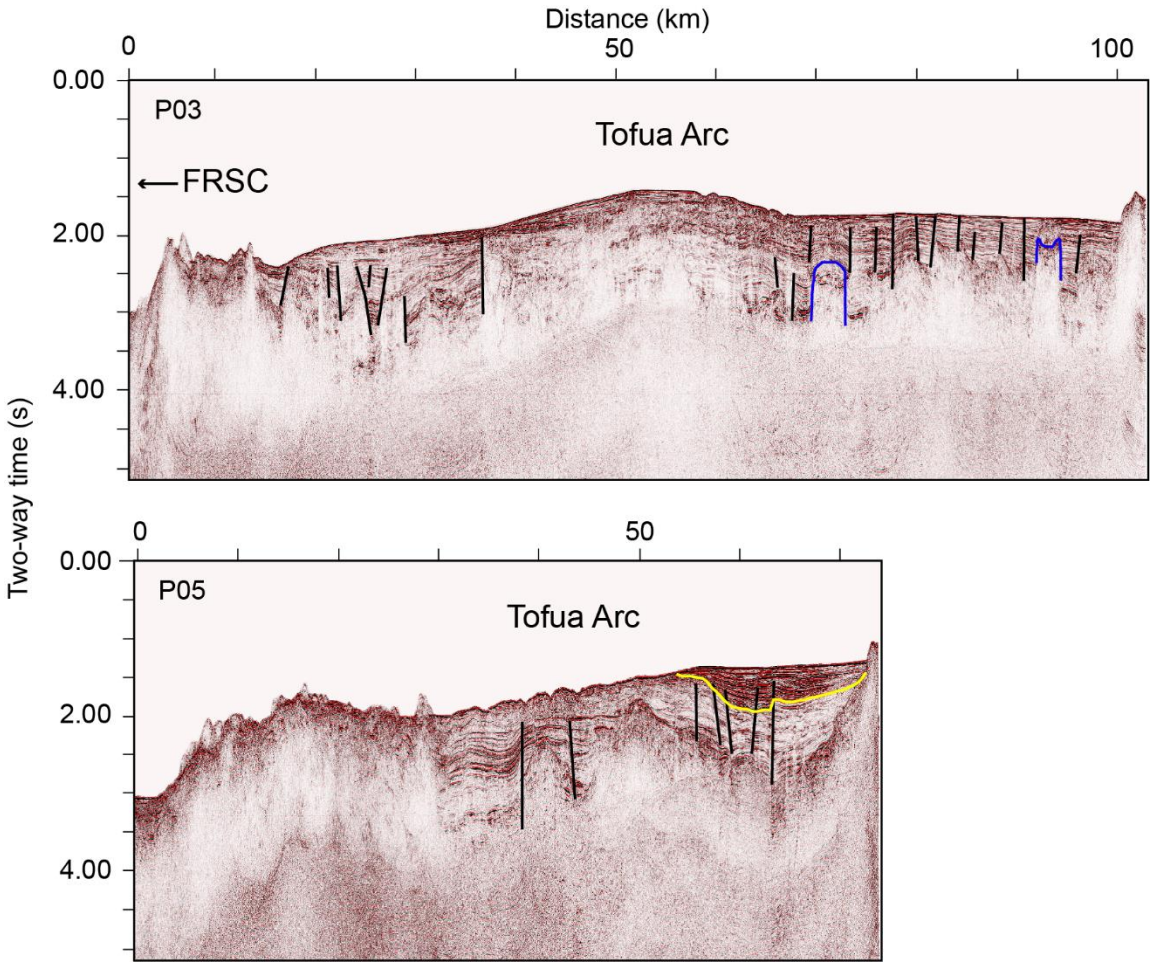

Figure 3.4 Deformation in the Tofua Arc as seen in seismic reflection profiles along transects P03 and P05. Faults are annotated in black, and magmatic intrusions in blue. Yellow line in P05 marks a change from concave up sediment to flat-lying sediment.

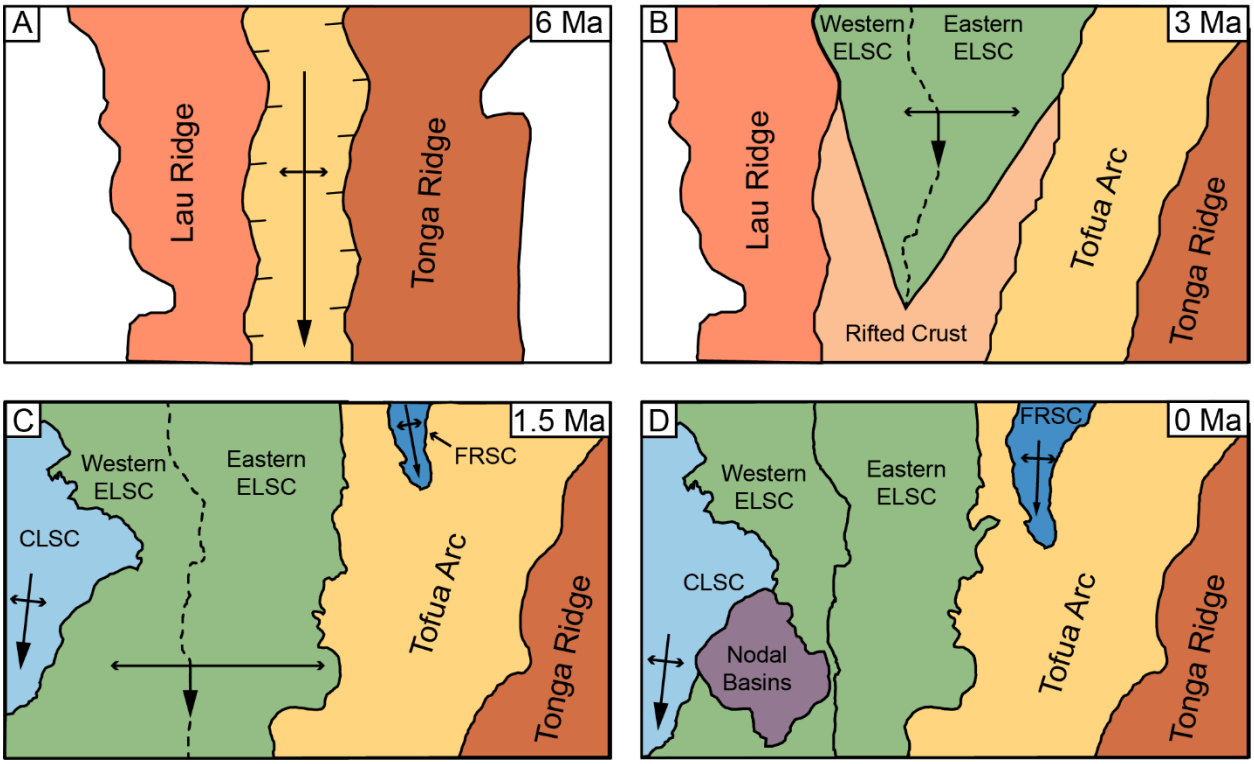

Figure 3.5 Tectonic evolution of the study area in the N.E. Lau Basin in four stages. A) At 6 Ma the Vitiaz Arc rifted, forming the Lau and Tonga Ridges and opening the sub-basins now found under the Tofua Arc. B) At around 3 Ma, the ELSC propagated from the north into the study area. Asymmetric, diachronous spreading resulted in the formation of older, wider sub-basins in the east and narrower, younger sub-basins in the west. During this time, Tofua Arc volcanism began, resuming volcaniclastic sedimentation. C) Around 1 Ma the CLSC and FRSC initiated, propagating southward, and are still actively rifting. D) Sometime between 0.78 Ma and 0.5 Ma, the ELSC and CLSC overlapped, forming the deep nodal basins.

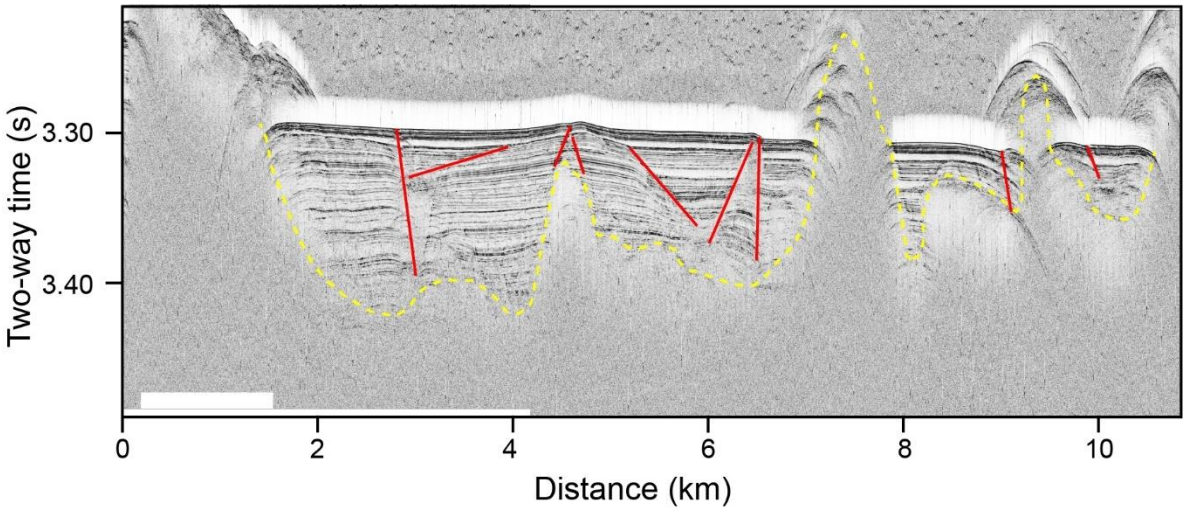

Figure 3.6 Normal faulting (in red) observed in echograms from P06-E. Each fault cross-cuts different sedimentary units, indicating different generations of faulting. Sedimentary basement and volcanic ridges are indicated by the yellow dashed line.

Table 3.1 Summary characteristics of sub-basin groups.

		Width (km)			Sediment thickness (m)			Sediment composition Wt. Avg. (%)		
Sub-basin group	**Sub-basins**	**Min.**	**Max.**	**Avg.**	**Min.**	**Max.**	**Avg.**	**Fine**	**Coarse**	**Undetermined [a]**
CLSC	P05-A, P05-B	1.7	7.9	4.8	0.0	0.0	0.0	0	0	0
West ELSC	P03-A - P03-F, P05-E - P05-H, P06-B - P06-D, P06-1	0.8	2.2	1.6	9.8	96.5	44.4	66	14	20
East ELSC	P03-G - P03-N, P04-A - P04-D, P05-1, P05-I - P05-L, P06-E - P06-I	0.8	34.0	9.7	19.8	448.4	153.2	84	16	0
FRSC	P03-P - P03-T, P04-G - P04-H	0.9	6.7	3.0	28.1	257.6	125.9	59	41	0
Tofua Arc	P03-1, P03-U - P03-W, P04-1 - P04-3, P04-E, P04-F, P04-I, P05-M, P05-N, P06-J, P06-K, P06-2	1.3	45.0	12.0	17.5	1081.0	421.8	72	28	0
Nodal Basins	P05-C, P05-D, P06-A	2.6	8.4	5.9	44.8	238.6	144.7	58	42	0

[a] Echo facies 6A and 6B do not provide sedimentological information, only sediment thickness, so those echo facies are considered "undetermined".

Table 3.2: Minimum and maximum ages of sub-basin initiation and average sedimentation rate of each sub-basin group.

Sub-basin group	Min. Magnetic Chron Age (Ma) [a]	Max. Magnetic Chron Age (Ma) [a]	Average Sediment Thickness (m)	Average Sedimentation Rate (mm/ka) [b]
CLSC	0.01	0.78	0.15	8
Western ELSC	0.78	2.4	44.4	38
Eastern ELSC	0.78	2.6	153.2	128
FRSC	0.34	1.5	125.9	227
Tofua Arc	0.14	6	421.8	1542
Nodal Basins	0.5	0.78	144.7	237

[a] Minimum and maximum ages were determined from magnetic data (Zellmer & Taylor, 2001; Cande and Kent, 1992), assemblage age (Stewart et al., 2022) and basin initiation age (Hawkins et al., 1995).

[b] Average sedimentation rate was calculated by taking the average of the minimum and maximum sedimentation rates, which were calculated using the average sediment thickness from each sub-basin group and the maximum and minimum ages of sub-basin initiation.

References

Anastasakis, G., 2007. The anatomy and provenance of thick volcaniclastic flows in the Cretan Basin, South Aegean Sea. Marine Geology 240, 113–135. https://doi.org/10.1016/j.margeo.2007.02.019

Argus, D.F., Gordon, R.G., DeMets, C., 2011. Geologically current motion of 56 plates relative to the no-net-rotation reference frame. Geochemistry, Geophysics, Geosystems 12. https://doi.org/10.1029/2011GC003751

Artemieva, I.M., 2023. Back-arc basins: A global view from geophysical synthesis and analysis. Earth-Science Reviews 236, 104242. https://doi.org/10.1016/j.earscirev.2022.104242

Athy, L.F., 1930. Density, Porosity and Compaction of Sedimentary Rocks. Bulletin of the American Association of Petroleum Geologists 14, 1–24. AAPG Bulletin (1930) 14 (1): 1–24. https://doi.org/10.1306/3D93289E-16B1-11D7-8645000102C1865D

Baker, E.T., Walker, S.L., Massoth, G.J., Resing, J.A., 2019. The NE Lau Basin: Widespread and Abundant Hydrothermal Venting in the Back-Arc Region Behind a Superfast Subduction Zone. Front. Mar. Sci. 6, 382. https://doi.org/10.3389/fmars.2019.00382

Baxter, A.T., Hannington, M.D., Stewart, M.S., Emberley, J.M., Breker, K., Krätschell, A., Petersen, S., Brandl, P.A., Klischies, M., Mensing, R., Anderson, M.O., 2020. Shallow Seismicity and the Classification of Structures in the Lau Back-Arc Basin. Geochem. Geophys. Geosyst. 21. https://doi.org/10.1029/2020GC008924

Bednarz, U., Schmincke, H.-U., 1994. Composition and origin of volcaniclastic sediments in the Lau Basin (Southwest Pacific), Leg 135 (Sites 834-839), in: Hawkins, J., Parson, L., Allan, J., et al. (Eds.), Proceedings of the Ocean Drilling Program, 135 Scientific Results. Ocean Drilling Program. https://doi.org/10.2973/odp.proc.sr.135.1994

Berktay, H.O., 1965. Possible exploitation of non-linear acoustics in underwater transmitting applications. Journal of Sound and Vibration 2, 435–461. https://doi.org/10.1016/0022-460X(65)90122-7

Bevis, M., Taylor, F.W., Schutz, B.E., Recy, J., Isacks, B.L., Helu, S., Singh, R., Kendrick, E., Stowell, J., Taylor, B., Calmantli, S., 1995. Geodetic observations of very rapid

convergence and back-arc extension at the Tonga arc. Nature 374, 249–251. https://doi.org/10.1038/374249a0

Billen, M.I., Gurnis, M., 2001. A low viscosity wedge in subduction zones. Earth and Planetary Science Letters 193, 227–236. https://doi.org/10.1016/S0012-821X(01)00482-4

Bird, P., 2003. An updated digital model of plate boundaries. Geochemistry, Geophysics, Geosystems 4, 1027. https://doi.org/doi:10.1029/2001GC000252.

Boggs, S., 2013. Principles of sedimentology and stratigraphy, 5th ed. Pearson Education, Limited.

Born, P., 1996. A sedimentary basin analysis of the Abitibi Greenstone belt in the Timmins area, Northern Ontario, Canada. (Doctor of Philosophy). Carleton University, Ottawa, Ontario. https://doi.org/10.22215/etd/1996-03256

Bouma, A., H., 1962. Sedimentology of some Flysch deposits; a graphic approach to facies interpretation. Elsevier, Amsterdam.

Brandl, P.A., Schmid, F., Augustin, N., Grevemeyer, I., Arculus, R.J., Devey, C.W., Petersen, S., Stewart, M., Kopp, H., Hannington, M.D., 2020. The 6–8 Aug 2019 eruption of 'Volcano F' in the Tofua Arc, Tonga. Journal of Volcanology and Geothermal Research 390, 106695. https://doi.org/10.1016/j.jvolgeores.2019.106695

Busby-Spera, C.J., 1988. Evolution of a Middle Jurassic back-arc basin, Cedros Island, Baja California: Evidence from a marine volcaniclastic apron. Geological Society of America Bulletin 100, 218–233. https://doi.org/10.1130/0016-7606(1988)100<0218:EOAMJB>2.3.CO;2

Campbell, M.E., Rowland, J.V., Wright, I.C., Smith, I.E.M., 2007. Oblique rifting along the central and southern Kermadec Arc front (30°–36°S), SW Pacific. Geochemistry, Geophysics, Geosystems 8. https://doi.org/10.1029/2006GC001504

Cattaneo, A., Badhani, S., Caradonna, C., Bellucci, M., Leroux, E., Babonneau, N., Garziglia, S., Poort, J., Akhmanov, G.G., Bayon, G., Dennielou, B., Jouet, G., Migeon, S., Rabineau, M., Droz, L., Clare, M., 2020. The Last Glacial Maximum Balearic Abyssal Plain megabed

revisited. Geological Society, London, Special Publications 500, 341–357. https://doi.org/10.1144/SP500-2019-188

Chapman, R.E. (Ed.), 1983. Chapter 3 Compaction of Sediment and Sedimentary Rocks, and its Consequences, in: Developments in Petroleum Science. Elsevier, pp. 41–65. https://doi.org/10.1016/S0376-7361(08)70087-6

Clift, P.D., Bednarz, U., Boe, R., Rothwell, R.G., Hodkinson, R.A., Ledbetter, J.K., Pratt, C.E., Soakai, S., 1994. Sedimentation on the Tonga Forearc related to arc rifting, subduction erosion and ridge collision: a synthesis of results from sites 840 and 841, in: Hawkins, J., Parson, L., Allan, J., et al. (Eds.), Proceedings of the Ocean Drilling Program, 135 Scientific Results, Proceedings of the Ocean Drilling Program. Ocean Drilling Program. https://doi.org/10.2973/odp.proc.sr.135.1994

Clift, P.D., Dixon, J.E., 1994. Variations in arc volcanism and sedimentation related to rifting of the Lau basin (Southwest Pacific), in: Hawkins, J., Parson, L., Allan, J., et al. (Eds.), 3. Variations in Arc Volcanism and Sedimentation Related to Rifting of the Lau Basin (Southwest Pacific). Ocean Drilling Program. https://doi.org/10.2973/odp.proc.sr.135.1994

Collot, J., Vendé-Leclerc, M., Rouillard, P., Lafoy, Y., Géli, L., 2011. Structural provinces of the Southwest Pacific, first. ed. Geological Survey of New Caledonia, Direction de l'Industrie, des Mines et de l'Energie de Nouvelle Calédonie (DIMENC), L'Institut Français de Recherche pour l'Exploitation de la Mer (IFREMER), Noumea, New Caledonia.

Damuth, J.E., 1980. Use of high-frequency (3.5–12 kHz) echograms in the study of near-bottom sedimentation processes in the deep-sea: A review. Marine Geology 38, 51–75. https://doi.org/10.1016/0025-3227(80)90051-1

Damuth, J.E., 1978. Echo character of the Norwegian—Greenland Sea: Relationship to Quaternary sedimentation. Marine Geology 28, 1–36. https://doi.org/10.1016/0025-3227(78)90094-4

Damuth, J.E., 1975. Echo character of the western equatorial Atlantic floor and its relationship to the dispersal and distribution of terrigenous sediments. Marine Geology 18, 17–45. https://doi.org/10.1016/0025-3227(75)90047-X

Damuth, J.E., 1973. The Western Equatorial Atlantic: Morphology, Quaternary Sediments, and Climatic Cycles (PhD Thesis). Columbia University, New York, N.Y.

Damuth, J.E., Hayes, D.E., 1977. Echo character of the East Brazilian continental margin and its relationship to sedimentary processes. Marine Geology 24, 73–95. https://doi.org/10.1016/0025-3227(77)90002-0

Damuth, J.E., Olson, H.C., 2015. Latest Quaternary sedimentation in the northern Gulf of Mexico Intraslope Basin Province: I. Sediment facies and depositional processes. Geosphere 11, 1689–1718. https://doi.org/10.1130/GES01090.1

Einsele, G., 1992. Basin Classification and Depositional Environments (Overview), in: Einsele, G. (Ed.), Sedimentary Basins: Evolution, Facies, and Sediment Budget. Springer Berlin Heidelberg, Berlin, Heidelberg, pp. 3–16. https://doi.org/10.1007/978-3-642-77055-5_1

Elsasser, W.M., 1971. Sea-floor spreading as thermal convection. J. Geophys. Res. 76, 1101–1112. https://doi.org/10.1029/JB076i005p01101

Embley, R.W., 1975. Studies of Deep-Sea Sedimentation Processes Using High-Frequency Seismic Data (PhD Thesis). Columbia University, New York, N.Y.

Fassbender, M.L., 2023. Volcanism in Modern Back-arc Regimes and Their Implications for Ancient Greenstone Belts (PhD Thesis). University of Ottawa, Ottawa.

Fierens, R., Droz, L., Toucanne, S., Raisson, F., Jouet, G., Babonneau, N., Miramontes, E., Landurain, S., Jorry, S.J., 2019. Late Quaternary geomorphology and sedimentary processes in the Zambezi turbidite system (Mozambique Channel). Geomorphology 334, 1–28. https://doi.org/10.1016/j.geomorph.2019.02.033

Franz, G., 2021. Crustal Structure of the nascent Fonualei Rift and Spreading Center, Lau basin, derived from Magnetotelluric Measurements.

Gaskell, T.F., Hill, M.N., Swallow, J.C., 1958. Seismic Measurements Made by H.M.S Challenger in the Atlantic, Pacific and Indian Oceans and in the Mediterranean Sea, 1950-53. Philosophical Transactions of the Royal Society of London. Series A, Mathematical and Physical Sciences 251, 23–83.

German, C.R., Baker, E.T., Connelly, D.P., Lupton, J.E., Resing, J., Prien, R.D., Walker, S.L., Edmonds, H.N., Langmuir, C.H., 2006. Hydrothermal exploration of the Fonualei Rift and Spreading Center and the Northeast Lau Spreading Center: LAU BASIN HYDROTHERMAL VENTING. Geochem. Geophys. Geosyst. 7, n/a-n/a. https://doi.org/10.1029/2006GC001324

Global Volcanism Program, 1991. Report on Pinatubo (Philippines), in: McClelland, L. (Ed.), Bulletin of the Global Volcanism Network, 16:8. Smithsonian Institution. https://doi.org/10.5479/si.GVP.BGVN199108-273083

Grant, A., Schreiber, R., 1990. Modern Swathe Sounding and Sub-Bottom Profiling Technology for Research Applications: The Atlas Hydrosweep and Parasound Systems 11.

Gray, A., 2022. Geology of the Monowai Rift Zone and Louisville Segment of the Tonga-Kermadec Arc: Regional Controls on Arc Magmatism and Hydrothermal Activity (MSc Thesis). University of Ottawa, Ottawa.

Hannington, M.D., De Ronde, C.E.J., Petersen, S., 2005. Sea-Floor Tectonics and Submarine Hydrothermal Systems, in: One Hundredth Anniversary Volume. Society of Economic Geologists. https://doi.org/10.5382/AV100.06

Hannington, M.D., Kopp, H., Schnabel, M., 2019. RV SONNE Fahrtbericht/ Cruise Report SO267: ARCHIMEDES I: Arc Rifting, Metallogeny and Microplate Evolution – an Integrated Geodynamic, Magmatic and Hydrothermal Study of the Fonualei Rift System, NE Lau Basin. GEOMAR.

Hawkins, J., Parson, L., Allan, J., et al., 1994. Proceedings of the Ocean Drilling Program, 135 Scientific Results. Ocean Drilling Program, College Station, TX.

Hawkins, J.W., 1995. The Geology of the Lau Basin, in: Taylor, B. (Ed.), Backarc Basins: Tectonics and Magmatism. Springer US, Boston, MA, pp. 63–138. https://doi.org/10.1007/978-1-4615-1843-3_3

Henley, R.W., Adams, D.P.M., 1992. Strike-slip fault reactivation as a control on epithermal vein-style gold mineralization. Geology 20, 443–446. https://doi.org/10.1130/0091-7613(1992)020%3C0443:SSFRAA%3E2.3.CO;2

Hollister, C.D., 1967. Sediment Distribution and Deep Circulation in the Western North Atlantic (PhD Thesis). Columbia University, Palisades, N.Y.

Hussong, D.M., Uyeda, S., Blanchet, Bleil, U., Ellis, C.H., Francis, T.J.G., Fryer, P., Horai, K.-I., Kling, S., Meijer, A., Nakamura, K., Natland, J.H., Packham, G.H., Sharaskin, A.Y., 1982. Site 455; east side of the Mariana Trough (No. 60), Initial Reports of the Deep Sea Drilling Project.

Jackson, C.A.-L., Schofield, N., Golenkov, B., 2013. Geometry and controls on the development of igneous sill-related forced folds: A 2-D seismic reflection case study from offshore southern Australia. Geological Society of America Bulletin 125, 1874–1890. https://doi.org/10.1130/B30833.1

Jegen, A., Dannowski, A., Schnabel, M., Barckhausen, U., Brandl, P. A., Riedel, M., et al. (2023). Extension dynamics of the northern Fonualei Rift and Spreading Center and the southern Mangatolu Triple Junction in the Lau Basin at 16°S. Geochemistry, Geophysics, Geosystems, 24, e2022GC010550. https://doi.org/10.1029/2022GC010550

Karig, D.E., 1971. Origin and development of marginal basins in the western Pacific. J. Geophys. Res. 76, 2542–2561. https://doi.org/10.1029/JB076i011p02542

Karig, D.E., Moore, G.F., 1975. Tectonically controlled sedimentation in marginal basins. Earth and Planetary Science Letters 26, 233–238.

Kim, J., Son, S.-K., Son, J.-W., Kim, K.-H., Shim, W.J., Kim, C.H., Lee, K.-Y., 2009. Venting sites along the Fonualei and Northeast Lau Spreading Centers and evidence of hydrothermal activity at an off-axis caldera in the northeastern Lau Basin. Geochem. J. 43, 1–13. https://doi.org/10.2343/geochemj.0.0164

Kimura, G., Tamaki, K., 1986. Collision, rotation, and back-arc spreading in the region of the Okhotsk and Japan Seas. Tectonics 5, 389–401.

Klein, G. de V., Lee, Y.I., 1984. A preliminary assessment of geodynamic controls on depositional systems and sandstone diagenesis in back-arc basins, western Pacific Ocean. Geodynamics of back-arc regions 102, 19–152.

Kneller, E.A., van Keken, P.E., 2008. Effect of three-dimensional slab geometry on deformation in the mantle wedge: Implications for shear wave anisotropy. Geochemistry, Geophysics, Geosystems 9. https://doi.org/10.1029/2007GC001677

Koson, S., Chenrai, P., Choowong, M., 2014. Seismic Attributes and Their Applications in Seismic Geomorphology. Bulletin of Earth Sciences of Thailand 6, 1–9.

Large, R.R., 1992. Australian volcanic-hosted massive sulfide deposits; features, styles, and genetic models. Economic Geology 87, 471–510. https://doi.org/10.2113/gsecongeo.87.3.471

Lee, C., Wada, I., 2017. Clustering of arc volcanoes caused by temperature perturbations in the back-arc mantle. Nature Communications 8, 15753. https://doi.org/10.1038/ncomms15753

Li, S., Suo, Y., Li, X., Liu, B., Dai, L., Wang, G., Zhou, J., Li, Y., Liu, Yiming, Cao, X., Somerville, I., Mu, D., Zhao, S., Liu, J., Meng, F., Zhen, L., Zhao, L., Zhu, J., Yu, S., Liu, Yongjiang, Zhang, G., 2018. Microplate tectonics: new insights from micro-blocks in the global oceans, continental margins and deep mantle. Earth Science Reviews 185, 1029–1064. https://doi.org/10.1016/j.earscirev.2018.09.005

Lupton, J., Rubin, K.H., Arculus, R., Lilley, M., Butterfield, D., Resing, J., Baker, E., Embley, R., 2015. Helium isotope, C/3He, and Ba-Nb-Ti signatures in the northern Lau Basin: Distinguishing arc, back-arc, and hotspot affinities. Geochemistry, Geophysics, Geosystems 16, 1133–1155. https://doi.org/10.1002/2014GC005625

Macdonald, K.C., Fox, P.J., 1983. Overlapping spreading centres: new accretion geometry on the East Pacific Rise. Nature 302, 55–58. https://doi.org/10.1038/302055a0

Martinez, F., Okino, K., Ohara, Y., Reysenback, A.-L., Goffredi, S.K., 2007. Back-Arc Basins. Oceanography 20, 116–127. https://doi.org/10.5670/oceanog.2007.85

McKee, E.D., Weir, G.W., 1953. Terminology for Stratification and Cross-Stratification in Sedimentary Rocks. Bulletin of the Geological Society of America 64, 381–390.

Mensing, R., 2020. The tectonic and volcanic evolution of the Mangatolu Triple Junction (MSc Thesis). Geodynamics Research Group Martin Luther University Halle-Wittenberg. https://doi.org/10.5194/egusphere-egu2020-19897

Moberly, R., 1972. Origin of Lithosphere behind Island Arcs, with Reference to the Western Pacific, in: Shagam, R., Hargraves, R.B., Morgan, W.J., Van Houten, F.B., Burk, C.A., Holland, H.D., Hollister, L.C. (Eds.), Studies in Earth and Space Sciences. Geological Society of America. https://doi.org/10.1130/MEM132-p35

Molnar, P., Atwater, T., 1978. Interarc spreading and Cordilleran tectonics as alternates related to the age of subducted oceanic lithosphere. Earth and Planetary Science Letters 41, 330–340. https://doi.org/10.1016/0012-821X(78)90187-5

Mueller, W., Donaldson, J.A., 1992. Development of sedimentary basins in the Archean Abitibi belt, Canada: an overview. Can. J. Earth Sci. 29, 2249–2265. https://doi.org/10.1139/e92-177

Murauchi, S., Den, N., Asano, S., Hotta, H., Yoshii, T., Asanuma, T., Hagiwara, K., Ichikawa, K., Sato, T., Ludwig, W.J., Ewing, J.I., Edgar, N.T., Houtz, R.E., 1968. Crustal structure of the Philippine Sea. Journal of Geophysical Research (1896-1977) 73, 3143–3171. https://doi.org/10.1029/JB073i010p03143

Murphy, M.A., Salvador, A., 1999. International Stratigraphic Guide - An abridged edition. Episodes 22, 255–271. https://doi.org/10.18814/epiiugs/1999/v22i4/002

O'Connell, R.J., Gable, C.W., Hager, B.H., 1991. Toroidal-Poloidal Partitioning of Lithospheric Plate Motions, in: Sabadini, R., Lambeck, K., Boschi, E. (Eds.), Glacial Isostasy, Sea-Level and Mantle Rheology. Springer Netherlands, Dordrecht, pp. 535–551. https://doi.org/10.1007/978-94-011-3374-6_25

Okino, K., Kasuga, S., Ohara, Y., 1998. A New Scenario of the Parece Vela Basin Genesis. Marine Geophysical Researches 20, 21–40. https://doi.org/10.1023/A:1004377422118

Okino, K., Ohara, Y., Kasuga, S., Kato, Y., 1999. The Philippine Sea: New survey results reveal the structure and the history of the marginal basins. Geophysical Research Letters 26, 2287–2290. https://doi.org/10.1029/1999GL900537

Otofuji, Y.-I., 1996. Large tectonic movement of the Japan Arc in late Cenozoic times inferred from paleomagnetism: Review and synthesis. Island Arc 5, 229–249. https://doi.org/10.1111/j.1440-1738.1996.tb00029.x

Parson, L., Hawkins, J., Allan, J., et al., 1992a. Introduction, Background and Principle Results of Leg 135, Lau Basin, in: Parson, L., Hawkins, J., Allan, J. (Eds.), Proceedings of the Ocean Drilling Program, Initial Reports.

Parson, L., Hawkins, J., Allan, J., et al., 1992b. Proceedings of the Ocean Drilling Program, 135 Initial Reports. Ocean Drilling Program, College Station, TX.

Parson, L., Hawkins, J.W., 1994. Two-Stage Ridge Propagation and the Geological History of the Lau Backarc Basin, in: Proceedings of the Ocean Drilling Program, 135 Scientific Results. Ocean Drilling Program. https://doi.org/10.2973/odp.proc.sr.135.1994

Parson, L.M., Rothwell, R.G., MacLeod, C.J., 1994. Tectonics and sedimentation in the Lau Basin (Southwest Pacific), in: Hawkins, J., Parson, L., Allan, J., et al. (Eds.), Proceedings of the Ocean Drilling Program, 135 Scientific Results. Ocean Drilling Program. https://doi.org/10.2973/odp.proc.sr.135.1994

Pearce, J.A., Lippard, S.J., Roberts, S., 1984. Characteristics and tectonic significance of supra-subduction zone ophiolites, in: Geology of Marginal Basins. Geol. Soc. London. Spec. Publ., pp. 77–94.

Pelletier, B., Lagabrielle, Y., Benoit, M., Cabioch, G., Calmant, S., Garel, E., Guivel, C., 2001. Newly identified segments of the Pacific–Australia plate boundary along the North Fiji transform zone. Earth and Planetary Science Letters 193, 347–358. https://doi.org/10.1016/S0012-821X(01)00522-2

Reineck, H.-E., Singh, I.B., 1980. Depositional Sedimentary Environments. Springer-Verlag, New York.

Resing, J.A., Embley, R.W., Ratmeyer, V., Merle, S., 2012. Submarine Ring of Fire-2012 (SRoF-12) Northeast Lau Basin: R/V Roger Revelle Expedition RR1211 (Cruise Report).

Ricard, Y., Doglioni, C., Sabadini, R., 1991. Differential rotation between lithosphere and mantle: A consequence of lateral mantle viscosity variations. Journal of Geophysical Research: Solid Earth 96, 8407–8415. https://doi.org/10.1029/91JB00204

Rothwell, R.G., Bednarz, U., Boe, R., Clift, P.D., Hodkinson, R.A., Ledbetter, J.K., Pratt, C.E., Soakai, S., 1994a. Sedimentation and sedimentary processes in the Lau backarc basin:

Results from Leg 135, in: Proceedings of the Ocean Drilling Program, 135 Scientific Results. Ocean Drilling Program. https://doi.org/10.2973/odp.proc.sr.135.1994

Rothwell, R. G., Weaver, P.P.E., Hodkinson, R.A., Pratt, C.E., Styzen, M.J., Higgs, N.C., 1994b. Clayey nannofossil ooze turbidites and hemipelagites at sites 834 and 835 (Lau Basin, southwest Pacific), in: Proceedings of the Ocean Drilling Program, 135 Scientific Results. Ocean Drilling Program. https://doi.org/10.2973/odp.proc.sr.135.1994

Salvador, A., 1994. International Stratigraphic Guide: A Guide to Stratigraphic Classification, Terminology, and Procedure, second. ed. International Subcommission on Stratigraphic Classification of International Union of Geological Services, International Commission on Stratigraphy, Trondheim, Norway.

Schmid, F., Kopp, H., Schnabel, M., Dannowski, A., Heyde, I., Riedel, M., Hannington, M.D., Engels, M., Beniest, A., Klaucke, I., Augustin, N., Brandl, P.A., Devey, C., 2020. Crustal Structure of the Niuafo'ou Microplate and Fonualei Rift and Spreading Center in the Northeastern Lau Basin, Southwestern Pacific. J. Geophys. Res. Solid Earth 125. https://doi.org/10.1029/2019JB019184

Schmid, F., Cremanns, M., Augustin, N., Lange, D., Petersen, F., Kopp, H., 2021. Microseismicity and Lava Flows Hint at Magmato-Tectonic Processes Near the Southern Tip of the Fonualei Rift and Spreading Center in the Lau Basin. J Geophys Res Solid Earth 126. https://doi.org/10.1029/2020JB021340

Scholz, C.H., Campos, J., 1995. On the mechanism of seismic decoupling and back arc spreading at subduction zones. J. Geophys. Res. 100, 22103–22115. https://doi.org/10.1029/95JB01869

Shemenda, A.I., 1993. Subduction of the lithosphere and back arc dynamics: Insights from physical modeling. Journal of Geophysical Research: Solid Earth 98, 16167–16185.

Shor, G.G., 1964. Structure of the Berings Sea and the Aleutian Ridge. Marine Geology 1, 213–219. https://doi.org/10.1016/0025-3227(64)90059-3

Sleep, N., Toksöz, M.N., 1971. Evolution of Marginal Basins. Nature 233, 548–550. https://doi.org/10.1038/233548a0

Sleeper, J.D., Martinez, F., 2016. Geology and kinematics of the Niuafo'ou microplate in the northern Lau Basin: NEW LAU BASIN KINEMATIC MODEL. J. Geophys. Res. Solid Earth 121, 4852–4875. https://doi.org/10.1002/2016JB013051

Sleeper, J.D., Martinez, F., Arculus, R., 2016. The Fonualei Rift and Spreading Center: Effects of ultraslow spreading and arc proximity on back-arc crustal accretion: Ultraslow Back-Arc Spreading Center. J. Geophys. Res. Solid Earth 121, 4814–4835. https://doi.org/10.1002/2016JB013050

Stewart, M.S., Hannington, M.D., Emberley, J., Baxter, A.T., Krätschell, A., Petersen, S., Brandl, P.A., Anderson, M.O., Mercier-Langevin, P., Mensing, R., Breker, K., Fassbender, M.L., 2022. A new geological map of the Lau Basin (southwestern Pacific Ocean) reveals crustal growth processes in arc-backarc systems. Geosphere 17, 34. https://doi.org/10.1130/GES02340.1

Taylor, B., Zellmer, K., Martinez, F., Goodliffe, A., 1996. Sea-floor spreading in the Lau back-arc basin. Earth and Planetary Science Letters 144, 35–40. https://doi.org/10.1016/0012-821X(96)00148-3

Uyeda, S., Kanamori, H., 1979. Back-arc opening and the mode of subduction. Journal of Geophysical Research: Solid Earth 84, 1049–1061. https://doi.org/10.1029/JB084iB03p01049

Venzke, E., 2022. Global Volcanism Program: Hunga Tonga-Hunga Ha'apai.

von Stackelberg, 1985. Geoscientific investigations with F.S. SONNE (SO-35-2/3): Back arc hydrothermalism of the Lau Basin and North Fiji Basin (Southwest Pacific). Federal Institute for Geosciences and Natural Resources Hanover.

Westervelt, P.J., 1963. Parametric Acoustic Array. The Journal of the Acoustical Society of America 35, 535–537. https://doi.org/10.1121/1.1918525

Wickham, D., 2009. Calculating the Volume of the May 18, 1980 Eruption of Mount St. Helens. Portland State University. https://doi.org/10.15760/mem.29

Wirth, E.A., Korenaga, J., 2012. Small-scale convection in the subduction zone mantle wedge. Earth and Planetary Science Letters 357–358, 111–118. https://doi.org/10.1016/j.epsl.2012.09.010

Zellmer, K.E., Taylor, B., 2001. A three-plate kinematic model for Lau Basin opening. Geochemistry, Geophysics, Geosystems 2. https://doi.org/10.1029/2000GC000106

APPENDIX A – Volume Calculation Methodology

Once the sub-basin was selected for the volume calculation, the manual horizon picking tool in Kingdom was used to digitize the contact between the seafloor sediment and seawater, and the contact between the sediment and underlying basement. We picked these horizons in each of the seismic reflection and Parasound sections available in the sub-basin (Figure 2.22). These horizons were used as the upper and lower limits of the sedimentary infill, from which the total sediment volume between them was calculated.

The horizons were first converted from two-way time (s) to depth (m), using the Dynamic Depth Conversion (DDC) feature in Kingdom. This tool converts data points from time to depth using assigned sound velocities for each horizon. The sound velocity for the seawater-seafloor sediment contact was 1500 m/s, and 1520 m/s for the sediment-basement contact. The calculation interpolated the horizon data points and produced a depth grid of the seafloor and a depth grid of the sediment-basement interface, both gridded at 80 m.

After the dynamic depth conversion was completed, new depth grids were created using the Create Grid feature in Kingdom. The input data were the grids created by the DDC, and the new grids were gridded at 30 m and limited to the extent of sub-basin P05-D. The grids were created using the Flex Grid algorithm. Once the two grids were created, we then moved on to the volume calculation.

The volumetrics tool in Kingdom calculates the gross volume between the seawater-seafloor sediment grid and the sediment-basement contact grid and limits the calculation to the extent of the sub-basin polygon. The following equation is used to calculate the volume of each grid cell, where Z value is the depth value from the grid:

$$Gross\ Volume = Area\ \times\ Z\ value$$

The volume calculation delivered a gross volume of the selected area in cubic metres. For visualization of the model, the seawater-seafloor sediment contact and the sediment-basement contact are displayed in VuPak.

APPENDIX B – Sub-Basin Fill Descriptions

P03-A

P03-A is 2 km wide and contains at least 57 m of sediment (Figure C.1), although the sediment-basement contact is not visible in Parasound or seismic reflection data. There is only one sedimentary unit identified (P03-A-i) which consists of overlapping hyperbolae with sub-bottom reflections (echo facies 6A) due to rugged terrain.

P03-B

P03-B is 1.4 km wide and contains 20.5 m of sediment (Figure C.2). Two sedimentary units are visible in this section. The top unit (P03-B-i) is 9.9 m thick and consists of strong, thin, continuous reflections (echo facies 1). The underlying unit (P03-B-ii) is 10.6 m thick, consisting of acoustically transparent echoes with frequent interbeds of strong, thin reflections (echo facies 3B). The echoes are slightly hyperbolic in this sub-basin due to the rugged seafloor topography.

P03-C

P03-C is 1.3 km wide and contains at least 31.9 m of sediment (Figure C.3), although the sediment-basement contact is not visible in the Parasound or seismic reflection data. The one visible sedimentary unit (P03-C-i) consists of hyperbolic echoes with sub-bottom reflections (echo facies 6A).

P03-D

P03-D is 0.8 km wide and contains 18.2 m of sediment (Figure C.4). This comprises only one sedimentary unit (P03-D-i) which consists of acoustically transparent echoes with occasional interbeds of strong, thin reflections (echo facies 3A). The echoes are hyperbolic due to rugged seafloor topography, and a fault in the centre of the sub-basin offsets the seafloor and the reflections.

P03-E

P03-E is 1.5 km wide and contains at least 18.2 m of sediment (Figure C.5). The sediment-basement contact is not visible in this sub-basin, due to the hyperbolic nature of the Parasound

data. There is one sedimentary unit in this sub-basin (P03-E-i) which consists of hyperbolic echoes with sub-bottom reflections (echo facies 6A).

P03-F

P03-F is 1.7 km wide and contains 9.9 m of sediment (Figure C.6). One sedimentary unit is present (P03-F-i) and consists of hyperbolic echoes with sub-bottom reflections (echo facies 6A).

P03-G

P03-G is 1.0 km wide with 23.6 m of sediment (Figure C.7). The sediment comprises only one sedimentary unit, which is a prolonged echo with an incoherent internal structure (echo facies 5).

P03-H

P03-H is 1.2 km wide and contains 95.8 m of sediment (Figure C.8). Three sedimentary units are present in this sub-basin. The top unit (P03-H-i) is 30.4 m thick and consists of strong, thin, continuous reflections (echo facies 1). The underlying unit (P03-H-ii) is 16.7 m thick and is an acoustically transparent echo (echo facies 2). Within P03-H-ii, some faint, thin reflections are visible. The bottom unit (P03-H-iii) is 48.6 m thick, consisting of strong, thin, continuous reflections (echo facies 1). Units are flat-lying and there are no faults.

P03-I

P03-I is 12.0 km wide with a sedimentary infill that measures 104.9 m thick, which is divided into 5 sedimentary units (Figure C.9). The top unit (P03-I-i) is 16.0 m thick, consisting of strong, thin, continuous reflections (echo facies 1). Next is P03-I-ii, which is 16.0 m thick and is made up of acoustically transparent echoes with frequent interbeds of strong, thin reflections (echo facies 3B). The next unit (P03-I-iii) is 9.1 m thick and is an acoustically transparent echo (echo facies 2). Sedimentary unit P03-I-iv is 21.3 m thick, comprising acoustically transparent echoes with occasional interbeds of strong, thin reflections (echo facies 3B). The bottom unit visible in Parasound (P03-I-v) is 42.6 m thick and consists of acoustically transparent echoes with occasional interbeds of strong, thin reflections (echo facies 3A). The sediment-basement contact is undulatory and the overlying sedimentary units infill the topography. The bottom three units (P03-I-iii, P03-I-iv and P03-I-v) are not continuous along the entire sub-basin due to the varying basement topography. In both the east and west of the sub-basin there are normal faults cross

cutting all five sedimentary units which result in the offset of the seafloor. Additionally, prolonged echoes (echo facies 5) in the western end of the sub-basin suggest the presence of MTDs.

P03-J

P03-J is a 3.4 km wide sub-basin containing 50.9 m of sediment (Figure C.10). It contains only one sedimentary unit (P03-J-i) which consists of acoustically transparent echoes with frequent interbeds of strong, thin reflections (echo facies 3B). There are some hyperbolic echoes in the Parasound profile due to uneven seafloor topography, and the reflections are not all continuous across the sub-basin. Additionally, within the unit there are sub-vertical patches of acoustically transparent echoes that crosscut the entire unit, which may be related to faulting.

P03-K

P03-K is 0.8 km wide and contains at least 19.8 m of sediment since the sediment-basement contact is not visible in Parasound or in the seismic reflection data (Figure C.11). Only one sedimentary unit is visible (P03-K-i), and it consists of acoustically transparent echoes with occasional interbeds of strong thin reflections (echo facies 3A). The sediment dips slightly to the east.

P03-L

P03-L is 6.2 km wide and contains a 28.8 m thick succession of sediment (Figure C.12). We identified two sedimentary units in this sub-basin. The top unit (P03-L-i) is 6.8 m thick, comprising strong, thin, continuous reflections (echo facies 1). The underlying unit (P03-L-ii) is 22.0 m thick and consists of a prolonged echo with an incoherent internal structure (echo facies 5). Some reflections are present in this unit but are laterally discontinuous and chaotic. The contact between P03-L-i and P03-L-ii is inclined toward the west, and reflections in P03-L-i are flat lying, resulting in an angular unconformity between the two units.

P03-M

P03-M is 1.9 km wide and contains 37.2 m of sedimentary infill (Figure C.13). It is a single sedimentary unit (P03-M-i) which consists of strong, thin, continuous reflections (echo facies 1). The seafloor and consequently, the sub-bottom reflections, are offset in the centre of the sub-

basin by approximately 23 m, with uplift in the eastern portion. Additionally, several small faults offset the sub-bottom reflections in other regions of the sub-basin.

P03-N

P03-N is a 25.8 km wide sub-basin that contains a 319.2 m thick sedimentary succession (Figure C.14). Parasound images the top 133.0 m of sediment, which is sub-divided into six sedimentary units. The top unit (P03-N-i) is 15.2 m thick and consists of strong, thin, continuous reflections (echo facies 1). The underlying unit (P03-N-ii) is 17.5 m thick and consists of acoustically transparent echoes with frequent interbeds of strong, thin reflections (echo facies 3B). Next is unit P03-N-iii, which is 12.9 m thick and comprises strong, thin, continuous reflections (echo facies 1). P03-N-iv is 7.6 m thick and also consists of strong, thin, continuous reflections (echo facies 1), but the reflections are thicker and higher amplitude than in P03-N-iii. The next unit (P03-N-v) is 15.2 m thick and is an acoustically transparent echo (echo facies 2). The deepest unit visible in Parasound (P03-N-vi) is 64.6 m thick and consists of acoustically transparent echoes with frequent interbeds of strong, thin reflections (echo facies 3B). The contact between P03-N-v and P03-N-vi is an unconformity, identified by numerous normal faults that are present only in P03-N-vi. The deformation in this unit results in an undulatory surface upon which the overlying units draped and infilled the topography. This results in units P03-N-ii, P03-N-iii, P03-N-iv and P03-N-v thin toward the margins of the sub-basin, in some cases pinching out entirely. Several normal faults that crosscut the other sedimentary units are present as well. In the west of the sub-basin there are two clouds of strong reflections with a stippled texture (echo facies 8), beneath which the acoustic signal fades out. These two anomalies are within P03-N-vi and are located beneath or at the intersection of two faults.

P03-1

P03-1 is 1.3 km wide and contains 111.7 m of sediment (Figure C.15). The top 60.8 m of sediment are imaged by Parasound and are sub-divided into two sedimentary units. These units are deposited along a slope that is inclined toward the west. The top unit (P03-1-i) is 15.2 m thick and consists of strong, thin, continuous reflections (echo facies 1). It pinches out to the west, downslope. The underlying unit (P03-1-ii) is 45.6 m thick and consists of acoustically transparent echoes with frequent interbeds of strong, thin reflections (echo facies 3B).

P03-P

P03-P is 1.0 km wide and contains 185.4 m of sediment (Figure C.16). Only the top 21.3 m of sediment are imaged by Parasound and are a single sedimentary unit (P03-P-i). P03-P-i is a prolonged echo with an incoherent internal structure (echo facies 5).

P03-Q

P03-Q is 1.8 km wide and contains 127.7 m of sediment (Figure C.17). The top 89.7 m of sediment are imaged by Parasound and are divided into two sedimentary units. The top unit (P03-Q-i) is a prolonged echo with an incoherent internal structure (echo facies 5) in the east of the sub-basin, but consists of strong, thin, continuous reflections (echo facies 1) in the west of the sub-basin. The lower unit (P03-Q-ii) is 69.9 m thick and consists of acoustically transparent echoes with occasional interbeds of strong, thin reflections (echo facies 3A). Both units dip slightly to the west.

P03-R

P03-R is 0.9 km wide and contains 88.9 m of sediment (Figure C.18). The entire succession is one sedimentary unit (P03-R-i) which consists of acoustically transparent echoes with an incoherent internal structure (echo facies 5).

P03-S

P03-S is 2.9 km wide with 108.7 m of sediment, which is divided into two sedimentary units (Figure C.19). The top unit (P03-S-i) is 32.7 m thick and consists of acoustically transparent echoes with occasional interbeds of strong, thin reflections (echo facies 3A). The sub-bottom reflections in this unit are slightly undulatory. The lower unit (P03-S-ii) is 76.0 m thick, consisting of a prolonged echo with an incoherent internal structure (echo facies 5).

P03-T

P03-T is 2.5 km wide, containing 85.1 m of sediment (Figure C.20). The top 58.5 m of sediment are imaged by Parasound and comprise one sedimentary unit (P03-T-i). In the eastern end of the sub-basin, the sediment is characterised by a prolonged echo with an incoherent internal structure (echo facies 5), while in the western end of the sub-basin the sediment is characterised by acoustically transparent echoes with frequent interbeds of strong, thin reflections (echo facies

3B). The sedimentary units and seafloor are sloped toward the east. The transition from echo facies 3B upslope to echo facies 5 downslope occurs through the lateral disappearance of sub-bottom reflections.

P03-U

P03-U is 3.0 km wide and contains 345.0 m of sediment, of which the top 31.9 m are imaged by Parasound (Figure C.21). There are two sedimentary units, and the top unit (P03-U-i) is 10.6 m thick, comprising strong, thin, continuous reflections (echo facies 1). The underlying unit (P03-U-ii) is 21.9 m thick and consists of acoustically transparent echoes with occasional interbeds of strong thin reflections (echo facies 3A).

P03-V

P03-V is 20.0 km wide and contains 954.6 m of sediment (Figure C.22). The top 36.9 m of sediment are visible in Parasound, and this portion has been divided into two sedimentary units. The top unit (P03-V-i) is 6.8 m thick and consists of a prolonged echo with an incoherent internal structure (echo facies 5). The underlying unit (P03-V-ii) is 30.1 m thick and is an acoustically transparent echo (echo facies 2). This sub-basin is to the west of the Tofua Arc and contains a thick succession of sediment that is bound at depth by a tilted basement block to the west and the arc to the east. Over time the sediment has infilled the bounding structures and the uppermost sediment belongs to the sediment drape over the Tofua Arc.

P03-W

P03-W is 45.0 km wide and contains a sedimentary infill that is 483.4 m thick (Figure C.23). The upper 48.6 m of sediment are imaged by Parasound and are divided into two sedimentary units. The top unit (echo facies 1) is 2.3 m thick and consists of strong, thin, continuous reflections (echo facies 1). The next unit (P03-W-ii) is 46.3 m thick and consists of acoustically transparent echoes with frequent interbeds of strong, thin reflections (echo facies 3B). Similar to P03-V, the sedimentary succession is very thick in P03-W, and the upper sedimentary units are a part of the sediment drape over the Tofua Arc. In this case, however, the western boundary is the arc, and the eastern boundary is a tilted block that has not been buried by sediment. Additionally, the basement underlying this sub-basin is very blocky, faulted and tilted.

P04-A

P04-A is an elongate, trough-like sub-basin located to the west of the seismic transect where only Parasound data are available (Figure C.24). The sub-basin is 3.2 km wide and contains at least 117.0 m of sediment, although the sediment-basement contact is not visible. The sedimentary infill is divided into four sedimentary units. The top unit (P04-A-i) is 10.6 m thick and consists of strong, thin, continuous reflections (echo facies 1). The next unit (P04-A-ii) is 35.0 m thick and is comprised of acoustically transparent echoes with occasional interbeds of strong, thin reflections (echo facies 3A). The underlying unit (P04-A-iii) is 26.6 m thick, comprising acoustically transparent echoes with frequent interbeds of strong, thin reflections (echo facies 3B). The lowest unit (P04-A-iv) is 44.8 m thick and consists of acoustically transparent echoes with frequent interbeds of strong, thin reflections (echo facies 3B). It is slightly inclined to the west and contains some small faults, resulting in an angular unconformity between P04-A-iii and P04-A-iv.

P04-B

P04-B is located to the west of the seismic transect where only Parasound data are available (Figure C.25). It is 6.4 km wide and contains 95 m of sediment which are sub-divided into three sedimentary units. The top unit (P04-B-i) is 11.4 m thick and is composed of strong, thin, continuous reflections (echo facies 1). The next unit (P04-B-ii) is 33.4 m thick and is composed of acoustically transparent echoes with occasional interbeds of strong, thin reflections (echo facies 3A). The bottom unit (P04-B-iii) is 50.2 m thick, consisting of acoustically transparent echoes with frequent interbeds of strong, thin reflections (echo facies 3B). The contact between P04-B-ii and P04-B-iii is undulatory, due to faulting and folding in P04-B-iii.

P04-C

P04-C is 24.0 km wide with 221.9 m of sediment (Figure C.26). The top 103.4 m are visible in Parasound, and this portion is divided into four sub-units. The top unit (P04-C-i) is 14.4 m thick and consists of strong, thin continuous reflections (echo facies 1). The next unit (P04-C-ii) is 40.3 m thick, composed of acoustically transparent echoes with occasional interbeds of strong, thin reflections (echo facies 3A). The lowest unit before the acoustic signal fades (P04-C-iii) is 48.6 m thick and is made up of acoustically transparent echoes with frequent interbeds of strong,

thin reflections (echo facies 3B). P04-C-iii is an undulatory unit, with some uplift and faulting in the centre of the sub-basin. P04-C-ii drapes undeformed over P04-C-iii, creating an angular unconformity between the two units. Additionally, the depth at which the acoustic signal fades is inconsistent.

P04-D

P04-D is 34.0 km wide and contains 448.4 m of sediment, although only the top 31.2 m are imaged by Parasound (Figure C.27). Three units make up the sedimentary succession. The top unit (P04-D-i) is 7.6 m thick and comprises strong, thin, continuous reflections (echo facies 1). The next unit (P04-D-ii) is 10.6 m thick, consisting of undulatory, acoustically transparent echoes with frequent interbeds of strong, thin reflections (echo facies 3C). In this unit the undulations appear to be sediment waves. In at least two locations, between P04-D-i and P04-D-ii, there are acoustically transparent lenticular units (echo facies 7) that measure 600 m and 700 m wide, with 1.9 m and 3.0 m of sediment respectively. They correspond to an area with several sinuous channels on the western flank of the FRSC. The deepest visible unit (P04-D-iii) is 12.9 m thick and consists of acoustically transparent echoes with occasional interbeds of strong, thin reflections (echo facies 3B). The seafloor and all of the contacts between the units are undulatory and irregular, due to post-depositional folding, deposition on an undulatory seafloor or the deposition of undulatory bedforms.

P04-1

P04-1 is the first slope deposit along this seismic transect and is 4.7 km wide (Figure C.28). The sediment basement contact is not visible in the Parasound or the seismic reflection data, but the top 40.3 m of sediment are imaged by Parasound. It is located in a graben extending from the western flank of the FRSC. There is only one unit (P04-1-i), and it consists of strong, thin, continuous reflections (echo facies 1). The terrain is undulatory, resulting in some hyperbolic echoes.

P04-E

P04-E is 3.4 m wide and contains 47.1 m of sediment which are divided into two sedimentary units (Figure C.29). The top unit (P04-E-i) is 4.6 m thick and consists of strong, thin, continuous reflections (echo facies 1). The lower unit is 42.6 m thick and consists of acoustically transparent

echoes with occasional interbeds of strong, thin reflections (echo facies 3A). Both units dip to the west, and are slightly deformed, crosscut by several small faults.

P04-F

P04-F is 3.2 km wide and contains 17.5 m of sediment which is divided into two sedimentary units (Figure C.30). The top unit (P04-F-i) is 3.0 m thick and consists of strong, thin reflections (echo facies 1). The lower unit (P04-F-ii) is 14.5 m thick and comprises a prolonged echo with an incoherent internal structure (echo facies 5). The seafloor is rugged and irregular in this sub-basin, resulting in a slightly hyperbolic echo.

P04-G

P04-G is 6.7 km wide and contains 257.6 m of sediment, of which the top 44.8 m are imaged by Parasound (Figure C.31). This top sedimentary succession is divided into two sedimentary units. The top unit (P04-G-i) is 15.2 m thick and consists of strong, thin, continuous reflections (echo facies 1). The next unit (P04-G-ii) is 29.6 m thick and is a prolonged echo with an incoherent internal structure (echo facies 5). P04-G-ii is deformed, sloping toward the east with an irregular topography. The presence of truncated reflections in this unit suggests that the deformation occurred after deposition. P04-G-i is flat-lying, infilling the topography of P04-G-ii.

P04-H

P04-H is 4.9 km wide and contains at least 28.2 m of sediment, although the sediment-basement contact is not visible in the Parasound or seismic reflection data (Figure C.32). There is only one sedimentary unit (P04-H-i), and it is a prolonged echo with an incoherent internal structure (echo facies 5). The hyperbolic echoes make additional details difficult to identify.

P04-2

P04-2 is 5.7 wide and contains 117.8 m of sediment, of which the top 28.9 m are imaged by Parasound (Figure C.33). The sediment visible in Parasound is a single sedimentary unit (P04-2-i) and is a prolonged echo with an incoherent internal structure (echo facies 5). The seafloor domes in the centre of the deposit, and sediment is thicker to the west of the dome than to the east.

P04-3

P04-3 is 4.1 km wide and contains 136.8 m of sediment (Figure C.34). The top 35.0 m of sediment are imaged by Parasound and consist of a single sedimentary unit (P04-3-i). P04-3-i is a prolonged echo with an incoherent internal structure (echo facies 5). The seafloor is irregularly undulatory along this slope deposit.

P04-I

P04-I is 14.2 km wide and contains at least 31.9 m of sediment (Figure C.35). There are no seismic reflection data for this sub-basin, and the sediment-basement contact is not visible in the Parasound data. Two sedimentary units are visible in the Parasound. The top unit (P04-I-i) is 7.6 m thick and consists of strong, thin, continuous reflections (echo facies 1). The next unit (P04-I-ii) is 24.3 m thick and is a prolonged echo with an incoherent internal structure (echo facies 5). This sub-basin slopes slightly toward the east, and the echo facies change downslope, along strike. In the west, the two units are well defined, but becomes hyperbolic toward the east. In the easternmost end of the sub-basin, the echo facies return to flat-lying reflections, and the two units are well defined again.

P05-A

P05-A lies just to the west of the seismic transect, so the only acoustic dataset available for this sub-basin is Parasound (Figure C.36). P05-A is 7.9 km wide, and the echo-character is hyperbolic, with no indication of any significant sediment cover, and in the bathymetry, we see a hummocky flow texture. Although there is sediment in this sub-basin, it is clearly a depression in the seafloor with accommodation space, qualifying it as a sub-basin.

P05-B

P05-B is much narrower, measuring 1.7 km wide (Figure C.37). In this sub-basin there is also no significant sediment cover, and the seafloor has a hummocky flow texture. Similar to P05-A, this is considered a sub-basin despite its lack of sediment since it fits the sub-basin definition.

P05-C

P05-C is located in a region comprised of deep, round, nodal sub-basins (Figure C.38). It is 2.6 km wide with 44.8 m of sediment, which can be divided into two sedimentary units. The upper unit (P05-C-i) is 6.8 m thick and comprises strong, thin, continuous reflections (echo facies 1).

The lower unit (P05-C-ii) is 38 m thick, and is mostly acoustically transparent, with two strong, thin reflection interbeds (echo facies 3A).

P05-D

P05-D is in the same region of nodal basins as sub-basin C. It is 8.4 km wide and has a thick sedimentary succession of up to 238.6 m, but only the top 162.6 m are visible in Parasound (Figure C.39). The basin fill can be divided into five sedimentary units. The uppermost unit (P05-D-i) consists of strong, thin, continuous reflections (echo facies 1) and is 3.8 m thick. Unit P05-D-ii is a repeating sequence of acoustically transparent basal echoes overlain by strong, thin reflections (echo facies 4) and measures 66.2 m thick. The acoustically transparent sub-units grade from a lighter to a darker grey up stratigraphy. The middle unit (P05-D-iii) is 26.6 m thick and consists of acoustically transparent echoes with frequent interbeds of strong, thin reflections (echo facies 3B). Unit P05-D-iv is an acoustically transparent echo (echo facies 2) that is 14.4 m thick. The lowest unit visible in the Parasound, P05-D-v, is 51.7 m thick and is acoustically transparent with occasional interbeds of strong, thin reflections (echo facies 3A).

P05-E

P05-E is 1.8 km wide with 53.2 m of sediment infill (Figure C.40). The surrounding terrain is rugged which creates hyperbolic echoes in the Parasound, making it more difficult to identify the echo facies. There is one sedimentary unit visible (P05-E-i), which comprises acoustically transparent echoes with occasional interbeds of strong, thin reflections (echo facies 3A).

P05-F

P05-F is 1.5 km wide, with a minimum thickness of 50.1 m (Figure C.41). The sediment-basement contact is not visible in either the Parasound or seismic reflection data. The sediment is split into two units. The top unit, P05-F-i, is 6.8 m thick, and is comprised of 3-5 strong, thin, continuous reflections (echo facies 1). The lower unit, P05-F-ii, is 43.3 m thick and consists of acoustically transparent echoes with occasional interbeds of strong, thin reflections (echo facies 3A).

P05-G

P05-G is 1.3 km wide, with 58.5 m of sediment, divided into 4 sedimentary units (Figure C.42). The top unit (P05-G-i) is 6.1 m thick, comprising strong, thin, continuous reflections (echo facies 1). The unit below (P05-G-ii) is 15.2 m thick, consisting of acoustically transparent echoes with frequent interbeds of strong, thin reflections (echo facies 3B). Unit P05-G-iii is an acoustically transparent echo (echo facies 2) and is 6.8 m thick. The bottom unit (P05-G-iv) is 30.4 m thick, made up of an acoustically transparent echo with frequent interbeds of strong, thin reflections (echo facies 3B).

P05-H

P05-H is 1.0 km wide and has 31.2 m of sediment infill (Figure C.43). The echo-character is not clear due to hyperbolic echoes, but two units are still visible. The top unit (P05-H-i) is a prolonged echo with an incoherent internal structure (echo facies 5), measuring 3.8 m thick. The lower unit (P05-H-ii) is 27.4 m thick and comprises acoustically transparent echoes with occasional interbeds of strong, thin reflections (echo facies 3A).

P05-1

P05-1 is a slope deposit, which measures 1.6 km wide with 85.9 m of sediment (Figure C.44). It is divided into four sedimentary units. The top unit (P05-1-i) comprises strong, thin, continuous reflections (echo facies 1) and is 8.4 m thick. Unit P05-1-ii is 20.5 m thick, consisting of acoustically transparent echoes with frequent interbeds of strong, thin reflections (echo facies 3B). The unit below (P05-i-iii) is a 5.3 m thick acoustically transparent unit (echo facies 2). The lowest unit (P05-1-iv) is acoustically transparent with frequent interbeds of strong, thin reflections, measuring 51.7 m thick.

P05-I

P05-I is 11.7 km wide, with 95 m of infilling sediment (Figure C.45). Since P05-I is much wider than P05-1, there are visible changes in the units that occur along strike of the transect. Unit P05-I-i comprises strong, thin, continuous reflections (echo facies 1) is 9.1 m thick, and unit P05-I-ii is 48.6 m thick, consisting of acoustically transparent echoes with frequent interbeds of strong, thin reflections (echo facies 3B). Unit P05-I-iii is an 11.4 m thick acoustically transparent echo (echo facies 2), that pinches and swells along strike, disappearing completely in the eastern portion of the sub-basin. The bottom unit, P05-I-iv, is 41.8 m thick and comprises acoustically

transparent echoes with frequent interbeds of strong, thin reflections (echo facies 3B). This unit is quite discontinuous, interrupted by the presence of buried ridges. In some areas the acoustic signal becomes unclear and distorted, which could be the result of faulting or due to the decrease in acoustic signal strength with depth.

P05-J

P05-J is 5.6 km wide with 186.2 m of sediment, although only the top 123.1 m are imaged by Parasound (Figure C.46). There are four sedimentary units in this sub-basin. The top unit (P05-J-i) is comprised of strong, thin, continuous reflections (echo facies 1) and is 9.9 m thick. Unit P05-J-ii is 47.1 m thick and is made up of acoustically transparent echoes with frequent interbeds of strong, thin reflections (echo facies 3B). In the west of the sub-basin this unit slopes toward the east. The unit below (P05-J-iii) is a 7.6 m thick acoustically transparent echo (echo facies 2) which pinches out in the far west of the sub-basin. The bottom unit (P05-J-iv) is 58.5 m thick and consists of acoustically transparent echoes with frequent interbeds of strong, thin reflections (echo facies 3B).

P05-K

P05-K is 8.4 km wide with 194.6 m of sediment (Figure C.47). Parasound images the top 85.1 m where four sedimentary units are visible. The top unit (P05-K-i) is 17.5 m thick and consists of strong, thin, continuous reflections (echo facies 1). The unit below (P05-K-ii) is 24.3 m thick, composed of acoustically transparent echoes with frequent interbeds of strong, thin reflections (echo facies 3B). Unit P05-K-iii is 6.1 m thick and is acoustically transparent (echo facies 2). Finally, the bottom unit (P05-K-iv) is 37.2 m thick and consists of acoustically transparent echoes with frequent interbeds of strong, thin reflections (echo facies 3B). The units are all flat-lying in the west but are shallowly west-dipping in the east of the sub-basin, to the east of a normal fault that crosscuts all the units.

P05-L

P05-L is 28.5 km wide, with 304 m of sediment (Figure C.48). The top 98.8 m are imaged by Parasound, which is divided into two sedimentary units. The top unit (P05-L-i) is 25.8 m thick and consists of acoustically transparent echoes with frequent interbeds of strong, thin, continuous reflections (echo facies 3B). In the east of the sub-basin, where the seafloor is sloped near faults

and volcanic ridges, unit P05-L-i develops a lenticular shape and a prolonged echo with an incoherent internal structure (echo facies 5). The unit below (P05-L-ii) is 73.0 m thick, consisting of acoustically transparent echoes with occasional interbeds of strong, thin reflections (echo facies 3A). Towards the east, the strong reflections fade, and the sediment appears to be predominantly acoustically transparent. This is likely a result of the acoustic signal fading with depth. In this same unit, some of the upper beds pinch and swell toward the east.

There is an interesting feature present in the seismic reflection data. Just beneath unit P05-L-ii there is a very strong reflection that spans almost the entire sub-basin. It is parallel to bedding and represents a very large change in acoustic amplitude. It correlates approximately to the deepest reflection in the Parasound, suggesting that it is a feature preventing 3.5 kHz signal from penetrating deeper into the sub-basin.

P05-M

P05-M is approximately 20 km wide, with 997.1 m of sediment (Figure C.49). There are two sedimentary units visible in Parasound within the top 33.4 m of sediment. The top unit (P05-M-i) is 9.1 m thick and consists of strong, thin, continuous reflections (echo facies 1). The next unit (P05-M-ii) is 24.3 m thick, comprising acoustically transparent echoes with occasional interbeds of strong, thin reflections (echo facies 3A). The surface of this sub-basin is undulatory and sloped toward the west. In the seismic data, the undulations appear to be sediment waves. There are also some chaotic reflections in the seismic data that could be mass transport deposits. It is difficult to constrain the boundaries of this sub-basin on the seafloor, since P05-M and P05-N appear to once have been separate sub-basins, but with time have both been filled with sediment such that they are connected.

P05-N

P05-N is 23 km wide, with 873.2 m of sediment (Figure C.50). Only the top 56.2 m are imaged by Parasound, and this portion is divided into two sedimentary units. The top unit (P05-N-i) is 7.6 m thick and consists of strong, thin, continuous reflections (echo facies 1). The lower unit (P05-N-ii) is 48.6 m thick and comprises acoustically transparent echoes with occasional interbeds of strong, thin reflections (echo facies 3A). In the seismic data, the sediment is sunken in the middle, causing a concave up shape in most of the deeper sediment. This is likely a result

of regional extensional stresses. There is a change in reflection strength at approximately 1.90 s TWT, where the reflection strength increases toward the surface. Above this depth, the sediment begins to infill the topography, and the reflections begin to flatten out. Unlike sub-basin M whose top layer of sediment is deposited on a steep slope, sub-basin N is deposited on the shallow slope of the active arc and has a flat-lying upper sedimentary layer. The sediment here is much better stratified and is more continuous than sub-basin M downslope, where many of the seismic reflections are chaotic and irregular. Still, some onlapping of some sedimentary layers is visible in the seismic data, marking an angular unconformity that slopes toward the east.

P06-A

P06-A is 6.75 km wide and contains 150.5 m of sediment (Figure C.51). The sedimentary succession is divided into two units. The top unit (P06-A-i) is 63.8 m thick and consists of a repeating sequence of acoustically transparent basal echoes overlain by strong, thin reflections (echo facies 4). Each sub-unit consisting of a basal, acoustically transparent unit with upper strong, thin reflections, is approximately the same thickness, (0.02 s TWT = 15 m approx.). Within the acoustically transparent portion, there are occasional interbeds of strong, thin reflections. The lower unit (P06-A-ii) is 86.6 m thick and is composed of acoustically transparent echoes with sporadic interbeds of strong, thin reflections (echo facies 3A).

P06-B

P06-B is 2.2 km wide, with a sediment thickness of 41.1 m (Figure C.52). The echo character is hyperbolic in some parts of the sub-basin, which makes it difficult to characterise the sedimentary units and determine their lateral continuity. The maximum penetration depth is irregular along this profile, which may represent the sediment-basement contact, or may be an acoustic artifact caused by the uneven seafloor topography. Nevertheless, there are two visible units in this sub-basin. The first unit (P06-B-i) is 4.6 m thick and is composed of strong, thin, continuous reflections (echo facies 1) that drape over the underlying unit, following the topography. The lower unit (P06-B-ii) comprises acoustically transparent echoes with frequent interbeds of strong, thin reflections (echo facies 3B), and is 36.5 m thick.

P06-C

P06-C is 2.0 km wide and has a sediment thickness of 48.6 m (Figure C.53). The echoes in this sub-basin are hyperbolic due to the uneven topography. In the eastern end of the sub-basin, two units are visible, but in the western end of the sub-basin, on the other side of a ridge, only the top unit is visible. The upper unit (P06-C-i) is flat-lying, 4.6 m thick, and comprises several strong, thin, continuous reflections (echo facies 1). The bottom unit (P06-C-ii) consists of acoustically transparent echoes with a single strong, thin reflection in the center (echo facies 3A) and is 44.1 m thick.

P06-1

P06-1 is 1.6 km wide and comprises a sedimentary succession that is 85.9 m thick (Figure C.54). The deposit is sub-horizontal in the east of the deposit but toward the west, develops on a west-dipping slope. There are at least two sedimentary units, but with increasing depth, hyperbolic echoes appear, making it difficult to identify deeper units. The uppermost unit (P06-1-i) is 3.1 m thick and is composed of strong, thin, continuous reflections (echo facies 1). The lower unit (P06-1-ii) is 82.8 m thick and consists mostly of acoustically transparent echoes, with strong, thin interbeds which are clustered in groups of 2-6 (echo facies 3A).

P06-D

Sub-basin D, the easternmost sub-basin in this group, is 1.7 km wide with a sediment thickness of 96.5 m (Figure C.55). There are four sedimentary units. The top unit (P06-D-i) is 13.7 m thick and comprises multiple thin, strong, continuous reflections (echo facies 1) with few interbeds of acoustically transparent material. The second unit (P06-D-ii) consists of acoustically transparent echoes with regularly spaced, frequent interbeds of strong-thin reflections (echo facies 3B) and is 19.8 m thick. The third unit (P06-D-iii) is an acoustically transparent echo (echo facies 2) that is 6.8 m thick. The bottom unit (P06-D-iv) is 56.2 m thick and is composed of acoustically transparent echoes with occasional interbeds of strong, thin reflections spaced at random intervals (echo facies 3A).

P05-E

P05-E is 8.9 km wide with 98.0 m of sediment (Figure C.56). There are 6 sedimentary units in this sub-basin. The top unit (P06-E-i) is 5.3 m thick, and is composed of strong, thin, continuous reflections that drape over the topography (echo facies 1). The second unit (P06-E-ii) is acoustically transparent (echo facies 2) and is 3.0 m thick. This unit pinches and swells slightly along strike but increases in thickness overall toward the east. The third unit (P06-E-iii) is 17.5 m thick and is composed of acoustically transparent echoes with frequent interbeds of strong, thin reflections (echo facies 3B). The fourth unit (P06-E-iv) is made up of acoustically transparent echoes with occasional interbeds of strong, thin reflections (echo facies 3A), and is 15.2 m thick. It pinches and swells along strike, its thickest point just to the west of the largest ridge in the sub-basin. The fifth unit (P06-E-v), measuring 23.6 m thick, is composed of acoustically transparent echoes with occasional, regularly spaced interbeds of strong, thin reflections (echo facies 3A). The sixth unit (P06-E-vi) is 33.4 m thick and is composed mainly of acoustically transparent echoes with occasional interbeds of strong, thin reflections (echo facies 3A).

Along a fault, there is a feature with a prolonged echo that is a darker grey than the surrounding transparent sedimentary units. It is about 200 m wide and extends from just below the seafloor to approximately 30 mbsf. Reflections reappear in the units below this feature, suggesting that it is not a ridge, but some change in density that is causing the change in acoustic character. There is a similar feature in the west end of the sub-basin along a normal fault. It extends from approximately 15 m – 68 m below the seafloor, and the echo character becomes increasingly acoustically transparent, dissecting the reflections on either side. In the top portion of this feature, there are a few reflections that can be discerned but are not very clear.

P06-F

P06-F is 7.3 km wide with 68.4 m of infilling sediment (Figure C.57). There are two sedimentary units in this sub-basin. The first unit (P06-F-i) is made up of strong, thin reflections (echo facies 1) and is 10.6 m thick. The second unit (P06-F-ii) is 57.8 m thick and comprises acoustically transparent echoes with frequent interbeds of strong, thin reflections (echo facies 3B). The seafloor in this sub-basin is undulatory, so the sedimentary units are laterally discontinuous. It is difficult to discern the boundaries of this sub-basin as some of the sedimentary units are present on the bounding ridges. Because of the undulatory seafloor, the sedimentary units on the western

sub-basin margin dipping to the east resemble a slope deposit. These deposits are characterised by a lateral transition from bedded reflections to prolonged echoes (echo facies 5).

P06-G

P06-G is 3.5 km wide with 151.2 m of sediment infill (Figure C.58). The top 64.6 m of sediment are imaged by Parasound, and we do not see the sediment-basement contact. There are five sedimentary units which are visible on the eastern side of a central ridge but are less visible to the west of the ridge because the penetration depth is shallower. The top unit (P06-G-i) is 3.0 m thick and is made up of strong, thin, continuous reflections (echo facies 1). The second unit (P06-G-2) is 12.9 m thick and consists of acoustically transparent echoes with frequent interbeds of strong, thin reflections (echo facies 3B). The acoustically transparent echoes here are a darker grey than in other units of echo facies 3B, appearing almost to be a prolonged echo of echo facies 5, with interbeds of strong, thin reflections. The third unit (P06-G-iii) is 16.0 m thick and comprises mainly acoustically transparent echoes, with frequent interbeds of strong, thin reflections (echo facies 3B). The acoustically transparent echoes in this unit are lighter than those in P06-G-ii. The fourth unit (P06-G-iv) is 32.7 m thick and is composed of acoustically transparent echoes with few interbeds of strong, thin reflections (echo facies 3A).

P06-H

P06-H is 4.3 km wide and contains a sedimentary infill measuring 215.1 m thick (Figure C.59). The top 64.6 m are imaged by Parasound and are divided into two units. The top unit (P06-H-i) is 9.9 m thick, consisting of strong, thin, continuous reflections (echo facies 1). The second unit (P06-H-ii) is 54.7 m thick and consist of acoustically transparent echoes with occasional interbeds of strong, thin reflections (echo facies 3A). The reflections in this unit are anomalously faint and low amplitude, which may be a result of unit P06-H-i reflecting more of the acoustic signal.

P06-I

P06-I is 13.3 km wide with 394.4 m of sediment (Figure C.60). Parasound images the top 85.1 m, which is divided into two sedimentary units. The first unit (P06-I-i) is 12.2 m thick and consists of strong, thin, continuous reflections (echo facies 1). The next unit (P06-I-ii) comprises acoustically transparent echoes with frequent interbeds of strong, thin reflections (echo facies

3B) and is 73.0 m thick. The sediment is on the western flank of a volcano, and slopes gently toward the west.

P06-J

P06-J is 13.45 km wide and contains 817.0 m of sedimentary infill (Figure C.61). 60.8 m of sediment are imaged by Parasound and are divided into three units. The top unit (P06-J-i) comprises strong, thin, continuous reflections (echo facies 1) and is 6.1 m thick. This unit drapes over the underlying topography. Also measuring 6.1 m thick, is unit P06-J-ii, which is an acoustically transparent echo (echo facies 2). This unit pinches and swells along strike, reaching its maximum thickness in the center of the sub-basin and pinching out in the west. The lowest unit (P06-J-iii) is 48.6 m thick and consists of acoustically transparent echoes with occasional interbeds of strong, thin reflections (echo facies 3). The reflections in this unit become slightly undulatory in the center of the sub-basin and are flat lying on the margins.

In the seismic data, there are two angular unconformities from onlapping sedimentary units, and both chaotic and continuous reflections.

P06-K

P06-K is 3.7 km wide with 237 m of sediment (Figure C.62). The top 51.7 m are imaged by Parasound and have been divided into two sedimentary units. This sub-basin is located within a caldera. The top unit (P06-K-i) is 6.8 m thick and consists of strong, thin, continuous reflections (echo facies 1). The next unit (P06-K-ii) is 44.8 m thick, consisting of acoustically transparent echoes with frequent interbeds of strong, thin reflections (echo facies 3B). In the west of the sub-basin the slope of the seafloor increases, and reflections become less continuous. Here they adopt a prolonged echo (echo facies 5).

P06-2

P06-2 is 15.6 km wide and contains 1080.7 m of sediment (Figure C.63). The portion of this sediment imaged by Parasound is 50.2 m thick, which is divided into three units. The top unit (P06-2-i) consists of strong, thin, continuous reflections (echo facies 1) and is 4.6 m thick. The next unit (P06-2-ii) is 22.0 m thick and consists of acoustically transparent echoes with frequent interbeds of strong, thin reflections (echo facies 3B). The lowest unit (P06-2-iii) is 23.6 m thick

and is an acoustically transparent echo (echo facies 2). The contact between units P06-2-ii and P06-2-iii is very undulatory, which results in the overlying units infilling topography and adopting the undulatory character. In the bathymetry there are several sediment waves that run parallel to the cone to the east of the sub-basin.

APPENDIX C – Sub-Basin Echograms

The following echograms were exported from the Kingdom Suite software. Seafloor and sedimentary unit boundaries were drawn in Kingdom using the Manual Picking tool. Sedimentary units are indicated by lowercase Roman numerals, and the echo facies corresponding to each unit are listed in Appendix D. Detailed sub-basin descriptions are in Appendix B. Vertical scale is two-way time (TWT) in seconds. In this study, a velocity of 1520 m/s in sediment was used to convert TWT to distance in meters. 0.1 s TWT is approximately equal to 76 m.

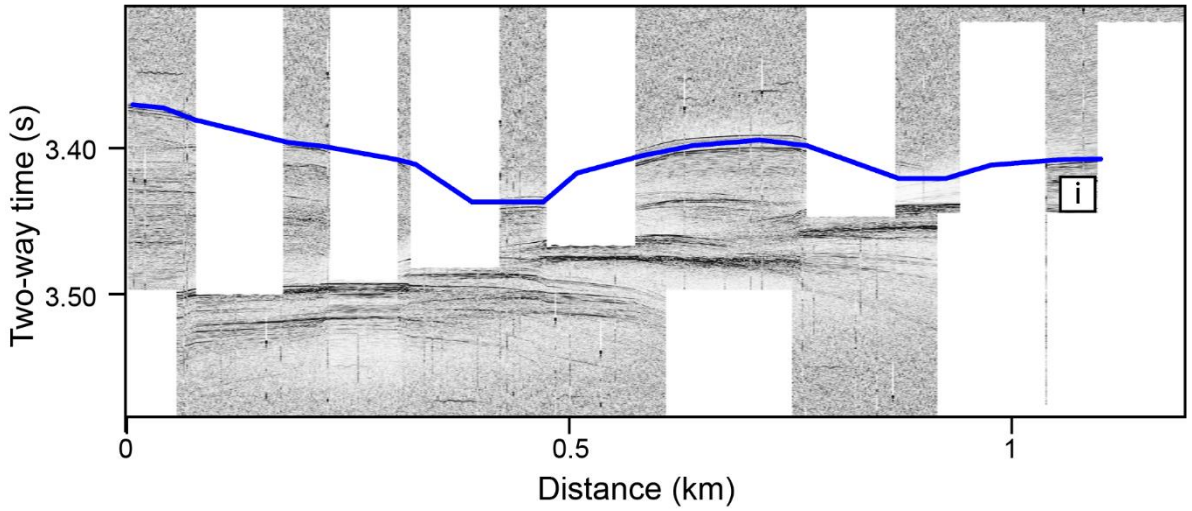

Figure C.1 Echogram of sub-basin P03-A.

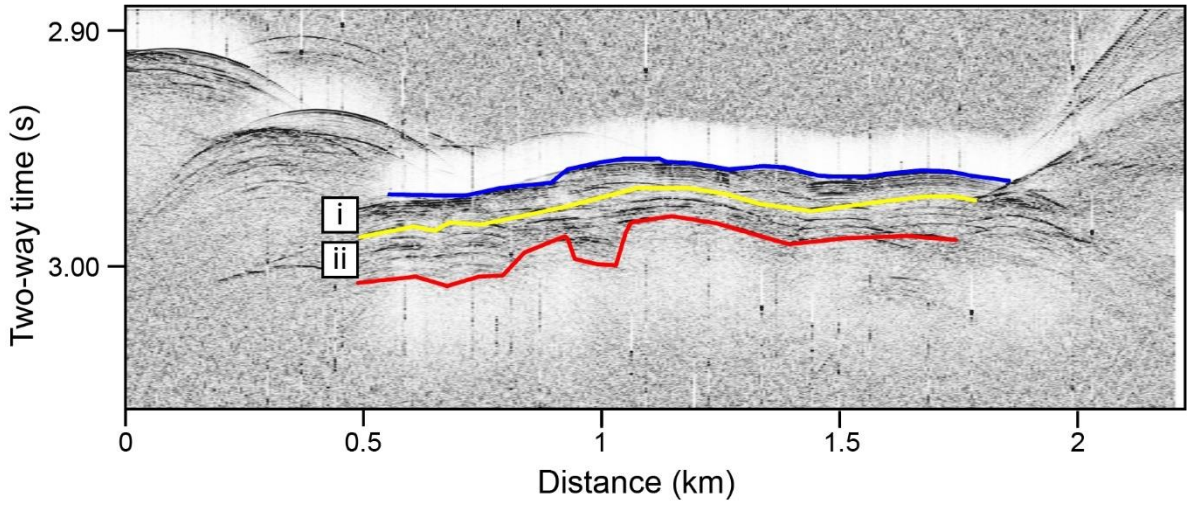

Figure C.2 Echogram of sub-basin P03-B.

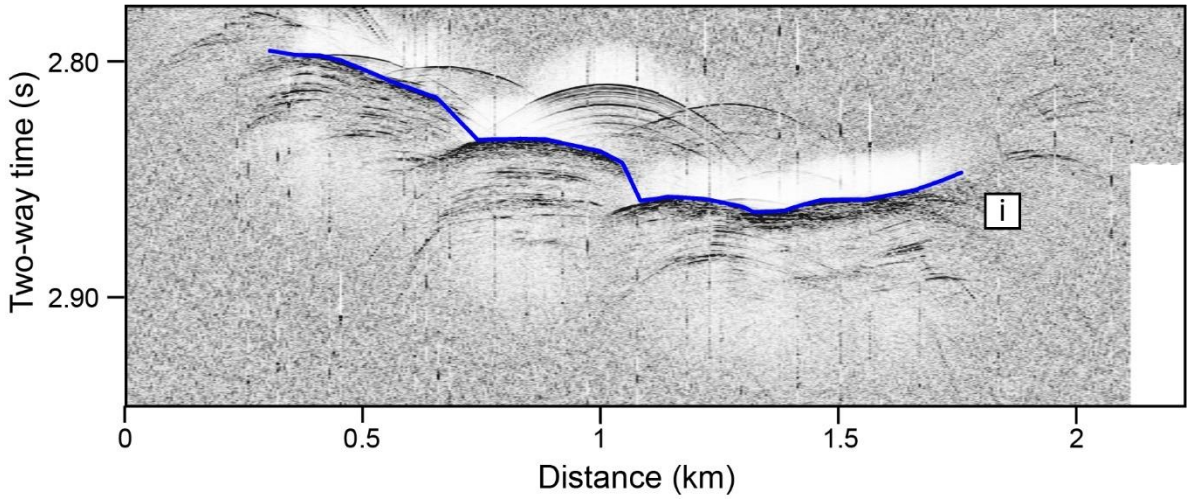

Figure C.3 Echogram of sub-basin P03-C.

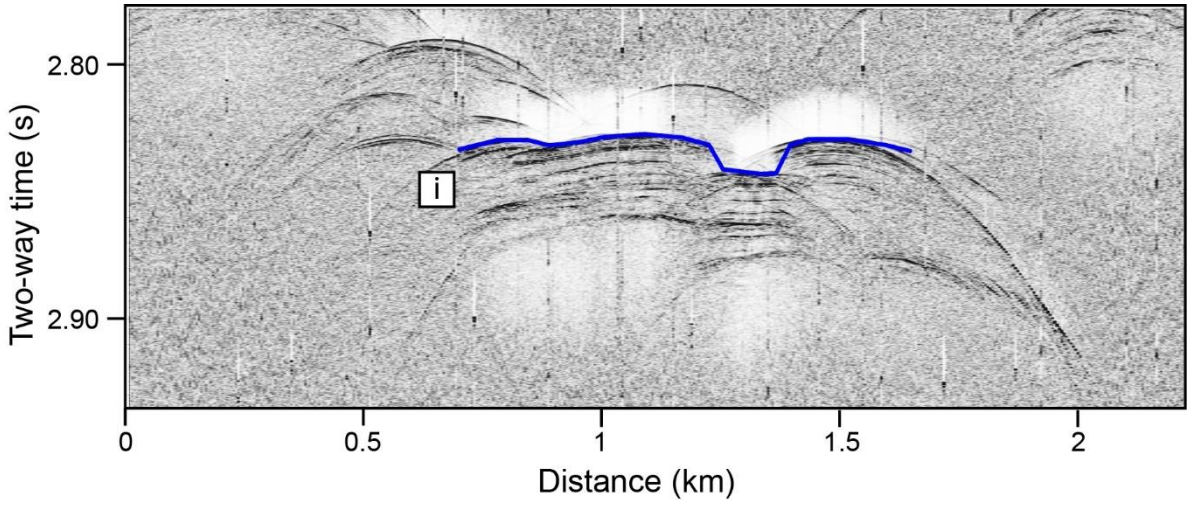

Figure C.4 Echogram of sub-basin P03-D.

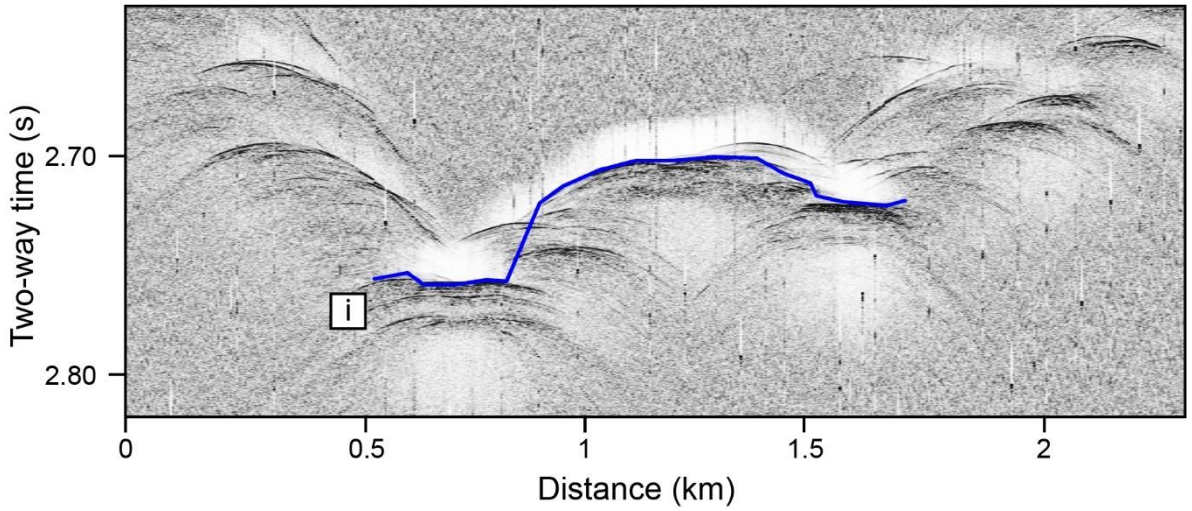

Figure C.5 Echogram of sub-basin P03-E.

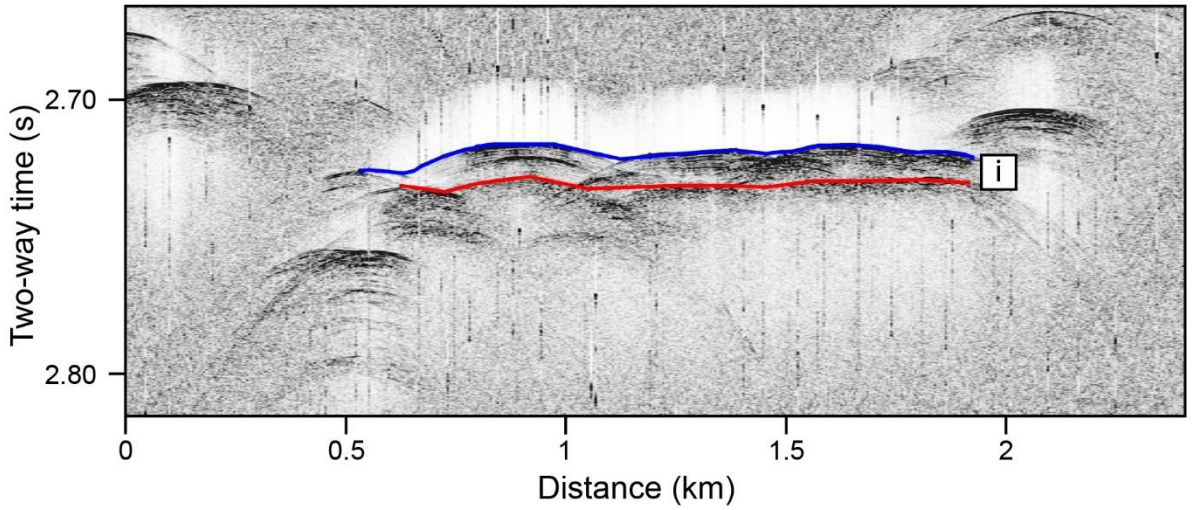

Figure C.6 Echogram of sub-basin P03-F.

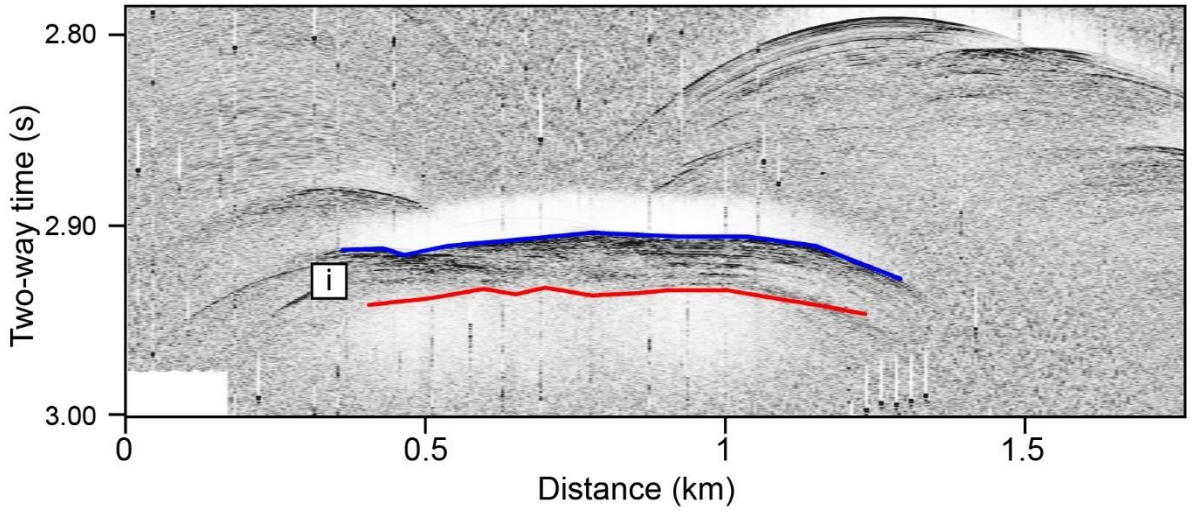

Figure C.7 Echogram of sub-basin P03-G.

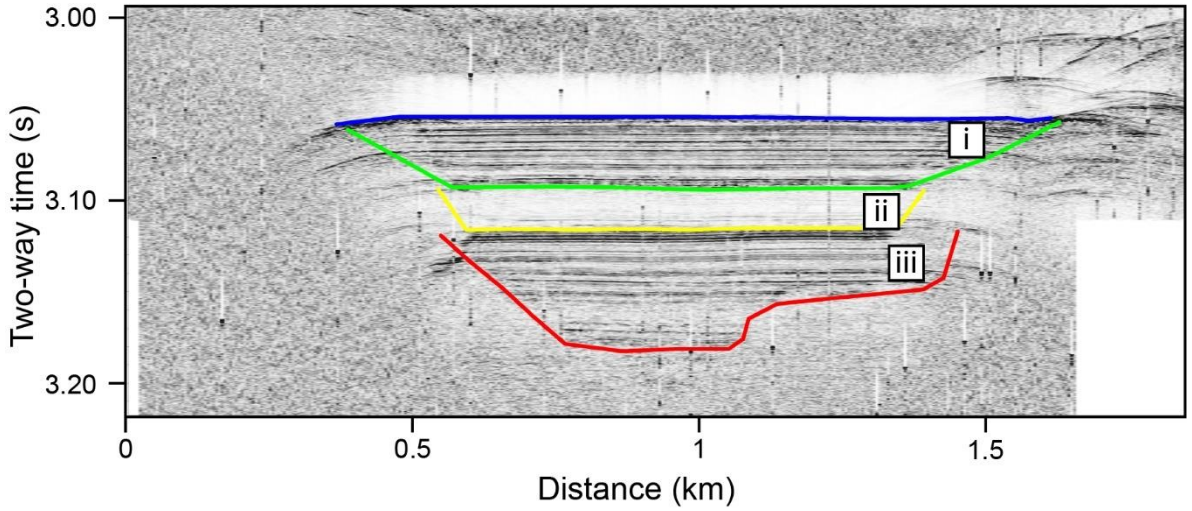

Figure C.8 Echogram of sub-basin P03-H.

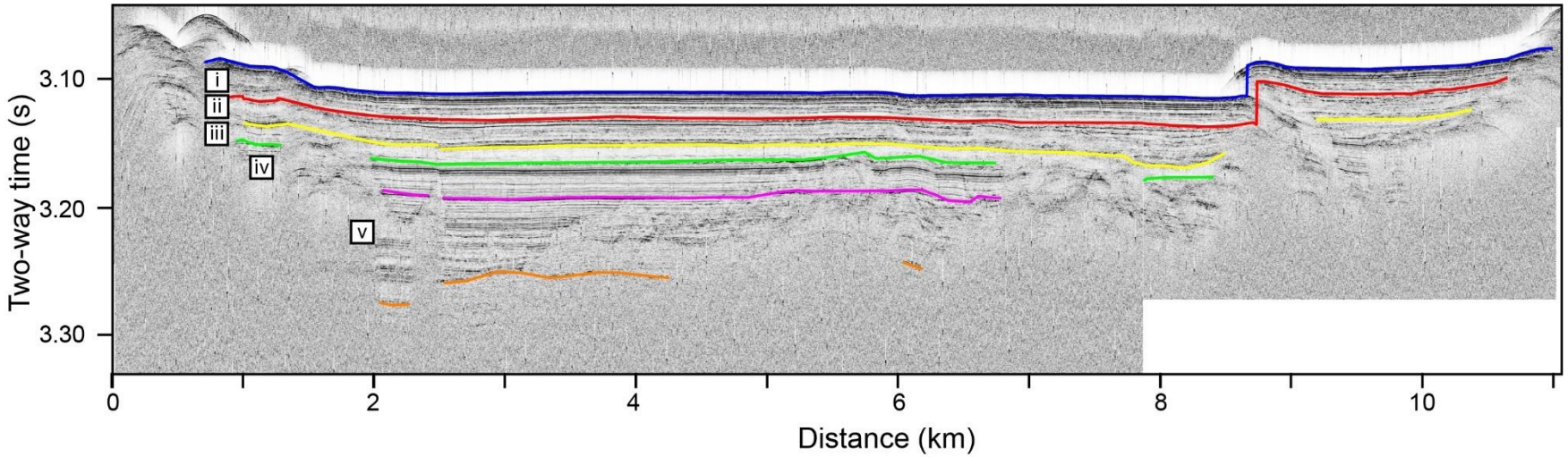

Figure C.9 Echogram of sub-basin P03-I.

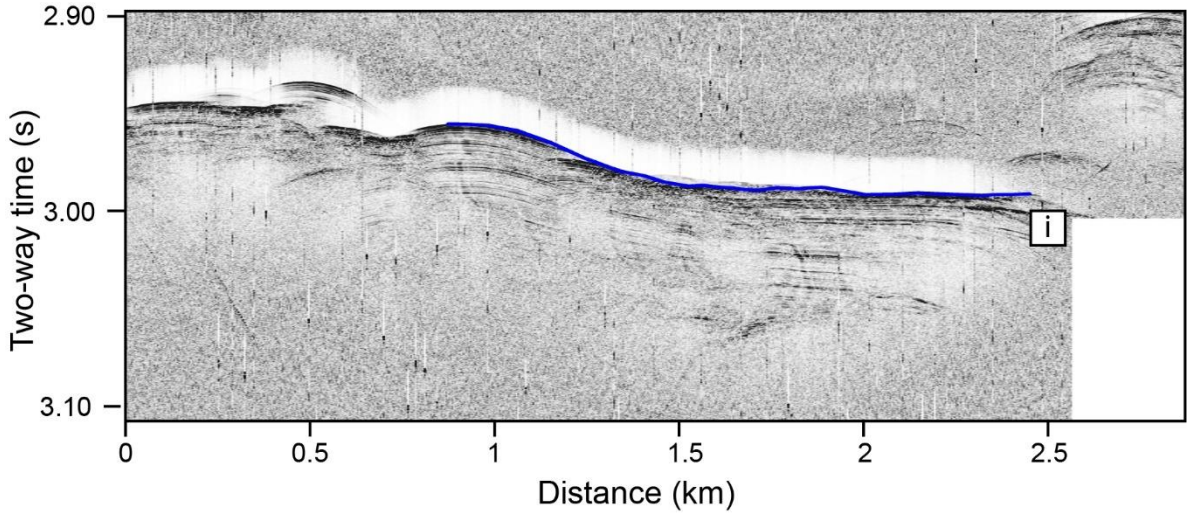

Figure C.10 Echogram of sub-basin P03-J.

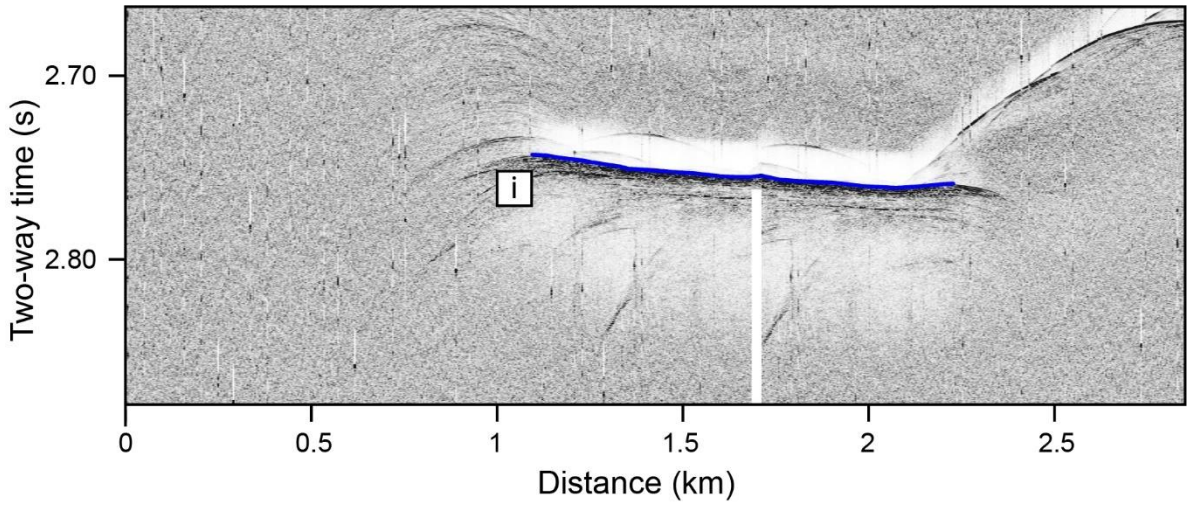

Figure C.11 Echogram of sub-basin P03-K.

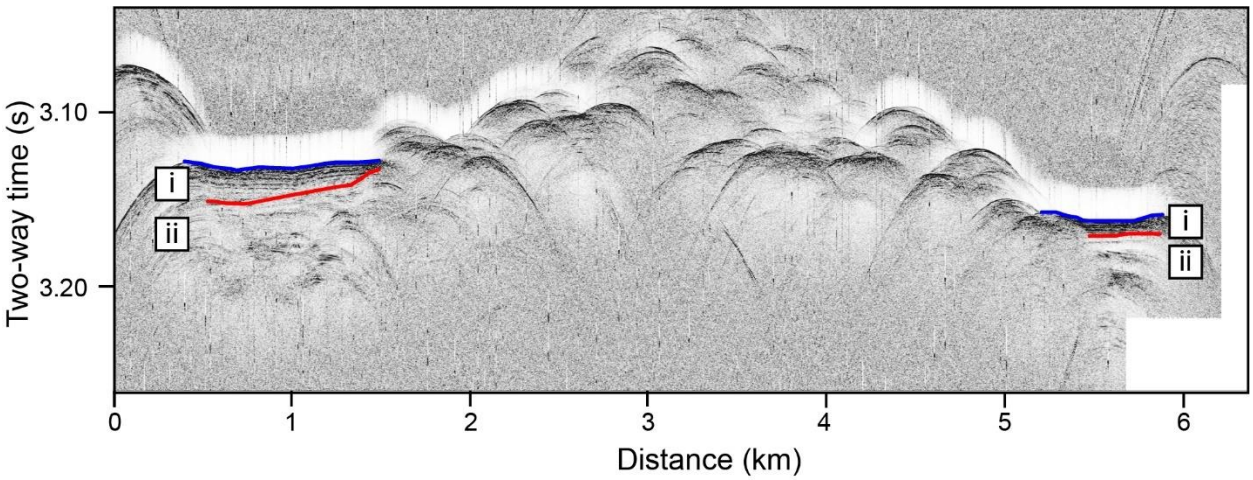

Figure C.12 Echogram of sub-basin P03-L.

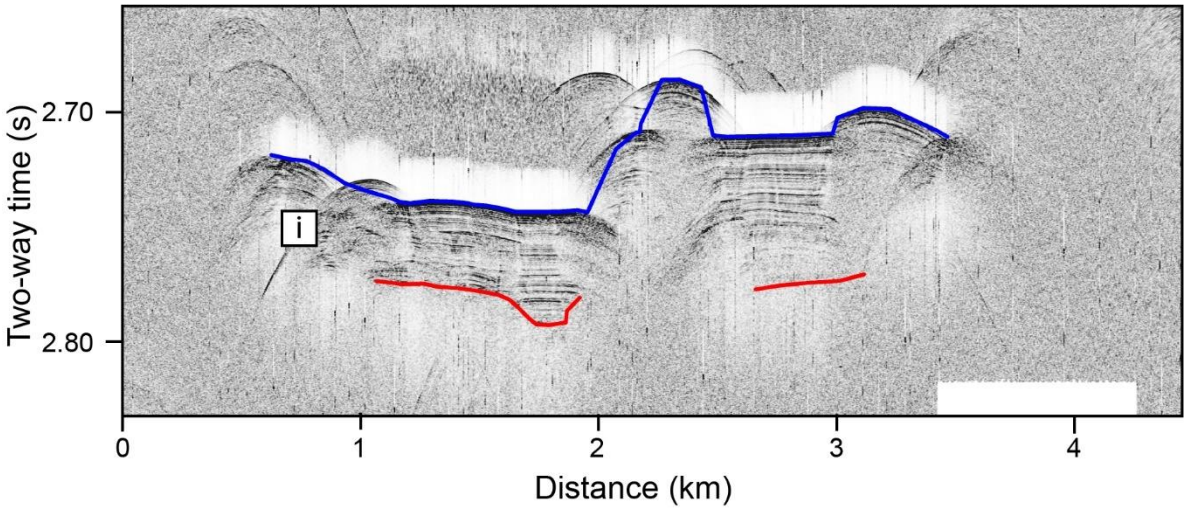

Figure C.13 Echogram of sub-basin P03-M.

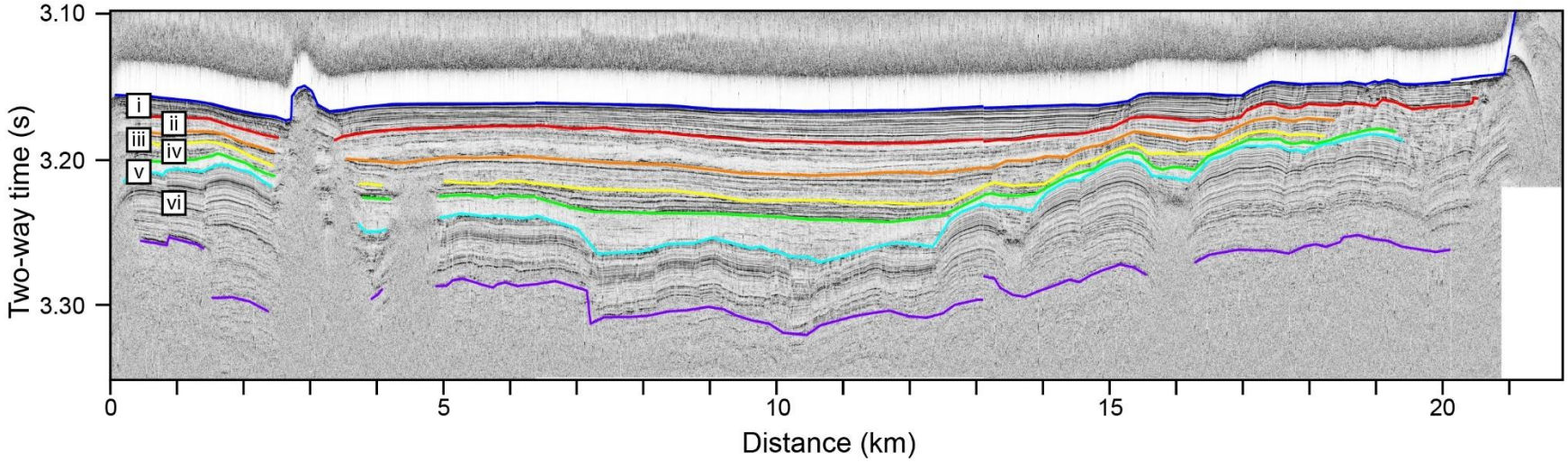

Figure C.14 Echogram of sub-basin P03-N.

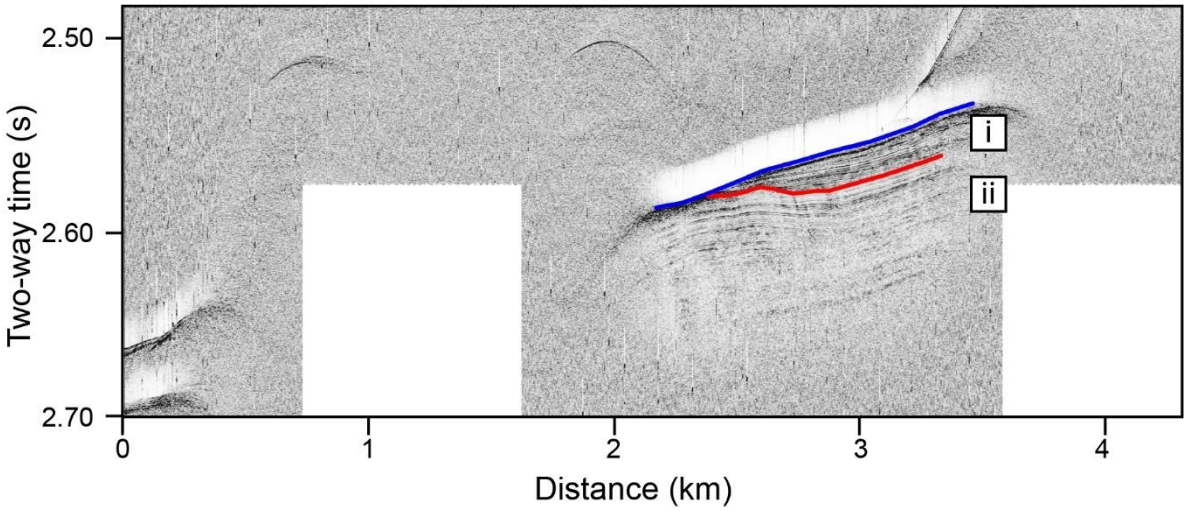

Figure C.15 Echogram of slope deposit P03-1.

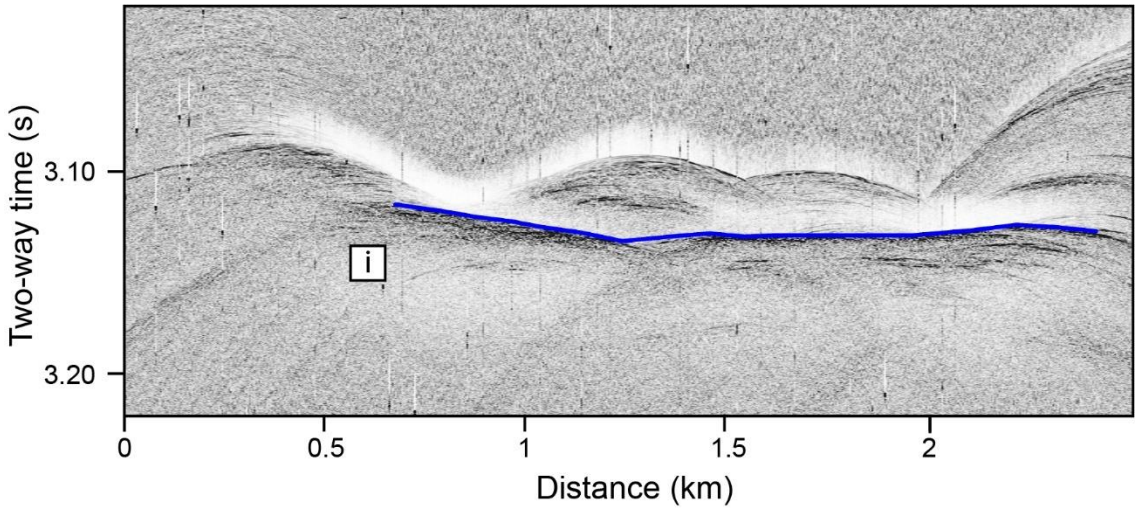

Figure C.16 Echogram of sub-basin P03-P.

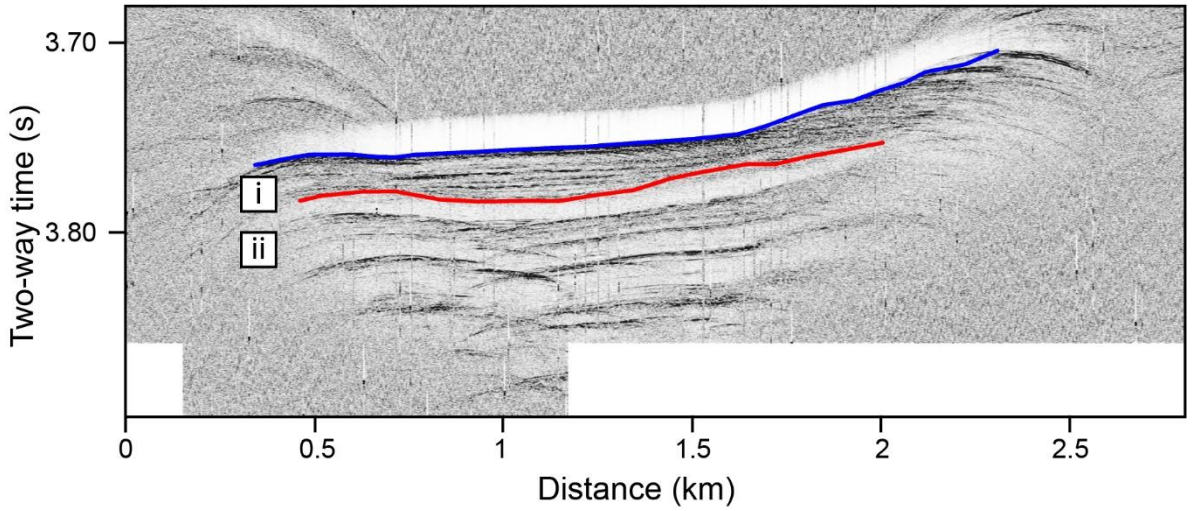

Figure C.17 Echogram of sub-basin P03-Q.

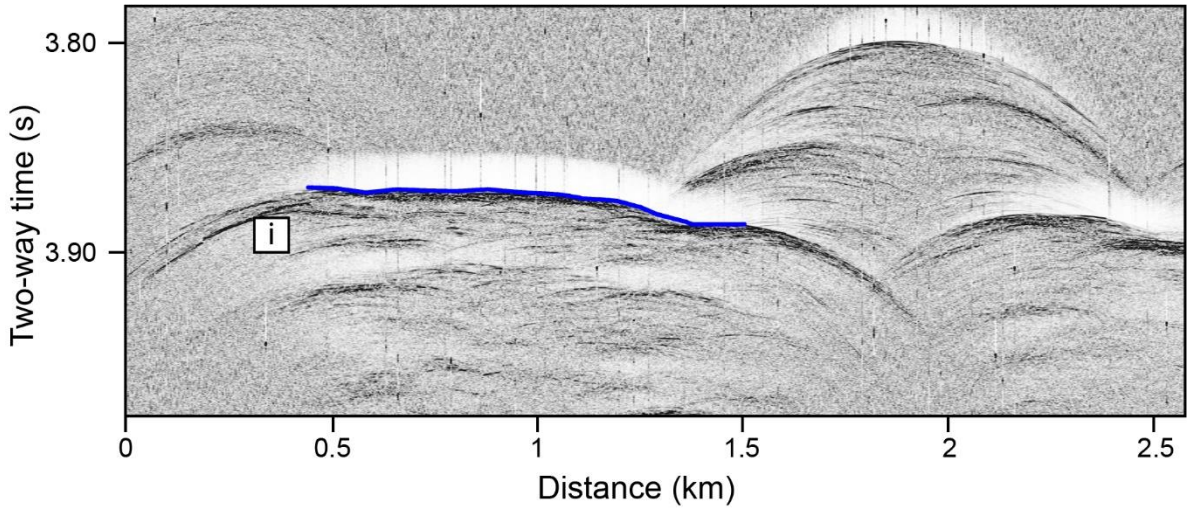

Figure C.18 Echogram of sub-basin P03-R.

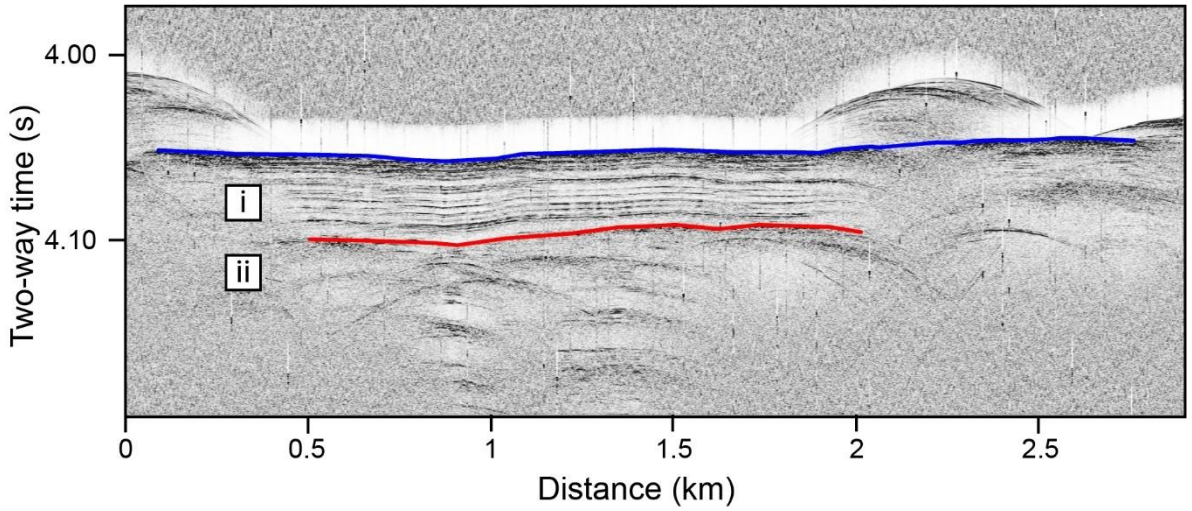

Figure C.19 Echogram of sub-basin P03-S.

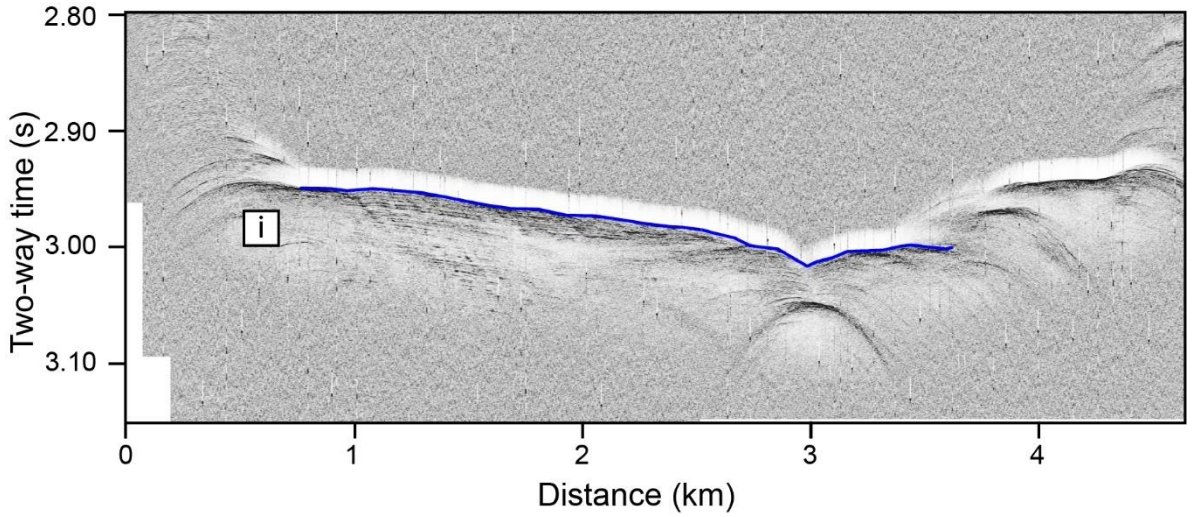

Figure C.20 Echogram of sub-basin P03-T.

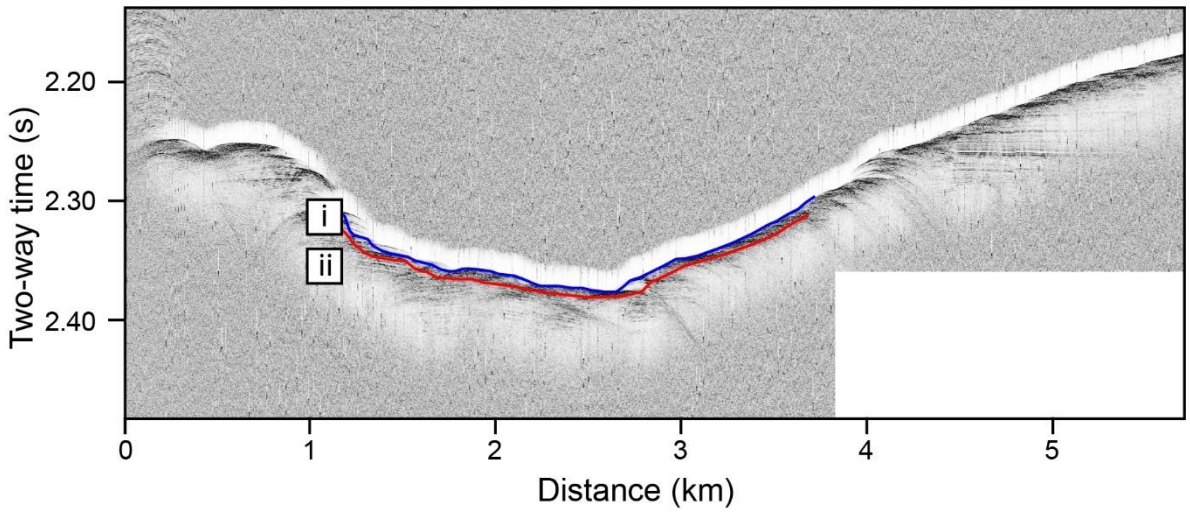

Figure C.21 Echogram of sub-basin P03-U.

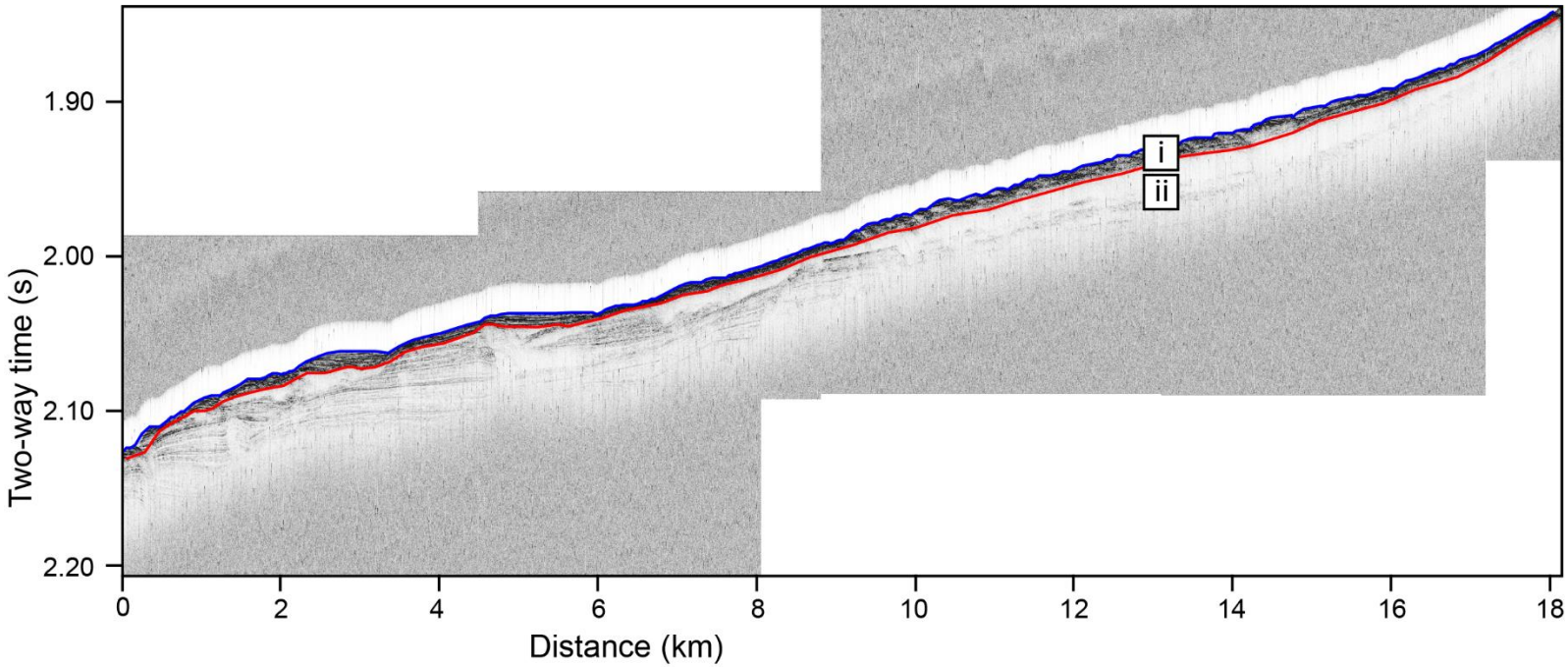

Figure C.22 Echogram of sub-basin P03-V.

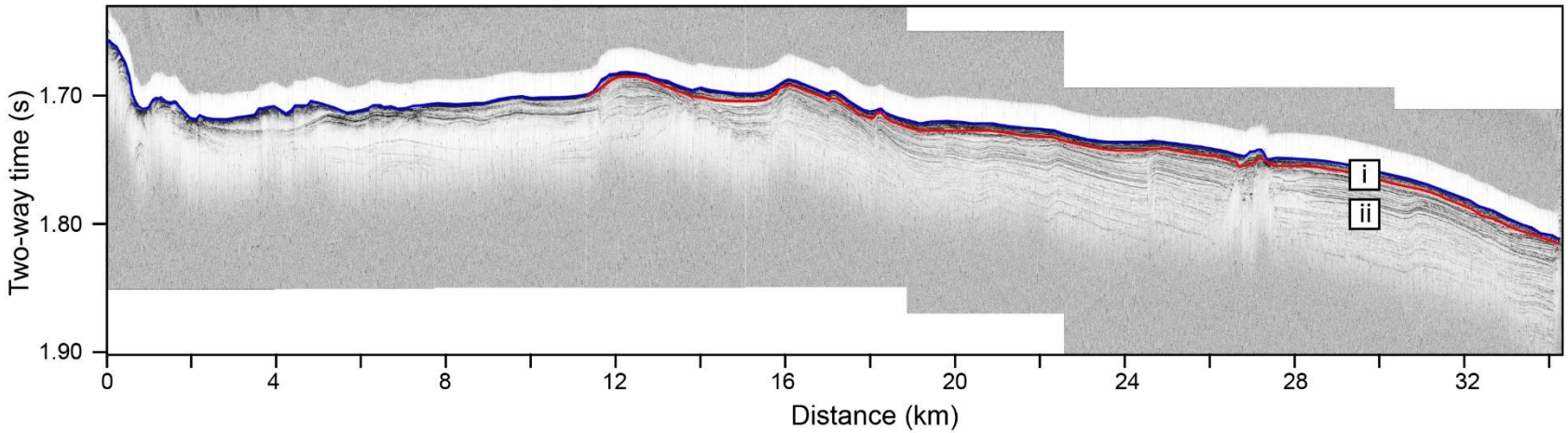

Figure C.23 Echogram of sub-basin P03-W.

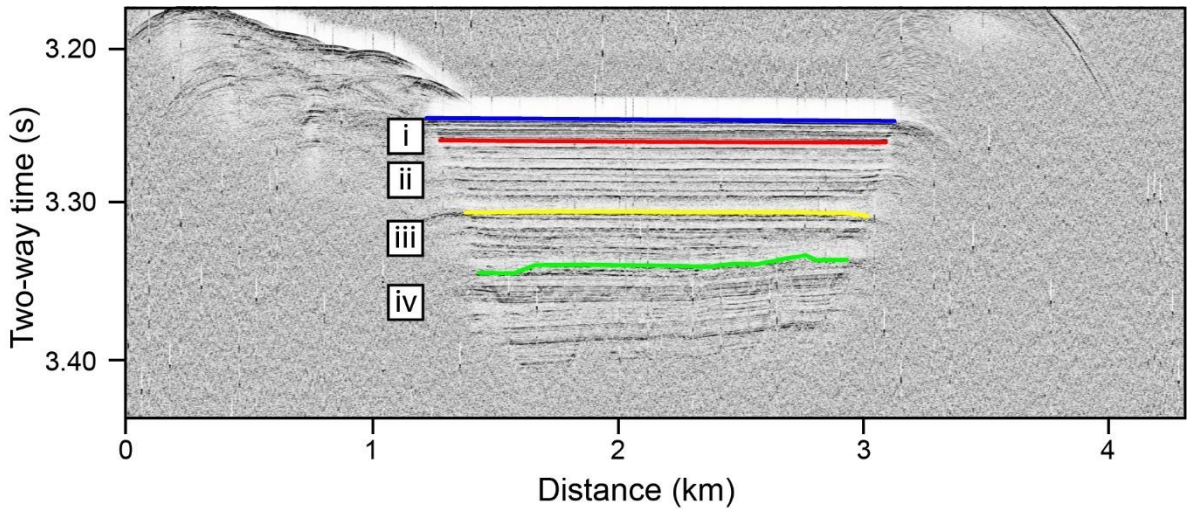

Figure C.24 Echogram of sub-basin P04-A.

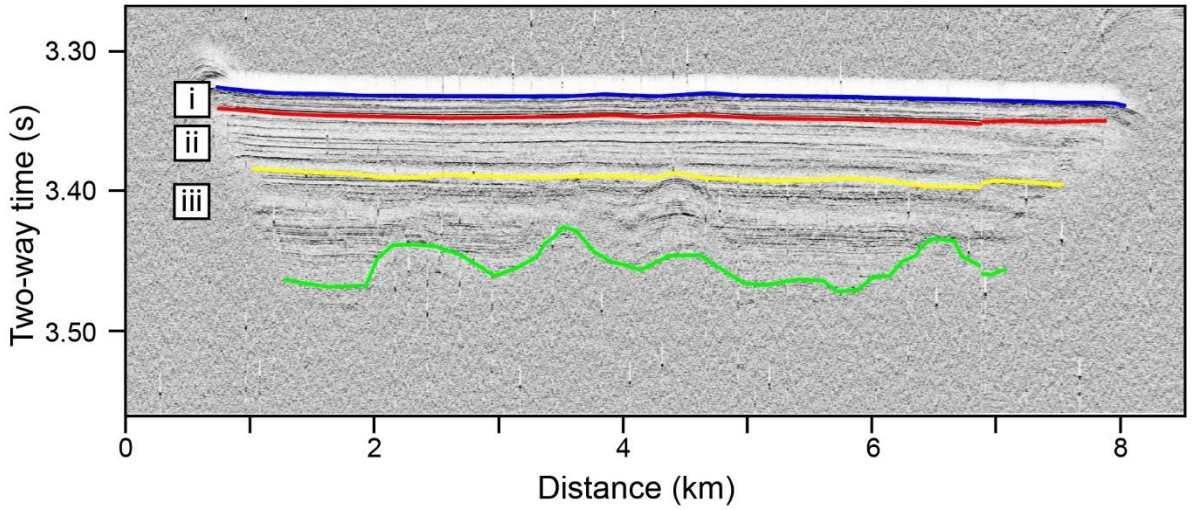

Figure C.25 Echogram of sub-basin P04-B.

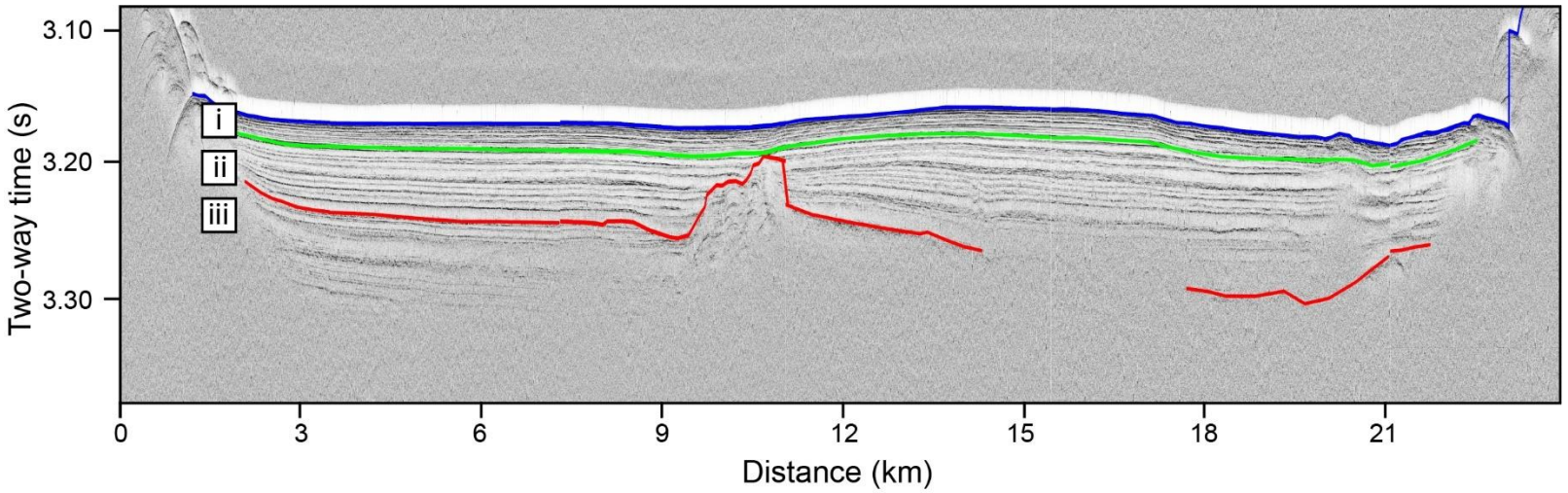

Figure C.26 Echogram of sub-basin P04-C.

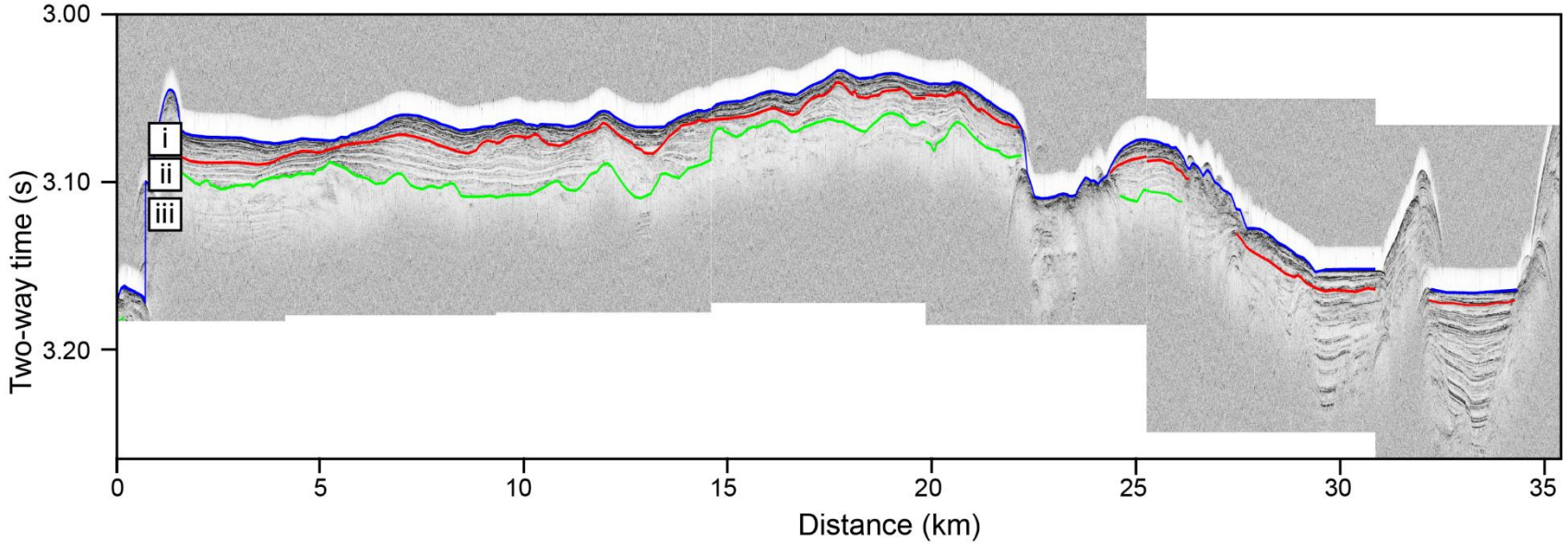

Figure C.27 Echogram of sub-basin P04-D.

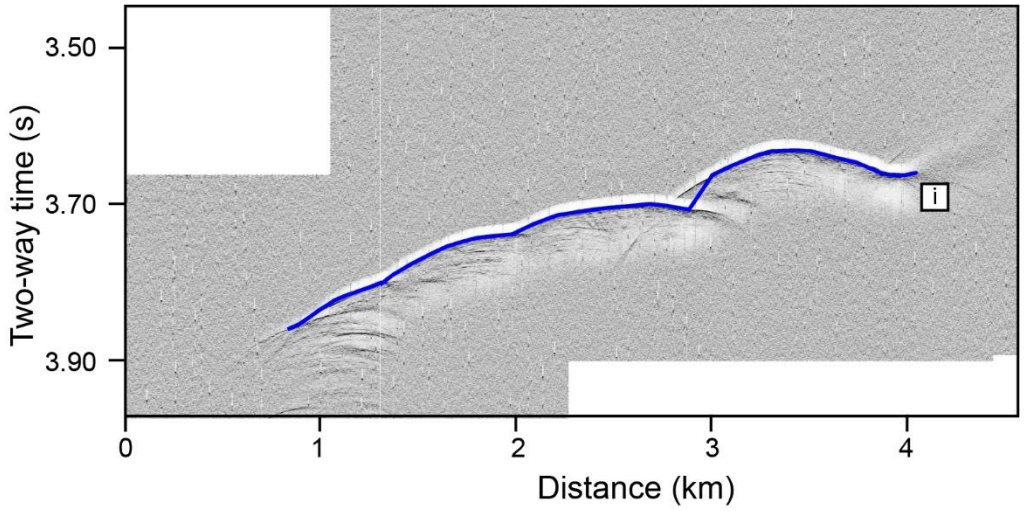

Figure C.28 Echogram of slope deposit P04-1.

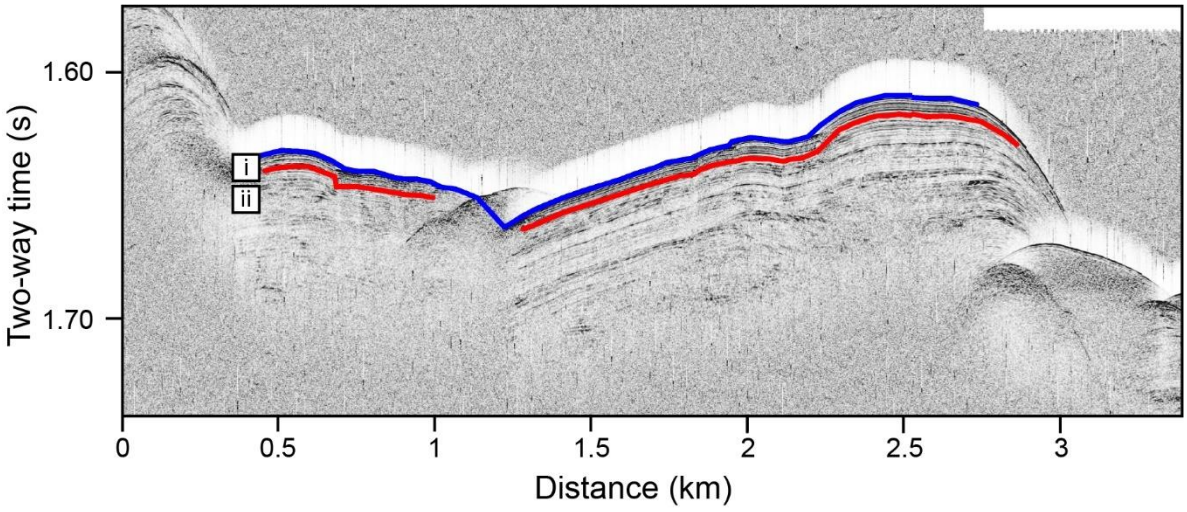

Figure C.29 Echogram of sub-basin P04-E.

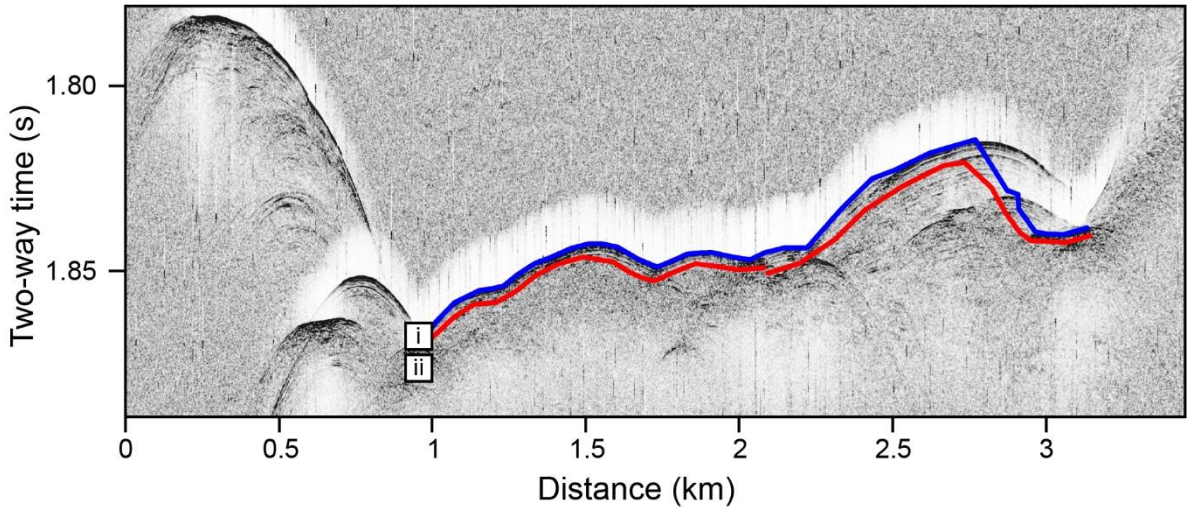

Figure C.30 Echogram of sub-basin P04-F.

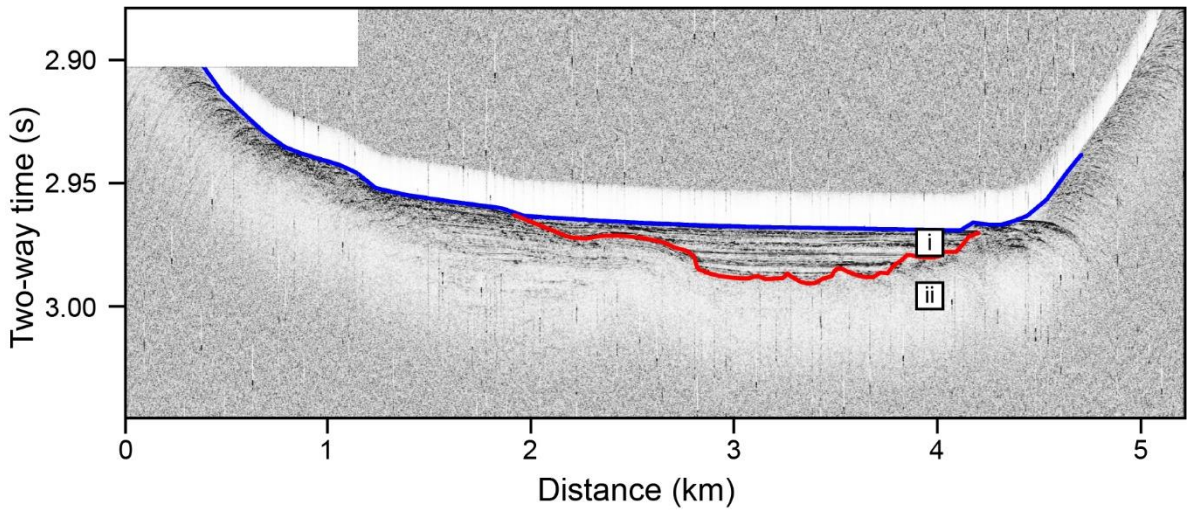

Figure C.31 Echogram of sub-basin P04-G.

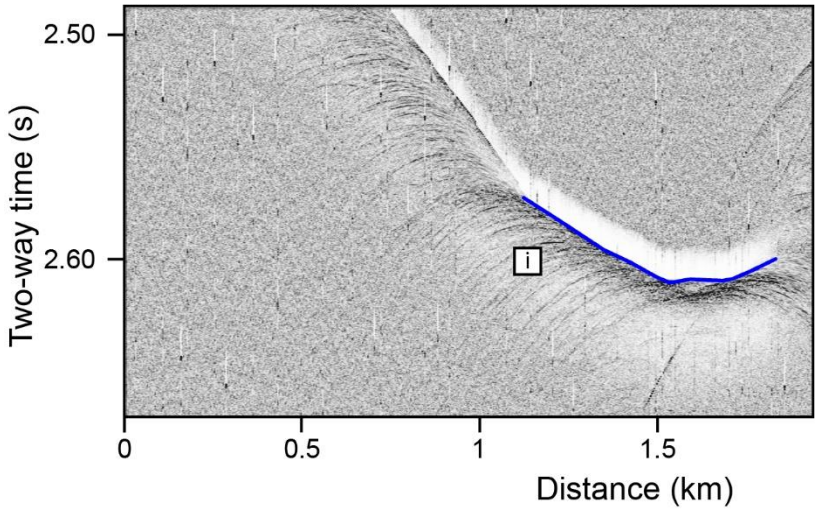

Figure C.32 Echogram of sub-basin P04-H.

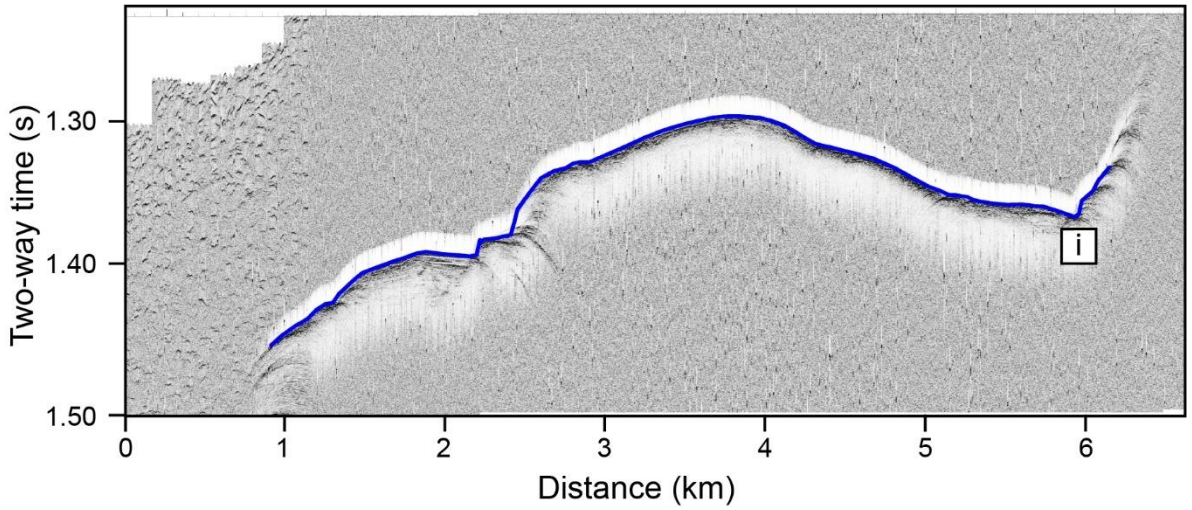

Figure C.33 Echogram of slope deposit P04-2.

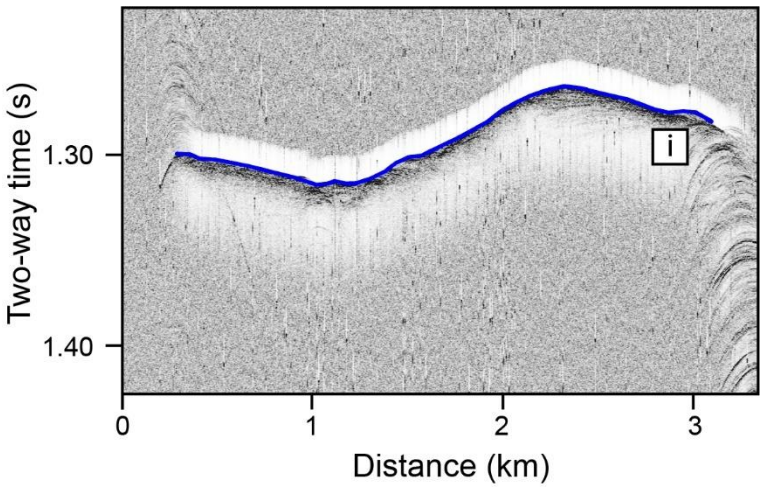

Figure C.34 Echogram of slope deposit P04-3.

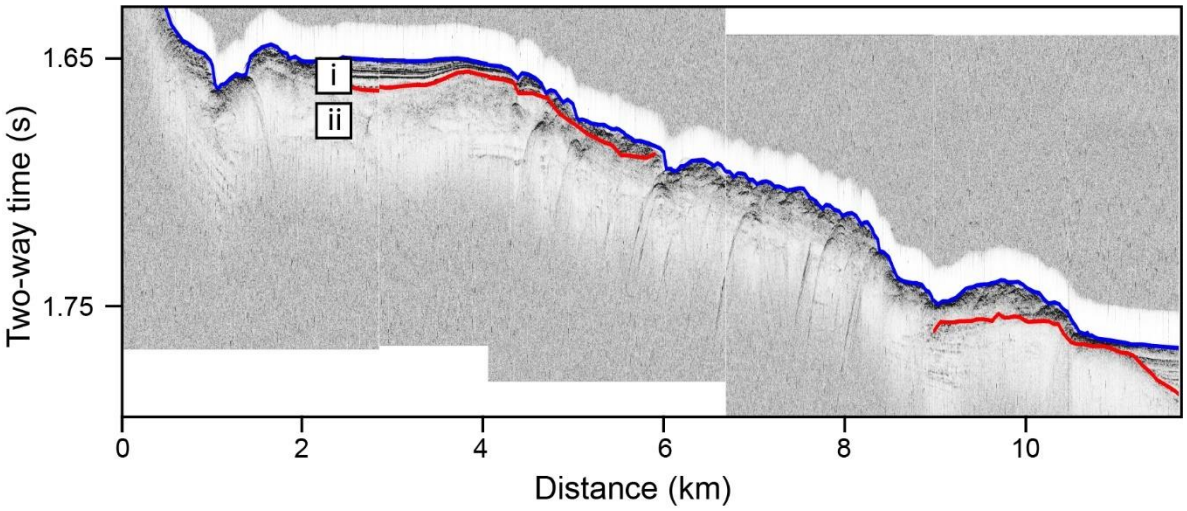

Figure C.35 Echogram of sub-basin P04-I.

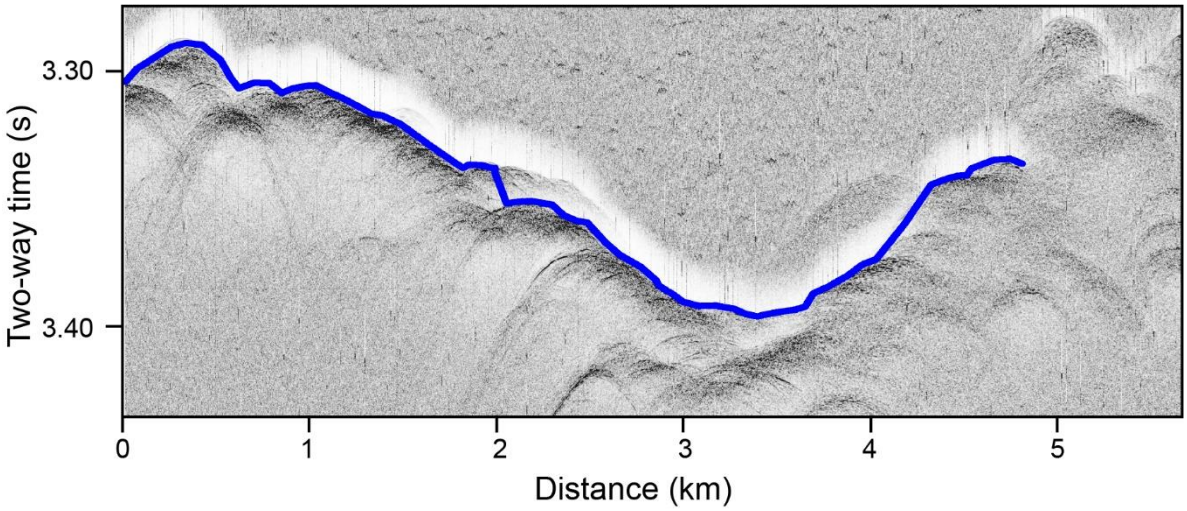

Figure C.36 Echogram of sub-basin P05-A.

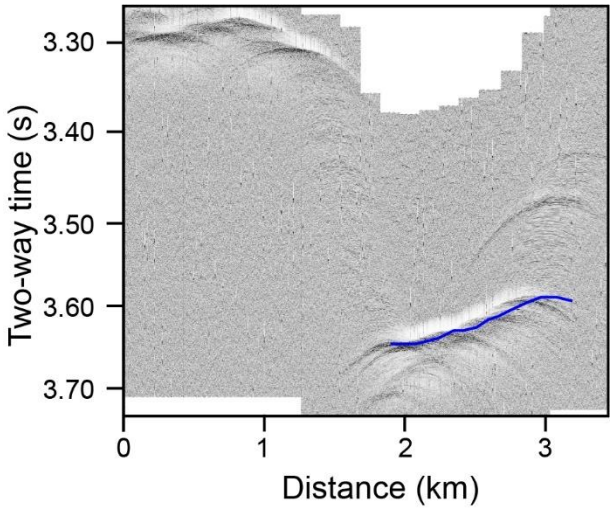

Figure C.37 Echogram of sub-basin P05-B.

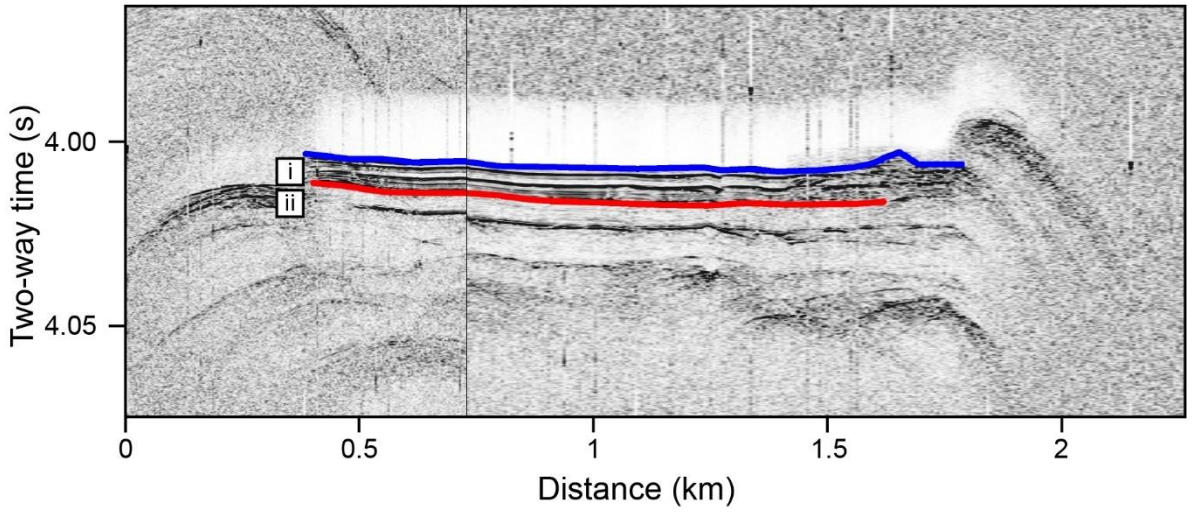

Figure C.38 Echogram of sub-basin P05-C.

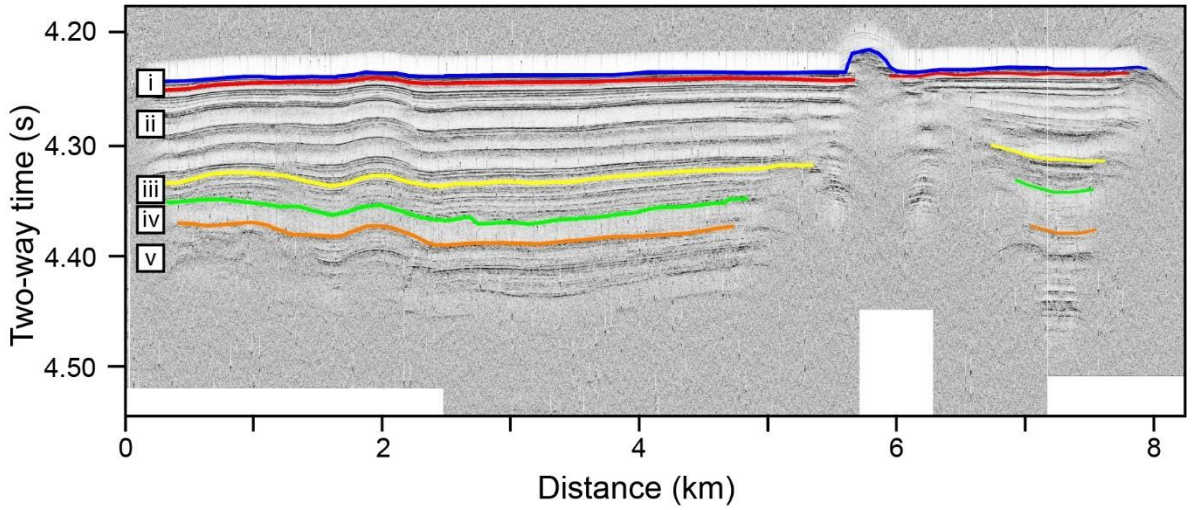

Figure C.39 Echogram of sub-basin P05-D.

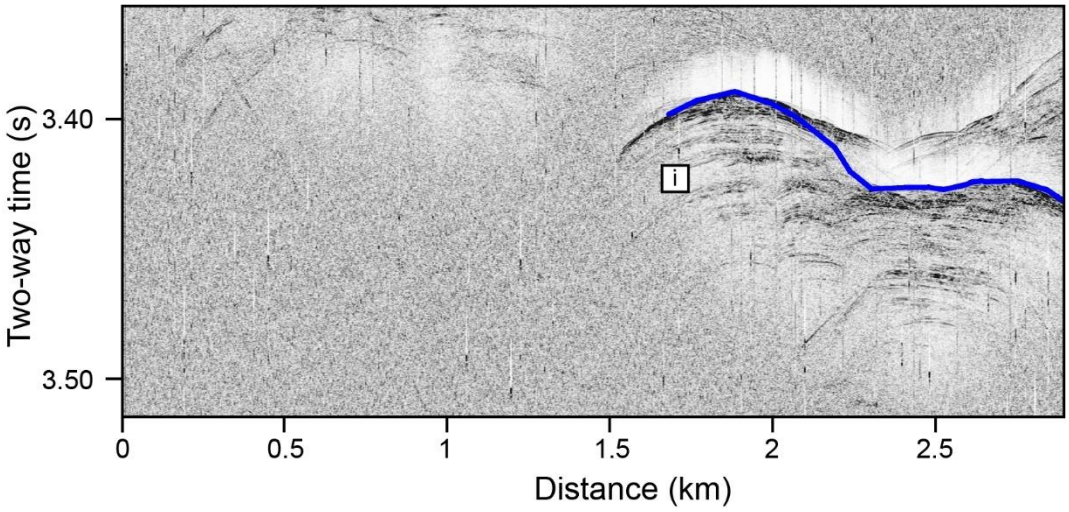

Figure C.40 Echogram of sub-basin P05-E.

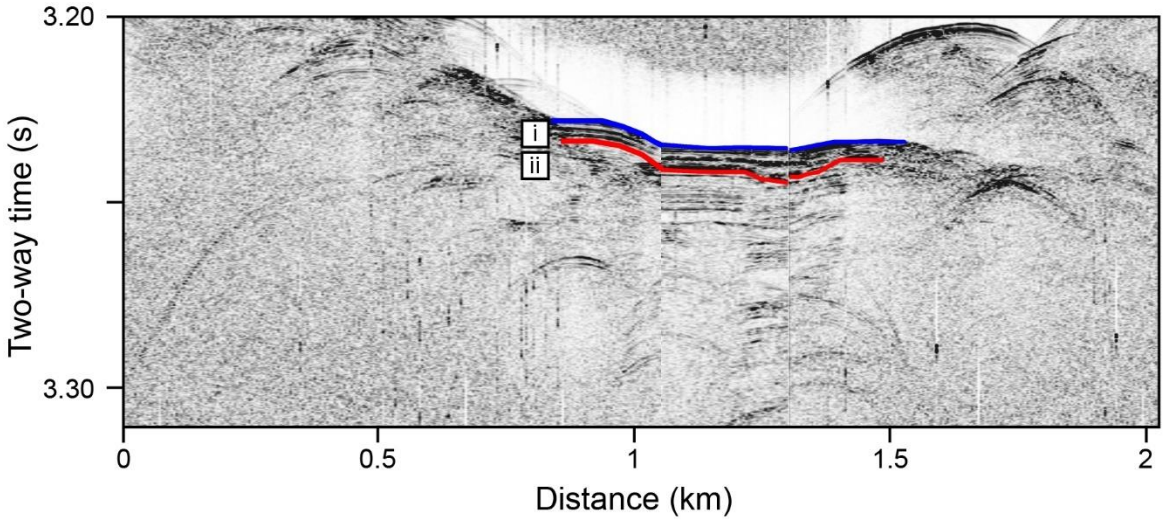

Figure C.41 Echogram of sub-basin P05-F.

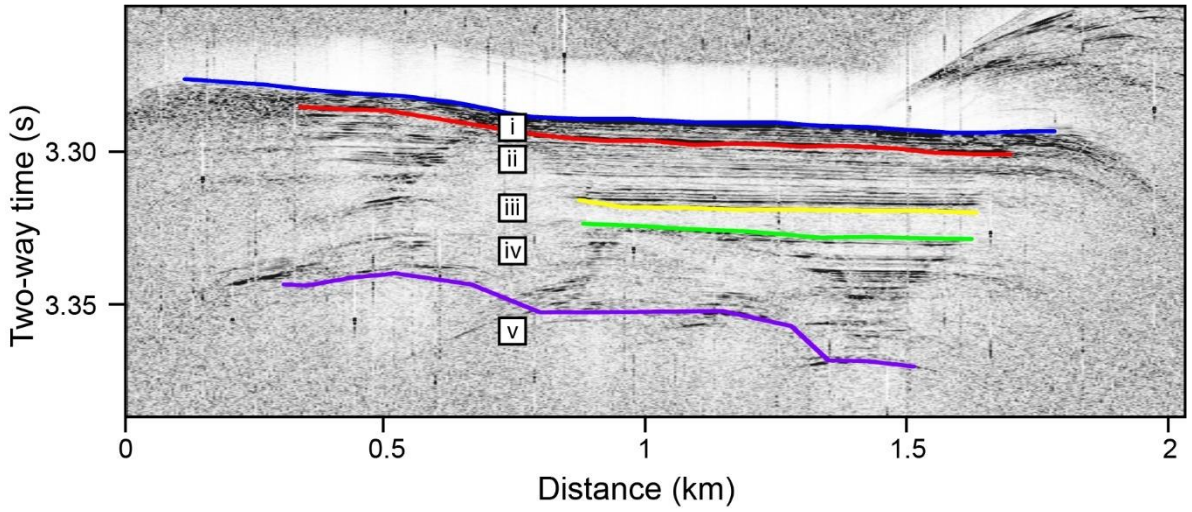

Figure C.42 Echogram of sub-basin P05-G.

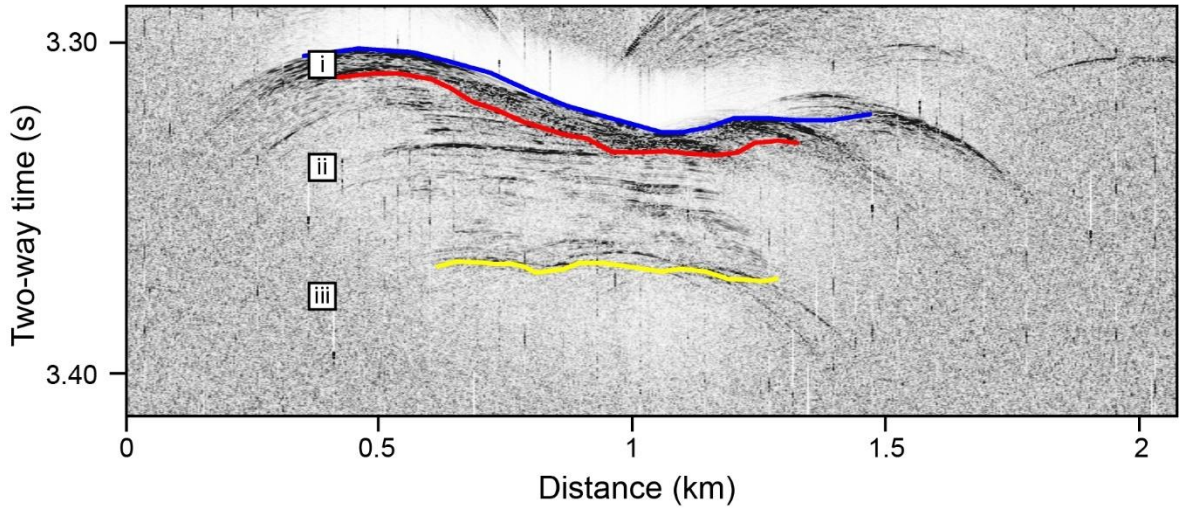

Figure C.43 Echogram of sub-basin P05-H.

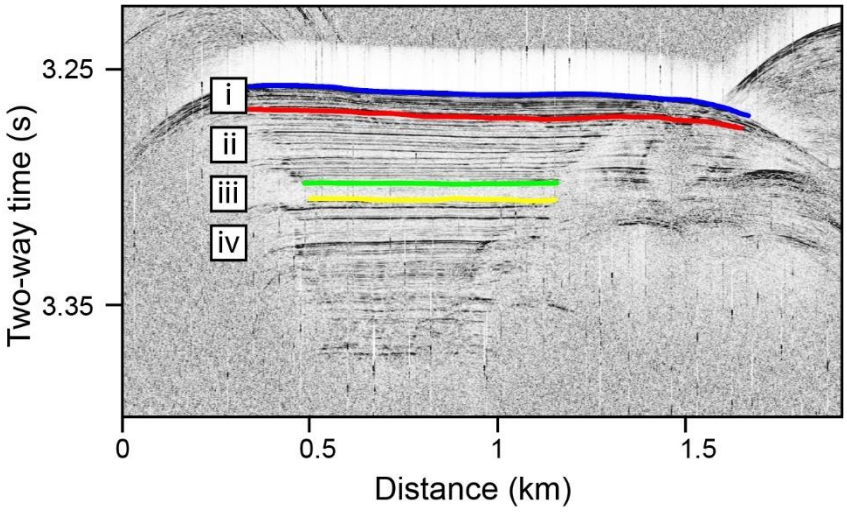

Figure C.44 Echogram of slope deposit P05-1.

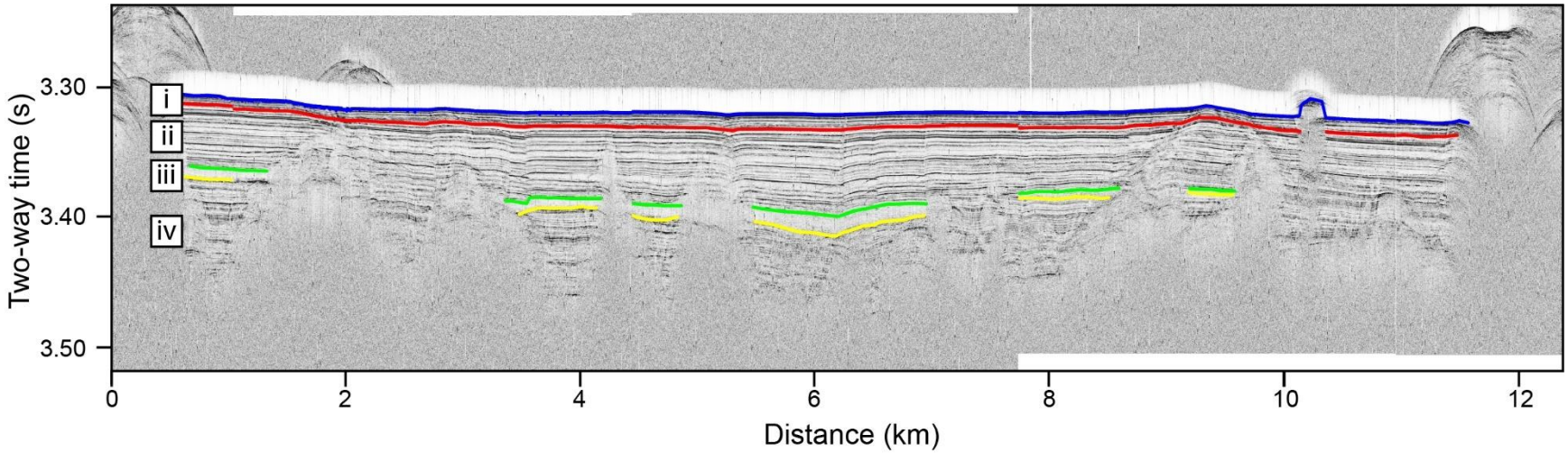

Figure C.45 Echogram of sub-basin P05-I.

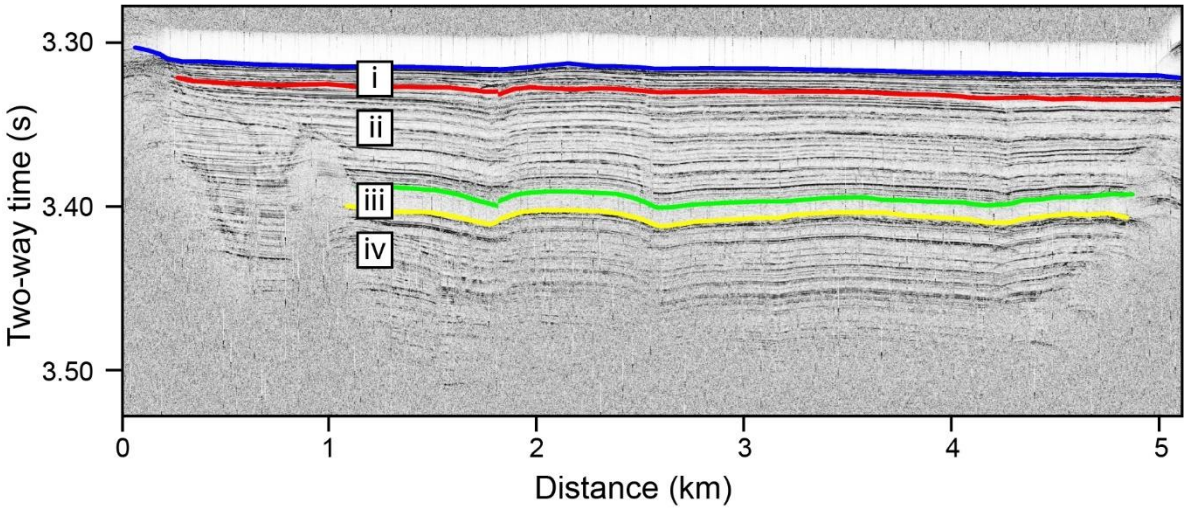

Figure C.46 Echogram of sub-basin P05-J.

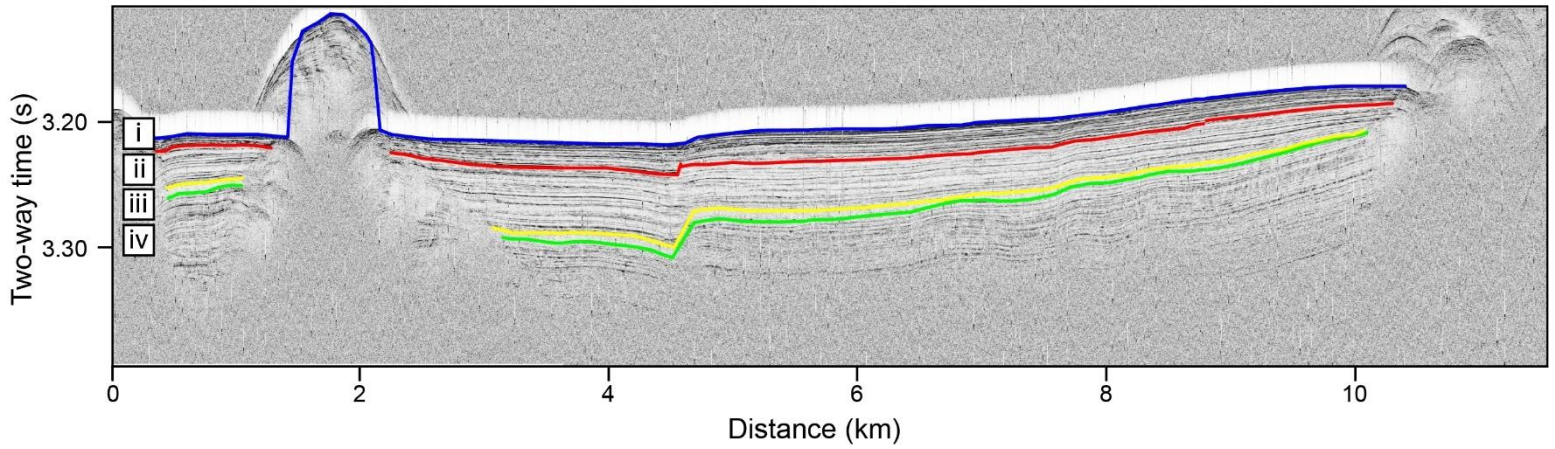

Figure C.47 Echogram of sub-basin P05-K.

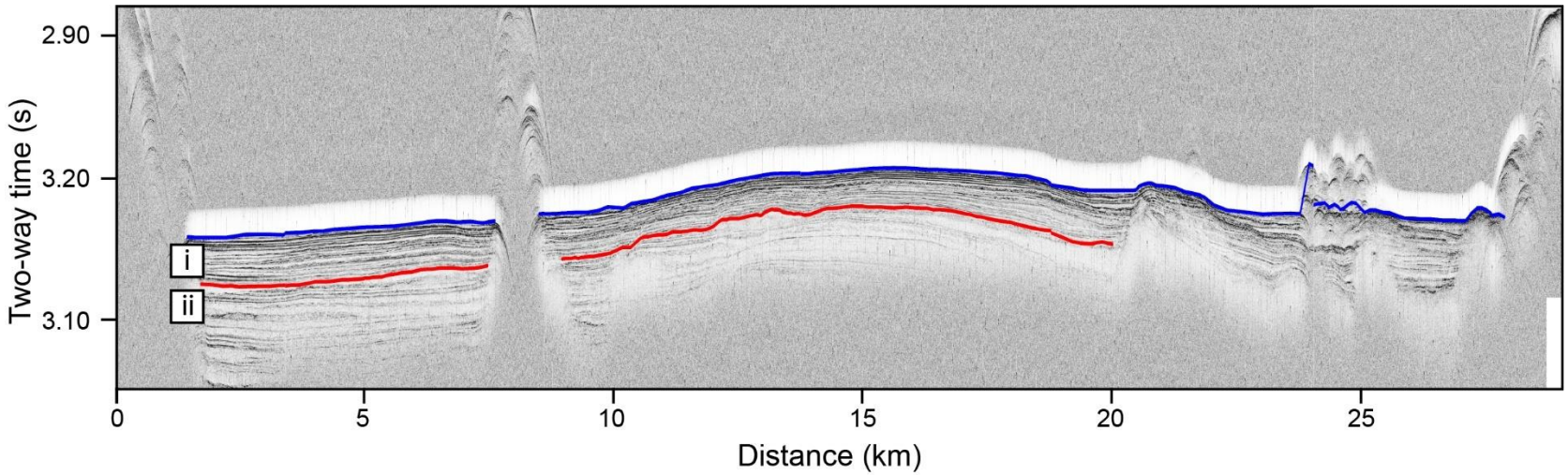

Figure C.48 Echogram of sub-basin P05-L.

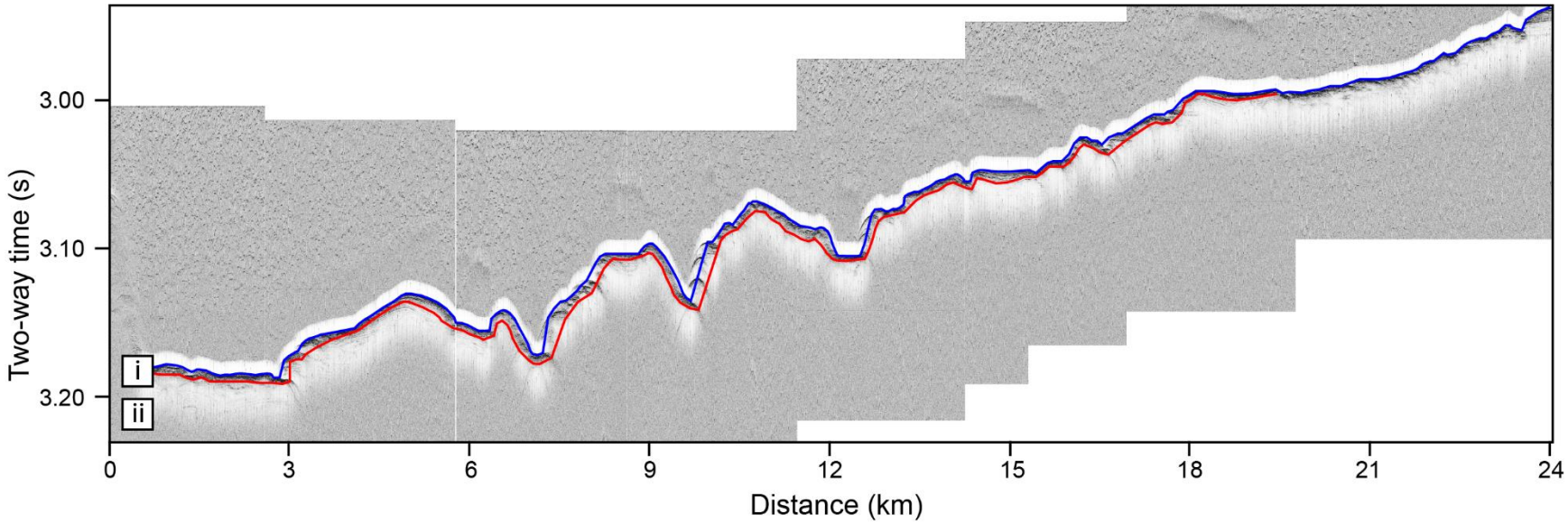

Figure C.49 Echogram of sub-basin P05-M.

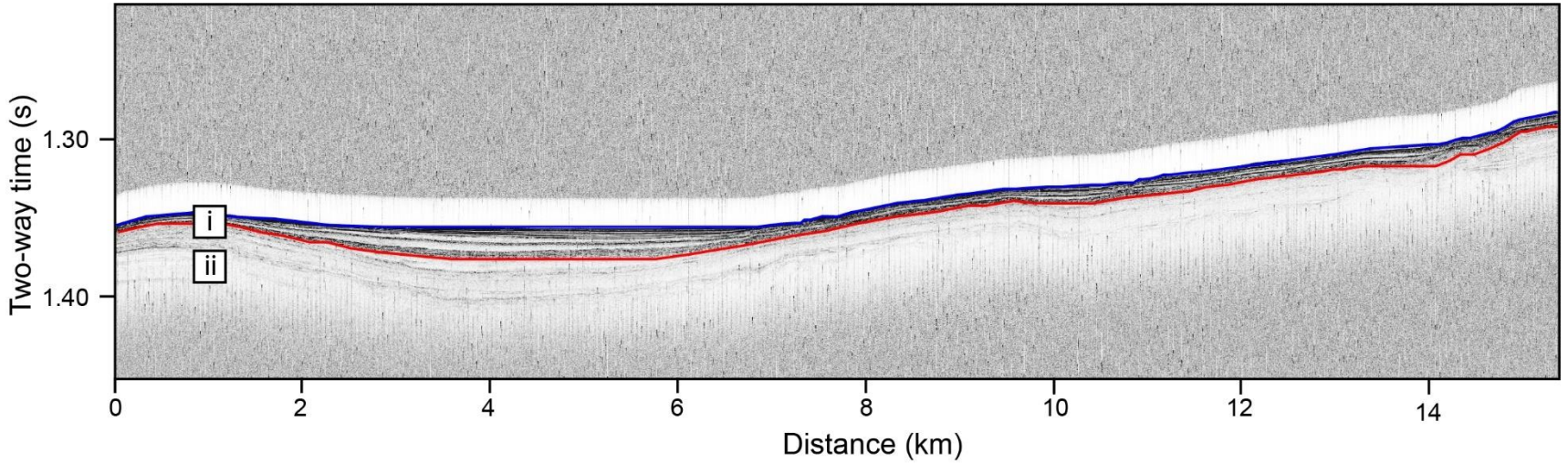

Figure C.50 Echogram of sub-basin P05-N.

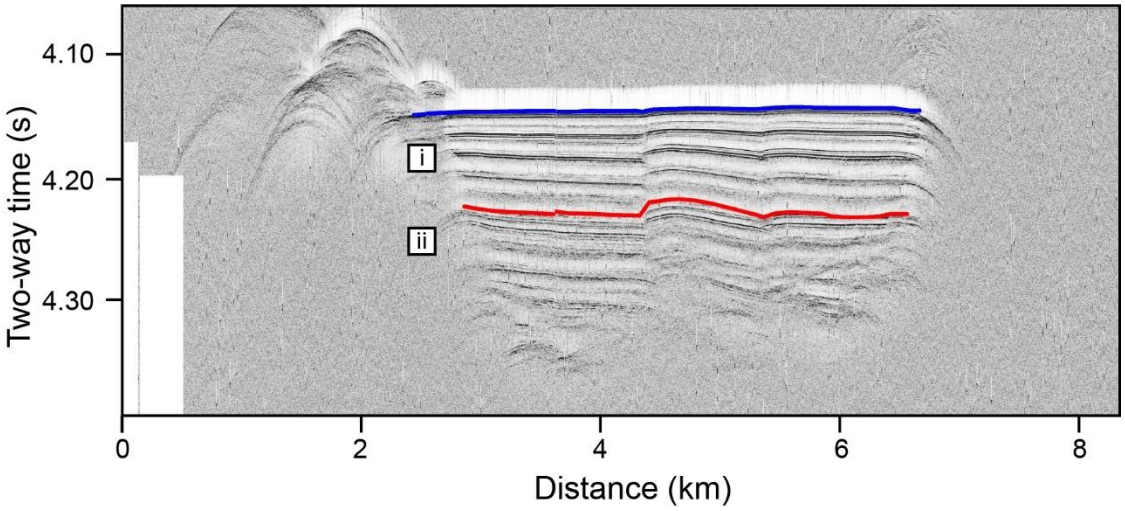

Figure C.51 Echogram of sub-basin P06-A.

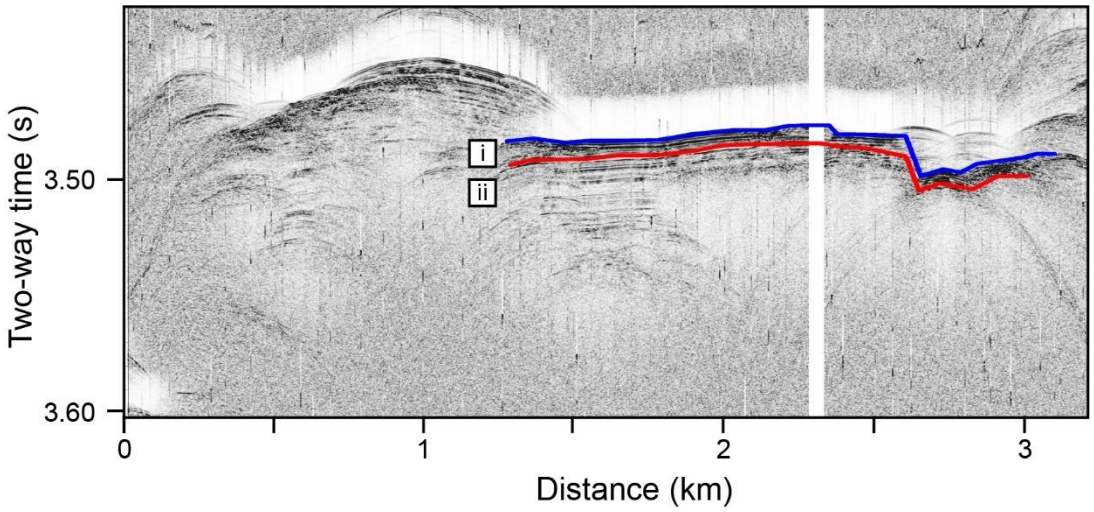

Figure C.52 Echogram of sub-basin P06-B.

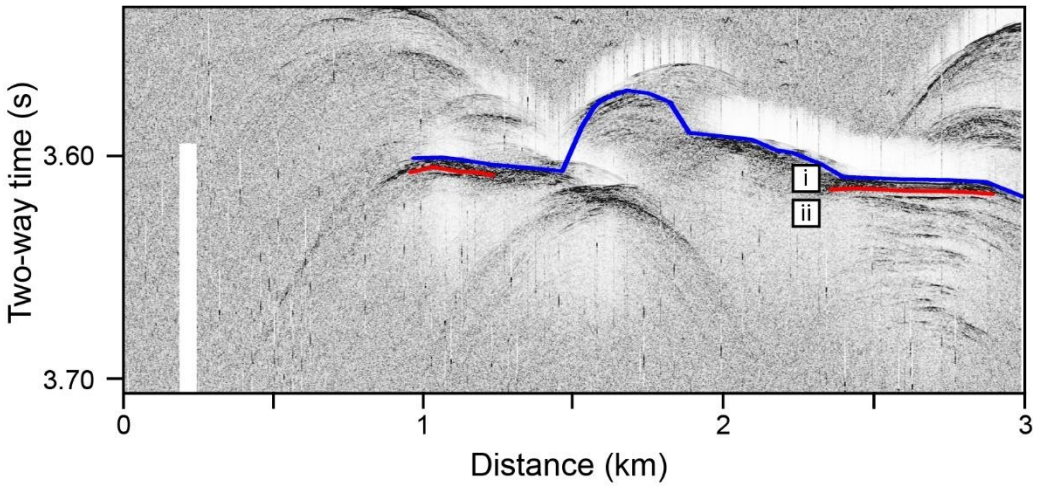

Figure C.53 Echogram of sub-basin P06-C.

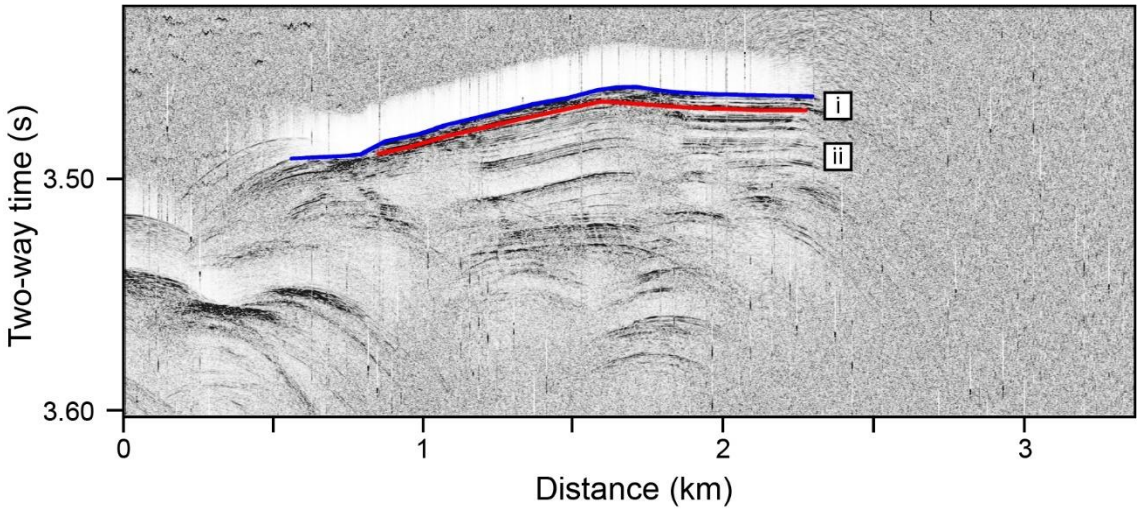

Figure C.54 Echogram of slope deposit P06-1.

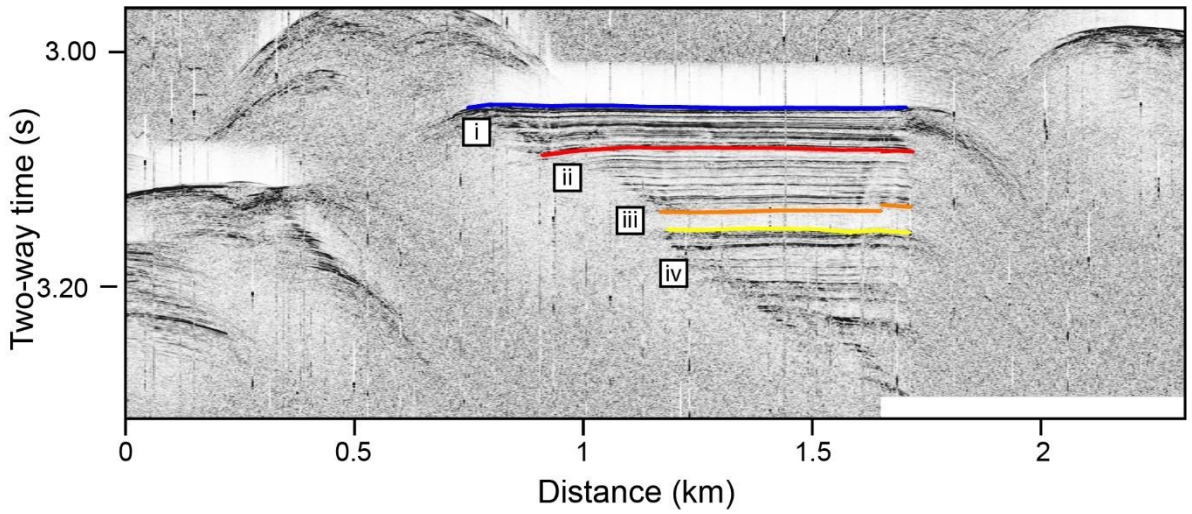

Figure C.55 Echogram of sub-basin P06-D.

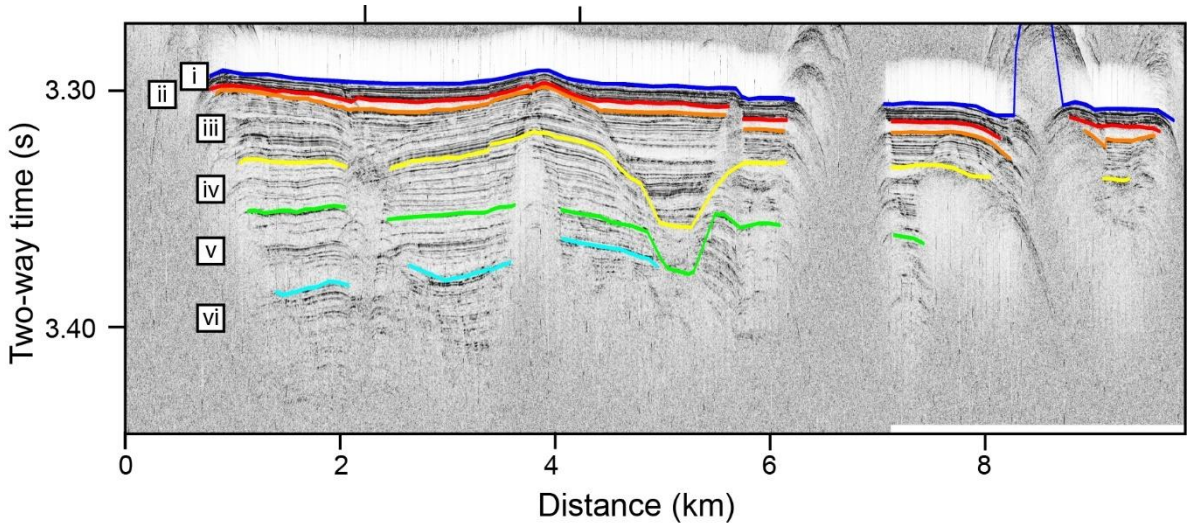

Figure C.56 Echogram of sub-basin P06-E.

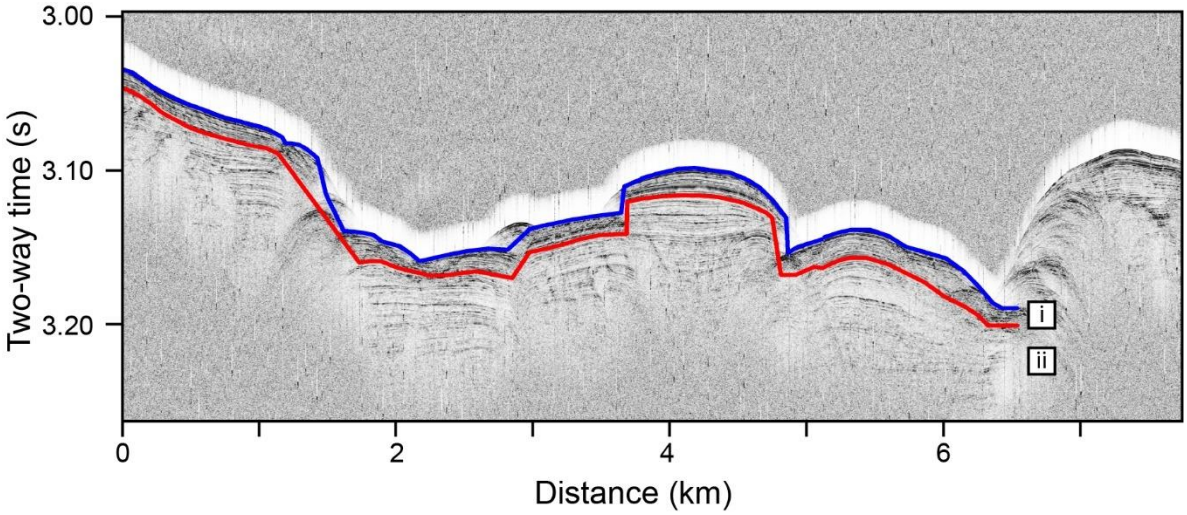

Figure C.57 Echogram of sub-basin P06-F.

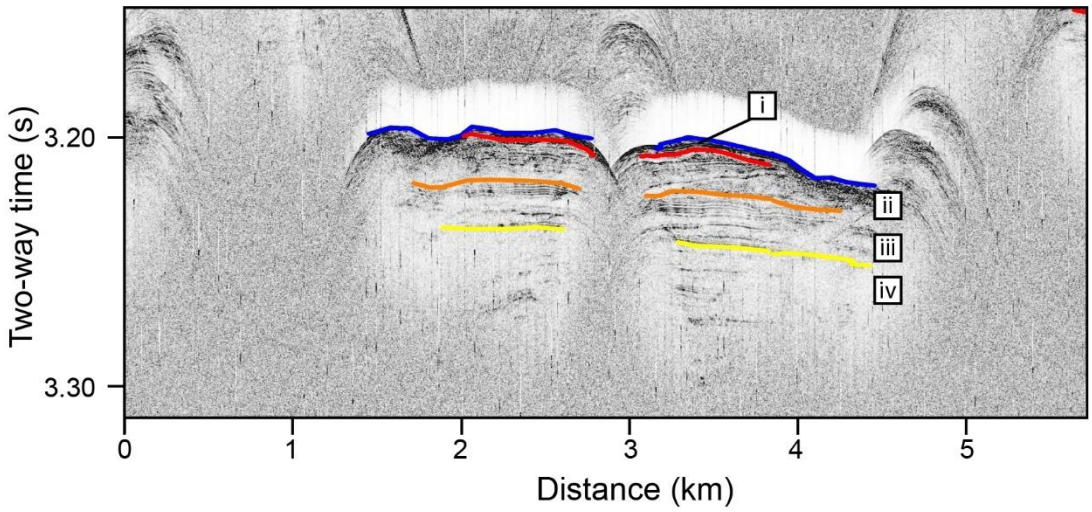

Figure C.58 Echogram of sub-basin P06-G.

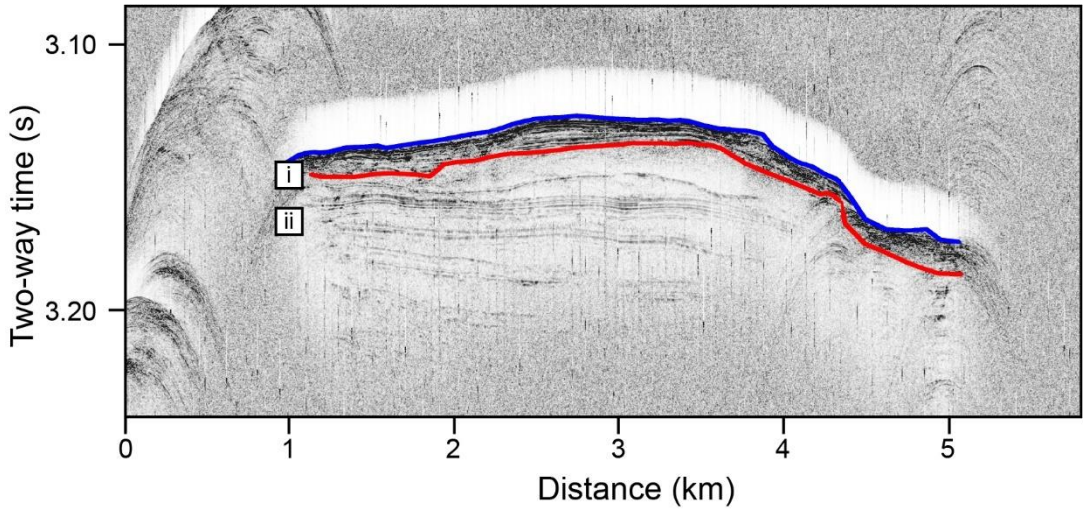

Figure C.59 Echogram of sub-basin P06-H.

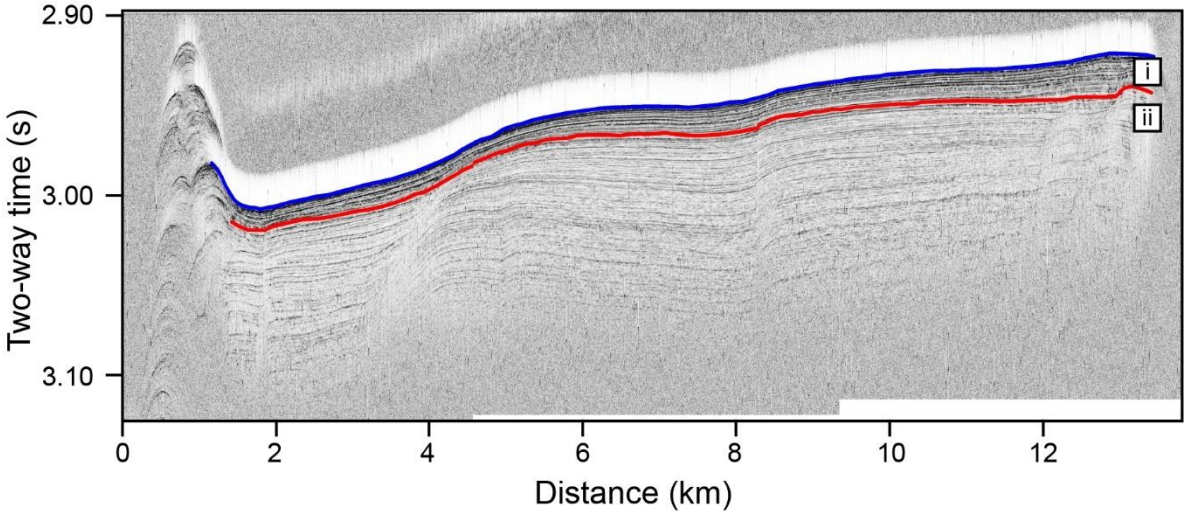

Figure C.60 Echogram of sub-basin P06-I.

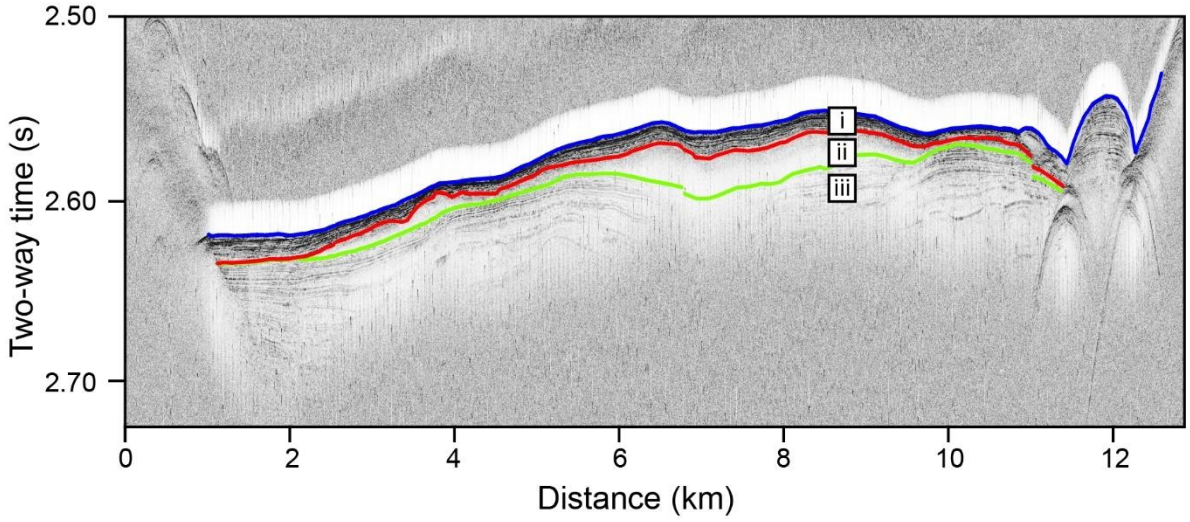

Figure C.61 Echogram of sub-basin P06-J.

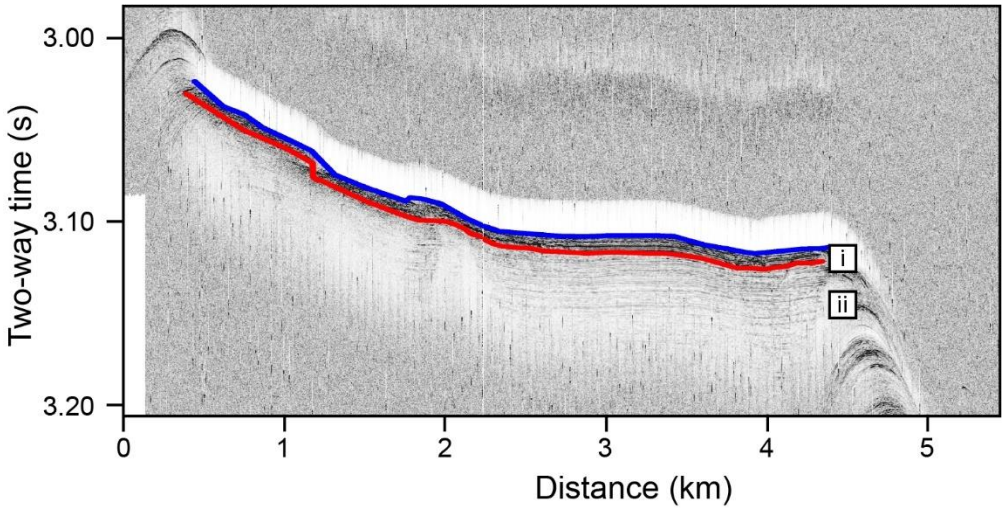

Figure C.62 Echogram of sub-basin P06-K.

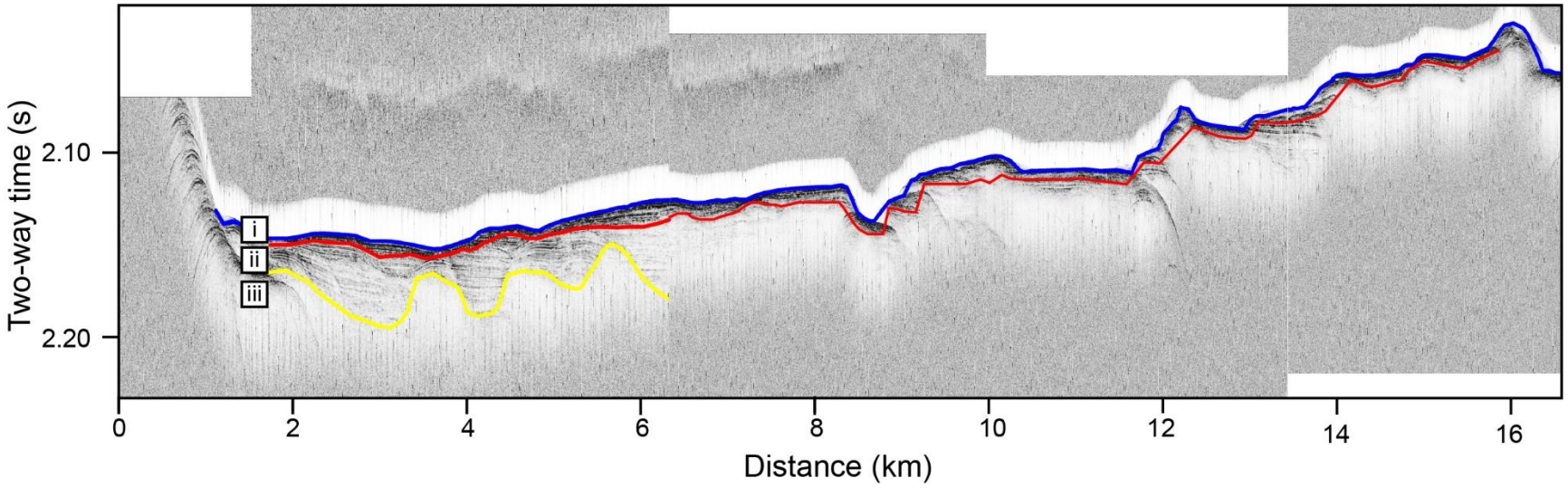

Figure C.63 Echogram of slope deposit P06-2.

APPENDIX D – Sub-Basin Database

Table D.1 P03 Sub-Basin Database

				Total sediment thickness				Sedimentary unit thickness					
Sub-Basin Group	**Sub-basin**	**Width (km)**	**Depth (m)**	**(s TWT)**	**(m)**	**Sedimentary Unit**	**Echo facies**	**(s TWT)**	**(m)**	**Prox. Value (unit 1)**	**Sediment-basement contact visible in Parasound?**	**Latitude**	**Longitude**
Western ELSC	A	2	-2598.3	0.075	57.0	P03-A-i	6A	0.075	57.0	NA	No	-17.33352119	-176.26249310
	B	1.4	-2225.6	0.027	20.5	P03-B-i	1	0.013	9.9	6	Yes	-17.33002429	-176.03200458
						P03-B-ii	3B	0.014	10.6				
	C	1.3	-2146.4	0.042	31.9	P03-C-i	6A	0.042	31.9	NA	No	-17.32988239	-175.99048248
	D	0.8	-2123	0.024	18.2	P03-D-i	3A	0.024	18.2	4	Yes	-17.33018963	-175.85669149
	E	1.5	-2070.6	0.024	18.2	P03-E-i	6A	0.024	18.2	NA	No	-17.33027756	-175.80122701
	F	1.7	-2042.3	0.013	9.9	P03-F-i	6A	0.013	9.9	NA	Yes	-17.33026380	-175.72640332
Eastern ELSC	G	0.96	-2181.4	0.031	23.6	P03-G-i	5	0.031	23.6	1	Yes	-17.32960035	-175.67053848
	H	1.2	-2294.1	0.126	95.8	P03-H-i	1	0.04	30.4	6	Yes	-17.32975469	-175.65250379
						P03-H-ii	2	0.022	16.7				
						P03-H-iii	1	0.064	48.6				
	I	12	-2335.1	0.138	104.9	P03-I-i	1	0.021	16.0	6	Yes	-17.32999028	-175.54675537
						P03-I-ii	3B	0.021	16.0				
						P03-I-iii	2	0.012	9.1				
						P03-I-iv	3B	0.028	21.3				
						P03-I-v	3A	0.056	42.6				
	J	3.4	-2242.3	0.067	50.9	P03-J-i	3B	0.067	50.9	5	Yes	-17.32991209	-175.41616690
	K	0.83	-2341.8	0.026	19.8	P03-K-i	3A	0.026	19.8	4	No	-17.33042067	-175.35691964
	L	6.2	-2374.8	0.038	28.9	P03-L-i	1	0.009	6.8	6	Yes	-17.33001409	-175.24761126
						P03-L-ii	5	0.029	22.0				
	M	1.9	-2059.2	0.049	37.2	P03-M-i	1	0.049	37.2	6	Yes	-17.33056573	-175.21098044
	N	25.8	-2376.1	0.42	319.2	P03-N-i	1	0.02	15.2	6	No	-17.32998844	-175.03339433
						P03-N-ii	3B	0.023	17.5				
						P03-N-iii	1	0.017	12.9				
						P03-N-iv	1	0.01	7.6				
						P03-N-v	2	0.02	15.2				
						P03-N-vi	3B	0.085	64.6				
						P03-N-vii	X	0.245	186.2				
Tofua Arc	1	1.3	-1916.5	0.147	111.7	P03-1-i	1	0.02	15.2	6	No	-17.32954565	-174.83909136
						P03-1-ii	3B	0.06	45.6				
						P03-1-iii	X	0.067	50.9				
FRSC	P	1	-2797.6	0.244	185.4	P03-P-i	5	0.028	21.3	1	No	-17.32942482	-174.68756854
						P03-P-ii	X	0.216	164.2				
	Q	1.8	-2818.3	0.168	127.7	P03-Q-i	5	0.026	19.8	1	No	-17.32989264	-174.65024917
						P03-Q-ii	3A	0.092	69.9				
						P03-Q-iii	X	0.05	38.0				
	R	0.9	-2906.7	0.117	88.9	P03-R-i	5	0.117	88.9	1	Yes	-17.32944560	-174.62281272
	S	2.9	-3042.2	0.143	108.7	P03-S-i	3A	0.043	32.7	4	Yes	-17.33006585	-174.55288764
						P03-S-ii	5	0.1	76.0				
	T	2.5	-2220.7	0.112	85.1	P03-T-i	5	0.077	58.5	1	No	-17.33002260	-174.43814042
						P03-T-ii	X	0.035	26.6				
Tofua Arc	U	3	-1783.1	0.454	345.0	P03-U-i	1	0.014	10.6	6	No	-17.32993379	-174.28020303
						P03-U-ii	3A	0.028	21.3				
						P03-U-iii	X	0.412	313.1				
	V	20	-1430	1.256	954.6	P03-V-i	5	0.009	6.8	1	No	-17.32965427	-174.09284583
						P03-V-ii	2	0.0395	30.0				
						P03-V-iii	X	1.2075	917.7				
	W	45	-1278.3	0.636	483.4	P03-W-i	1	0.003	2.3	6	No	-17.33008385	-173.65222391
						P03-W-ii	3B	0.061	46.4				
						P03-W-iii	X	0.572	434.7				

Table D.2 P04 Sub-Basin Database

				Total sediment thickness				Sedimentary unit thickness					
Sub-Basin Group	**Sub-basin**	**Width (km)**	**Depth (m)**	**(s TWT)**	**(m)**	**Sedimentary Unit**	**Echo facies**	**(s TWT)**	**(m)**	**Prox. Value (unit 1)**	**Sediment-basement contact visible in Parasound?**	**Latitude**	**Longitude**
Eastern ELSC	A	3.24	-2432.1	0.154	117.0	P04-A-i	1	0.014	10.6	6	No	-17.79628883	-175.50618408
						P04-A-ii	3A	0.046	35.0				
						P04-A-iii	3B	0.035	26.6				
						P04-A-iv	3B	0.059	44.8				
	B	6.43	-2498.7	0.125	95.0	P04-B-i	1	0.015	11.4	6	Yes	-17.82354949	-175.47046125
						P04-B-ii	3A	0.044	33.4				
						P04-B-iii	3B	0.066	50.2				
	C	23.97	-2377.6	0.292	221.9	P04-C-i	1	0.019	14.4	6	No	-17.79886837	-175.32900010
						P04-C-ii	3A	0.053	40.3				
						P04-C-iii	3A	0.064	48.6				
						P04-C-iv	X	0.156	118.6				
	D	34	-2276.8	0.59	448.4	P04-D-i	1	0.01	7.6	6	No	-17.79984964	-174.99122336
						P04-D-ii	3C	0.014	10.6				
						P04-D-iii	3B	0.017	12.9				
						P04-D-iv	X	0.549	417.2				
Tofua Arc	1	4.7	-2031.2	0.053	40.3	P04-1-i	1	0.053	40.3	6	No	-17.80017865	-174.81467221
	E	3.36	-1240.2	0.062	47.1	P04-E-i	1	0.006	4.6	6	Yes	-17.79996002	-174.71750650
						P04-E-ii	3A	0.056	42.6				
	F	3.2	-1393.5	0.023	17.5	P04-F-i	1	0.004	3.0	6	Yes	-17.79965297	-174.68671765
			-1393.5	0.023	17.5	P04-F-ii	5	0.019	14.4				
FRSC	G	6.7	-2226.1	0.339	257.6	P04-G-i	3B	0.02	15.2	5	No	-17.79995651	-174.58576150
						P04-G-ii	5	0.039	29.6				
						P04-G-iii	X	0.28	212.8				
	H	4.9	-1960.1	0.037	28.1	P04-H-i	5	0.037	28.1	1	No	-17.79994882	-174.48408999
Tofua Arc	2	5.7	-2355.7	0.155	117.8	P04-2-i	5	0.038	28.9	1	No	-17.80051594	-174.44685331
						P04-2-ii	X	0.117	88.9				
	3	4.1	-958.58	0.226	171.8	P04-3-i	5	0.046	35.0	1	No	-17.79963695	-174.35229917
						P04-3-ii	X	0.18	136.8				
	I	14.2	-1247	0.042	31.9	P04-I-i	1	0.01	7.6	6	No	-17.79959250	-174.30394358
						P04-I-ii	5	0.032	24.3				

Table D.3 P05 Sub-Basin Database

				Total sediment thickness				Sedimentary unit thickness					
Sub-Basin Group	**Sub-basin**	**Width (km)**	**Depth (m)**	**(s TWT)**	**(m)**	**Sedimentary Unit**	**Echo facies**	**(s TWT)**	**(m)**	**Prox. Value (unit 1)**	**Sediment-basement contact visible in Parasound?**	**Latitude**	**Longitude**
CLSC	A	7.86	-2560.7		0.0	P05-A-i	6B	NA	NA	NA	NA	-18.20035890	-176.31056095
	B	1.7	-2503.9		0.0	P05-B-i	6B	NA	NA	NA	NA	-18.20017013	-176.20780273
Nodal Basins	C	2.58	-3007	0.059	44.8	P05-C-i	1	0.009	6.8	6	Yes	-18.20029471	-176.03404549
						P05-C-ii	3A	0.05	38.0				
	D	8.44	-3182.1	0.314	238.6	P05-D-i	1	0.005	3.8	6	No	-18.20006718	-175.86370453
						P05-D-ii	4	0.087	66.1				
						P05-D-iii	3B	0.035	26.6				
						P05-D-iv	2	0.019	14.4				
						P05-D-v	3A	0.068	51.7				
						P05-D-vi	X	0.1	76.0				
Western ELSC	E	1.76	-2574	0.07	53.2	P05-E-i	3A	0.07	53.2	4	Yes	-18.20008861	-175.75225995
	F	1.48	-2431.3	0.066	50.2	P05-F-i	1	0.009	6.8	6	No	-18.19967759	-175.69134678
						P05-F-ii	3A	0.057	43.3				
	G	1.34	-2470.3	0.077	58.5	P05-G-i	1	0.008	6.1	6	Yes	-18.20002451	-175.64950758
						P05-G-ii	3B	0.02	15.2				
						P05-G-iii	2	0.009	6.8				
						P05-G-iv	3B	0.04	30.4				
	H	1.03	-2496.9	0.041	31.2	P05-H-i	5	0.005	3.8	1	Yes	-18.20002409	-175.62452430
						P05-H-ii	3A	0.036	27.4				
Eastern ELSC	1	1.6	-2446	0.113	85.9	P05-1-i	1	0.011	8.4	6	Yes	-18.20012725	-175.59099470
						P05-1-ii	3B	0.027	20.5				
						P05-1-iii	2	0.007	5.3				
						P05-1-iv	3B	0.068	51.7				
	I	11.7	-2490.5	0.146	111.0	P05-I-i	1	0.012	9.1	6	Yes	-18.20023798	-175.52440405
						P05-I-ii	3B	0.064	48.6				
						P05-I-iii	2	0.015	11.4				
						P05-I-iv	3B	0.055	41.8				
	J	5.6	-2491.1	0.245	186.2	P05-J-i	1	0.013	9.9	6	No	-18.20010527	-175.43092406
						P05-J-ii	3B	0.062	47.1				
						P05-J-iii	2	0.01	7.6				
						P05-J-iv	3B	0.077	58.5				
						P05-J-v	X	0.083	63.1				
	K	8.4	-2400.4	0.256	194.6	P05-K-i	1	0.023	17.5	6	No	-18.20016447	-175.33749056
						P05-K-ii	3B	0.032	24.3				
						P05-K-iii	2	0.008	6.1				
						P05-K-iv	3B	0.049	37.2				
						P05-K-v	X	0.144	109.4				
	L	28.5	-2282.9	0.4	304.0	P05-L-i	3B	0.034	25.8	5	No	-18.19987644	-175.19590661
						P05-L-ii	3A	0.096	73.0				
						P05-L-iii	X	0.27	205.2				
Tofua Arc	M	20	-1348	1.312	997.1	P05-M-i	1	0.012	9.1	6	No	-18.20006686	-174.62723187
						P05-M-ii	3A	0.032	24.3				
						P05-M-iii	X	1.268	963.7				
	N	23	-1028.1	1.149	873.2	P05-N-i	1	0.01	7.6	6	No	-18.20013118	-174.40998820
						P05-N-ii	3A	0.064	48.6				
						P05-N-iii	X	1.075	817.0				

Table D.4 P06 Sub-Basin Database

				Total sediment thickness				Sedimentary unit thickness					
Sub-Basin Group	**Sub-basin**	**Width (km)**	**Depth (m)**	**(s TWT)**	**(m)**	**Sedimentary Unit**	**Echo facies**	**(s TWT)**	**(m)**	**Prox. Value (unit 1)**	**Sediment-basement contact visible in Parasound?**	**Latitude**	**Longitude**
Nodal Basins	A	6.75	-3114.2	0.198	150.5	P06-A-i	4	0.084	63.8	3	Yes	-18.72968279	-175.83490341
						P06-A-ii	3A	0.114	86.6				
Western ELSC	B	2.2	-2615.1	0.054	41.0	P06-B-i	1	0.006	4.6	6	Yes	-18.73006238	-175.68954189
						P06-B-ii	3B	0.048	36.5				
	C	2.01	-2709.7	0.064	48.6	P06-C-i	1	0.006	4.6	6	Yes	-18.72978512	-175.64321517
						P06-C-ii	3A	0.058	44.1				
	1	1.6	-2603.5	0.113	85.9	P06-1-i	1	0.004	3.0	6	Yes	-18.72972472	-175.62648904
						P06-1-ii	3A	0.109	82.8				
	D	1.7	-2420	0.127	96.5	P06-D-i	1	0.018	13.7	6	Yes	-18.73025829	-175.59795505
						P06-D-ii	3B	0.026	19.8				
						P06-D-iii	2	0.009	6.8				
						P06-D-iv	3A	0.074	56.2				
Eastern ELSC	E	8.94	-2472.5	0.129	98.0	P06-E-i	1	0.007	5.3	6	Yes	-18.72993573	-175.56927304
						P06-E-ii	2	0.004	3.0				
						P06-E-iii	3B	0.023	17.5				
						P06-E-iv	3A	0.02	15.2				
						P06-E-v	3A	0.031	23.6				
						P06-E-vi	3A	0.044	33.4				
	F	7.3	-2365.5	0.09	68.4	P06-F-i	1	0.014	10.6	6	Yes	-18.72997320	-175.45805114
						P06-F-ii	3B	0.076	57.8				
	G	3.5	-2403.3	0.199	151.2	P06-G-i	1	0.004	3.0	6	No	-18.72998791	-175.38682177
						P06-G-ii	3B	0.017	12.9				
						P06-G-iii	3B	0.021	16.0				
						P06-G-iv	3A	0.043	32.7				
						P06-G-v	X	0.114	86.6				
	H	4.33	-2347	0.283	215.1	P06-H-i	1	0.013	9.9	6	No	-18.73013872	-175.35243049
						P06-H-ii	3A	0.072	54.7				
						P06-H-iii	X	0.198	150.5				
	I	13.33	-2215	0.519	394.4	P06-I-i	1	0.016	12.2	6	No	-18.73008377	-175.27293486
						P06-I-ii	3B	0.096	73.0				
						P06-I-iii	X	0.407	309.3				
Tofua Arc	J	13.45	-1940.6	1.075	817.0	P06-J-i	1	0.008	6.1	6	No	-18.73129379	-175.09689372
						P06-J-ii	2	0.008	6.1				
						P06-J-iii	3A	0.064	48.6				
						P06-J-iv	X	0.995	756.2				
	K	3.77	-1437	0.313	237.9	P06-K-i	1	0.009	6.8	6	No	-18.72902049	-174.95668337
						P06-K-ii	3B	0.059	44.8				
						P06-K-iii	X	0.245	186.2				
	2	15.6	-1609.9	1.422	1080.7	P06-2-i	1	0.006	4.6	6	No	-18.73001060	-174.90247819
						P06-2-ii	3B	0.029	22.0				
						P06-2-iii	2	0.031	23.6				
						P06-2-iv	X	1.356	1030.6				